Doctor of Philosophy

Engineering 2D Graphitic Carbon Nitride/Graphene Nanosheets for Enhancing Photocatalytic Hydrogen Evolution under Visible Light Irradiation

The Graduate School of the University of Ulsan

Department of Chemical Engineering

Dang Thanh Truong

Engineering 2D Graphitic Carbon Nitride/Graphene Nanosheets for Enhancing Photocatalytic Hydrogen Evolution under Visible Light Irradiation

by

Dang Thanh Truong

Submitted to Graduate School of the University of Ulsan

in Partial Fulfillment of the Requirements for the Degree of

Doctor of Philosophy

at the

UNIVERSITY OF ULSAN

June 2023

Author.....

Department of Chemical Engineering

June 9, 2023

Certified by.....

Chung Jin Suk

Professor of Chemical Engineering

Thesis Supervisor

Accepted by.....

Sung Gu Kang

Professor of Chemical Engineering

Chairman, Dean of the Department of Chemical Engineering

Engineering 2D Graphitic Carbon Nitride/Graphene Nanosheets for Enhancing Photocatalytic Hydrogen Evolution under Visible Light Irradiation

This certifies that the dissertation

of Dang Thanh Truong is approved

_____

Committee Chair Prof. Sung Gu Kang

_____

Committee Vice-chair Prof. Chung Jin Suk

_____

Committee Member Prof. Eun Woo Shin

_____

Committee Member Prof. Seung Hyun Hur

_____

Committee Member Dr. Hang Su Woo

Department of Chemical Engineering

University of Ulsan, Korea

June 2023

Engineering 2D Graphitic Carbon Nitride/Graphene Nanosheets for Enhancing Photocatalytic Hydrogen Evolution under Visible Light Irradiation

by

Dang Thanh Truong

Submitted to Graduate School of the University of Ulsan

on June 9, 2023, in Partial Fulfillment of the Requirements for the Degree of

Doctor of Philosophy

ABSTRACT

Solar energy is the most sustainable energy replacement for fossil fuels as it is a plentiful, widely distributed, and continuously renewable source of energy. Water is the basis for all life on Earth, which contains hydrogen and oxygen. Water is considered the most favorable hydrogen energy carrier because it has the potential to exist for as long as civilization. The polymeric semiconductor, g-C_3N_4 as a novel noble metal-free photocatalyst with a bandgap of 2.7 eV, a delocalized π system, and diverse synthetic modularity has emerged as a promising visible light-responsive photocatalyst due to its facile synthesis, appealing optical bandgap and semiconducting properties, high chemical and thermal stability as well as a variety of textures and structures. Graphene, a sheet of sp^2-bonded carbon atoms packed in a honeycomb lattice one atom thick, is used as a supporting material for photocatalysts due to its superior electron mobility at room temperature and its superior electrical conductivity, which allows it efficiently to accept and mediate photoinduced electrons from excited electron donors. More effective separation and migration of electron-hole pairs prevent the recombination of charge carriers. Hence, photocatalytic hydrogen evolution reaction by half-reaction of water-splitting has been intensively studied for green, low-cost, and large-scale production of H_2 fuels. This thesis focuses on the nanostructural design of 2D graphitic carbon nitride, graphene, and the engineering oxidation state of platinum cocatalyst for photocatalytic green hydrogen production.

In order to develop an advanced nanostructure of graphitic carbon nitride to maximize catalytic accessible active sites, thus reducing material cost and enhancing the efficiency of the photocatalytic process for commercial technologies, this work provides a strategy to exfoliate bulk graphitic carbon nitride into a single-layer, generating holey structure of graphitic carbon nitride for enhancing photoactivity and discovering the formation of self-assembled graphene phenomenon. Furthermore, this work studies fundamental processes that occur in solar-driven hydrogen production by photocatalyst systems. The online gas chromatography assessment method and an optimization method for hydrogen evolution performance were introduced for a more accurate and transparent photocatalytic hydrogen production measurement benchmark. Multiple characterizations have been performed to understand crystallographic nature, chemical composition, morphology and microstructure, optical properties, photoinduced charge carrier separation and transfer, and newly phenomenon of graphene formation via the solvothermal treatment of graphitic carbon nitride. Moreover, density functional theory calculations were applied to study the adsorption energy of used organic solvents on g-C_3N_4 sheets and the charge density differences for all adsorbates on the s-heptazine sheet. The distinguished behaviors of interaction between the O atom of the adsorbate and the C atom of the sheet further verified the mechanism of solvolysis of graphitic carbon nitride to form a holey-defect structure. Methyl alcohol, isopropyl alcohol, tetrahydrofuran, and dimethylformamide were chosen for exfoliating and modifying graphitic carbon nitride sheets based on their compatibility with graphitic carbon nitride in Hansen parameters. Uniformly holey-defects on 2D graphitic carbon nitride nanosheets were successfully engineered using tetrahydrofuran solvent in a facile solvothermal process. The introduction of N vacancies in heptazine units and the formation of the holey structure of tetrahydrofuran-modified graphitic carbon nitride (C_3N_4-THF) sample led to excellent photocatalytic performance due to enhanced mass transfer, shortening of the charge diffusion lengths, increased charge separation during the photocatalysis process, and maximizing accessible reducing and oxidizing active sites. As a result, the C_3N_4-THF sample achieved superior photocatalytic activity with a hydrogen evolution rate at the stationary point as high as 31,256.9 $\mu mol\ h^{-1}\ g^{-1}$ under 1 Sun illumination of a Solar Simulator, which was 13.9 times higher than that of the bulk sample.

Furthermore, this work studies the solid-state structure transformation through the solvothermal treatment of bulk graphitic carbon nitride in an environmentally sustainable ethyl

alcohol solvent for photocatalytic mass production of green hydrogen. The new structure of grid-like monolayered graphitic carbon nitride nanosheets was achieved using a facile solvothermal process. The formation of self-assembled graphene on graphitic carbon nitride during the process facilitated charge transfer and separation on the photocatalyst, as confirmed by density functional theory calculations. A higher proportion and a better distribution of oxidized platinum cocatalyst enable the ability to suppress hydrogen oxidation reactions, which prefer the direction of hydrogen generation.

In order to get a step closer to a homogeneous photocatalyst, this work generates a highly dispersion of holey graphene/graphitic carbon nitride composite in aqueous by using holey graphene as the carrier in 2D/2D photocatalyst hybrid. A high-surface-area-inspired water-soluble holey graphene/graphitic carbon nitride colloidal nanoparticles for hydrogen evolution was successfully synthesized using a mere mixing process of holey graphene oxide with oxidized graphitic carbon nitride, followed by hydrogen reduction in aqueous to restore the initial photocatalytic active sites but maintain highly soluble in reaction media.

The recent extreme weather gets a boost from climate change and the global energy security conundrum has posed extensive studies on boosting the conversion of solar energy to chemical energy through photocatalysis. The demonstrations of photocatalytic solar green hydrogen production based on a facile method of synthesizing an advanced nanostructure of 2D graphitic carbon nitride/graphene photocatalyst and the optimization of the performance evaluation system and assessment method for this photocatalyst indicates the large-scale applicability viability as well as technical challenges toward practical mass green hydrogen production.

ACKNOWLEDGMENTS

With whom I've had the privilege to interact over the course of my Ph.D. journey, I've been able to complete this thesis because of the passion and support of a number of dedicated and supportive individuals. I would like to take this opportunity to acknowledge many of them here, and to assure those whom I have missed that I am equally grateful for their support as well.

I wish to thank, first and foremost, my advisor Prof. Jin Suk Chung, for his unwavering support and for providing me with unfathomable opportunities for collaborations, research facilities, and professional growth. I want to express my special appreciation and thanks to Prof. Chung, who has mentored me tremendously. He has had the greatest professional influence on my improvement during my master's and doctoral course. With his kind support and full advice, I have improved my weaknesses, developed my abilities, and exploited my strengths. I am supremely grateful to my advisor for his kind guidance, full support, and enthusiasm.

Prof. Chung has also attracted an exceptional group of talented individuals who comprise his research group. Throughout this journey, I have learned a great deal from all of them, along with their companionship. I want to specifically thank Dr. Tahereh Mahvelati-Shamsabadi for all of her research help, scientifically encouraging, motivating me to achieve my goals, and her friendship in the lab and the office.

I want to explicitly thank Prof. Eun Woo Shin, Prof. Sung Gu Kang, Prof. Koo-Hyun Chung, Prof. Nam T.S. Phan, Dr. Viet Hung Pham, and Prof. Bao Khanh Vu for their relentless and kind support during this great journey. Special thanks go to Ms. Thi Kim Anh Nguyen and Ms. Vo Kim Hieu Van, who built the initial work together with me and made hours of nanostructure measurement of my materials, respectively. Throughout my study, Dr. K. C. Bhamu built theoretical concepts with me and performed the DFT calculations that contributed not only to my scientific progress but also enabled me to gain a deeper understanding of some fascinating phenomena.

I also want to thank my doctoral committee members, including Prof. Eun Woo Shin, Prof. Seung Hyun Hur, Prof. Sung Gu Kang, and Dr. Hang Su Woo for spending their time serving my

committee, reviewing my dissertation, and providing lots of valuable comments and suggestions on the work.

I must give thanks to all my lab members and collaborators for having the pleasure of working and making friends with talented and warm individuals. I would not have accomplished my great work without their collaboration, discussion, and support. I would like to thank all of my friends around the world, who are always by my side for sharing and encouraging me during this time.

Lastly, my family has been an integral part of my life journey and my Doctoral journey. I can't thank them enough for providing me with all I've needed. No words can express how grateful I am to my beloved sisters and brothers for all of the sacrifices and support they provided me so far. Thanks to their hard work and sacrifice, I hope I've taken advantage of the opportunities that they've given me.

Several foundations have contributed to enabling the possibility performed in this work. I thank the National Research Foundation of Korea (NRF) grant funded by the Korea government (MSIT) (No. 2020R1A4A4079954), the Regional Innovation Strategy (RIS) through the National Research Foundation of Korea (NRF) funded by the Ministry of Education (MOE)(2021RIS-003), and the Research Fund of the University of Ulsan.

This work is dedicated to my parents in Heaven,

for teaching me the value of hard work

and giving me a pure heart to pursue my passions.

This is just a small thank you.

Table of Contents

ABSTRACT ..... **i**

ACKNOWLEDGMENTS ..... **iv**

LIST OF FIGURES ..... **x**

LIST OF TABLES ..... **xvi**

CHAPTER 1 ..... **1**

1. Introduction **1**

1.1. Solar Light Harvesting 1

1.2. Hydrogen Economy 4

1.3. Photocatalytic Hydrogen Evolution 9

1.4. Graphitic Carbon Nitride 11

1.5. Graphene-based Photocatalytic Applications 16

1.6. Motivation 18

1.7. Thesis Scope 20

1.8. Thesis Procedures 22

CHAPTER 2 ..... **24**

2. Engineering Holey-defects on 2D Graphitic Carbon Nitride Nanosheets by Solvolysis in Organic Solvents **25**

2.1. Introduction 25

2.2. Experimental and Methods 27

2.2.1. Materials 27

2.2.2. Synthesis of Solvothermal Treatment G-C_3N_4 Photocatalyst 27

2.2.3. Photocatalytic H_2 Evolution 28

2.2.4. Characterizations 28

2.2.5. Electrochemical Measurement 29

2.2.6. Computational Methods 30

2.3. Results and Discussion 31

2.3.1. Synthetic Strategy to Design Holey-defects on g-C_3N_4 Nanosheets 31
2.3.2. Crystal Structure and Chemical Composition of Solvothermal Modified g-C_3N_4 33
2.3.3. The Morphology of Solvothermal Modified g-C_3N_4 45
2.3.4. Mechanism of Solvolysis of g-C_3N_4 to Form Holey-defects Structure 61
2.3.5. Optical Bandgap and Charge Carrier Separation and Transfer 68
2.3.6. Graphene Formation via The Solvothermal Treatment of g-C_3N_4 76
2.3.7. Photocatalytic Performance and Mechanism 81
2.3.7.1. Photocatalytic H_2 Evolution Performance Optimization 81
2.3.7.1.1. Equipment Calibration 81
2.3.7.1.2. Specific Reaction Conditions 84
2.3.7.1.2.1. Light Source Information 84
2.3.7.1.2.2. Reactor 87
2.3.7.1.2.3. Online GC Gas Measurement Method 89
2.3.7.1.3. Reaction Media 89
2.3.7.1.3.1. Water Quality 89
2.3.7.1.3.2. Photosentisizer 90
2.3.7.1.3.3. Temperature 90
2.3.7.1.4. Optimization H_2 Production Rate 90
2.3.7.2. Photocatalytic Performance 90
2.3.7.3. The AQY at The Stationary Point of C_3N_4-THF Calculation 97
2.3.8. Photocatalytic Parameters and Mechanism 102
2.4. Conclusions 106
CHAPTER 3 108
3. Oxidized Platinum Cocatalyst and Self-Assembled Graphene over Graphitic Carbon Nitride for Photocatalytic Hydrogen Evolution 109
3.1. Introduction 109
3.2. Experimental and Methods 111

3.3. Results and Discussion 124
3.4. Conclusion 156
CHAPTER 4 157
4. Highly Dispersion of Holey Graphene/g-C_3N_4 Composite for Photocatalytic Hydrogen Evolution Under Simulated Sunlight Irradiation 158
4.1. Introduction 158
4.2. Experimental and Methods 160
4.3. Results and Discussion 163
4.4. Conclusion 179
CHAPTER 5 180
5. Conclusions and Outlook 180
5.1. Summary 180
5.2. Outlook 182
5.2.1. Photoreforming of Graphene Oxide over Graphitic Carbon Nitride Photocatalyst 182
5.2.2. Artificial Leaf-like Structure of Atomic Metal on Graphene/Graphitic Carbon Nitride as Gradient Photocatalyst for Overall Water Splitting 183
References 186

LIST OF FIGURES

Figure 1. (a) Annual global energy consumption (EJ) by fuel source from 2000 through 2021, (b) Fossil CO_2 emissions by fuel type and cement production from 2000 through 2021. Average annual growth rates shown under brackets for the period 2016 through 2021.....1
Figure 2. World energy consumption mix, 1965 to 2021. 2
Figure 3. Water splitting.....3
Figure 4. Solar water splitting methods.....4
Figure 5. An overview of hydrogen economy integration (source: U.S. DOE).[5] 5
Table 1. Key hydrogen suppliers (2021) 7
Figure 6. Renewable hydrogen cycle. 7
Figure 7. Hydrogen production sources in recent years.....8
Figure 8. Principles of overall water splitting.....9
Figure 9. a) Energy diagrams for photocatalytic water splitting without ① or with ② the presence of cocatalysts. b) Band profiles of photocatalytic splitting water into H_2 and O_2. E_a, activation energy; NHE, normal hydrogen electrode.[7] 10
Figure 10. Potential sustainable hydrogen fuel cycle based on photocatalytic water splitting.[10] 11
Figure 11. Bandgaps and band-edge positions with respect to the vacuum level and NHE for selected semiconductors. The horizontal red lines represent the conduction-band edges. The horizontal green lines represent the valence-band edges. The two dashed lines indicate the water redox reaction potentials.[11] 12
Figure 12. Structures of (a) triazine and (b) tri-*s*-triazine. 12
Figure 13. Number of Publications Over Time Using (a) "g-C_3N_4", "photocatalytic" + "hydrogen", and "photocatalytic" + "hydrogen" + "g-C_3N_4" keywords. (b) "hydrogen" + "g-C_3N_4" and "hydrogen" + "graphene" + "g-C_3N_4". (c) Times Cited and Publications Over Time Using "hydrogen" + "g-C_3N_4" keywords. Data from Web of Science Core Collection on May 30th 2023.....13
Scheme 1. Schematic of solvothermal modified g-C_3N_4 preparation.....31
Table 2. Dispersive, Polar, Hydrogen Bonding Hansen Parameters, and Relative polarity for the solvents used in this work. 32
Figure 14. (a) XRD spectra of C_3N_4-bulk, C_3N_4-MA, C_3N_4-IPA, C_3N_4-DMF, and C_3N_4-THF. (b) inset XRD spectra of C_3N_4-MA, C_3N_4-IPA, C_3N_4-DMF, and C_3N_4-THF.....33
Figure 15. FT-IR survey spectra C_3N_4-bulk, C_3N_4-MA, C_3N_4-IPA, C_3N_4-DMF, and C_3N_4-THF. 34
Table 3. Element compositions and calculated C/N, O/N atomic ratios of the samples analyzed by elemental analysis (C, H, N, O, S analyzer). 35
Figure 16. XPS survey spectra C_3N_4-bulk, C_3N_4-MA, C_3N_4-IPA, C_3N_4-DMF, and C_3N_4-THF..36
Figure 17. XPS spectra of C_3N_4-bulk, C_3N_4-MA, C_3N_4-IPA, C_3N_4-DMF, and C_3N_4-THF. (a) C1s spectra, (b) N1s spectra. 37
Table 4. Calculation of delocalized π-π electrons system on C1s and N1s XPS data.....38

Figure 18. Deconvolution of O1s XPS spectra of C_3N_4-bulk, C_3N_4-MA, C_3N_4-IPA, C_3N_4-DMF, and C_3N_4-THF.....40
Figure 19. (a) Deconvolution of the XPS Pt4f spectra of C_3N_4-MA, C_3N_4-IPA, C_3N_4-DMF, and C_3N_4-THF. (b) HR-TEM image of C_3N_4-THF and corresponding (c) Fourier-transform (FFT) image, (d) High-resolution inverse FFT image (IFFT), and (e) lattice fringe pattern image, which shows a d-spacing of 0.19 nm (the (200) planes of Pt). 42
Figure 20. HR-TEM images of (a) C_3N_4-THF, (c) C_3N_4-DMF, (e) C_3N_4-IPA, (g) C_3N_4-MA, corresponding to the Pt particles size distribution in (b) C_3N_4-THF, (d) C_3N_4-DMF, (f) C_3N_4-IPA, (h) C_3N_4-MA, respectively. 43
Figure 21. HR-TEM images of (a) C_3N_4-IPA, (b) C_3N_4-MA corresponding to their STEMS images.....44
Table 5. ICP-OES data analysis. 45
Table 6: Adsorption Energy (ΔE) of the Adsorbates on s-Heptazine Sheet. 46
Figure 22. AFM, HR-TEM, and FE-SEM images of (a, f & k) C_3N_4-bulk, (b, g & l) C_3N_4-MA, (c, h & m) C_3N_4-IPA, (d, i & n) C_3N_4-DMF, and (e, j & o) C_3N_4-THF.....47
Table 7: Total Solvation Energy of the adsorbates. 48
Figure 23. The visualization polarity of MA, IPA, and THF molecules, which supports the evidence of steric effects of IPA compared to MA and THF. 48
Figure 24. AFM topography images of (a, f, k) C_3N_4-bulk, (b, g, l) C_3N_4-MA, (c, h, m) C_3N_4-IPA, (d, i, n) C_3N_4-DMF, and (e, j, o) C_3N_4-THF at different scales, corresponding with their height profiles. 49
Figure 25. (a) AFM topography images of THF-modified g-C_3N_4 sample, (b) AFM inset image at 10x10 μm scale, corresponding to (e) holes size distribution in AFM image (b), (c) original CS-STEM image of C_3N_4-THF layer, and (d) image with color added to highlight the typical holes.....51
Figure 26. AFM topography images of C_3N_4-THF prepared sample I. (a, c, e) height images at three different positions, corresponding to (b, d, f) phase images, respectively. 52
Figure 27. AFM topography images of C_3N_4-THF prepared sample II. (a, c, e) height images at three different positions, corresponding to (b, d, f) phase images, respectively. 53
Figure 28. AFM topography images of C_3N_4-THF prepared sample III. (a, c, e) height images at three different positions, corresponding to (b, d, f) phase images, respectively. 54
Figure 29. AFM topography images of C_3N_4-THF at different scales, corresponding with its height profile (c & d). The dark brown and dark yellow colors represent for the SiO_2 substrate, and C_3N_4-THF layer, respectively. Typical holes in figure 29c are marked as red circles. Figure 29d shows the height profile of the C_3N_4-THF layer and holes, corresponding with position of the holes in figure 29c. 55
Figure 30. AFM topography images of C_3N_4-THF of different as-prepared samples. Sample I: (a) height image of C_3N_4-THF, corresponding with (b) height profile, and (c) phase image, respectively. Sample II: (a) height image of C_3N_4-THF, corresponding with (b) height profile, and (c) phase image, respectively. 56
Figure 31. FE-SEM images of (a) C_3N_4-bulk, (b) C_3N_4-MA, (c) C_3N_4-IPA, (d) C_3N_4-DMF, and (e) C_3N_4-THF at different magnification. 58

Figure 32. FE-SEM images of (a) C_3N_4-bulk, (b) C_3N_4-MA, (c) C_3N_4-IPA, (d) C_3N_4-DMF, and (e) C_3N_4-THF at different magnification. 59
Figure 33. (a) N_2 adsorption/desorption isotherms onto bulk and freeze-dried g-C_3N_4 and (b) obtained pore diameter distribution. 60
Table 8. Textural data and bandgaps of the as-prepared g-C_3N_4 photocatalysts. 61
Figure 34. A 3x3 Unit cell of s-heptazine. 62
Figure 35a. The charge density for MA on s-heptazine sheet: interaction between O_a-C_s and H_a-N_s. 63
Figure 35b. The charge density for IPA on s-heptazine sheet: interaction between O_a-C_s and H_a-N_s. 65
Figure 35c. The charge density for THF on s-heptazine sheet: interaction between O_a-C_1 and O_a-C_2 (C_1 and C_2 carbon positions were shown in Figure 34). 65
Figure 35d. The charge density for DMF on s-heptazine sheet: interaction between O_a-C_s and O_a-N_s. 66
Figure 36. Charge distribution on N atoms as N accepts the charge (e^-) from C in pristine s-heptazine sheet. 67
Scheme 2. Proposed S_N1 reaction pathway of THF interacting with g-C_3N_4 at (a) C_1 and (b) C_2 in the heptazine rings. 67
Scheme 3. Proposed S_N1 reaction pathway of (a) MA and (b) IPA interact with g-C_3N_4 at C_1 in the heptazine rings. 68
Figure 37. (a) UV-Vis absorption spectra and (b) (c) (d) (e) (f) corresponding Tauc plots of Energy (eV) and $(\alpha h\nu)^2$ for all prepared samples. 70
Figure 38. The densities of states (DOS) for the pristine and holey structures of g-C_3N_4. 72
Figure 39. (a) PL emission spectra, (b) EIS Nyquist plots, and (c) TRPL spectra. 73
Table 9. Radiative fluorescence lifetimes and their corresponding percentages of photoexcited charge carriers in all prepared photocatalysts. 75
Figure 40. Raman spectra and LSCM images of C_3N_4-THF at different sites on the surfaces of the sample: (a & d) at the black spot, (b & e) at the black blur spot. (c & f) Raman spectra and LSCM images of C_3N_4-bulk. XRD spectra of (h) C_3N_4-THF and (g) C_3N_4-THF's residue (self-assembly-Graphene/Pt) after annealing C_3N_4-THF sample at 700 ℃ for 2 h in Ar atmosphere. ..77
Figure 41. DTG curves of C_3N_4-bulk, C_3N_4-MA, C_3N_4-IPA, C_3N_4-DMF, and C_3N_4-THF. 79
Figure 42. TGA thermograms and high-resolution inset of C_3N_4-bulk, C_3N_4-MA, C_3N_4-IPA, C_3N_4-DMF, and C_3N_4-THF. 80
Table 10. Approximate graphene content in the catalysts. 81
Table 11. Calibration data of H_2 concentration vs. GC peak area. 82
Figure 43. Calibration curves for the molecular hydrogen obtained from the GC-TCD. 83
Figure 44. Ideal spectral match defined by IEC 60904-9 of LHS-7320 simulated sunlight. 84
Figure 45. LHS-7320 solar simulator specifications. 85
Figure 46. LHS-7320 spectrum and LHS-7320 spectral match. 86
Figure 47. Quartz flask reactor (300 mL, diameter: 70 mm, and height: 80 mm), side view. 87
Figure 48. Quartz flask reactor (300 mL, diameter: 70 mm, and height: 80 mm), top view. 88
Figure 49. Online GC system for photocatalytic H_2 evolution measurement. 89

Table 12. Water quality from Puris-Evo UP WATER SYSTEM.....89
Figure 50. a) Dependence of amount of H_2 evolution rate on photocatalyst concentration for C_3N_4-bulk, C_3N_4-IPA, C_3N_4-DMF, C_3N_4-MA, and C_3N_4-THF. b) Averaged H_2 evolution rate at the stationary points of the corresponding photocatalyst. c) Amount of H_2 produced vs. reaction time of C_3N_4-bulk, C_3N_4-IPA, C_3N_4-DMF, C_3N_4-MA, and C_3N_4-THF at the stationary points...92
Figure 51. Optimization photocatalytic activity toward H_2 evolution of C_3N_4-bulk, C_3N_4-IPA, C_3N_4-DMF, C_3N_4-MA, and C_3N_4-THF.....93
Figure 52. Photocatalytic hydrogen evolution rate (HER) of as-prepared samples: HER versus mass and surface area. 94
Table 13. Comparison of photocatalytic activity toward H_2 evolution of the reported g-C_3N_4 and its composites.....95
Figure 53. H_2 evolution of C_3N_4-THF at the stationary point (0.1 $mg.mL^{-1}$), using 420 nm bandpass filter (Newport 20BPF10-420 Bandpass Filter, 50.8x50.8 mm, 420±2 nm Center, 10±2 nm FWHM).....99
Table 14. Turnover Number (TON), Turnover Frequency (TOF) calculations for C_3N_4-IPA, C_3N_4-DMF, C_3N_4-MA, and C_3N_4-THF.....100
Figure 54. Photocatalytic H_2 evolution at the stationary point of C_3N_4-THF, oxygenated C_3N_4-THF, and hydrogenated C_3N_4-THF.....101
Figure 55. Photocatalytic H_2 evolution stability estimation of C_3N_4-THF. The first test of 3 h reaction was obtained on 08/2021. The product was stored in the solution for 340 days before the second test. 102
Figure 56. (a) UV-Vis of all samples, (b) UV-DRS of powder samples, and (c) corresponding Tauc plots of E(eV) and $(\alpha h\nu)^2$ for all prepared samples.....104
Figure 57. Schematic illustration of the photocatalytic mechanism for C_3N_4-THF under simulated sunlight irradiation. 106
Scheme 4. Schematic for mass production of hCN-G and CN-b.....111
Table 15. Calibration data of H_2 concentration vs. GC peak area. 113
Figure 58. Calibration curves for the molecular hydrogen obtained from the GC-TCD. 114
Figure 59. Ideal spectral match defined by IEC 60904-9 of LHS-7320 simulated sunlight.....114
Figure 60. LHS-7320 solar simulator specifications. 115
Figure 61. LHS-7320 spectrum and LHS-7320 spectral match.....116
Figure 62. Online GC system for photocatalytic H_2 evolution measurement.....117
Figure 63. H_2 evolution of hCN-G using 420 nm bandpass filter (Newport 20BPF10-420 Bandpass Filter, 50.8x50.8 mm, 420±2 nm Center, 10±2 nm FWHM).....122
Figure 64. (A) HRP-XRD spectra, (B) FT-IR spectra, and (C, D) XPS C1s spectra of hCN-G and CN-b. 125
Table 17. Elemental compositions and atomic ratio calculations of the resultant samples. 126
Figure 65. XPS survey spectra of CN-b and hCN-G.....127
Figure 66. (A, B) FE-SEM images and (C, D) HR-TEM images of CN-b and hCN-G samples. 128
Figure 67. (A, B) AFM topography images of CN-b and hCN-G samples, corresponding to their height profiles (C, D). Spherical aberration–corrected scanning transmission electron microscope

(CS-STEM) image of the hCN-G sample, (E) the original image, and (F) with color added to highlight the feature. 129
Figure 68. AFM topography at different scale of hCN-G sample. 130
Figure 69. The charge density for ethyl alcohol on s-heptazine sheet: interaction between O atom of ethyl alcohol and C atom on the sheet. The adsorption energy = -0.94 eV /atom (-13.14 eV /g-C_3N_4). 132
Scheme 5. Proposed S_N1 reaction pathway of ethyl alcohol interacts with g-C_3N_4 at C (N2-C-N) atom in the heptazine rings. 132
Figure 70. (A and B) High-resolution XPS Pt 4f spectra of CN-b and hCN-G. (C and D) HR-TEM images of CN-b and hCN-G, corresponding (E and I) Fast Fourier-transform (FFT) images, (F and J) high-resolution inverse FFT images, and (G and K) lattice fringe pattern images. (H and L) Co-catalyst nanoparticle size distributions. 133
Figure 71. Deconvolution of (A) N1s and (B) O1s XPS spectra of CN-b and hCN-G, respectively. 134
Figure 72. HR-TEM images of hCN-G corresponding to its STEMS images. 135
Figure 73. (A) N_2 adsorption-desorption isotherms of CN-b and hCN-G. (b) Pore-size distributions of CN-b and hCN-G. 136
Table 18. Textural data and bandgaps of the samples. 137
Figure 74. Raman spectra of (A) CN-b and (B) hCN-G, (C) TGA thermograms and high-resolution inset of the as-prepared samples, and (D) XRD patterns of hCN-G and Pt/graphene (TGA residue of hCN-G). 138
Figure 75. (A) UV-DRS spectra, (B) corresponding Tauc plots: hν (eV) and $(\alpha h\nu)^{0.5}$, (C) UV-vis absorption spectra, (D) EIS Nyquist plots, (E) PL emission spectra, and (F) TR-PL spectra for CN-b and hCN-G samples. 141
Figure 77. Optimized geometry for hCN-G for side view (A) and top view (B), for graphene (C) and for hCN (D). 144
Figure 78. Charge-density difference plots: (A) side view and (B) top view, showing an electron-hole puddle on the graphene layer. Brown, silver, and pink balls represent carbon, nitrogen, and hydrogen atoms, respectively. (C) The absorption coefficient of hCN and the heterostructure (hCN-G). (D) Band structure and partial density of states for the heterostructure (hCN-G). The plot in the inset represents the enlarged view of the band edges at the band edges. 145
Figure 79. Band structure and partial density of states for graphene. 146
Figure 80. Band structure and partial density of states for holey g-C_3N_4 (hCN) structure. 147
Figure 81. A) Optimization study on H_2 evolution rate vs. photocatalyst concentration for CN-b and hCN-G, corresponding to the amount of H_2 produced vs. reaction time at different concentrations of photocatalysts. B) hCN-G and C) CN-b. D) Averaged H_2 evolution rate at the optimized points vs. photocatalyst mass and specific surface area. E) Photocatalytic mechanism for hCN-G under simulated sunlight irradiation 149
Figure 82. Cyclic stability test of hCN-G for photocatalytic H_2 production. 150
Figure 83. XRD spectra of hCN-G before and after the photocatalytic stability test. 151
Figure 84. AFM images of hCN-G before and after the photocatalytic stability test. 152

Table 19. Comparison of photocatalytic activity toward H_2 evolution of the reported g-C_3N_4 and its composites. 153
Scheme 6. Schematic of highly dispersion of HoCN-GO preparation. 164
Figure 85. (a) XRD spectra of CN-bulk, oCN, HoCN, and HoCN-GO. (b) inset XRD spectra of CN-bulk, oCN, HoCN, and HoCN-GO. 165
Table 20. Element compositions and calculated C/N, O/N, C/O atomic ratios of the samples analyzed by elemental analysis. 166
Figure 86. XPS spectra of CN-bulk, oCN, HoCN, and HoCN-G40. (a) C1s spectra, (b) N1s spectra. 167
Figure 87. FE-SEM images of (a, b, c) CN-bulk, (d, e, f) oCN, (g, h, i) HoCN, and (j, k, l) HoCN-G40 at different magnifications. 168
Figure 88. AFM topography of (a, b) HoCN-G40 in 3D, (c) holey GO image in 2D and (d) in 3D. 169
Figure 89. HR-TEM CS-STEM images of (a, b) CN-bulk, (c, d) HoCN, and (e, f) HoCN-G40. CS-STEM images of (g) HoCN-G40, (h) inset image of g, corresponding to (i) Fourier-transform (FFT) image, (j) High-resolution inverse FFT image (IFFT), and (k) lattice fringe pattern image, which shows a d-spacing of 0.35 nm of g-C_3N_4. 171
Figure 90. UV-Vis spectra of as-prepared samples. (a) UV-Vis spectra of oCN by reduction time, (b) UV-Vis spectra of oCN mixed with 10 % v/v TEOA, (c) UV-Vis spectra of oCN mixed with holey GO (GO number is a weight ratio of holey GO vs. oCN), and (d) UV-Vis spectra of HoCN-GO with eosin Y (EY). 172
Figure 91. UV-DRS spectra. (a) UV-DRS spectra of powder samples, the intensity of absorbance. (b) corresponding Tauc plots of Energy (eV) and $(\alpha h\nu)^{1/2}$ for as-prepared samples. 173
Figure 92. PL spectra of as-prepared samples. (a) PL spectra of oCN by reduction time, (b) PL spectra of oCN mixed with 10 % v/v TEOA, (c) PL spectra of oCN mixed with holey GO (GO number is a weight ratio of holey GO vs. oCN), and (d) PL spectra of HoCN-GO with eosin Y (EY). 174
Figure 93. EIS Nyquist plots of as-prepared samples from EIS measurement. 175
Figure 94. Photocatalytic hydrogen evolution under visible light irradiation. 176
Figure 95. Photocatalytic hydrogen evolution under visible light irradiation. 178
Figure 96. Schematic of mass production of g-C_3N_4/RGO by photoreforming of GO over thermally exfoliated g-C_3N_4. 182
Figure 97. Photocatalytic hydrogen evolution performance of g-C_3N_4/RGO by photoreforming of GO over thermally exfoliated g-C_3N_4 samples. 183
Figure 98. The overall water splitting process on atomic scale metal (Pt-G/gC_3N_4-Ru) gradient photocatalyst under sunlight irradiation. 184
Figure 99. Proposed mechanism for GO and g-C_3N_4 amide group formation. 185
Figure 100. Illustration for the synthesis of atomic scale metal leaf-like structure Pt-G/gC_3N_4-Ru gradient photocatalyst. 185

LIST OF TABLES

Table 1. Key hydrogen suppliers (2021) 7
Table 2. Dispersive, Polar, Hydrogen Bonding Hansen Parameters, and Relative polarity for the solvents used in this work. 32
Table 3. Element compositions and calculated C/N, O/N atomic ratios of the samples analyzed by elemental analysis (C, H, N, O, S analyzer). 35
Table 4. Calculation of delocalized π-π electrons system on C1s and N1s XPS data. 38
Table 5. ICP-OES data analysis. 45
Table 6: Adsorption Energy (ΔE) of the Adsorbates on s-Heptazine Sheet. 46
Table 7: Total Solvation Energy of the adsorbates. 48
Table 8. Textural data and bandgaps of the as-prepared g-C_3N_4 photocatalysts. 61
Table 9. Radiative fluorescence lifetimes and their corresponding percentages of photoexcited charge carriers in all prepared photocatalysts. 75
Table 10. Approximate graphene content in the catalysts 81
Table 11. Calibration data of H_2 concentration vs. GC peak area. 82
Table 12. Water quality from Puris-Evo UP WATER SYSTEM 89
Table 13. Comparison of photocatalytic activity toward H_2 evolution of the reported g-C_3N_4 and its composites. 95
Table 14. Turnover Number (TON), Turnover Frequency (TOF) calculations for C_3N_4-IPA, C_3N_4-DMF, C_3N_4-MA, and C_3N_4-THF. 10000
Table 15. Calibration data of H_2 concentration vs. GC peak area. 11313
Table 16. Water quality from Puris-Evo UP WATER SYSTEM 118
Table 17. Elemental compositions and atomic ratio calculations of the resultant samples. 12626
Table 18. Textural data and bandgaps of the samples. 13737
Table 19. Comparison of photocatalytic activity toward H_2 evolution of the reported g-C_3N_4 and its composites. 15353
Table 20. Element compositions and calculated C/N, O/N, C/O atomic ratios of the samples analyzed by elemental analysis. 16666

LIST OF ABBREVIATIONS AND SYMBOLS

A

atomic force microscopy
AFM, 41

C

carbon capture, utilization, and storage
CCUS, 27
conduction band
CB, 28

D

density functional theory
DFT, 42
Dicyandiamide
DCDA, 46

E

electrochemical impedance spectra
EIS, 41

F

field emission scanning electron microscopes
FE-SEM, 41
Fourier transform infrared spectroscopy
FT-IR, 47
Fourier-transform infrared spectroscopy
FT-IR, 42

H

high-resolution transmission electron microscopy
HR-TEM, 41
hydrogen evolution reaction
HER, 37
hydrogen internal combustion engine vehicle
HICEV, 22

I

inductively coupled plasma-optical emission spectrometer
ICP-OES, 47
isopropyl alcohol
IPA, 45

K

Korea Hydrogen Industry Association
KHIA, 25

L

laser scanning confocal microscope
LSCM, 42

M

Mesoporous and microposrous g-C_3N_4
MMCN, 34
Mesoporous g-C_3N_4
MGCN, 34
Methyl alcohol
MA, 45
million metric tonnes
(MMT), 26

N

N,N-dimethylformamide
DMF, 45
normal hydrogen electrode
NHE, 29

O

oxygen evolution reaction

OER, 37

P

Perdew-Burke-Ernzerh
PBE, 49
photoluminescence
PL, 41

S

specific surface area
SSA, 35

T

tetrahydrofuran-modified g-C_3N_4 sample
C3N4-THF, 43
thermal conductive detector
TCD, 47
Thermogravimetric analysis
TGA, 48
time-resolved photoluminescence
TR-PL, 41
triethanolamine
TEOA, 46

U

U.S. Department of Energy
U.S. DOE, 24
Ultraviolet–visible diffuse reflectance spectroscopy
UV-DRS, 41

V

valence band
VB, 28
van-der-Waals
vdW, 49

X

X-ray diffraction
XRD, 41
X-ray photoelectron spectroscopy
XPS, 41

CHAPTER 1

1. Introduction

1.1. Solar Light Harvesting

In continuously developing civilizations, energy consumption has speedily increased due to economic development, rising population, and growing technology-driven modernization society (Figure 1a).[1] Along with the rapid growth of industries and human activities, global fossil CO_2 emissions increase in proportion to energy consumption (Figure 1b). Historically speaking, the main energy resource during industrial era was fossil fuels, and they still account for an overwhelming proportion compared to other energy sources so far (Figure 2). The recent extreme weather gets a boost from climate change and the global energy security conundrum has posed extensive an urgent matter on boosting solar light harvesting, thus increasing the market share of solar energy among other energy resources.

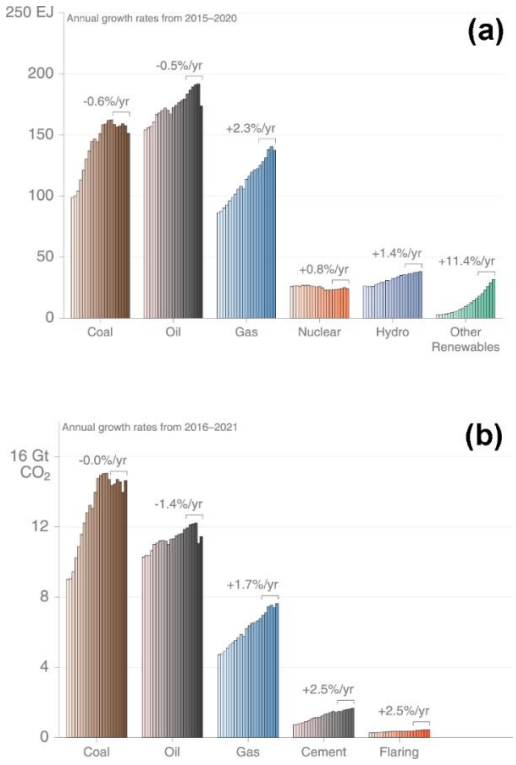

Figure 1. (a) Annual global energy consumption (EJ) by fuel source from 2000 through 2021, (b) Fossil CO_2 emissions by fuel type and cement production from 2000 through 2021. Average annual growth rates shown under brackets for the period 2016 through 2021.

The Earth receives a significant amount of solar radiation, approximately 174 petawatts (PW), in its upper atmosphere. About 30% of this radiation is reflected back into space, while the remaining portion is absorbed by clouds, seas, and land masses. On the Earth's surface, solar radiation mainly consists of visible and near-infrared wavelengths, with a smaller proportion falling in the near-ultraviolet range. In terms of insolation levels, the majority of the world's population resides in areas with a range of 150 to 300 watts/m^2, equivalent to 3.5 to 7.0 kWh/m^2 per day. A variety of technologies can be used to harness solar energy, such as solar power to generate electricity, solar thermal energy, solar light harvesting systems, etc. According to the International Energy Agency, "The development of affordable, inexhaustible and clean solar energy technologies will have huge longer-term benefits. It will increase countries' energy security through reliance on an indigenous, inexhaustible and mostly import-independent resource, enhance sustainability, reduce pollution, lower the costs of mitigating climate change, and keep fossil fuel prices lower than otherwise. These advantages are global."

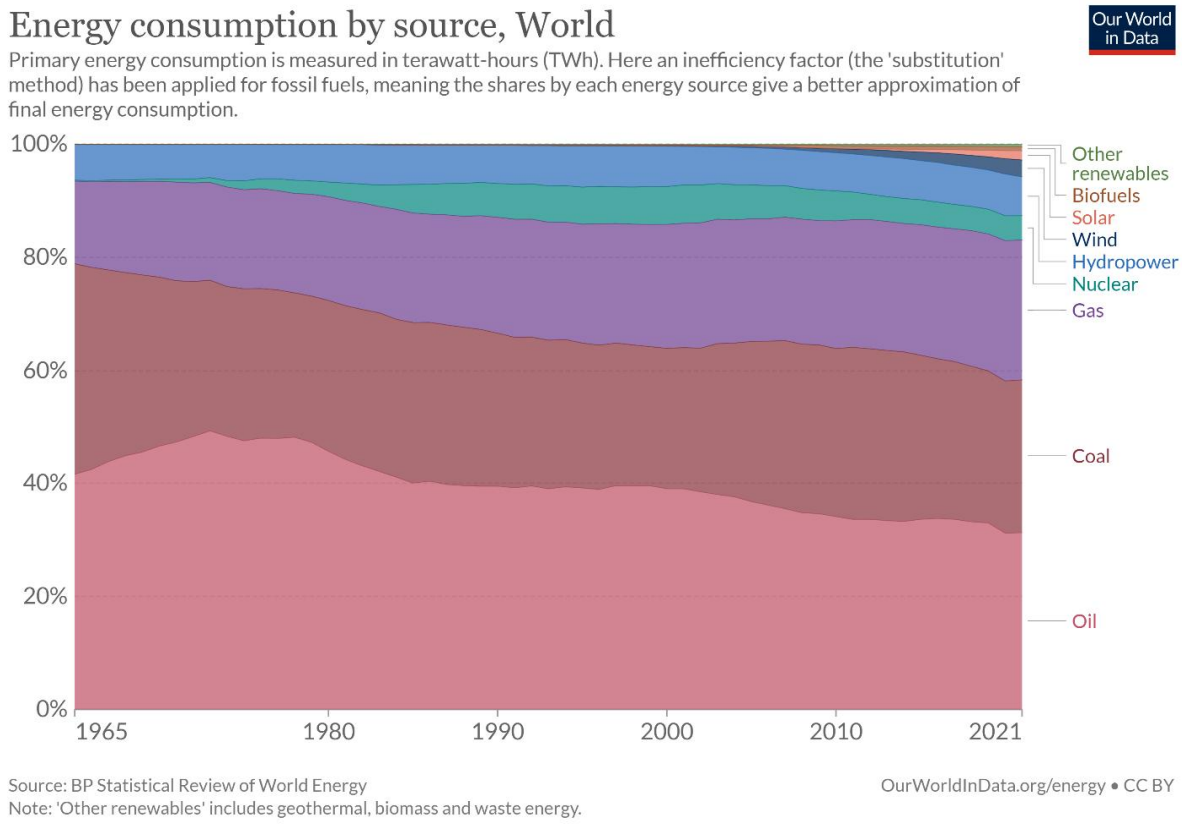

Figure 2. World energy consumption mix, 1965 to 2021.

In order to utilize solar light, it is necessary to convert sun energy into a chemical fuel that can be stored, transported, and used when needed. An earth-abundant energy storage option is water, which contains energy that is stored in the bonds between O_2 and H_2 molecules (Equation 1-1). The fuels can be reversedly combined to form H_2O in a hydrogen fuel cell to generate electricity on-site[2] or a hydrogen internal combustion engine vehicle (HICEV) (Equation 1-3). Hydrogen is a clean alternative to fossil fuels due to its high gravimetric energy density (120 - 140 MJ kg^{-1}), abundance on earth, and eco-friendliness. As the most abundant element in the universe, hydrogen makes up about 75 percent of its normal matter. It was created in the Big Bang, when the universe was formed. On Earth, hydrogen is the third most abundant element after oxygen and silicon. Thus, the production of hydrogen from water is a highly desirable approach for solar energy conversion to clean chemical fuel. Water splitting (Figure 3) can proceed via various methods, such as electrolysis, photosynthesis, photoelectrolysis, photocatalysis, radiolysis, thermal decomposition, nuclear-thermal, or solar-thermal method, etc. Among solar H_2 production methods (Figure 4), photocatalytic water splitting, which accelerates photoreaction using a photocatalyst, is a possible method for green hydrogen production since Fujishima and Honda first discovered photoelectrochemical water splitting into H_2 over titanium dioxide electrodes in 1972.[3]

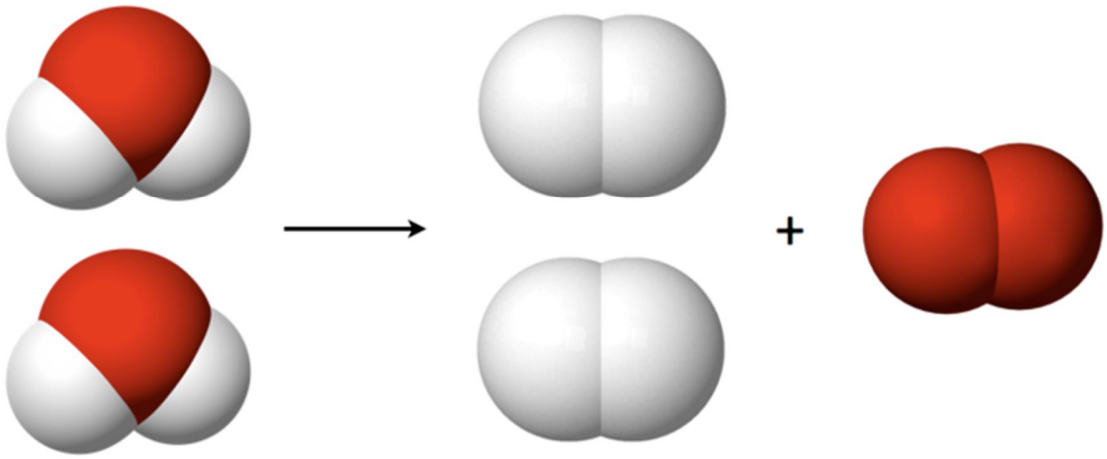

Figure 3. Water splitting.

Electrolysis: $2H_2O \xrightarrow{e^-} H_2 + O_2$ *Equation 1-1*

Photocatalysis: $2H_2O \xrightarrow[\text{Catalyst}]{h\nu} H_2 + O_2 \quad \Delta G^{\circ}_{298K} = +273 \text{ kJ mol}^{-1}$ *Equation 1-2*

Fuel cell: $2H_2 + O_2 \longrightarrow 2H_2O$ *Equation 1-3*

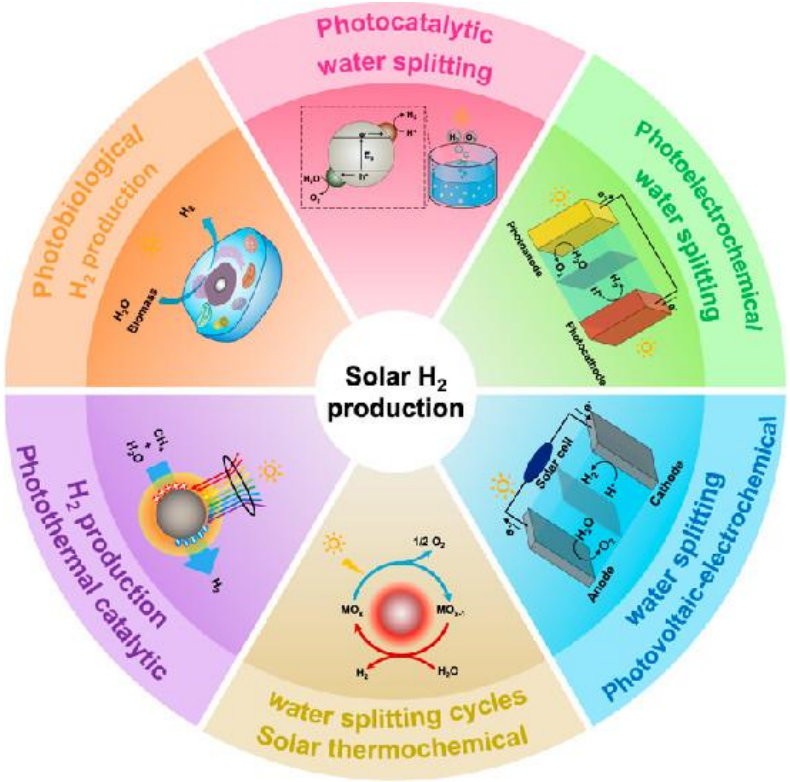

Figure 4. Solar water splitting methods.

1.2. Hydrogen Economy

The world hydrogen economy[4] refers to the future vision of using hydrogen as a zero-emission fuel source in order to displace the current fossil-fuels-based economy. The use of hydrogen as a core factor to develop and operate the civilization is highly desirable for a long-term sustainable economy due to some reasons below:

- Hydrogen can be used in a fuel cell with air to produce electricity, in HICEV to run the engine, or burned to produce heat. Instead of carbon dioxide or other greenhouse gases or particulates, only water is produced as a by-product.

- Hydrogen fuel cells are efficient, operating at an efficiency of 80%, much higher than electricity generated at a power station and transmitted over power lines. Burning fossil fuels at a power station generates electricity at only 35% efficiency, plus 10% of it is lost during transmission over power lines due to electrical resistance.
- In contrast to gasoline derived from petroleum, hydrogen is abundant and has no finite limit.
- As part of the hydrogen cycle, water is converted to hydrogen and oxygen, then transformed into fuel and electricity, and finally 'recycled' back into water.
- Sustainable economic development ensures that humankind develops harmoniously with nature through hydrogen economies.

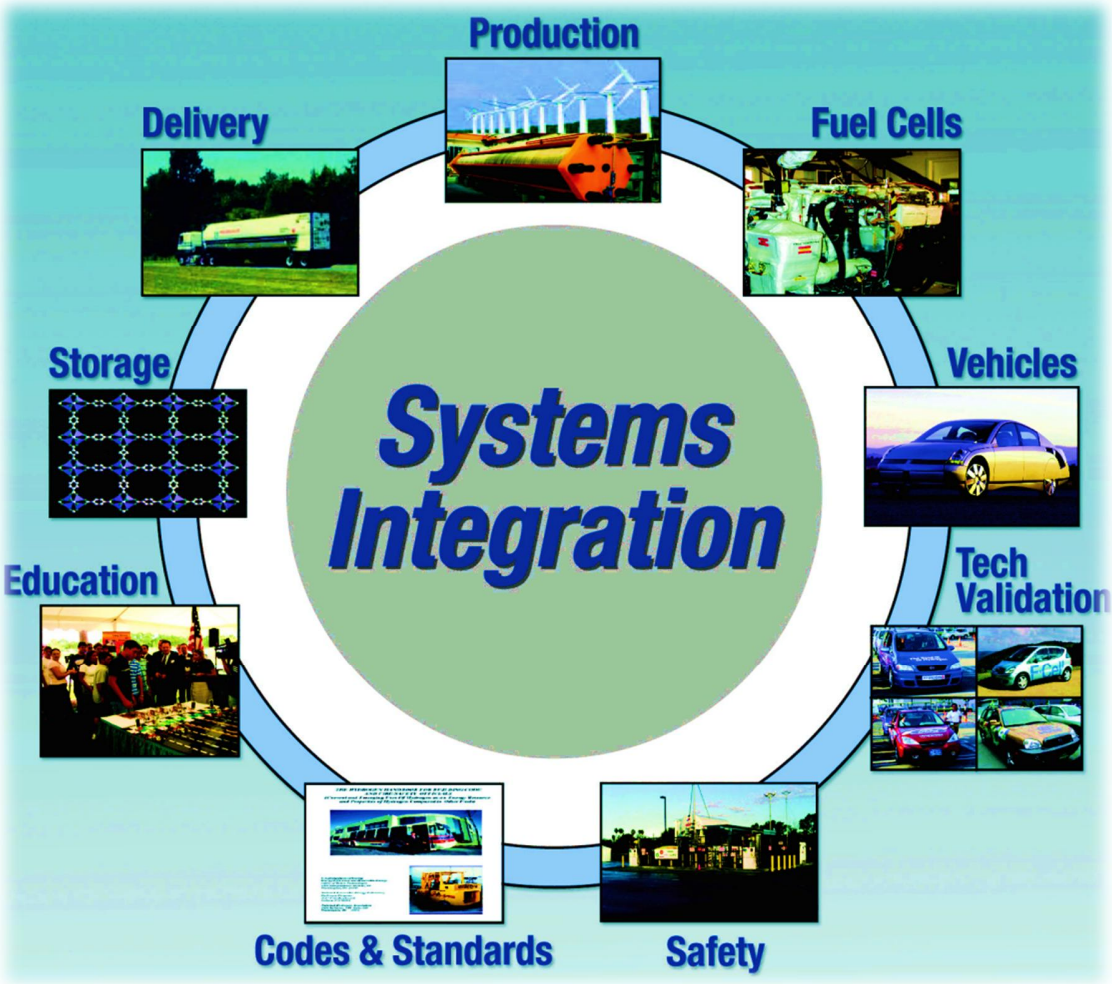

Figure 5. An overview of hydrogen economy integration (source: U.S. DOE).[5]

The hydrogen cycle starts with water (H_2O). Hydrogen and oxygen is typically split through some processes such as photosynthesis, photoelectrolysis, photocatalysis, or photoelectrocatalysis. It is also possible to extract hydrogen from natural materials like wood, plants, and other organic materials. The hydrogen can then be burned by conventional engines, or even better, used in fuel cells in order to produce electricity, for example. The only waste/exhaust produced by hydrogen cells is pure water. A major obstacle to green hydrogen production is finding a clean energy source (wind, solar, nuclear, wave, tidal, hydro, etc), to generate the electricity needed to split water into hydrogen and oxygen. In the case of coal and oil-fired power plants supplying electricity, pollution is the result. Furthermore, hydrogen storage is costly and it is a bottleneck in a scenario of hydrogen economy. Additionally, water that is less than pure incurs additional costs because it is more difficult for water splitting.

As one of the most proactive advocates for hydrogen society, Korea passed the world's first hydrogen economy law in 2020. With the 2050 Carbon Neutral Strategy of Korea plan, the hydrogen market in Korea will almost double in size from 14.1 trillions in 2020 to 26.8 trillions by 2030, with the growth driven largely by investment from local companies such as Hyundai, SK, POSCO, Doosan, Hanwha, and Hyosung, etc (Table 1). In 2019, the Korean government introduced the Hydrogen Economy Roadmap, which sets forth ambitious goals for the deployment of utility-scale and commercial/residential fuel cells. By 2040, the roadmap aims to establish 15GW of utility-scale and 2.1GW of commercial and residential fuel cells. In terms of transportation, the plan targets 5.9 million fuel cell cars and 60,000 fuel cell buses on the roads by 2040, supported by 1,200 hydrogen refueling stations. The Korean government's announcement of the Green New Deal in July 2020, which entails a KRW 74 trillion investment in 'green' public-private capital by 2025, is expected to contribute significantly to the achievement of these ambitious long-term objectives. According to Korea Hydrogen Industry Association (KHIA), a total of 320,000 tons of hydrogen was produced in 2020, with 85% of it produced as a result of naphtha cracking. About 14% of hydrogen is produced in Korea by large-scale steam methane reformers, while less than 1% comes from water electrolysis. Hence, green hydrogen mass production in Korea still has lots of room to develop crucially.

Table 1. Key hydrogen suppliers (2021)

	Company	Capacity (Nm^3 /h)	Market Share (%)	Type of Hydrogen
1.	Deokyang	180,000	47.7	
2.	SPG	98,000	26.0	
3.	Air Liquide	75,000	19.9	
4.	Linde	13,000	3.4	
5.	SDG	7,000	1.8	
6.	Changshin	3,000	0.8	
7.	Daesung	1,000	0.2	

Source: Korea Hydrogen Industry Association (KHIA)

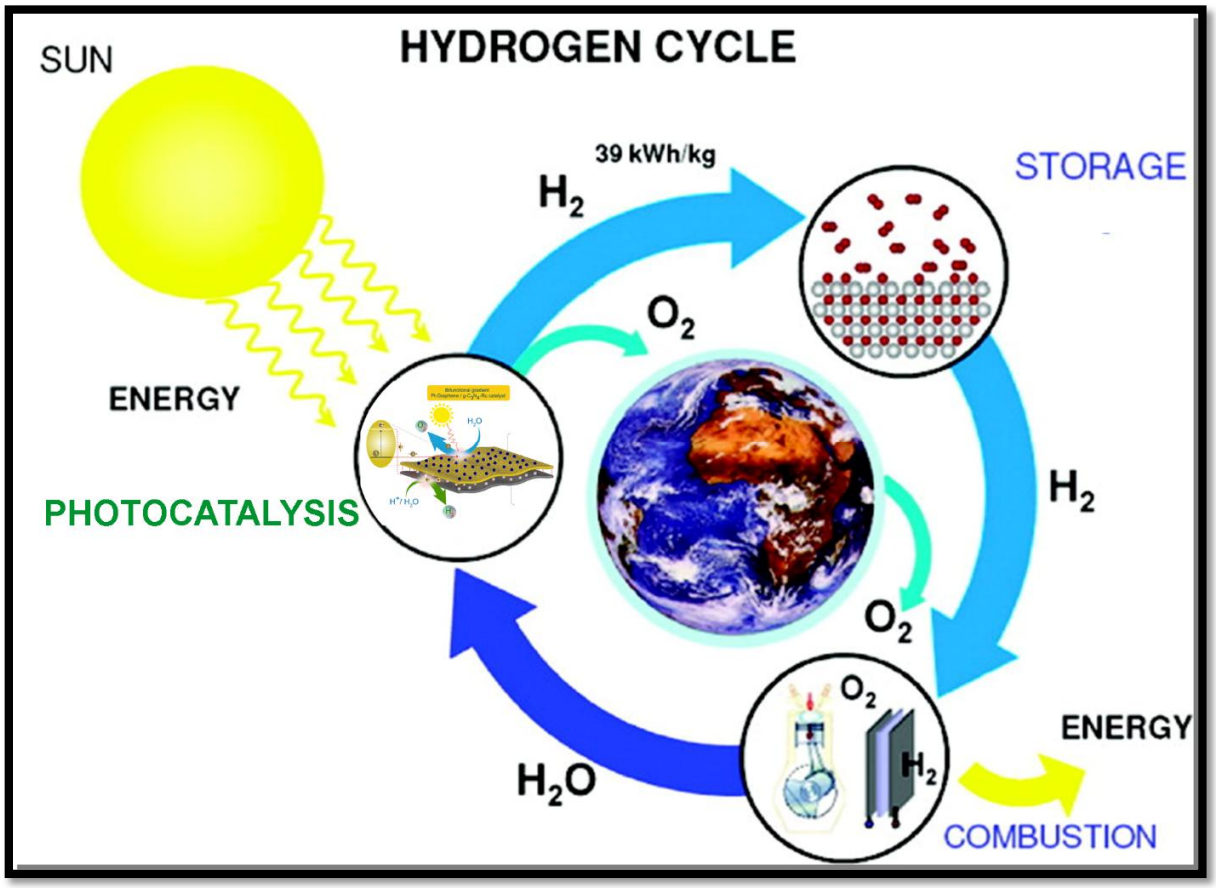

Figure 6. Renewable hydrogen cycle.

The demand for hydrogen is on the rise, with positive signals coming from key applications in the field. The demand for hydrogen in 2021 was 94 million metric tonnes (MMT), containing

about 2.5% of all energy consumed globally. Hydrogen is used today in two primary ways: in the Haber process, in which ammonia is produced, which is later used to produce fertilizers, or in the hydrocracking process, in which petroleum is converted into more widely available fuels. There was no benefit for mitigating climate change from increasing hydrogen demand in 2021, as most of it was produced from unabated fossil fuels. There was less than 1 MMT of low-emission hydrogen produced in 2021, mostly from fossil fuel plants with carbon capture, utilization, and storage (CCUS). Currently, hydrogen around the world is produced from four main sources: coal, oil, natural gas, and water electrolysis. The majority (62 %) of hydrogen production in 2021 relied on natural gas without CCUS. Another significant source (18 %) was the by-product of naphtha reforming in refineries, which was subsequently utilized for various refinery processes. Coal-based production accounted for 19 % of the total, predominantly concentrated in China, while a minimal amount (less than 1 %) of hydrogen was derived from oil sources. It is important to note that only a very small percentage of hydrogen is classified as "green hydrogen" (below 0.03 %). Consequently, green hydrogen production at a large scale has many opportunities and is urgently needed.

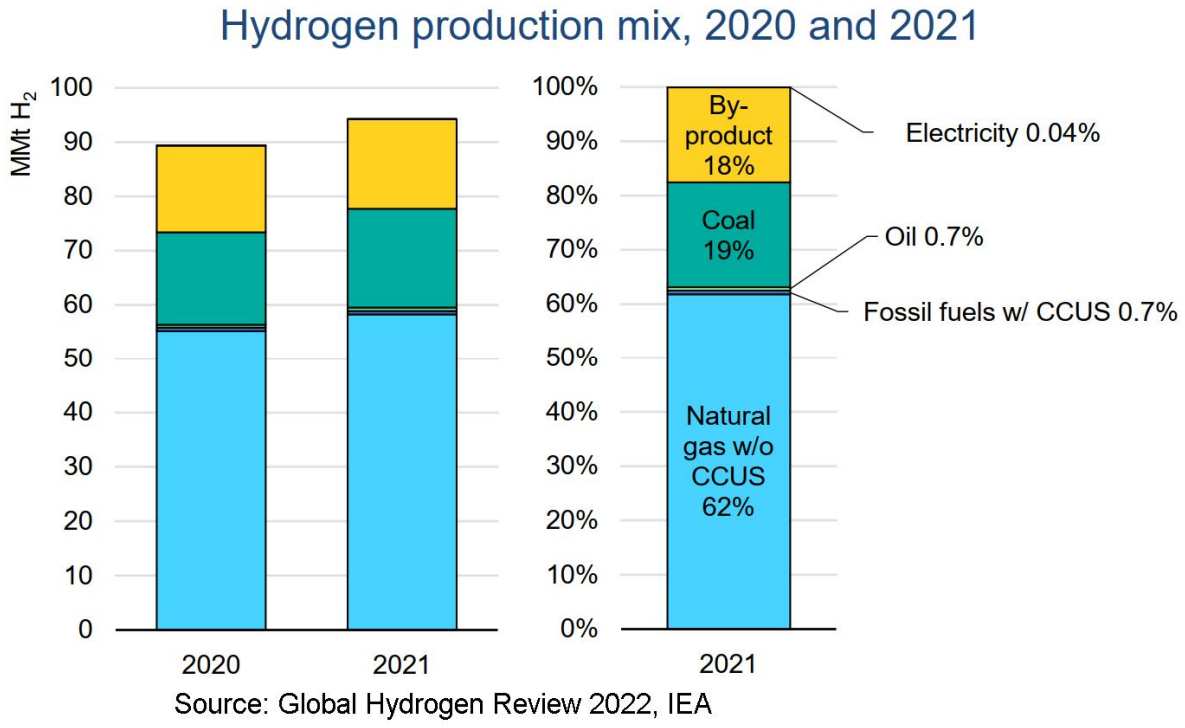

Figure 7. Hydrogen production sources in recent years.

1.3. Photocatalytic Hydrogen Evolution

The basic principles of overall water splitting is shown in Figure 8. The electrons that are present in the valence band (VB) of the photocatalyst can be excited to the conduction band (CB) upon irradiation with light, so that holes are created in the VB. Then, the photoinduced electrons and holes may transfer from the bulk to the surface of the photocatalyst, or they may recombine in the initial state. The successful transfer of electrons and holes at the surface of the photocatalyst are thermodynamically possible to reduce H^+/H_2O and oxidize H_2O molecules to generate H_2 and O_2, respectively. In most cases of H^+/H_2O reduction, however, we need to introduce a cocatalyst in conjunction with a photocatalyst for hydrogen evolution to facilitate electrons transfer to protons, create H_2 molecules, and dissociate H_2 from the surface of the cocatalyst. On the other hand, the many photocatalysts' surface itself works as an O_2 evolution active site. So a cocatalyst for H_2O oxidation is only applied to get higher efficiency of O_2 evolution. In a typical hydrogen electrode, the hydrogen proton redox potential and oxygen water redox potential locate at zero V and +1.23 V vs. NHE, respectively.

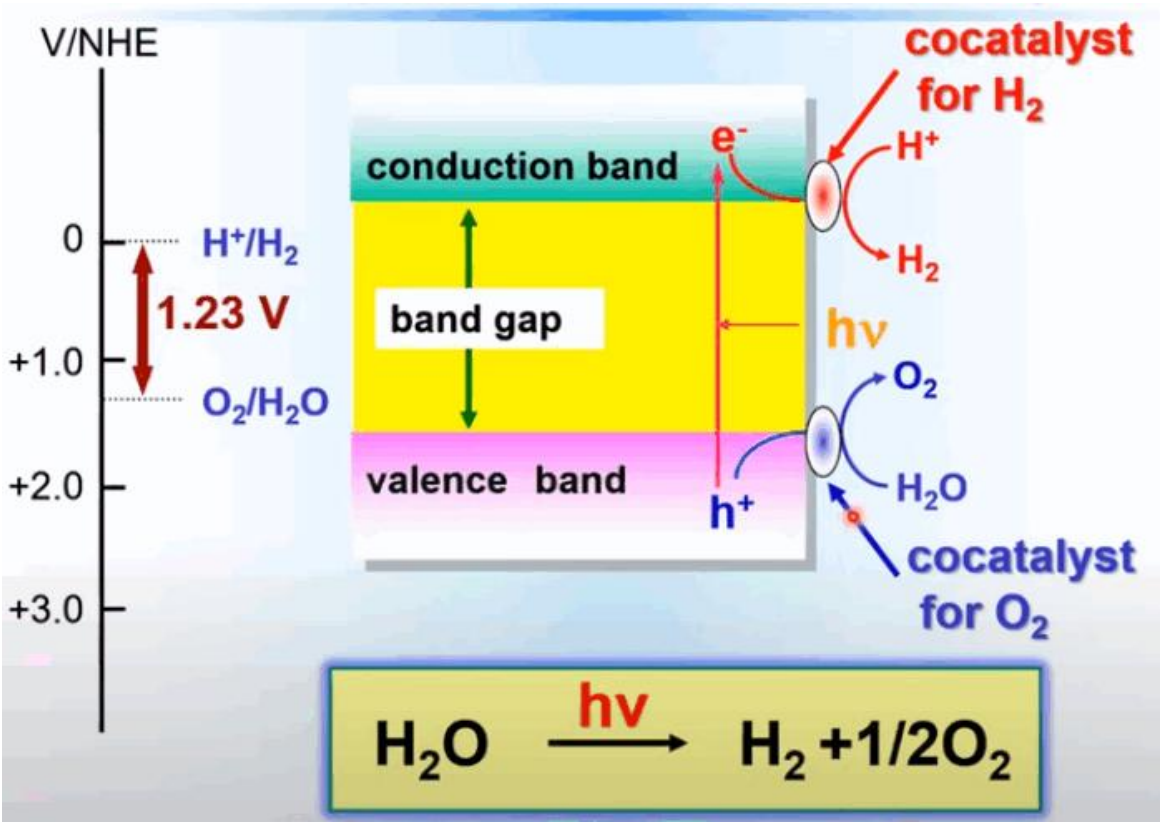

Figure 8. Principles of overall water splitting.

Based on this principle, the band edge potentials of the photocatalyst should be mounted on the redox potential of water. Toward achieving the conditions of evolution reactions, the CB minimum and VB maximum of the photocatalyst should be more negative than hydrogen evolution potential and more positive than O_2 evolution potential, respectively. The light harvesting efficiency, optimized bandgap, dynamically efficient charge separation and transfer, sufficient surface reactivity (surface adsorption and desorption), appropriate cocatalyst (cocatalyst properties, interaction with the photocatalyst), stability, and cost are the critical parameters for designing practically excellent photocatalysis. Since only approximately 5 percent of solar ultraviolet radiation penetrates the atmosphere to reach the Earth's surface,[6] the development of visible-light and IR-response photocatalysts is important due to their majority solar irradiance. Practically and kinetically designed photocatalysts require a moderately larger bandgap than theoretical due to the overpotential of the water splitting reaction (the loss for kinetic activation energy) (Figure 9).

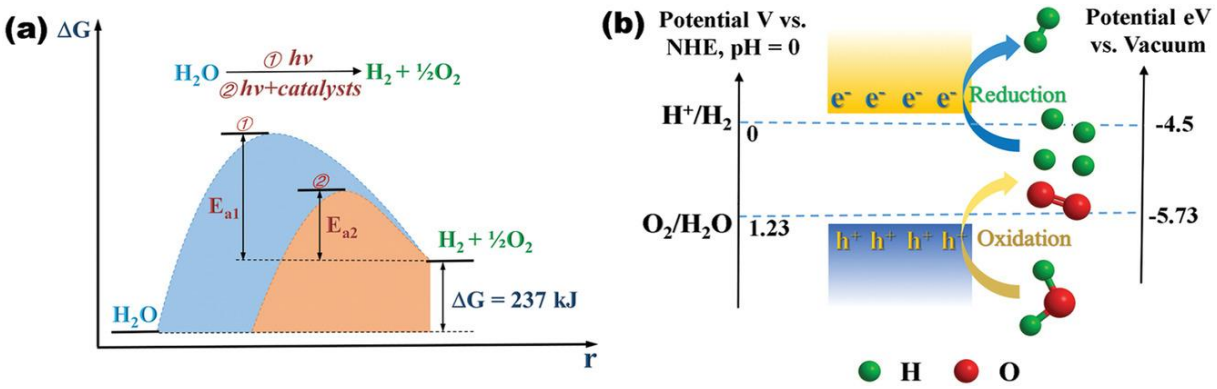

Figure 9. a) Energy diagrams for photocatalytic water splitting without ① or with ② the presence of cocatalysts. b) Band profiles of photocatalytic splitting water into H_2 and O_2. E_a, activation energy; NHE, normal hydrogen electrode.[7]

As a result of these aspects, the bandgap between 1.8 and 2.2 eV is regarded as an optimal energy range for the development of high efficiency photocatalysts.[8] The photocatalyst efficiency charge separation and transfer electrons/holes to the target active sites is crucial in photocatalysis process. Unlike photoelectrocatalyst, which separates two electrodes for H^+/H_2O reduction and H_2O oxidation redox processes, photocatalyst suffers a core issue of high recombination of photoexcited charge because reduction and oxidation sites are existed within a nanoscale of materials. This high combination rate of photoinduced electrons and holes is regarded

as the bottleneck hindering the practical application of photocatalysis.[9] In spite of the fact that cocatalysts are effective in several steps of photocatalysis, they are usually precious metals with high costs of production. Thus, inexpensive cocatalysts, long-lived systems and the production cost of the photocatalysts demonstrate the large-scale applicability viability as well as technical challenges toward practical mass green hydrogen production.

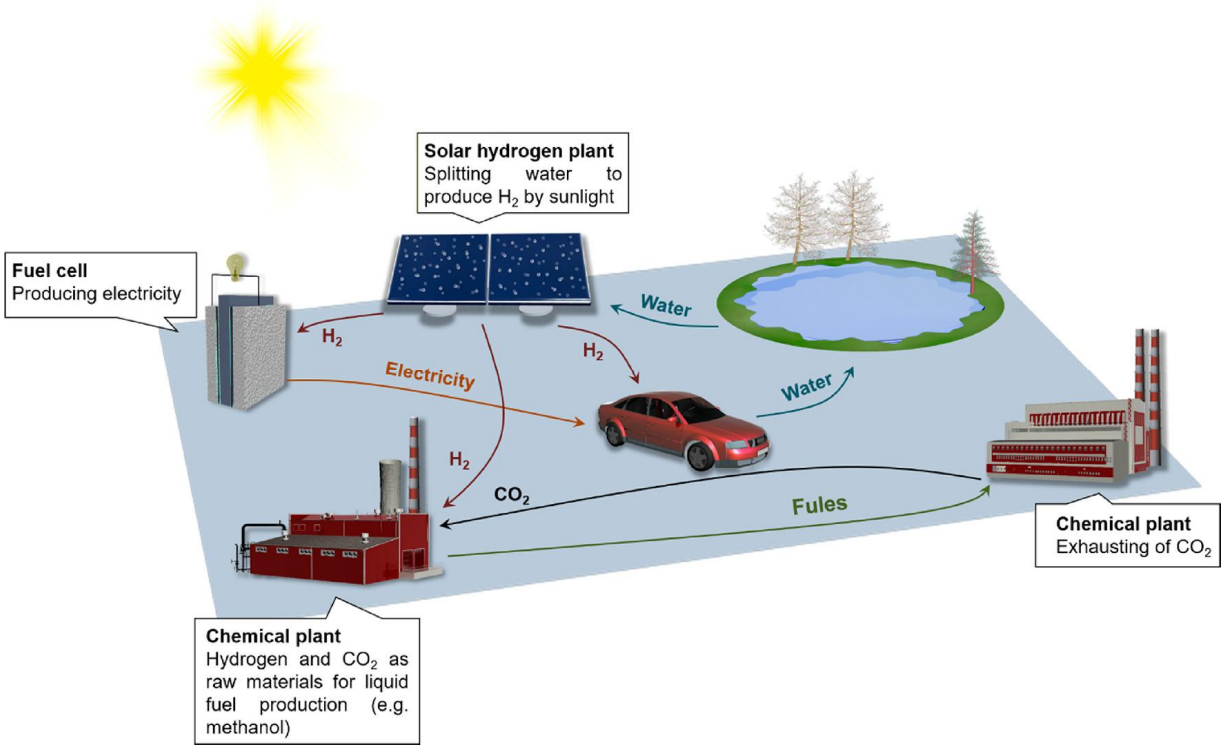

Figure 10. Potential sustainable hydrogen fuel cycle based on photocatalytic water splitting.[10]

1.4. Graphitic Carbon Nitride

Suitable semiconductors for photocatalytic H_2 evolution must adhere to specific requirements. An essential criterion is possessing a suitable band gap, which defines the range of light absorption. This particular characteristic is instrumental in facilitating the transfer of photoinduced electrons to the adsorbed reactants. Recent scientific research has focused on the exploration of visible-light-active photocatalysts and their practical applications. These comprise semiconductor metal oxides (TiO_2, Fe_2O_3, Cu_2O), nitride (C_3N_4, Ta_3N_5, InGaN), chalcogenide (CdS, MoS_2), plasmonic nanostructures (Au, Ag), and nanostructures of conducting polymers (PEDOT, PANI, PDPB) (Figure 11).

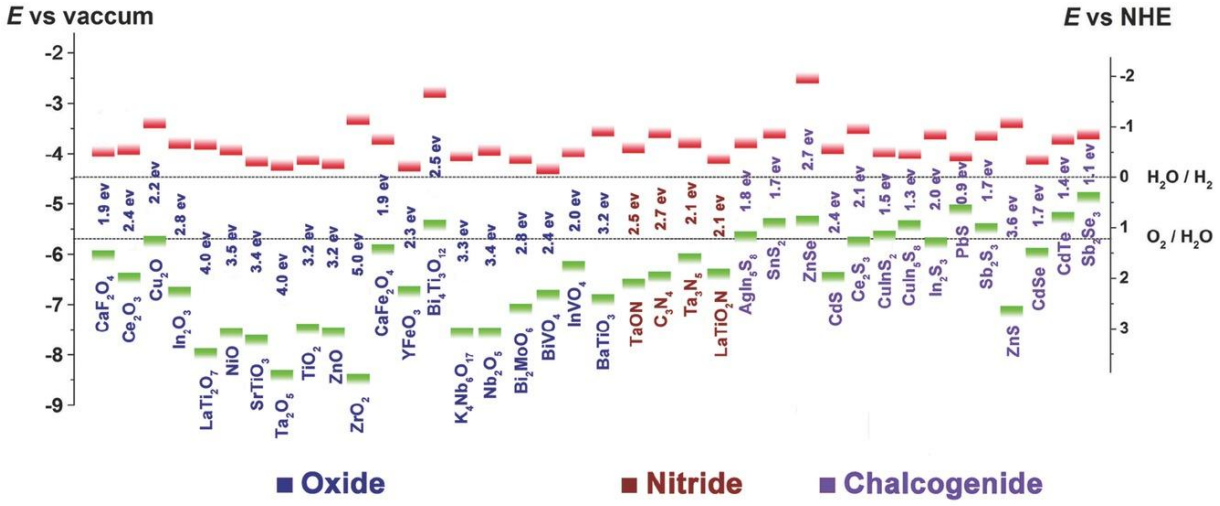

Figure 11. Bandgaps and band-edge positions with respect to the vacuum level and NHE for selected semiconductors. The horizontal red lines represent the conduction-band edges. The horizontal green lines represent the valence-band edges. The two dashed lines indicate the water redox reaction potentials.[11]

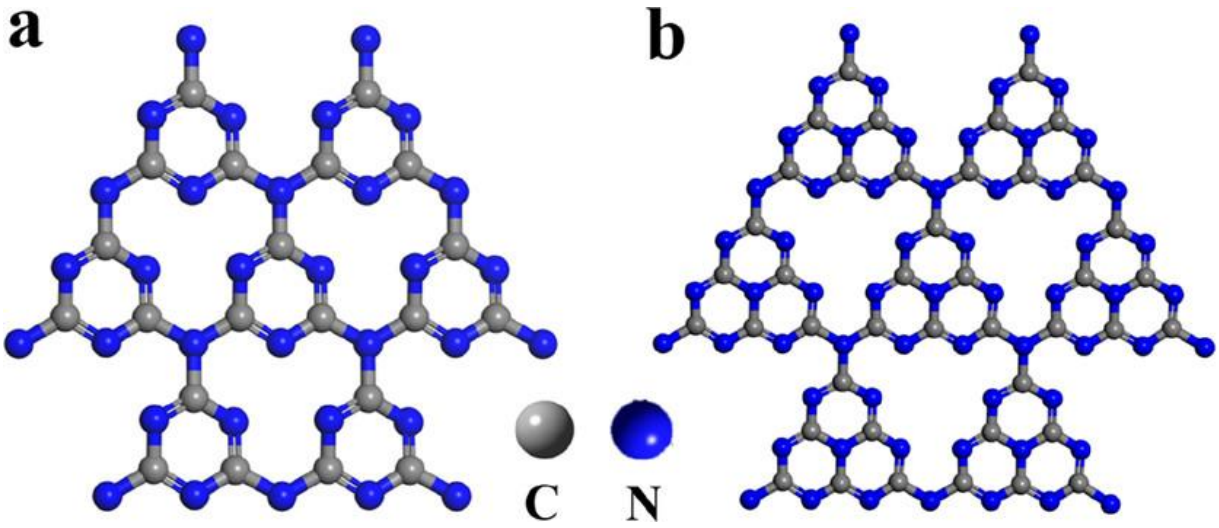

Figure 12. Structures of (a) triazine and (b) tri-*s*-triazine.

In the development branch of nonmetal-based catalysis, metal-free materials such as carbon nitride, graphene, carbon nanotubes, boron nitride, boron nitride nanotubes inspired numerous attractions in the research community to solve the energy and environmental crisis. Carbonic nitride (C_3N_4) polymers were first discovered in 1834. Melem, melam, melamine, and melon were considered as triazine - and tri-s-triazine-based units (Figure 12).[12] A solid yellow powder was obtained via the polymerization of aluminum chloride and potassium thiocyanate, so called "melon". In 1922, C_3N_4 was firstly introduced by Franklin,[13] who identified C_3N_4 as the

final product upon calcination of melon and proposed its structure. During the study, the concept of C_3N_4 was presented and demonstrated that C_3N_4 can be produced by polymerizing ammonia carbonic acids.

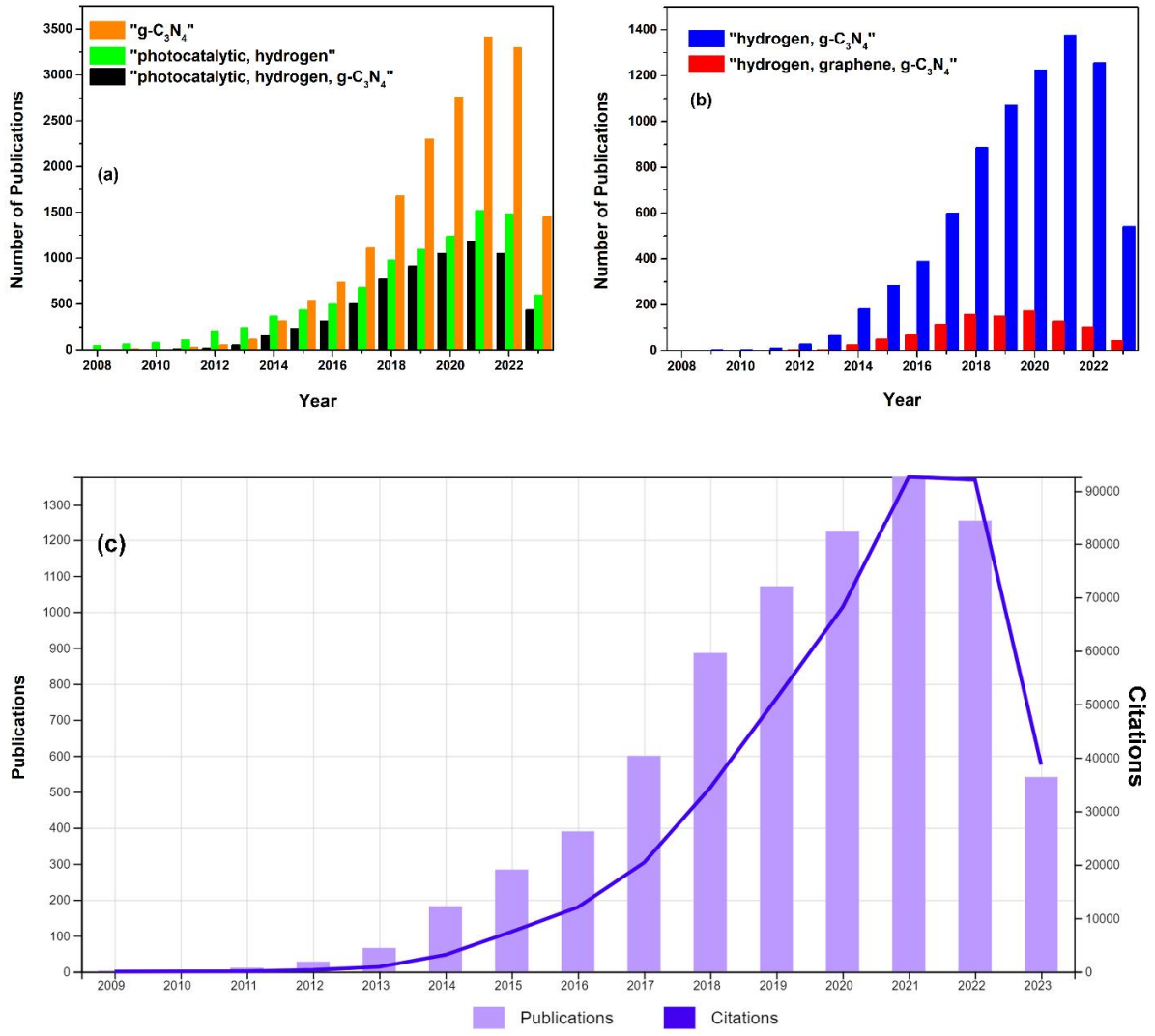

Figure 13. Number of Publications Over Time Using (a) "g-C_3N_4", "photocatalytic" + "hydrogen", and "photocatalytic" + "hydrogen" + "g-C_3N_4" keywords. (b) "hydrogen" + "g-C_3N_4" and "hydrogen" + "graphene" + "g-C_3N_4". (c) Times Cited and Publications Over Time Using "hydrogen" + "g-C_3N_4" keywords. Data from Web of Science Core Collection on May 30th 2023.

However, the melon-based C_3N_4 was not paid much attention due to a lack of exhaustive characterization. C_3N_4 is regarded as unconfirmed species for a long time because it is chemically stable and cannot be dissolved into most of solvents.[14] At present, studies on its characterization

and preparation are still underway. In general, C_3N_4 is composed of seven phases, including α-C_3N_4, β-C_3N_4, cubic C_3N_4, pseudocubic C_3N_4, g-h-triazine, g-o-triazine, and g-h-heptazine. Among them, graphitic carbon nitride (g-C_3N_4) has excellent stability, a simple synthesis from earth-abundant precursors, and a good semiconducting property. Thus, tri-s-triazine has been widely identified as the basic building block of g-C_3N_4. A catalytic activation of benzene using g-C_3N_4 was reported by Goettmann et al. in 2006.[15] Three years later, Wang and co-workers discovered that g-C_3N_4 is capable of photocatalytic hydrogen production upon visible light irradiation,[16] marking a significant milestone in metal-free photocatalysts. Thereafter, g-C_3N_4 has attracted universal attention due to its several features like being metal-free, non-toxic, facile synthesis from low cost materials, appealing electronic band structure, and physicochemically stable. Consequently, the studies and publications related to g-C_3N_4 materials have dramatically increased (Figure 13).

Typically, g-C_3N_4 is easily synthesized through thermal polymerization of abundant nitrogen-rich precursors such as melamine,[17, 18] cyanamide,[19] dicyandiamide (DCDA),[20, 21] urea,[22-26] thiourea,[27-29] 3-amino-1,2,4-triazole,[30] and ammonium thiocyanate.[31] Photocatalytic properties of C_3N_4 materials are strongly influenced by their composition, bandgap, crystallinity, and structure.[9, 32] Polymeric g-C_3N_4 is a metal-free p-type, indirect semiconductor. Compared to TiO_2, g-C_3N_4 has a moderate bandgap of 2.7 – 2.8 eV, which can be tunable by adjusting the nitrogen content in the structure. The narrow bandgap of g-C_3N_4 leads to an onset of visible-light absorption at around 450 – 460 nm. CB and VB positions of g-C_3N_4 locate at −1.3 V and 1.4 V, respectively (vs. NHE for photocatalytic water splitting at pH = 7). In all carbon nitride structures, g-C_3N_4 is the most thermally stable allotrope, maintaining a thermal stability of near 600°C in air, which is confirmed by thermogravimetric analysis (TGA), attributing to the aromatic C–N heterocycles.[14] Furthermore, g-C_3N_4 is chemically stable and not soluble in acids, alkalis, or organic solvents, which makes it robust under ambient conditions.[33] Therefore, the g-C_3N_4 is expected a promising metal-free semiconductor photocatalyst that has the potential to revolutionize the field of photocatalysis.

Although g-C_3N_4 exhibits intriguing properties, some disadvantages, such as its low surface area, high charge recombination rate, hydrophobic solubility, and limited visible-light absorption prevent its practical applications. Regarding to the first step of photocatalytic H_2

evolution, g-C_3N_4 will absorb the sunlight with an appropriate wavelength (shorter than 460 nm) to excite the charge carriers inside the photocatalyst. The negative charge (electrons) are presented in CB and leave the positive charges (holes) are left in VB. Step 2nd, the charge carriers diffuse from excited positions from bulk photocatalyst to accessible surface active sites. Photoinduced electron/hole pairs could be recombined to their original states by a reversible process of charge separation. The high recombination rate of photocatalysts is considered a bottleneck that has hindered the practical application of hydrogen production. Step 3rd, electrons and holes are transferred to reduction sites and oxidation sites on the surface of photocatalyst or cocatalyst, respectively, where the photoinduced charge carriers participate in the redox chemical reactions. This study will focus on the hydrogen evolution reaction (HER), a half-reaction of g-C_3N_4-based water splitting under simulated sunlight irradiation. The remaining oxidation reaction of holes will be taken by a sacrificial agent (TEA, TEOA).

To overcome these challenges for g-C_3N_4 in photocatalysis applications, numerous strategies have been attempted to overcome these shortcomings such as synthesis techniques,[20] electronic structure modulation,[34] nanostructure design,[35] metal doping,[36] nonmetal doping,[37] surface modification,[38] morphology control,[39] and coupling with another semiconductor.[40, 41] Among them, the nanostructure design of g-C_3N_4 nanostructure is promising as a facile and effective method to improve photocatalytic H_2 evolution due to its high polymeric flexibility. Various structures such as bulk g-C_3N_4, g-C_3N_4 nanosheets (g-C_3N_4 NSs),[42] g-C_3N_4 nanotubes (g-C_3N_4 NTs),[43, 44] and mesoporous g-C_3N_4 have been synthesized.[32] According to Zhu et al., g-C_3N_4 NTs displayed superior activity under visible light, whereas g-C3N4 NTs exhibited higher activity than bulk g-C_3N_4 and g-C_3N_4 NSs, possibly as a result of more active sites, higher photogenerated carrier transfer efficiency, and increased mass transfer.[43]

Mesoporous and microporous g-C_3N_4 (MMCN) have been paid great attention in terms of nanostructure design recently. Some methods for the synthesis of MMCN, including soft template, hard templating, and template-free approaches have been developed. The templating approaches are used to create ordered porosity and a high surface area in the MMCN nanostructures. Mesoporous g-C_3N_4 (MGCN) were reported for the first time by Vinu et al. in 2005, opening a new class of MgCN was described with large specific surfaces and pore diameters between 2 and

50 nm, which has been proposed for a wide range of applications. It has been the subject of intensive research over the last decade to exploit the structural and textural properties of MGCN, including its ordered structure, extremely high specific surface area (SSA), narrow pore size distribution, tuning of pore size, uniform particle size, controllable shape and morphology, and its crystallinity, semiconductivity, and surface engineering and functionalities (such as organic and inorganic nanostructures within its mesochannels). Guo et al. reported a MMCN using SBA-15 as a hard template, resulting in 8.6 times higher specific surface area and 9.7 times as high as photocatalytic H_2 evolution under visible-light irradiation compared to pristine g-C_3N_4, respectively. The higher photoactivity of MMCN could be attributed to its porous structure, more active sites, and high surface area. With a nano hard templating technique using mesoporous silicas, MGCN can achieve surface areas up to 1125 $m^2 g^{-1}$, pore volumes up to 1.8 cm g^{-1}, tuneable pore diameters, tunable bandgap, and a large number of basic active sites.[45] The soft-templating and hard-templating have huge disadvantages of the complex synthesis process, long synthesis time, high cost, and unscalable for mass production. Hence, the template-free approach prefers to for large-scale production of MMCN. However, the textural properties, the ordered nature, high SSA and uniformly pore diameters are still challenge to template-free approach development. Even though morphology control of g-C_3N_4 provides more surface area and active sites, it still exhibits weak visible-light absorption and a high recombination rate, which limits the practical application of g-C_3N_4-based photocatalysts. In this thesis, the study is focused on the solutions for facile and effective methods for the synthesis of advanced nanostructured of MMCN for mass production of green H_2.

1.5. Graphene-based Photocatalytic Applications

All life on Earth is made up of carbon, which is the most captivating element in the periodic table. Carbon can exist in a variety of allotropes, including graphite, diamond, fullerene, amorphous carbon, carbon nanotubes, and graphene, one of the most promising materials for the 21st century. Among them, graphene has been extensively studied since Andre Geim and Kostya Novoselov reported an isolated single layer of carbon atoms tightly packed into a two-dimensional (2D) honeycomb crystal structure in 2004.[46] The discovery on graphene triggered ripples of excitement in the technological and scientific communities due to the extraordinary properties of a monolayer of this material.[47] Andre Geim and Kostya Novoselov won the Nobel Prize in Physics 2010. Then, the "graphene-era gold rush" has expanded to numerous fields due to the

unique and outstanding structural, optical, mechanical, thermal, and electrical properties of graphene. One-atom-thick planar sheet of sp^2-bonded carbon atoms densely packed in a honeycomb crystal lattice, graphene, possesses the superior electrical conductivity and mobility, theoretically high specific surface area, excellent optical transmittance, and high chemical stability. In order to understand graphene's potential, one needs only look at its properties such as excellent charge carrier mobility (200 000 $cm^2\ V^{-1}\ s^{-1}$), thermal conductivity (5000 $W\ m^{-1}\ K^{-1}$), electrical conductivity (2000 $S\ m^{-1}$), extremely high theoretical specific surface area (2630 $m^2\ g^{-1}$), transparency (97.7%), mechanical strength (Young's modulus ~ 1 TPa), excellent environmental compatibility, and adsorption capacity for organic and inorganic molecules.[48] The outstanding performance of graphene in many applications makes it the most celebrated member of the carbon family as a promising material in the next century.

Graphene participated into the field of photocatalysis as a promising game-changer material. The integration of graphene into traditional semiconductor matrices primarily aims to enhance the photocatalytic performance of semiconductors by leveraging the co-catalyst function of graphene to augment the separation and transfer of photogenerated charge carriers from semiconductors, which is the critical step for photocatalytic reactions. Addressing future environmental and energy problems requires the efficient and cost-effective direct conversion of solar energy into chemical energy and fuels. Photocatalysis, a sustainable chemistry approach, offers a promising avenue for utilizing the abundantly available and clean solar energy as a viable technology, ultimately promising solutions for future fuel needs.

In photocatalytic H_2 generation from water splitting, graphene is generally credited with two advantages: electron acceptor and mediator, and cocatalyst. First, an electron mediator like graphene, which has a low Fermi level and unique electrical conductivity, facilitates charge carrier separation, promotes electron transfer, and boosts the activity of photocatalytic H_2 evolution. Second, the more negative reduction potential of graphene/graphene$^{\bullet-}$ than that of H^+/H_2, which means it can serve as an alternative cocatalyst beside noble metals.[49, 50] Hybrid graphene and g-C_3N_4 nanocomposite was calculated to open the bandgap in graphene and create electron–hole puddle between 2D/2D layers, which further enhances the charge transfer mechanism between two interfaces. As a similar 2D graphitic structure, g-C_3N_4 established a strong vdW interaction with graphene. The g-C_3N_4/graphene interface showed strong interlayer electron coupling, resulting in

band gap opening in graphene and increased visible absorption for the composite.[51] Thus, the high recombination rate bottleneck of g-C_3N_4 is resolved, resulting in the enhancement of photoactivity of 2D/2D of graphene/g-C_3N_4 hybrid.

1.6. Motivation

One of the most promising strategies for resolving the future environment and energy crisis is to convert solar energy directly into chemical energy and fuels. Using solar energy to split water may provide a clean and efficient method of storing and transporting hydrogen, which can be an alternative to fossil fuels. Green hydrogen production via photocatalysis is still held a superb small percentage of below 0.03 % of the world's hydrogen production in 2021. Over a century has passed since TiO_2 was first used for photocatalytic hydrogen evolution with high-energy UV light. However, only approximately 5 percent of solar ultraviolet radiation reaches the surface of the Earth through the atmosphere. In this regard, recent comprehensive research on semiconductor materials promoted by visible light has led to the development of hydrogen evolution photocatalysts. The polymeric semiconductor g-C_3N_4, as a novel noble metal-free photocatalyst, has emerged as an attractive photocatalyst that responds to visible light. It has simple synthesis, appealing optical gap and semiconducting properties, high chemical and thermal stability, as well as a wide variety of textures and structures, all of which make it an attractive photocatalyst. Overall water splitting through photocatalysis still faces extremely poor hydrogen evolution reaction (HER) performance, which hinders the use of photocatalysts for hydrogen production applications. The photocatalytic HER by half-reaction of water-splitting has been intensively studied for green, low-cost, and large-scale production of H_2 fuels, using inexpensive or waste dyes as sacrificial agents to replace water oxidation reactions. Thus, the hydrogen evolution rate is dramatically enhanced, which enables the opportunity to increase efficiencies and practical application of these renewable energy technologies.

In the case of hydrogen evolution reaction (Equation 1-4), only two electrons are required to generate one mol of H_2 gas, and only minimal electronic reorganization is necessary for the photocatalysis process. This reaction is favored by platinum cocatalyst because its kinetics are fast, and the mass transport of hydrogen and protons controls its outcome.[52] The story is much more complex for the oxygen evolution reaction (OER) (Figure 1-6), which is required four holes per mole of O_2 generation and a very complicated reorganization, processes in the formation of reaction

intermediates.[53] The design of an effective g-C_3N_4-based photocatalyst system for the HER is, therefore, a crucial opportunity to enhance efficiencies of photocatalytic green H_2 production technology, including the catalyst and cocatalyst engineering, photosensitizer, sacrificial agents, and performance optimization.

Hydrogen evolution reaction (HER):[10]

acidic solution: $2H^+ + 2e^- \longrightarrow H_2$ (Equation 1-4)

alkaline solution: $2H_2O + 2e^- \longrightarrow H_2 + 2OH^-$ (Equation 1-5)

Oxygen evolution reaction (OER):

acidic solution: $H_2O \xrightarrow{4h^+} O_2 + 4e^- + 4H^+$ (Equation 1-6)

alkaline solution: $4OH^- \xrightarrow{4h^+} O_2 + 4e^- + 2H_2O$ (Equation 1-7)

Since first discovered in 1834, carbonic nitride seems to be forgotten in the scientific community because it is recognized as unconfirmed species due to its insolubility in various solvents or chemical inertness. Lasting for over a century, Wang et al. discovered that g-C_3N_4 is possible for water splitting reaction in 2009, followed by the extensive research on g-C_3N_4-based photocatalytic applications have boomed. However, the g-C_3N_4 limitations imposed by inefficiencies below have declined the use of g-C_3N_4 photocatalyst in practical photocatalytic H_2 production:

- Low dispersion in reaction media, which reduces the light adsorption and blocks the accessible active sites.
- High recombination rate due to the generated electrons are highly unstable and they tend to reduce their energy to go back to the initial position instead of migrating to the H_2 evolution active site. This is recognized as a bottleneck in the photocatalysis process.
- Poor electrical conductivity. In contrast to graphene, g-C_3N_4 has very low electrical conductivity in basal planar and between multilayers of bulk, resulting in an energy barrier for excited electrons to move from generated point to the active site. As a result, the excited electron does not have enough energy to get over a high barrier immigration energy, and it prefers to recombine with the hole in the previous position.

- Low accessible active sites. As a 2D material, g-C_3N_4 has a theoretical SSA of 2630 $m^2\ g^{-1}$ when a single layer exists in the reaction media. However, due to the strong hydrogen bonding and van der Waals force, g-C_3N_4 has a tendency of stacking between interlayers, resulting in blocking the actives inny the photocatalyst.
- Low mass transfer, long charge diffusion range, and deficiency of reducing and oxidizing active sites on basal 2D planes.

From previous studies, we have experience in generating single layer and highly dispersion of graphene 2D material in organic solvents,[54] the knowledge of the dispersibility of 2D material like in solvents,[55, 56] along with our discovery of photocatalytic atomic hydrogen reduction of platinum precursor subsequently highly reduces graphene oxide.[57] The road map of g-C_3N_4 for photocatalytic H_2 evolution, therefore, inspired us to develop an advanced nanostructure design, *in situ* exfoliation, engineering of single layer 2D materials of g-C_3N_4 and graphene nanosheets for enhancing photocatalytic hydrogen evolution under simulated sunlight irradiation.

1.7. Thesis Scope

This thesis introduces a brand new surface science approach of the *in situ* exfoliation of graphitic carbon nitride (g-C_3N_4), engineering holey-defects on 2D g-C_3N_4 layers, and creation of self-assembled graphene via solvothermal treatment of g-C_3N_4 bulk in various organic solvents. Furthermore, a strategy of exfoliating g-C3N4 bulk and graphene into single layer via chemical oxidation, followed by a surface modification to enhance the nanostructure of the layer, and then restore the accessible active sites by catalytic hydrogen reduction. This thesis provides a fundamental understanding of various parameters that govern the photocatalytic H_2 evolution performance via the study of engineering nanostructure of single layer g-C_3N_4, engineering oxidation state of platinum cocatalyst, conjunction 2D/2D heterostructure of graphene and g-C_3N_4 hybrid, and photoreforming of graphene oxide by g-C_3N_4. These works enable quantification of the factors that contributed to photocatalytic performance, such as oxygen doping; self-assembled graphene formation; platinum co-catalyst oxidation states; nanostructure of the resultant catalysts; electronic band structure; and uniformly holey-defects creation. Moreover, density functional theory calculations are applied to offer deep insights what and why the difference in phenomena among the different reactant agents, and processes, which are supposed to shedding light on the reaction mechanisms and explanations.

Chapter 2 establishes both experimental and theoretical approaches to engineering holey-defects on 2D monolayer of g-C_3N_4 nanosheets by solvolysis in organic solvents, proposes the reaction mechanism for holes generating, and provides the optimization of the performance evaluation system and assessment method for these photocatalysts. This study introduces new insights to the optimization of the 2D holey g-C_3N_4 for photocatalytic H_2 evolution, where C_3N_4-THF shows the appropriate holey structure compared to C_3N_4-DMF (no holes), C_3N_4-MA (break the g-C_3N_4 structure and generate big holes), and C_3N_4-IPA (weak etching effectiveness). Furthermore, the new phenomenon of self-assembled graphene formation during the solvolysis process, and the division of Pt oxidation states into Pt^0 and Pt^{2+} (in PtO form) in the C_3N_4-THF sample, which are demonstrated to enhance the photocatalyst performance. DFT calculation on the adsorption energy of solvent molecule on heptazine sheet and the charge density of adsorbate on the sheet after adsorption reveals the reason for different etching levels among the used organic solvents and shedding light on the reaction mechanism.

Chapter 3 further considers a green method of solvolysis g-C_3N_4 bulk by using an environmentally friendly solvent (ethyl alcohol) for mass production of green H_2. The grid-like structure of the monolayered g-C_3N_4 nanosheets was achieved using a facile and green solvothermal process. The formation of self-assembled graphene on g-C_3N_4 during the process facilitated charge transfer and separation on the photocatalyst, as confirmed by density functional theory calculations. The grid-like structure of the g-C_3N_4 contributed to the formation of a platinum oxide co-catalyst, which enhances the hydrogen evolution rate by inhibiting the reversible reaction pathway of hydrogen gas to protons. Through DFT calculations, the reaction mechanism of grid-like structure g-C_3N_4 is proposed. These calculation investigations validate the experimental observations of the electron-hole puddle on the graphene sheet that facilitates photoinduced charge separation and immigration, and the enhanced photoabsorption in the visible region in graphene/g-C_3N_4 hybrid.

Chapter 4 aims to create a highly dispersion of holey graphene/g-C_3N_4 in aqueous, which maximizes the catalyst surface accessible active sites in reaction media. Since holey graphene can superior disperse in an aqueous solution, it is used as a carrier to maintain highly dispersion of g-C_3N_4 photocatalyst in reaction media. First, the single layer of g-C_3N_4 in the aqueous solution is achieved through the chemical oxidation of g-C_3N_4 bulk. Second, holey graphene and oxidized g-C_3N_4 hybrid is prepared by a simple stirring and mixing method. Finally, the photocatalyst

composite is reduced by catalytic hydrogen reduction in aqueous, resulting in a highly dispersion holey graphene/g-C_3N_4 hybrid with excellent photocatalytic H_2 evolution.

Chapter 5 summarized the conclusions and suggested a perspective road map for future works for the photoreforming of graphene oxide over g-C_3N_4 and a specific design for overall water splitting.

1.8. Thesis Procedures

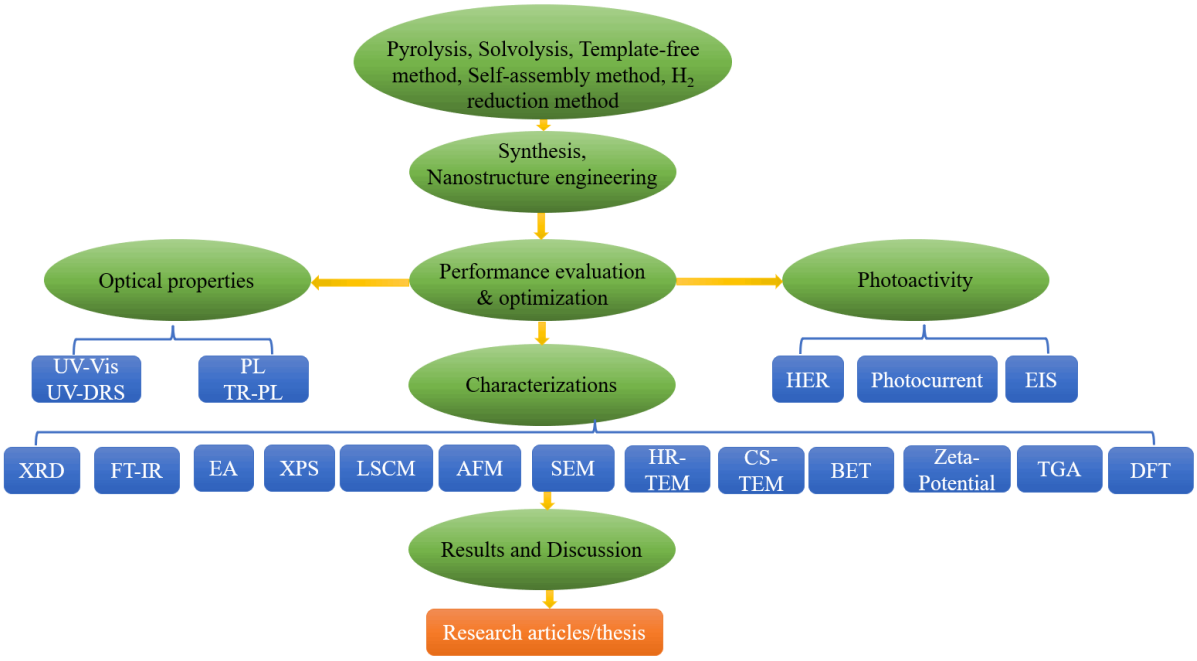

The research procedure of this thesis is shown in the scheme above. Firstly, the photocatalysts were mainly synthesized and nanostructure engineered through these methods: pyrolysis, solvolysis, template-free method, self-assembly method, and H_2 reduction method. Secondly, the optimized photocatalytic performance was evaluated by measuring the photocurrent response, electrochemical impedance spectra (EIS), and photocatalytic toward H_2 evolution. While the optical properties of the samples were measured by UV-Vis, Ultraviolet–visible diffuse reflectance spectroscopy (UV-DRS), photoluminescence (PL), and time-resolved photoluminescence (TR-PL). Thirdly, the crystal structure, surface electronic structure, chemical composition, morphology and microstructure, and thermal properties of the photocatalysts were characterized by a series of techniques, including electron microscopy (field emission scanning electron microscopes (FE-SEM), high-resolution transmission electron microscopy (HR-TEM), and atomic force microscopy (AFM)), X-ray diffraction (XRD), X-ray photoelectron spectroscopy (XPS), Fourier-

transform infrared spectroscopy (FT-IR), Raman spectroscopy, elemental analysis (C, H, N, O, S), laser scanning confocal microscope (LSCM), N_2 adsorption/desorption measurement, Zeta-potential, thermogravimetric analysis (TGA), and density functional theory (DFT) calculations. Finally, the results and discussion were presented in the research articles and this thesis.

CHAPTER 2

Overview of Chapter 2

This chapter presents the manuscript titled "Engineering Holey Defects on 2D Graphitic Carbon Nitride Nanosheets by Solvolysis in Organic Solvents", which was published in ACS Catalysis Journal (ACS Catal. 2022, 12, 21, 13763–13780).

The recent extreme weather gets a boost from climate change and the global energy security conundrum has posed extensive studies on boosting the conversion of solar energy to chemical energy through photocatalysis. The demonstration of photocatalytic solar green hydrogen production based on a facile method of synthesizing an optimized holey structure of 2D g-C_3N_4 photocatalyst and the optimization of the performance evaluation system and assessment method for this photocatalyst indicates the large-scale applicability viability as well as technical challenges toward practical mass green hydrogen production. In this work, we present the *in situ* exfoliation of graphitic carbon nitride (g-C_3N_4), engineering holey-defects on 2D g-C_3N_4 layers, and formation of self-assembled graphene via solvothermal treatment of g-C_3N_4 bulk in various organic solvents. Methyl alcohol, isopropyl alcohol, tetrahydrofuran, and dimethylformamide were chosen for exfoliating and modifying g-C_3N_4 sheets based on their compatibility with g-C_3N_4 in Hansen parameters. Uniformly holey-defects on 2D g-C_3N_4 nanosheets were successfully engineered using tetrahydrofuran solvent in a facile solvothermal process. The introduction of N vacancies in heptazine units and the formation of the holey structure of tetrahydrofuran-modified g-C_3N_4 sample (C_3N_4-THF) led to high photocatalytic performance due to enhanced mass transfer, shortening of the charge diffusion lengths, and increased charge separation during the photocatalysis process. Furthermore, full exfoliation of the engineered nanostructure of holey-defect C_3N_4-THF into a monolayer in reaction media led to maximizing accessible reducing and oxidizing active sites. As a result, the C_3N_4-THF sample achieved photocatalytic activity with a H_2 evolution rate at the stationary point as high as 31256.9 μmol h^{-1} g^{-1} under 1 Sun illumination of a Solar Simulator.

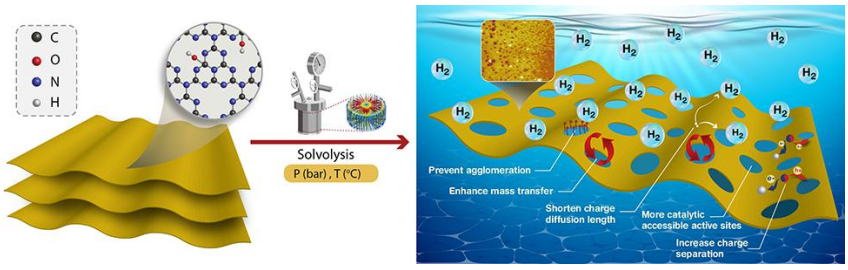

2. Engineering Holey-defects on 2D Graphitic Carbon Nitride Nanosheets by Solvolysis in Organic Solvents

2.1. Introduction

Solar energy is the most sustainable energy replacement for fossil fuels as it is a plentiful, widely distributed, and a continuously renewable source of energy. Hydrogen evolution brought by high-energy UV light has been well studied for over a century since the first observation with TiO_2 as a photocatalyst.[58] However, only approximately 5 percent of solar ultraviolet radiation penetrates the atmosphere to reach the Earth's surface.[6] Hence, extensive recent research in semiconductor materials promoted by visible light has led to the development in the use of photocatalysts for hydrogen evolution.[9, 10] Among these materials, the polymeric semiconductor, g-C_3N_4 as a novel noble metal-free photocatalyst with a bandgap of 2.7 eV,[59] a delocalized π system, and diverse synthetic modularity has emerged as a promising visible light-responsive photocatalyst due to its facile synthesis, appealing optical bandgap and semiconducting properties, high chemical and thermal stability as well as a variety of textures and structures.[23, 60] Furthermore, g-C_3N_4 can be easily fabricated via thermal polymerization of abundant precursors such as urea,[22] thiourea,[28, 29] melamine,[61, 62] cyanamide,[63, 64] and dicyandiamide.[20, 21, 65] Unfortunately, bulk g-C_3N_4 synthesized by this method suffers several obstacles and shortcomings such as low surface area resulting in low dispersion of accessible active sites in water,[65-67] high recombination rate of charge carriers, poor electrical conductivity, and the lack of visible light absorption above 460 nm.[68] Therefore, numerous modifications of bare g-C_3N_4, including synthesis approaches, nanostructure design, electronic structure and bandgap modulation[20, 35, 69, 70] have been employed to optimize photocatalyst performance.

The accessible surface active sites, morphologies, and lateral sizes of semiconductor materials greatly influence the photoactivity of photocatalysts. Theoretically, graphene-like g-C_3N_4 as a two-dimensional (2D) material is a promising candidate for various applications in photosynthesis due to its large specific surface area, which provides more reactive sites and shorter carrier diffusion lengths to prevent electron recombination. However, bulk g-C_3N_4 has strong hydrogen bonding and van der Waals stacking between interlayers, which leads to low dispersibility of g-C_3N_4 in reaction media.[67, 71] The accessibility of active surfaces in the reaction medium and the dispersibility of g-C_3N_4 in water are, therefore, crucial parameters. An exfoliation process could be used to achieve a monolayer structure of g-C_3N_4, which maximizes the basal active sites of 2D

g-C_3N_4 material for photocatalysis of H_2 evolution. However, the planar structure of g-C_3N_4 sheets has some drawbacks for photocatalytic toward the H_2 evolution reaction such as long charge diffusion to active sites, low mass transfer, and deficiency of reducing and oxidizing active sites on basal planes. From the perspective of nanostructure properties, holey-defect g-C_3N_4 nanosheets with multiple in-plane holes can significantly increase the efficiency of mass transport across holey-defects during photocatalysis and may also enhance the charge separation efficiency by decreasing the charge diffusion length. Additionally, these holey-defects not only greatly increase the number of accessible active sites, but also effectively act to prevent agglomeration by reducing the interaction sites between g-C_3N_4 layers. Although there are many advantages from achieving holey-defects with g-C_3N_4, synthesis of this structure of g-C_3N_4 nanosheet using ammonia-based toxic reagents poses a challenge.[72-75]

Herein, we report an integrated process of exfoliation, morphology transformation, and g-C_3N_4/self-assembled graphene formation via solvothermal treatment of g-C_3N_4 in various organic solvents. Methyl alcohol, isopropyl alcohol, tetrahydrofuran, and N,N-dimethylformamide were used as organic solvents for observable high-pressure solvothermal at 200 ℃, which modified the morphology and graphitic structure, and disrupted hydrogen and van der Waals bonding. It was interesting to observe that self-assembled graphene was created during the solvothermal treatment of g-C_3N_4, which may have resulted from the etching of g-C_3N_4 to form fragment units byproducts, followed by reforming into the graphitic structure of graphene. The modification of bulk g-C_3N_4 by a moderately polar solvent plays an important role in graphitic structure reforming and assists in the exfoliation of g-C_3N_4 in attempting to achieve the holey structure of monolayer g-C_3N_4 in reaction media. The holey-defects on 2D g-C_3N_4 nanosheets were successfully engineered using a facile solvothermal method with different organic solvents. Tetrahydrofuran was found to be the most appropriate solvent for engineering holey-defects on g-C_3N_4 layers, resulting in a uniformly holey-defects single layer structure of C_3N_4-THF. All the resultant g-C_3N_4 samples performed high hydrogen generation, in particular the tetrahydrofuran-modified g-C_3N_4 sample, which had an optimized hydrogen evolution rate as high as ca. 31256.9 μmol h^{-1} g^{-1}. The superior photocatalytic activity of solvothermal modified g-C_3N_4 was demonstrated by enhanced H_2 evolution rates under simulated sunlight using platinum nanoparticles decorating by hydrogen reduction as co-catalyst, triethanolamine as a sacrificial agent, and Eosin Y as a photosensitizer.

2.2. Experimental and Methods

2.2.1. Materials

Dicyandiamide was used as a bulk graphitic carbon nitride precursor by a thermal polymerization method. Dicyandiamide (DCDA), triethanolamine (TEOA), chloroplatinic acid solution (H_2PtCl_6, 8 wt. % in H_2O) were purchased from Sigma Aldrich. Eosin Y and organic solvents were purchased from Samchun Chemicals (Korea). Methyl alcohol (CH_3OH), isopropyl alcohol (IPA), tetrahydrofuran (THF), and N,N-dimethylformamide (DMF) were HPLC-grade. High-purity argon gas was purchased from the MS Gas Corporation (Korea). All chemicals were used as received without further purification.

2.2.2. Synthesis of Solvothermal Treatment G-C_3N_4 Photocatalyst

Preparation of bulk and thermal exfoliated g-C_3N_4

Specifically, 6 g of DCDA precursor was placed in a B-form crucible and covered by aluminum foil, which was annealed at 550 ℃ for 4 h in a muffle furnace with a ramping rate of 5 ℃/min. The sample was denoted as C_3N_4-bulk. Then, the sample was cooled down to ambient temperature before being uniformly ground in a mortar for 15 min. The product was heated to 500 ℃ with a heating rate of 5 ℃/min in the air atmosphere and held for 2 h, followed by natural cooling down to RT.

Synthesis of solvothermal treated g-C_3N_4

Typically, 1 g of the as-prepared g-C_3N_4 sample was added into a 100 ml vial, containing 70 ml of either methyl alcohol (MA), isopropyl alcohol (IPA), tetrahydrofuran (THF), or N,N-dimethylformamide (DMF), followed by sonication for 6 h (Jeiotech UC-10, 200 W). The ultrasonic bath temperature was kept around 25 ℃ by cooling water. The mixed suspension was transferred into a high-pressure microreactor (stirred reactor, HR-8200, Hanwoul Engineering, Korea) and performed the solvothermal reaction at 200 ℃ for 6 h. The pressure of the reaction medium was observed during the process. It was shown the working pressures of 42 bar, 25 bar, 20 bar, and 2 bar corresponding to the reacted organic solvents MA, IPA, THF, and DMF, respectively. After the reactor had naturally cooled to ambient temperature, deionized water was used to exchange for the solvents in this study. The solid-to-liquid ratio of the obtained suspension was calculated, and then the sample was diluted with deionized water to make a 0.2 mg mL^{-1} suspension in the triple-neck round bottom flask (Duran, Germany).

Decorating of platinum nanoparticles by hydrogen reduction in aqueous solution

Platinum (Pt) was used as a co-catalyst in this research. A designed amount of 3 wt. % platinum was decorated on the surface of the resultant g-C_3N_4 samples by hydrogen reduction in aqueous at 60 ℃ with chloroplatinic acid as the Pt precursor as in previous research.[57] Here, the suspension was vigorously stirred by a magnetic bar in the three necks round bottom flask, and hydrogen gas was injected from the bottom of the reactor at a flow rate of 25 sccm for 1 h. The products were washed with DI water by centrifugation at 10000 rpm for 15 min, and the separated catalysts were vacuum dried at 90 ℃ for 12 h for further characterization. The obtained catalysts with methyl alcohol, isopropyl alcohol, tetrahydrofuran, and N,N-dimethylformamide were denoted as C_3N_4-MA, C_3N_4-IPA, C_3N_4-THF, C_3N_4-DMF, respectively.

2.2.3. Photocatalytic H_2 Evolution

Photocatalytic H_2 evolution under visible-light irradiation in a quartz flask reactor (300 mL, diameter: 70 mm, and height: 80 mm) was implemented by a simulated sunlight source (Oriel® MiniSol model LHS-7320 Class ABA LED-based solar simulation, Newport, USA). The focused intensity of the light on the solution was 100 mW cm^{-2}. The evolved H_2 gas was measured via an automatic injection, online gas chromatography with a thermal conductive detector (TCD), and a Carboxen 1000 column (Sigma-Aldrich).

2.2.4. Characterizations

The Pt element composition of the as-prepared samples was investigated by an inductively coupled plasma-optical emission spectrometer (ICP-OES; 700-ES Varian, Mulgrave, Australia). The elemental compositions of the samples were analyzed using an elemental analyzer (Flash 2000, Thermo Scientific). Scanning electron microscopy (SEM; JSM-600F JEOL, Tokyo, Japan) was applied to investigate the microstructure and the catalyst morphology. The microstructure and distribution of the Pt nanoparticles were examined using high-resolution transmission electron microscopy (HR-TEM; JEL-2100F JEOL, Tokyo, Japan). CS-STEM (JEM-ARM300F, JEOL) was used to study holey structure of C_3N_4-THF sample with high spatial resolution at 300 kV electron beam. The crystalline structures of the acquired samples were analyzed using High-Resolution Powder X-ray diffraction (HRPXRD; Rigaku D/MAZX 2500 V/PC high-power diffractometer, Tokyo, Japan) with a Cu Kα X-ray source with a wavelength of λ = 1.5415 Å at a scan rate of 2° (2θ)/min. A Fourier transform infrared spectroscopy was used to characterize the

functional groups of the produced photocatalysts (FT-IR; Nicolet 380 spectrometer, Thermo Scientific Nicolet iS5 with an iD1 transmission accessory, Waltham, MA, USA). X-ray photoelectron spectroscopy was used to investigate the compositions, chemical states, and electronic states of the elements on the Thermo scientific K-Alpha system (XPS, Waltham, MA, USA). A zeta potential analyzer was used to carry out the zeta potential analysis (Zetasizer Nano ZS, Malvern Panalytical, Malvern, United Kingdom). UV-Vis absorption spectra (Specord 210 Plus, AnalytikJena, Germany) and UV–vis diffuse reflectance spectra (SCINCO S-4100 Diffuse Reflectance-Ultraviolet/Visible Spectrophotometer, SCINCO, Korea) were used to examine the photocatalyst optical characteristics. Photoluminescence spectroscopy was measured with a 473 nm diode laser at ambient temperature (Agilent Technologies, Cary Eclipse fluorescence spectrophotometer, Santa Clara, CA, U.S.A.). Time-resolved fluorescence (TRPL) spectra were performed under 400 nm laser excitation by a FS5 spectrofluorometer (Edinburgh Instruments Ltd, Livingston, UK). Tri-exponential functions were used to fit the emission decay profiles. The lateral sizes and height profiles measurement of the resulted g-C_3N_4 sheets were performed by a commercial atomic force microscopy (AFM, MFP-3D, Asylum Research). The optical images of resulted catalysts were captured using an Olympus laser scanning confocal microscope (LSCM). Raman spectra were obtained by confocal Raman microscopy with a 532 nm wavelength incident laser light (Thermo Scientific). Thermogravimetric analysis (TGA) was measured under an argon atmosphere at a heating rate of 10 ℃ min^{-1} (TGA 550 - TA Instruments).

2.2.5. Electrochemical Measurement

The electrochemical workstation (VSP BioLogic Science Instruments, Seyssinet–Pariset, France) was used to perform electrochemical impedance spectroscopy (EIS) measurements in a standard three-electrode system under UV irradiation at room temperature. The EIS was carried out in an open circuit, following a 10-minute delay, applied a frequency range of 100 kHz to 0.01 Hz with an amplitude of 10 mV and at a direct current potential of +0.8 VSCE.

A drip-coated method was used to prepare the membrane electrode. Typically, 20 mg catalyst powder was ground with 2 mg activated carbon by mortar in 20 min to obtain fine powder, followed by adding into 100 µL isopropanol 99.7% and 30 µL Nafion 5 wt. % (Sigma Aldrich, Korea). Then, 10 ml of a sodium hydroxide 1M (NaOH) solution was used as the electrolyte. The working electrode was a 6-mm standard-type glassy carbon electrode upon, in which 10 µL of the

sample was placed (1 μL of suspension per time by micro-pipet). The reference electrode was a RE-1BP (Ag/AgCl) electrode, while the counter electrode was a platinum wire. The SVC-3 voltammetry cell and the electrodes were purchased from ALS Co., Ltd. (Tokyo, Japan).

2.2.6. Computational Methods

The density functional theory (DFT) was employed in this study. The adsorption behavior of solvents on s-heptazine sheet, geometry optimization and structural relaxation, HOMO-LUMO, density of state, van-der-Waals (vdW) interactions of the adsorbed molecule with s-heptazine, and the charge density of the samples were performed using Quantum-Espresso and VESTA software.

To check the adsorption behavior of methanol, isopropanol, tetrahydrofuran, and dimethylformamide on s-heptazine sheet, a plane-wave basis sets-based density functional approach was employed using Quantum-Espresso[76] with the Perdew-Burke-Ernzerh (PBE) of generalized gradient approximation (GGA).[77] For geometry optimization and structural relaxation, ultrasoft pseudopotentials were employed, while the information of the HOMO-LUMO was extracted using the projector augmented wave pseudopotentials available on the Quantum-Espresso website.[76] K-mesh used for the Brillouin zone integration was 2×2×1. The kinetic-energy cutoffs for the charge density and the wave function were kept fixed at 45 Ry and 450 Ry, respectively for all calculations. The convergence criterion was set at 10^{-8} Ry, while the rest of the other parameters were kept at default settings. To avoid the periodic interaction between periodic images along z-direction, 15 Å vacuum was applied. To speed up the self-consistent calculations, a marzari-vanderbilt[78] type smearing (width: 0.01 Ry) was used. The van-der-Waals (vdW) interactions of the adsorbed molecule with s-heptazine were treated with Grimme-D3 type vdW-corrections[79]. VESTA software was used to visualize the charge density plots.[80] The adsorption energy was calculated as,[81]

$$\Delta E = E_{\text{mol+sheet}} - E_{\text{sheet}} - E_{\text{mol}} \qquad \text{(Equation 2-1)}$$

where $E_{\text{mol+sheet}}$, E_{sheet}, and E_{mol} are the energy of s-heptazine sheet with adsorbate, the energy of s-heptazine sheet without adsorbate, and the energy of the adsorbate.

2.3. Results and Discussion

2.3.1. Synthetic Strategy to Design Holey-defects on g-C_3N_4 Nanosheets

The detailed synthetic procedure of resultants g-C_3N_4 by solvothermal treatment in various organic solvents is illustrated in Scheme 1. MA, IPA, THF, and DMF solvents with dispersive parameters of 15.1, 15.8, 16.8, and 17.4 $MPa^{½}$, respectively, were chosen in comparison with g-C_3N_4 dispersive Hansen parameters of 17.8 $MPa^{½}$ (Table 2). As shown in Scheme 1, during the solvothermal process, solvent molecules may act as a wedge in the interlayer spacing of g-C_3N_4 inducing exfoliation. At the same time, the unbalanced compressive forces on two adjacent layers would cause shear-induced peeling. Furthermore, under the harsh condition of the solvothermal treatment, the selected solvents could attack the g-C_3N_4 structure to form holey-defects on the planar nanosheets. As a result, while highly polar solvent (MA) fragmented the skeleton of g-C_3N_4 layers, aprotic solvent DMF had no etching effect on the layers and maintained the lateral size. The moderately polar IPA created the structure of a centered sheet with holey-defects at the edges of g-C_3N_4. Interestingly, THF produced uniform holey-defects on the planar sheets without fracturing the skeleton of the g-C_3N_4 layers.

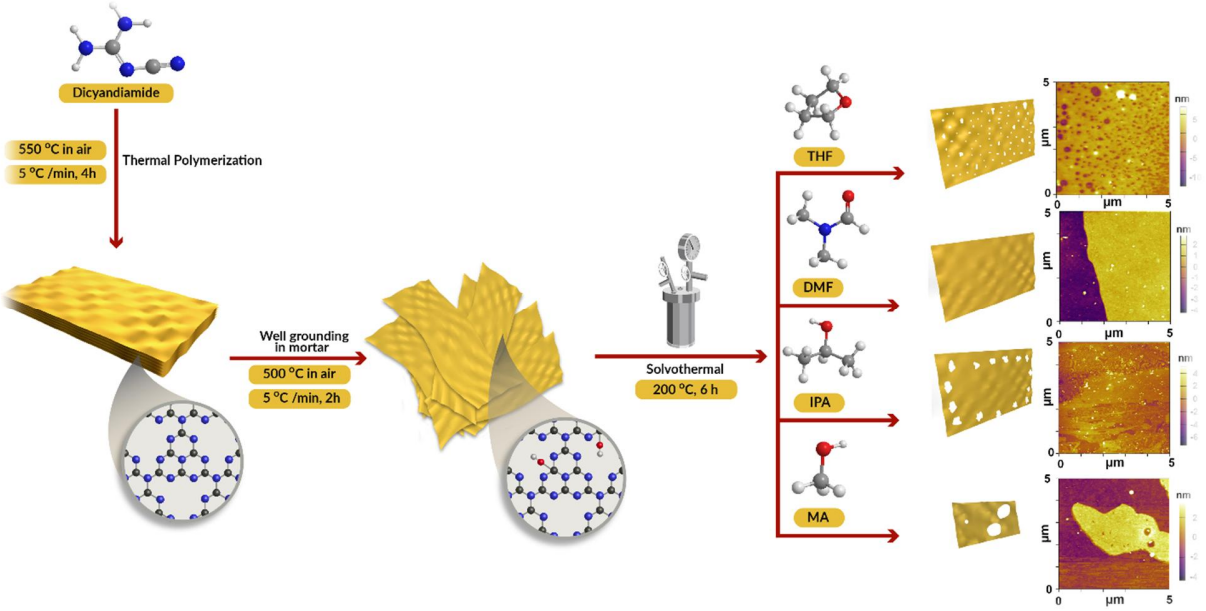

Scheme 1. Schematic of solvothermal modified g-C_3N_4 preparation.

Table 2. Dispersive, Polar, Hydrogen Bonding Hansen Parameters, and Relative polarity for the solvents used in this work.

Solvent	δ_D[(a)] $MPa^{1/2}$	δ_P $MPa^{1/2}$	δ_H $MPa^{1/2}$	$\delta_P + \delta_H$ $MPa^{1/2}$	δ_T $MPa^{1/2}$	Relative polarity to water[(b)]
Water	15.5	16.0	42.3	58.3	47.8	1.000
Methyl alcohol	15.1	12.3	22.3	34.6	36.2	0.762
Ethanol	15.8	8.8	19.4	28.2	26.5	0.654
IPA**[82]**	15.8	6.1	16.4	23.6	23.6	0.546
DMF	17.4	13.7	11.3	25.0	24.9	0.386
THF	16.8	5.7	8.0	13.7	19.5	0.207
g-C_3N_4**[56]**	17.8	10.8	15.4	26.2		
Graphene**[55]**	18 (15-21)	9.3 (3-17)	7.7 (2-18)	17.0		

(a) The dipole moment is typically a mathematically-calculated value based on the geometry, bond lengths, and charges of a molecule.

(b) Relative polarity is calculated based on the shift in the absorption spectrum of the solvent, relative to water.

2.3.2. Crystal Structure and Chemical Composition of Solvothermal Modified g-C_3N_4

The crystallographic nature and purity of the obtained samples were analyzed by XRD (Figure 1a). XRD patterns of all samples displayed two clear peaks at 13.1° and 27.7°, which were assigned to the (100) and (002) crystal planes of g-C_3N_4 (JCPDS 87-1526), corresponding to in-plane structural packing repeated heptazine motifs and interlayer stacking of conjugated aromatic systems, respectively.[83, 84] Thus, the general structure of g-C_3N_4 had been maintained after solvothermal treatment. An additional broad feature around 57.5° refined crystallized in the hexagonal space group with AB stacking of the triazine-based g-C_3N_4 layers.[85] The decreased intensity of the two main peaks of carbon nitride from the bulk to the solvothermal treated samples demonstrated successful exfoliation of the stacked layers in the graphitic structure after solvothermal treatment.

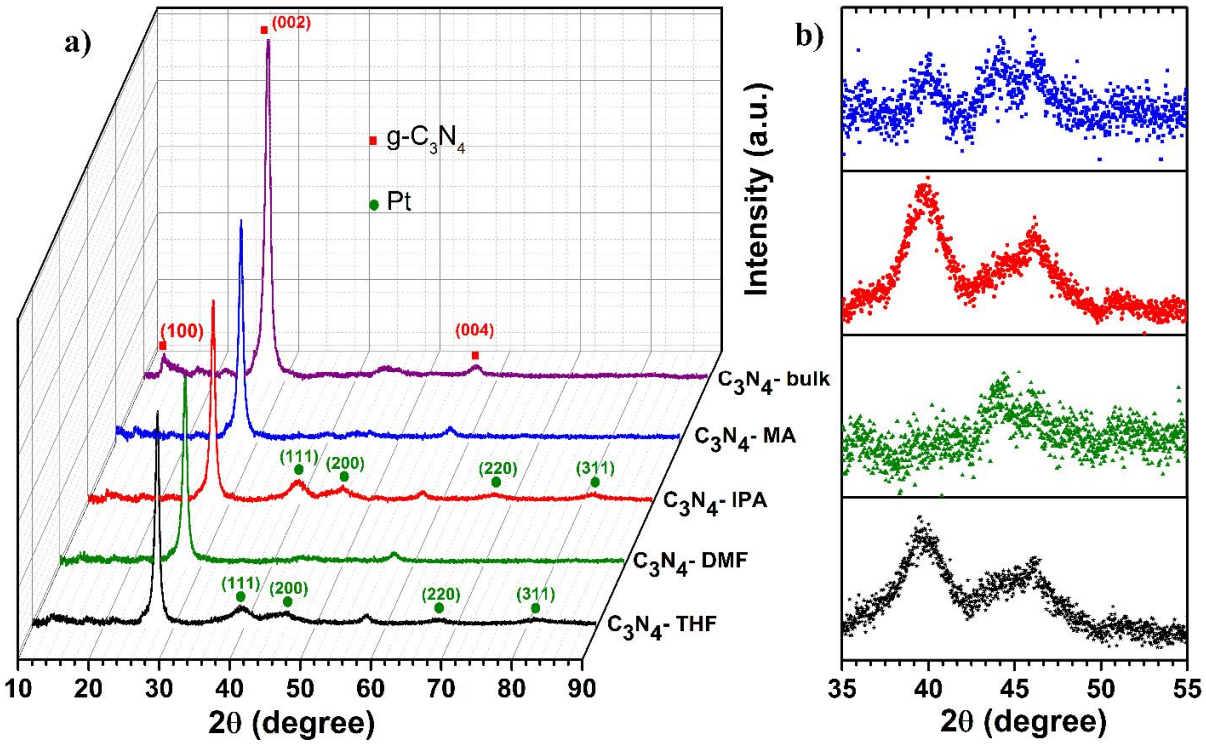

Figure 14. (a) XRD spectra of C_3N_4-bulk, C_3N_4-MA, C_3N_4-IPA, C_3N_4-DMF, and C_3N_4-THF. (b) inset XRD spectra of C_3N_4-MA, C_3N_4-IPA, C_3N_4-DMF, and C_3N_4-THF.

Furthermore, the peaks at ca. 39.8, 46.3, 67.5, and 81.4 belong to the face-centered cubic (fcc) structure of the Pt metal crystalline lattice, which was ascribed to the (111), (200), (220), and (311) crystalline planes, respectively. As shown in the inset figure (Figure 1b), C_3N_4-THF and C_3N_4-IPA displayed two clear crystalline planes (111) and (200) of the metal Pt lattice, while the C_3N_4-

MA sample showed weaker signals for those planes, and no obvious peaks were observed for the C_3N_4-DMF sample. The intensity of the Pt peaks may be related to different Pt oxidation states, which is further discussed in the XPS data.

To further investigate the structure of the resultant samples, Fourier transform infrared spectroscopy (FT-IR) was used to characterize the g-C_3N_4 chemical structures (Figure 15). All the samples had similar FT-IR spectra with three essential band ranges. The typical peaks at 810 cm^{-1} and 900-1700 cm^{-1} were assigned to the vibration mode of tris-s-triazine units and the characteristic stretching mode of C-N heterocycles as well as C-C aromatic rings, respectively.[86] Broadened bands at 3000-3500 cm^{-1} were attributed to N-H and the stretching mode of epoxide and hydroxyl groups.[87] In comparison with C_3N_4-bulk, solvothermal treated g-C_3N_4 samples showed stronger and more stretching peaks between 3000 cm^{-1} and 3500 cm^{-1}, which can be attributed to fewer N-H groups after solvothermal treatment.[88-90]

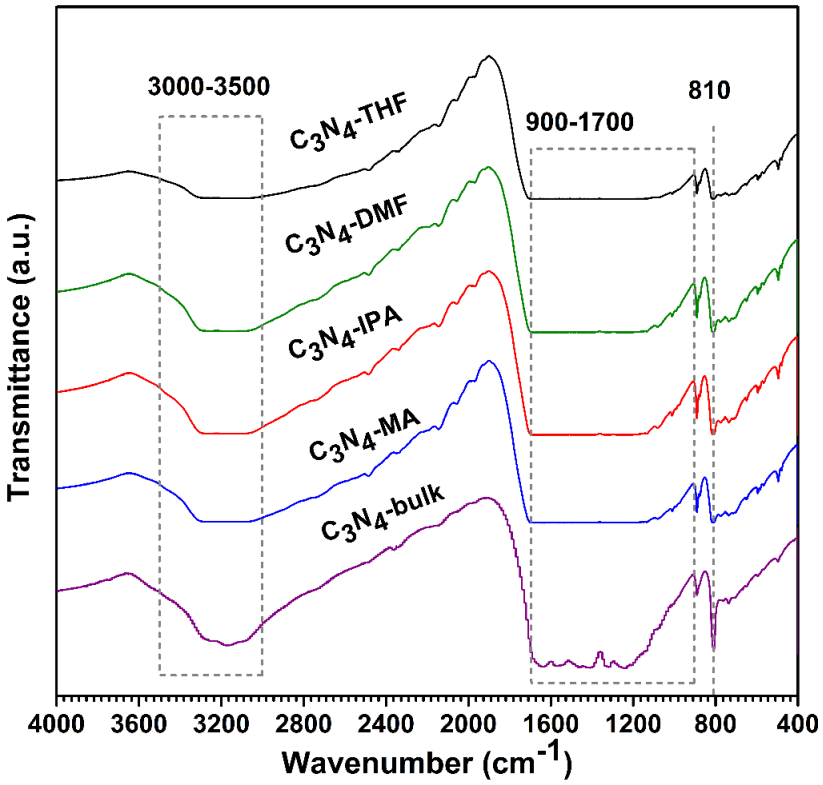

Figure 15. FT-IR survey spectra C_3N_4-bulk, C_3N_4-MA, C_3N_4-IPA, C_3N_4-DMF, and C_3N_4-THF.

The detailed elemental composition of the resultant samples was determined by elemental analysis (Table 3). All of the samples possessed a higher percent by mass of oxygen and hydrogen

elements than the starting C_3N_4-bulk material, which obviously suggests that more oxygen groups were formed into the g-C_3N_4 layers. The percentages of carbon and nitrogen in C_3N_4-bulk samples simultaneously decreased after reactions, along with equivalent C/N atomic ratios (around 0.65) of all samples. It is widely accepted that the C/O and O/N atomic ratios represent the relative oxidation level of graphitic structure materials.[57, 82] The as-prepared C_3N_4-bulk sample has a C/O atomic ratio of 10.22. Compared to C_3N_4-bulk, the C/O atomic ratio of C_3N_4-IPA, C_3N_4-DMF, C_3N_4-THF, and C_3N_4-MA decreased to 7.46, 7.11, 6.97, and 5.66, respectively, due to the oxidation of g-C_3N_4 with the introduction of more oxygen-containing functional groups. In contrast, the O/N atomic ratio of modified g-C_3N_4 samples increased consistent with the trend of the C/O ratio. The polar aprotic solvents (DMF, THF) and moderately polar protic solvent (IPA) showed mild oxygen functionalization, while the highly polar protic solvent (CH_3OH) possessed strong etching and higher functionalizing oxygen content on the g-C_3N_4 surface structures.[91]

Table 3. Element compositions and calculated C/N, O/N atomic ratios of the samples analyzed by elemental analysis (C, H, N, O, S analyzer).

Elemental analysis							
Sample	C (wt. %)	N (wt. %)	O (wt. %)	H (wt. %)	C/N	O/N	C/O
C_3N_4-bulk	35.31	54.93	3.45	1.65	0.64	0.063	10.22
C_3N_4-MA	33.69	50.84	5.95	2.01	0.66	0.12	5.66
C_3N_4-IPA	33.98	51.84	4.55	1.86	0.66	0.09	7.46
C_3N_4-DMF	33.55	50.84	4.72	1.86	0.66	0.09	7.11
C_3N_4-THF	33.85	51.45	4.85	1.89	0.66	0.09	6.97

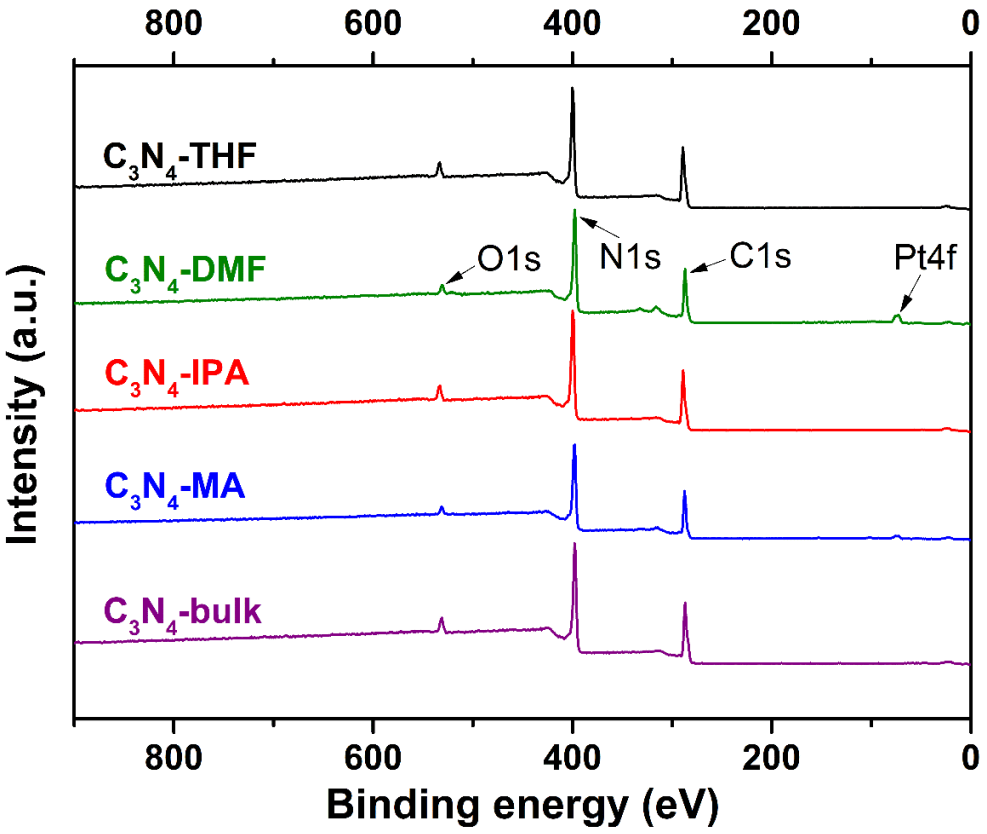

Figure 16. XPS survey spectra C_3N_4-bulk, C_3N_4-MA, C_3N_4-IPA, C_3N_4-DMF, and C_3N_4-THF.

The surface chemical states of as-prepared samples were investigated by XPS analysis. XPS survey spectra of C_3N_4-bulk and resultant samples (Figure 16) confirmed the existence of carbon, nitrogen, oxygen, and platinum. The C1s and N1s core level spectra deconvoluted into Gaussian shapes are shown in Figure 17. In the C1s XPS spectra (Figures 17a), the main carbon peaks at ca. 284.6.0 eV, and 288.0 eV, were attributed to graphitic structure (C=C or C-C) bonds and sp^2-hybridized carbon atoms bonded with three N (N_2-C=N-), respectively.[17, 18, 92] Core level spectra of N1s were used to reveal the distribution of nitrogen-containing groups in the samples. The lowest energy contribution (ca. 398.2 eV) of the N1s spectrum is attributed to nitrogen bonded with two carbon atoms in a graphitic sp^2 network (Figures 17b), whereas the peak at ca. 399.9 eV corresponds to the overlap of signals from bridging nitrogen atoms such as tertiary N (-N<), and amino groups ($-NH_x$), revealing the presence of tris-triazine rings in the g-C_3N_4 framework. In addition, a weak signal positioned around 293 eV in C1s and 403.8 eV in N1s spectra can be assigned to the π electrons delocalization in g-C_3N_4 heterocycles.

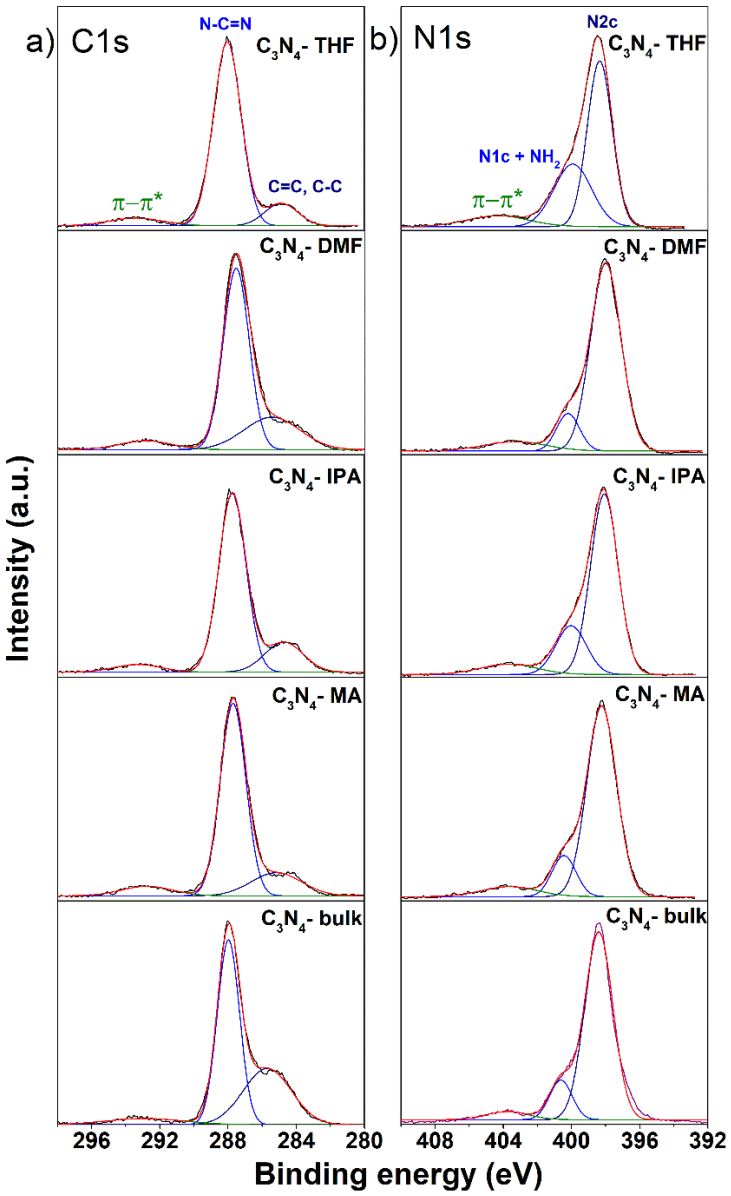

Figure 17. XPS spectra of C_3N_4-bulk, C_3N_4-MA, C_3N_4-IPA, C_3N_4-DMF, and C_3N_4-THF. (a) C1s spectra, (b) N1s spectra.

In Table 4, detailed parameters calculated from the N1s and C1s XPS peaks are described, in which we can obtain some structural information. The first column shows the ratio of N_{sp}^2 (nitrogen atoms in heptazine units) to the sum of $N_{primary}$ ($-NH_x$) and $N_{tertiary}$ (-N<) atoms at the surface of different samples. Comparing this ratio for all samples showed that C_3N_4-DMF has the highest portion of N_{sp}^2 compared to the other materials, while C_3N_4-THF showed the lowest value. The value of this parameter demonstrates maintenance of the g-C_3N_4 layer using DMF solvent,

which was confirmed in AFM images. On the other hand, this parameter indicates the loss of some heptazine units in the g-C_3N_4 structure by breakage of $N_{tertiary}$ in the cases of using MA, IPA, and THF solvents. The N_{sp^2}/C_{sp^2} parameter demonstrated the same pattern as $N_{sp^2}/N_{(p+t)}$ (Column 2, Table 4). This ratio depicted the reduction of N_{sp^2} compared with C_{sp^2} in heptazine units that can be a sign of nitrogen-vacancy in the g-C_3N_4 framework. This result indicates that the solvents can interact with the g-C_3N_4 layer via different positions, $N_{tertiary}$ (-N<) or N_{sp^2} bonds in the heptazine rings. As a result, two different kinds of defects can be introduced to the structure: heptazine unit vacancy and nitrogen deficiency. These two parameters showed production of a holey structure using IPA and THF. The difference between C_3N_4-IPA and C_3N_4-THF is the formation of more uniform holes in the sheets of C_3N_4-THF, and holes appearing at the edge of C_3N_4-IPA with a planar structure at the centered layers. The highest values in the C_3N_4-DMF and C_3N_4-MA samples signify no holey structures for those samples. The difference between C_3N_4-MA and C_3N_4-DMF is related to the formation of small sheets using MA, resulting in more $-NH_2$ groups in C_3N_4-MA. This result may be due to the strong etching effect of MA solvent on the g-C_3N_4 structure that fractures the skeleton of the graphitic structure into smaller fragments as discussed below in the morphology part (Section 2.3.3).

Table 4. Calculation of delocalized π-π electrons system on C1s and N1s XPS data.

	$N_{sp^2}/N_{(p+t)}$	N_{sp^2}/C_{sp^2}	$\frac{\pi\text{-}\pi^*}{C_{total}}(\%)$	$\frac{\pi\text{-}\pi^*}{N_{total}}(\%)$	O_2/O_{total}	$O3/O_{total}$
C_3N_4-bulk	5.95	2.30	7.0	5.6	0.36	0.59
C_3N_4-DMF	6.64	2.28	10.0	9.1	0.61	0.13
C_3N_4-MA	5.74	2.14	10.0	8.4	0.51	0.16
C_3N_4-IPA	3.36	1.83	7.3	9.1	0.77	0.03
C_3N_4-THF	1.74	1.47	8.0	10.4	0.61	0.34

Which N_{sp^2} is nitrogen, which bonded with two carbon atoms in a graphitic sp^2 network

$N_{(p+t)}$ is sum of primary N (-NH_x), and tertiary N (-N<)

N_{sp^2}/C_{sp^2}: ratio of N and C atoms in the heptazine units

Furthermore, there are two parameters of $\frac{\pi\text{-}\pi^*}{C_{total}}$ and $\frac{\pi\text{-}\pi^*}{N_{total}}$ calculated from C1s and N1s XPS spectra (Table 4), which are related to the redistribution of π-π* electrons on carbon and nitrogen atoms in the graphitic structure. The decrease of $\frac{\pi\text{-}\pi^*}{C_{total}}$ ratio in C_3N_4-IPA and C_3N_4-THF in comparison with C_3N_4-DMF and C_3N_4-MA demonstrates the loss of carbon atoms via introduction of holey-defects in the graphitic layer structure. The higher value of $\frac{\pi\text{-}\pi^*}{C_{total}}$ for C_3N_4-THF compared to C_3N_4-IPA depicted better minus charge localization on carbon atoms after holey-defects formation. In other words, IPA molecules damage the p-conjugated structure more than THF, which resulted in the lowest catalytic performance for the H_2 evolution reaction. Moreover, the highest value of $\frac{\pi\text{-}\pi^*}{N_{total}}$ for C_3N_4-THF also confirmed the presence of holey-defects through the loss of nitrogen atoms.

High-resolution O1s XPS spectra were used to confirm the existence of oxygen doping and oxygen group functionalization mirroring FT-IR and EA results. The deconvolution of O1s XPS exhibited three additional peaks located at 530.0 eV, 531.7 eV, and 532.3 eV in the C_3N_4-bulk. In addition, solvothermal treated g-C_3N_4 samples showed three bands at ca. 530.0 eV, ca. 531.7 eV, and ca. 532.8 eV (Figure 18), which were assigned to the C=O (O1), N-C-O (O_2), and O-H (O3) groups on the surface of g-C_3N_4.[17, 37, 92] The unavoidable oxygen functionalization resulted in peaks O1 and O3 during the thermal polymerization synthesis in air atmosphere.[92] In the solvothermal treated g-C_3N_4 samples, the ratio of O_2/O_{Total} increased compared to the bulk, which indicates oxygen doping to the g-C_3N_4 structure via solvothermal reactions, while the proportion of $O3/O_{Total}$ exhibited a clear reduction from the bulk to solvothermal treated g-C_3N_4 samples (Table 4). These results are consistent with FT-IR data in which the intensity of the O-H stretching band (3000-3500 cm^{-1}) decreased after solvothermal treatment. Indeed, from the EA results (Table 3), the oxygen content in solvothermal treated samples increased gradually from C_3N_4-bulk (3.5 wt. %) to C_3N_4-IPA (4.6 wt. %), C_3N_4-DMF (4.7 wt. %), C_3N_4-THF (4.9 wt. %), and C_3N_4-MA (6.0 wt. %). The O1s XPS spectra, FT-IR, and EA results together indicate that the O-H groups had been reduced, and oxygen doping had been introduced into the g-C_3N_4 structure during the solvothermal process.

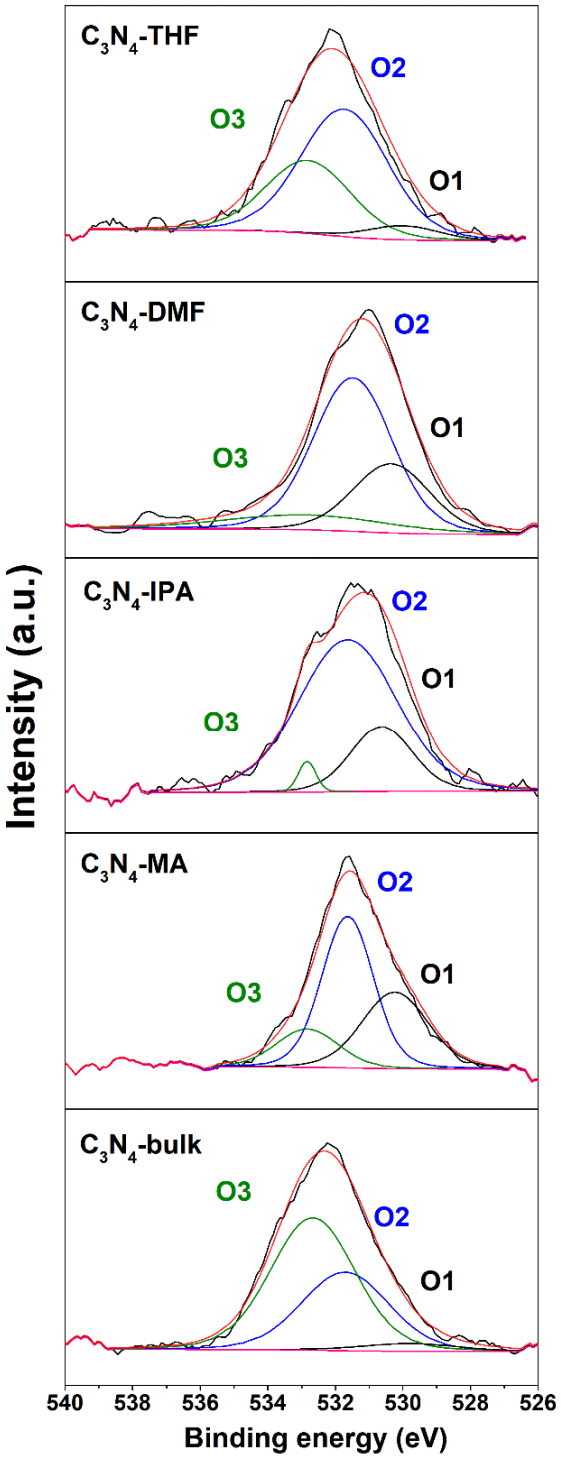

Figure 18. Deconvolution of O1s XPS spectra of C_3N_4-bulk, C_3N_4-MA, C_3N_4-IPA, C_3N_4-DMF, and C_3N_4-THF.

The designed amount of 3 wt.% platinum nanoparticles was successfully loaded onto the catalyst surface by hydrogen reduction of H_2PtCl_6 in aqueous solution, which was studied in our previous work.[57] The deconvolution of high-resolution Pt4f XPS spectra (Figure 19) revealed the oxidation states of Pt nanoparticles, including Pt^0 and Pt^{2+} in PtO. Zero-valent state Pt(111) peaks located at ca. 71.4 eV and 74.9 eV are ascribed to the binding energies of $Pt4f_{7/2}$ and $Pt4f_{5/2}$, respectively. Likewise, the Pt^{2+} state showed two bands at ca. 72.4 eV and 75.8 eV.[93, 94] Interestingly, C_3N_4-IPA contained only the Pt^0 oxidation state, C_3N_4-MA and C_3N_4-DMF achieved only the Pt^{2+} state, and C_3N_4-THF included both Pt^0 and Pt^{2+} states. As shown in Table 4, the $O3/O_{total}$ values of C_3N_4-IPA, C_3N_4-DMF, C_3N_4-MA, and C_3N_4-THF are 0.03, 0.13, 0.16, and 0.34, respectively. These results indicate that the presence of O-H groups on g-C_3N_4 may be responsible for converting Pt^0 to Pt^{2+} in C_3N_4-MA, C_3N_4-DMF, and C_3N_4-THF. While a very small value of O-H groups in C_3N_4-IPA resulted in the formation of only the Pt^0 state. It is notable that C_3N_4-THF had the highest number of O-H groups (highest $O3/O_{total}$) but contained a lower amount of Pt^{2+} in comparison with C_3N_4-MA and C_3N_4-DMF. This result suggests that only O-H groups in planar sites can promote the conversion of Pt^0 to Pt^{2+}. Since C_3N_4-THF has a uniform holey structure, most of its O-H groups are located at edge sites and there are fewer available O-H groups at planar sites compared to C_3N_4-MA and C_3N_4-DMF. PtO and metallic Pt nanoparticles can both act as co-catalyst sites for H_2 evolution on the host photocatalyst surface. The role of Pt oxidation states in the H_2 production reaction and the mechanism for Pt^{2+} formation from O-groups on g-C_3N_4 is still being studied. The actual amount of Pt loaded on the catalyst was determined by ICP-OES analysis. The amounts of 1.86 wt. %, 2.29 wt. %, 2.35 wt. %, and 2.28 wt. % Pt nanoparticles were loaded on C_3N_4-MA, C_3N_4-IPA, C_3N_4-DMF, and C_3N_4-THF, respectively (Table 5).

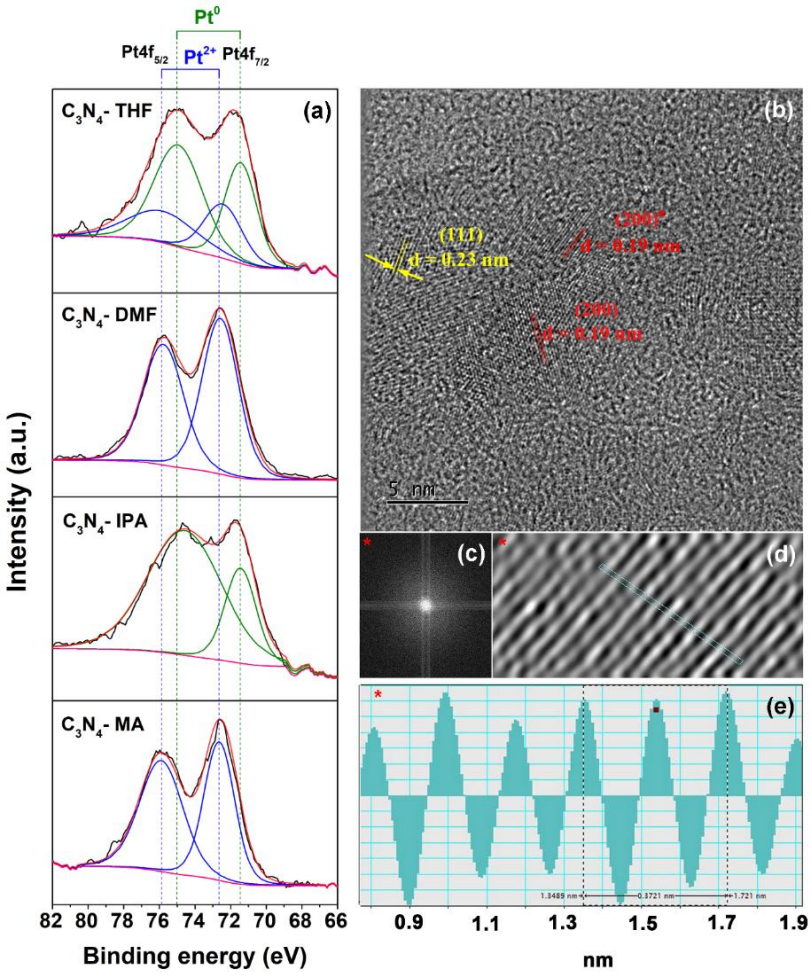

Figure 19. (a) Deconvolution of the XPS Pt4f spectra of C_3N_4-MA, C_3N_4-IPA, C_3N_4-DMF, and C_3N_4-THF. (b) HR-TEM image of C_3N_4-THF and corresponding (c) Fourier-transform (FFT) image, (d) High-resolution inverse FFT image (IFFT), and (e) lattice fringe pattern image, which shows a d-spacing of 0.19 nm (the (200) planes of Pt).

A lower amount of Pt decorated on the catalyst surface of C_3N_4-MA could be explained by the small lateral sizes of C_3N_4-MA that reduced the decorating yield of Pt during hydrogen reduction in water. The Pt particle sizes and distribution are shown in Figure 19b. These Pt nanoparticle grain sizes were typically 2.2 nm, and the size of these particles was mostly in the range of 1 nm to 3 nm (Figure 20, Figure 21). The g-C_3N_4 sheets acted as a capping agent, and the interaction of Pt cation with the functional groups of g-C_3N_4 may prevent agglomeration of Pt clusters during hydrogen reduction in aqueous solution. This new method of loading Pt content onto g-C_3N_4

catalyst achieved small sizes and good distribution of Pt nanoparticles on the surface of g-C_3N_4 sheets in comparison with photodecomposition and chemical reduction methods.[57, 95, 96]

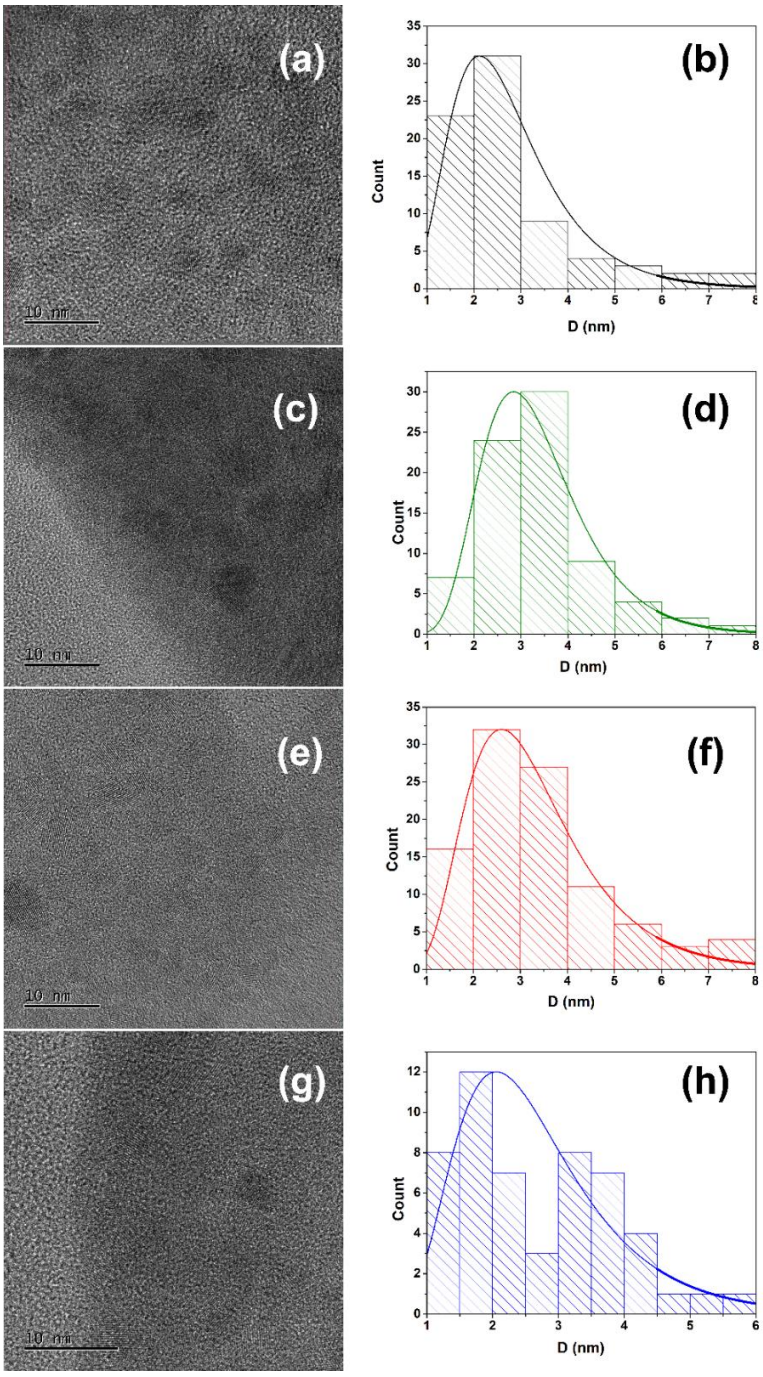

Figure 20. HR-TEM images of (a) C_3N_4-THF, (c) C_3N_4-DMF, (e) C_3N_4-IPA, (g) C_3N_4-MA, corresponding to the Pt particles size distribution in (b) C_3N_4-THF, (d) C_3N_4-DMF, (f) C_3N_4-IPA, (h) C_3N_4-MA, respectively.

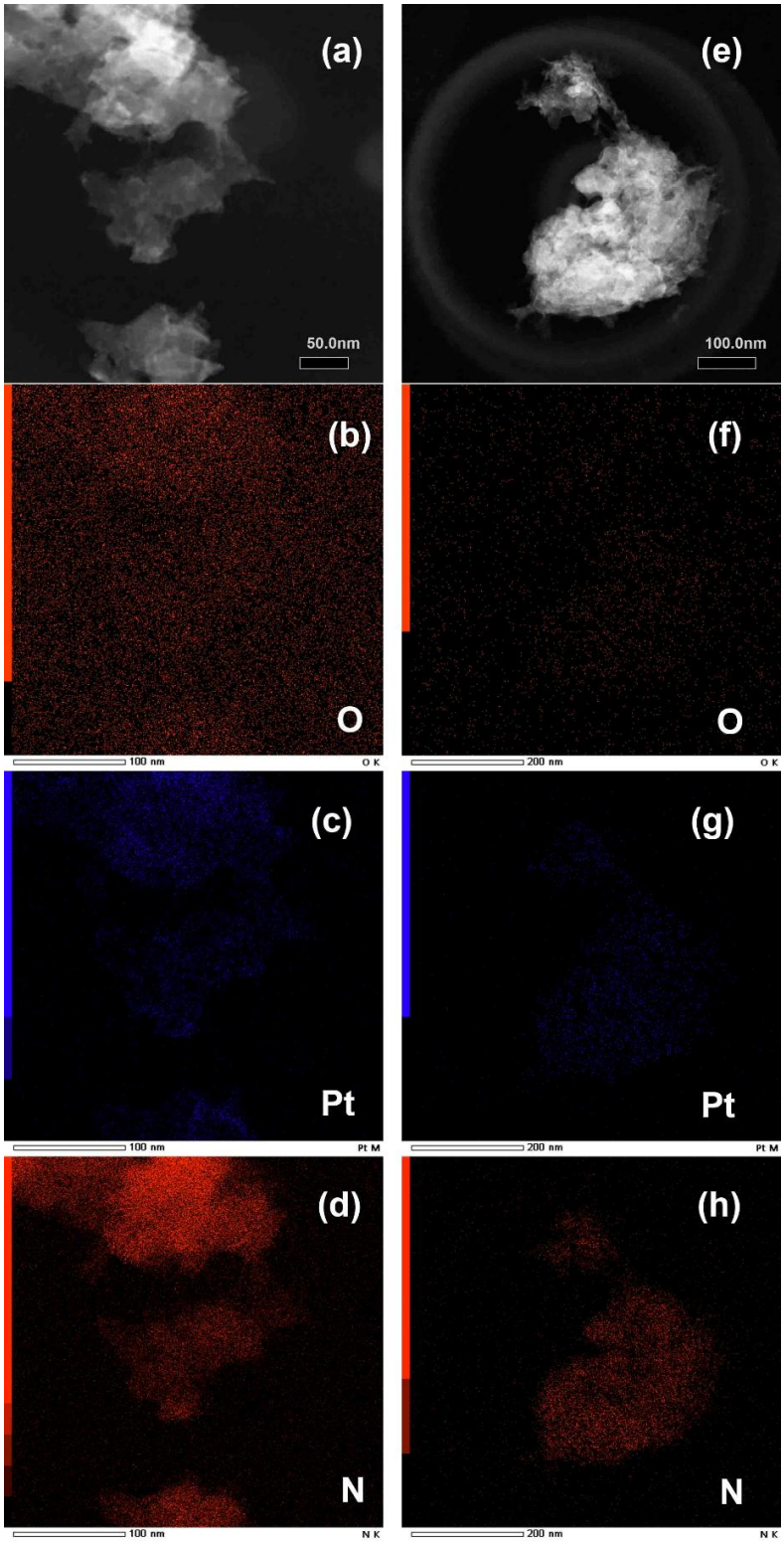

Figure 21. HR-TEM images of (a) C_3N_4-IPA, (b) C_3N_4-MA corresponding to their STEMS images.

Table 5. ICP-OES data analysis.

Sample	Designed Pt wt. %	ICP Pt wt. %	Solvent type
C_3N_4-MA	3	1.8641	Highly polar protic solvent
C_3N_4-IPA	3	2.2925	Moderately polar protic solvent
C_3N_4-DMF	3	2.3527	Moderately polar aprotic solvent
C_3N_4-THF	3	2.2858	Moderately polar aprotic solvent

2.3.3. The Morphology of Solvothermal Modified g-C_3N_4

The morphology transformation of g-C_3N_4 by solvothermal treatment in the aforementioned organic solvents was determined by AFM, FE-SEM, HR-TEM, and CS-STEM. AFM images of the monolayer of g-C_3N_4 samples showed the morphology had been reformed (Figure 22), and the layer structure had been modified to form holey g-C_3N_4 structures (C_3N_4-IPA, C_3N_4-THF) or sheet structures (C_3N_4-MA, C_3N_4-DMF). In particular, the C_3N_4-DMF sample indicated DMF as the most appropriate solvent for exfoliation of C_3N_4-bulk, which formed a monolayer after the reaction and maintained the lateral size of the g-C_3N_4 sheet (Figure 22d, Figure 24d). The extent of exfoliation during the solvothermal process could be explained by the Hansen parameters of g-C_3N_4 and organic solvents, representing dispersive, polar, and hydrogen bonding of the materials (Table 2). O'Neill et al. suggested that the dispersive Hansen parameter, δ_D, is the most sensitive factor for graphitic material dispersion ability in solvents, which is ascribed to the required energy to disperse material in a solvent.[55] The order of δ_D in Table 2 could be arranged as δ_D(MA) < δ_D(IPA) < δ_D(THF) < δ_D(DMF) < δ_D(g-C_3N_4), in which solvent nearer to g-C_3N_4 shows better peeling of g-C_3N_4 bulk into monolayer. The dispersibility of g-C_3N_4 in organic solvents is related to the physisorption of solvent adsorbates on the g-C_3N_4 sheet. The adsorption behavior of MA, IPA, THF, and DMF on a s-heptazine sheet was further confirmed by density functional theory (DFT) calculations using Quantum-Espresso with the Perdew-Burke-Ernzerhof (PBE) of generalized gradient approximation (GGA). We noticed that the adsorption strength of DMF was found to be higher than that of the other adsorbates (Table 6), which is consistent with the Hansen parameters, resulting in excellent g-C_3N_4 exfoliation by DMF. Of note, IPA has a higher physisorption energy on s-heptazine sheet (ΔE=-0.53 eV) than THF solvent (ΔE=-0.44 eV), which is opposite the dispersive Hansen parameter properties. This result may contribute to the Hansen

parameters for choosing the appropriate solvent for g-C_3N_4 exfoliation in Table 2. As a result, the organic solvent to use for g-C_3N_4 exfoliation in order of increasing efficiency could be reorganized as MA < THF < IPA < DMF.

Table 6: Adsorption Energy (ΔE) of the Adsorbates on s-Heptazine Sheet.

Adsorbate	ΔE (eV)
Methanol (MA)	-0.42
Isopropanol (IPA)	-0.53
Tetrahydrofuran (THF)	-0.44
Dimethylformamide (DMF)	-0.58

Figure 24b presents a single layer of the C_3N_4-MA sample, similar to C_3N_4-DMF but in smaller lateral layer size, which results from the strong etching effect of MA solvent on the g-C_3N_4 structure, fragmenting the skeleton of the graphitic structure into smaller layers. Likewise, the etching phenomenon was also found for C_3N_4-IPA, and C_3N_4-THF at different ways. While C_3N_4-IPA interestingly formed a grid structure at the edge and maintained a sheet structure in the center of the layer (Figure 22c, Figure 24c), C_3N_4-THF retained a large lateral size and was uniformly etched by THF solvent to achieve a holey g-C_3N_4 structure with a similar layer size to the initial precursor (Figure 22e). This result indicated that the etching effectiveness in order of MA>THF>IPA, while the polarity strength of solvents is in the order of MA>IPA>THF (Table 2, Table 7). The etching level of IPA is still stronger than THF, as evidenced by damage to

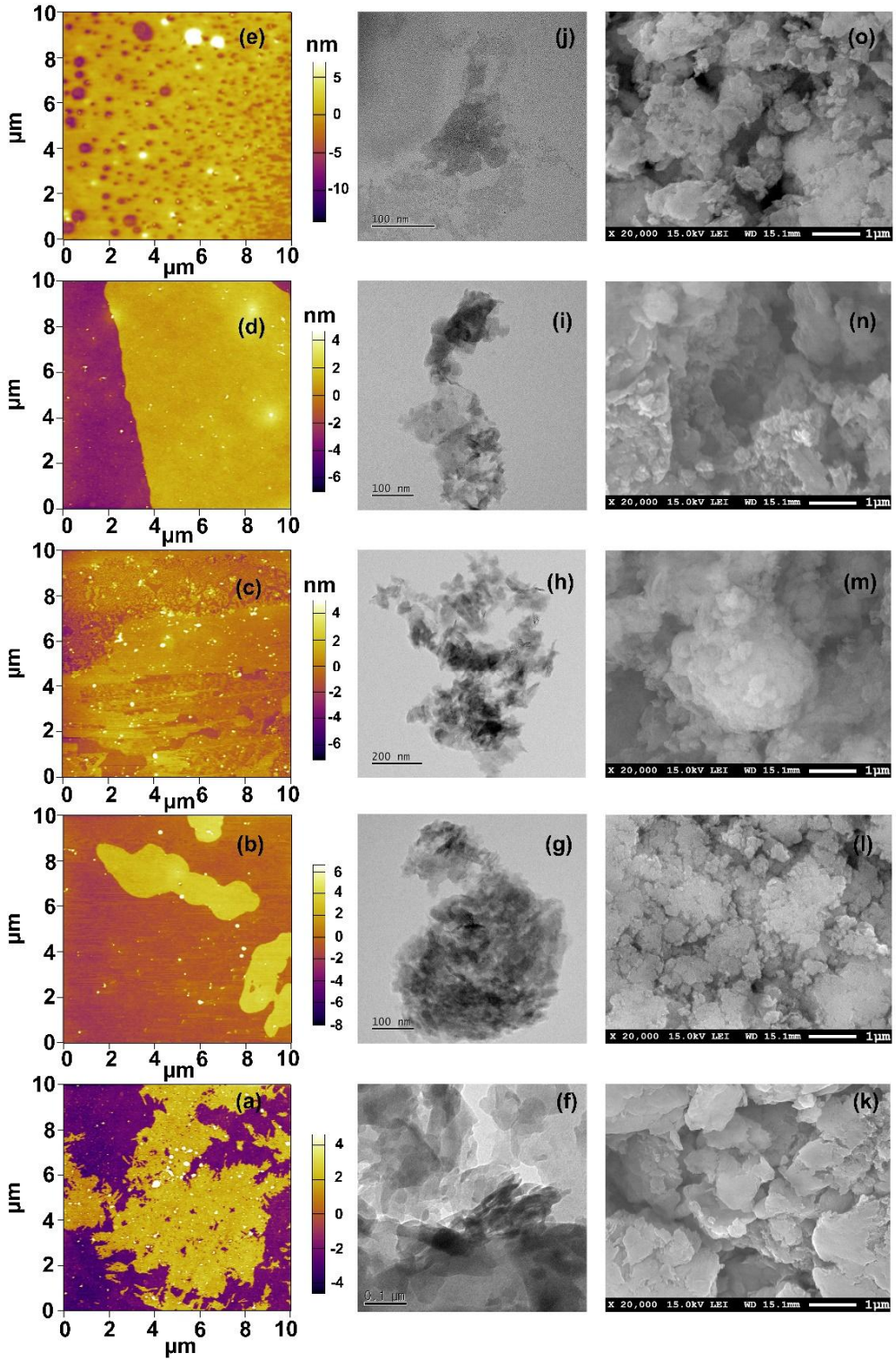

Figure 22. AFM, HR-TEM, and FE-SEM images of (a, f & k) C_3N_4-bulk, (b, g & l) C_3N_4-MA, (c, h & m) C_3N_4-IPA, (d, i & n) C_3N_4-DMF, and (e, j & o) C_3N_4-THF.

Table 7: Total Solvation Energy of the adsorbates.

Solvents	Total Solvation Energy[97] (kJ mol^{-1})
Methanol (MA)	-4.94
Isopropanol (IPA)	0.71
Tetrahydrofuran (THF)	2.43
Dimethylformamide (DMF)	-12.13

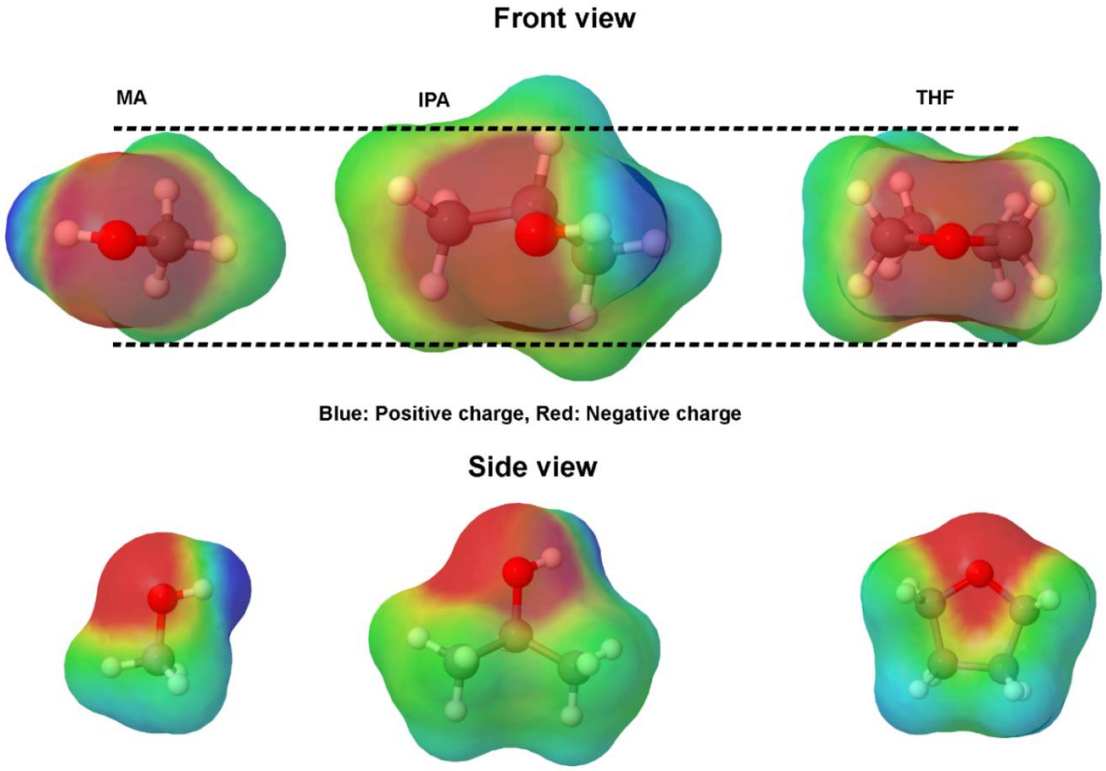

Figure 23. The visualization polarity of MA, IPA, and THF molecules, which supports the evidence of steric effects of IPA compared to MA and THF.

C_3N_4-IPA's structure at the edge of the sheet (Figure 24h). The steric effects of IPA on 2D g-C_3N_4 material and the highly different of δ_D(IPA) to δ_D(g-C_3N_4) are the most likely explanation for this result, in which the IPA molecule could not access the center of g-C_3N_4 stacked layers and perform the etching reaction (Table 2, Figure 23).[97, 98]

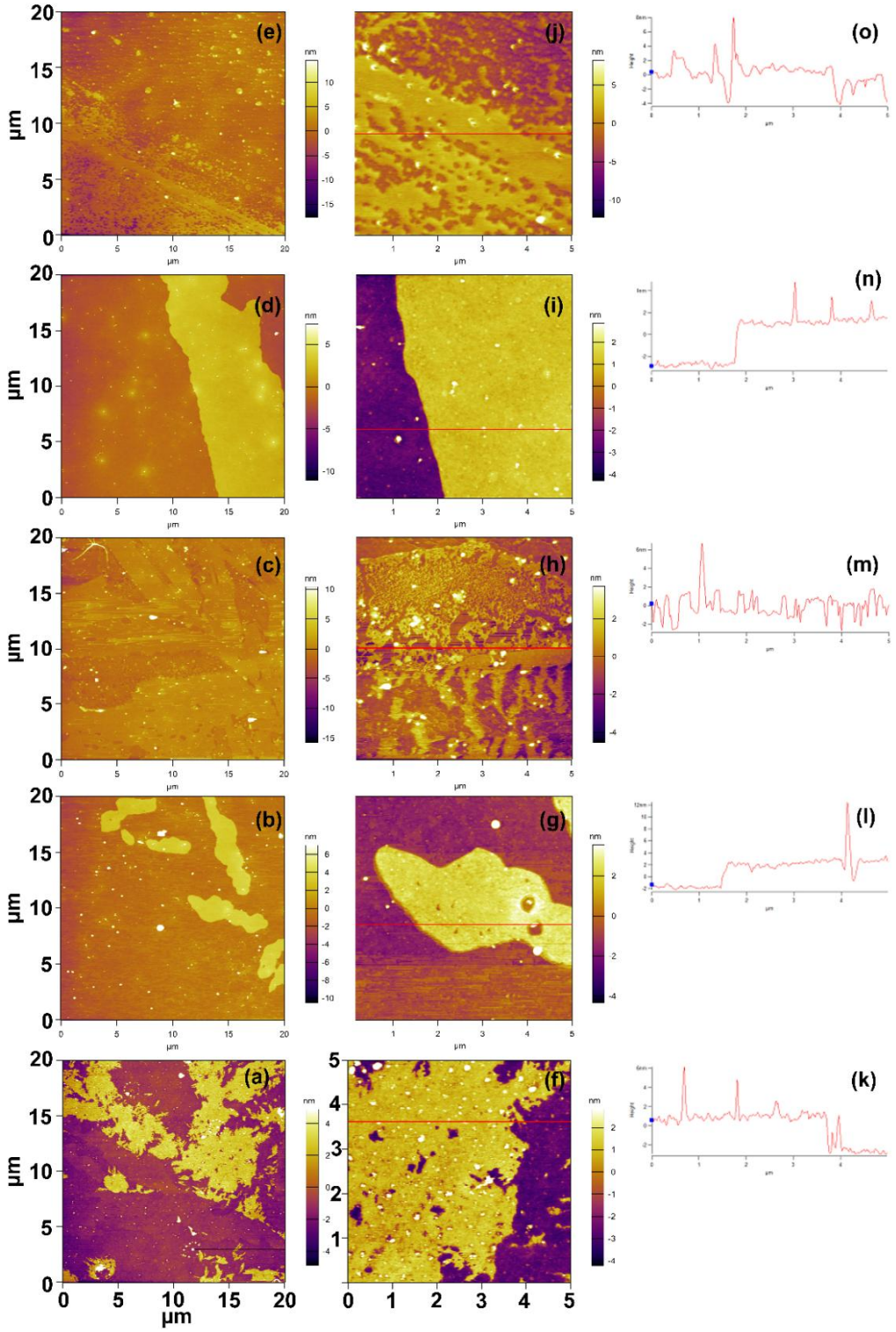

Figure 24. AFM topography images of (a, f, k) C_3N_4-bulk, (b, g, l) C_3N_4-MA, (c, h, m) C_3N_4-IPA, (d, i, n) C_3N_4-DMF, and (e, j, o) C_3N_4-THF at different scales, corresponding with their height profiles.

AFM images of the resultant samples and their height profiles are displayed in Figure 24, which was used to determine the thickness of the monolayer g-C_3N_4 samples, typically around 3.8 nm (including Pt nanoparticles). We also examined the AFM images of THF-modified g-C_3N_4 to investigate the thickness of such a monolayer and the holes distribution of the layer without Pt nanoparticles loaded, which are shown in Figure 25, and Figure 26, Figure 27, Figure 28, Figure 29. Through a random position measurement and different as-prepared samples, THF-modified g-C_3N_4 was observed to have uniformly holey defects. And the thickness of the monolayer C_3N_4-THF sample without Pt nanoparticles was in a range of 0.94 – 1.85 nm (Figure 30), which is consistent with the above result with Pt nanoparticles loaded (thickness of the monolayer plus nanoparticles size). The hole size distribution was shown in Figure 25, which was in a range of 57.7 to 833 nm and most of the holes had a diameter of ca. 130 nm. The hole density was calculated at 2.23 holes/μm^2. CS-STEM image of C_3N_4-THF layer further confirmed the holey structure at high spatial resolution (Figure 25c & d).

Moreover, the AFM height profiles also confirmed the centered sheet structure with a grid edge shape of C_3N_4-IPA (Figure 24c, Figure 24m), the sheet structures of C_3N_4-DMF (Figure 24i, Figure 24n) and C_3N_4-MA (Figure 24g, Figure 24l). As a comparison, C_3N_4-THF has an appropriate structure, which maintains the lateral size of C_3N_4-bulk with a moderately holey structure that keeps the skeletal g-C_3N_4 2D layer intact (Figure 24e, Figure 24o). This morphology structure would lead to the highest level of accessible active sites among the samples. HR-TEM confirmed the morphologies of the structural layers (Figure 22f-j). In particular, C_3N_4-THF achieved a good distribution of single-layer or few layers form (Figure 22j), compared to the other samples. These results confirmed the successful exfoliation of the bulk multilayer g-C_3N_4 structure into a monolayer of modified g-C_3N_4 by solvothermal treatment. As a result, a highly dispersion of g-C_3N_4 in water leads to maximizing the catalyst surface accessible active sites, which directly affects catalyst performance in H_2 evolution.

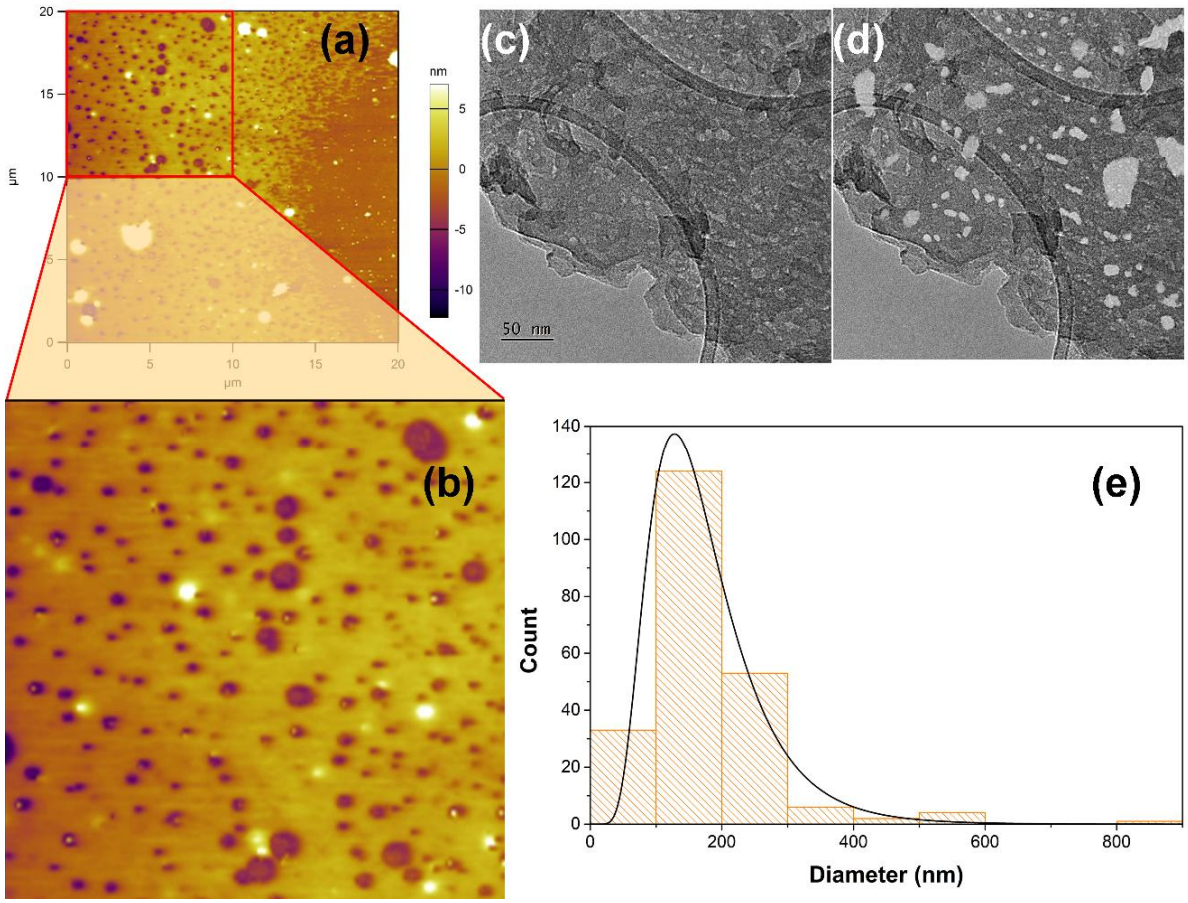

Figure 25. (a) AFM topography images of THF-modified g-C_3N_4 sample, (b) AFM inset image at 10x10 µm scale, corresponding to (e) holes size distribution in AFM image (b), (c) original CS-STEM image of C_3N_4-THF layer, and (d) image with color added to highlight the typical holes.

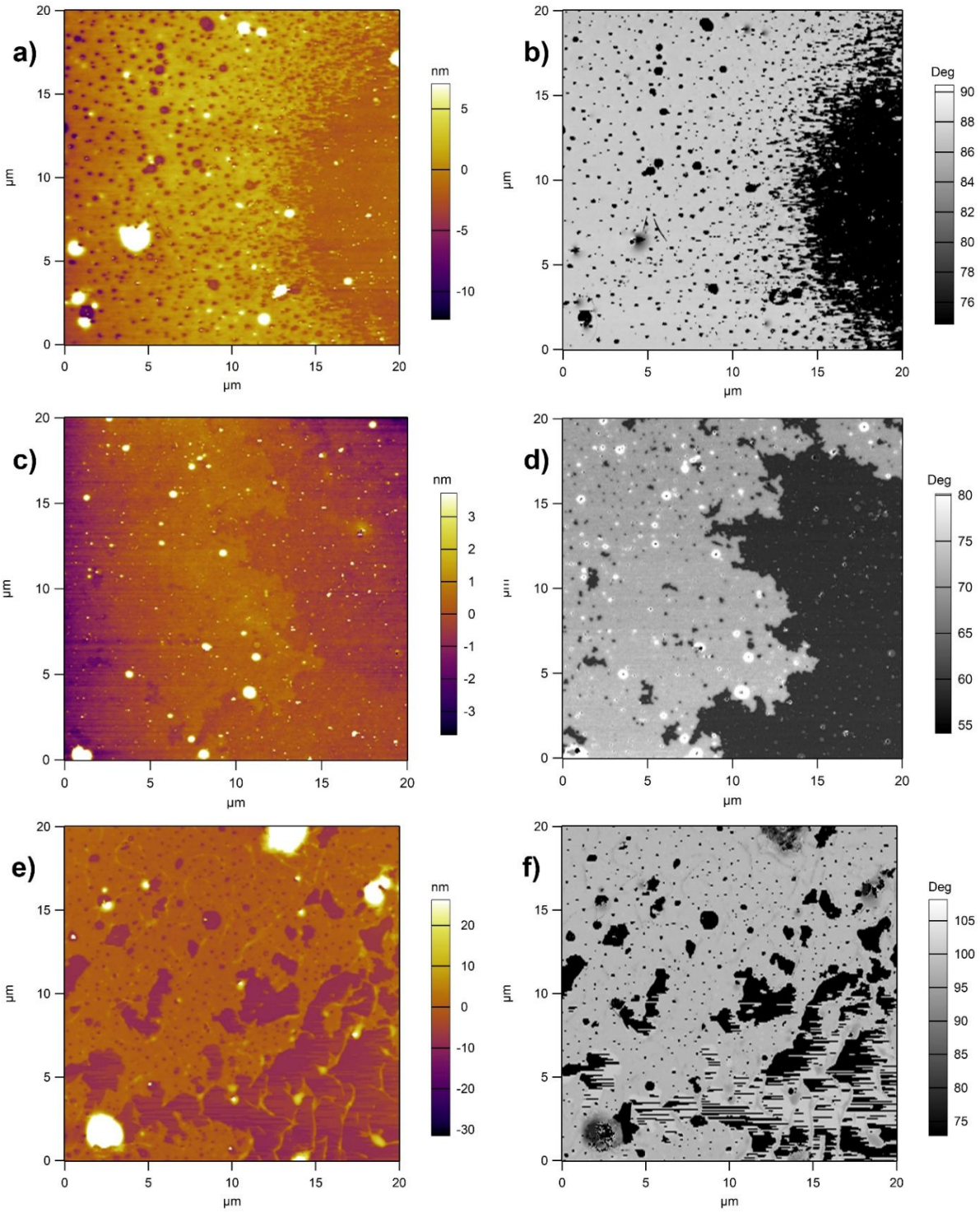

Figure 26. AFM topography images of C_3N_4-THF prepared sample I. (a, c, e) height images at three different positions, corresponding to (b, d, f) phase images, respectively.

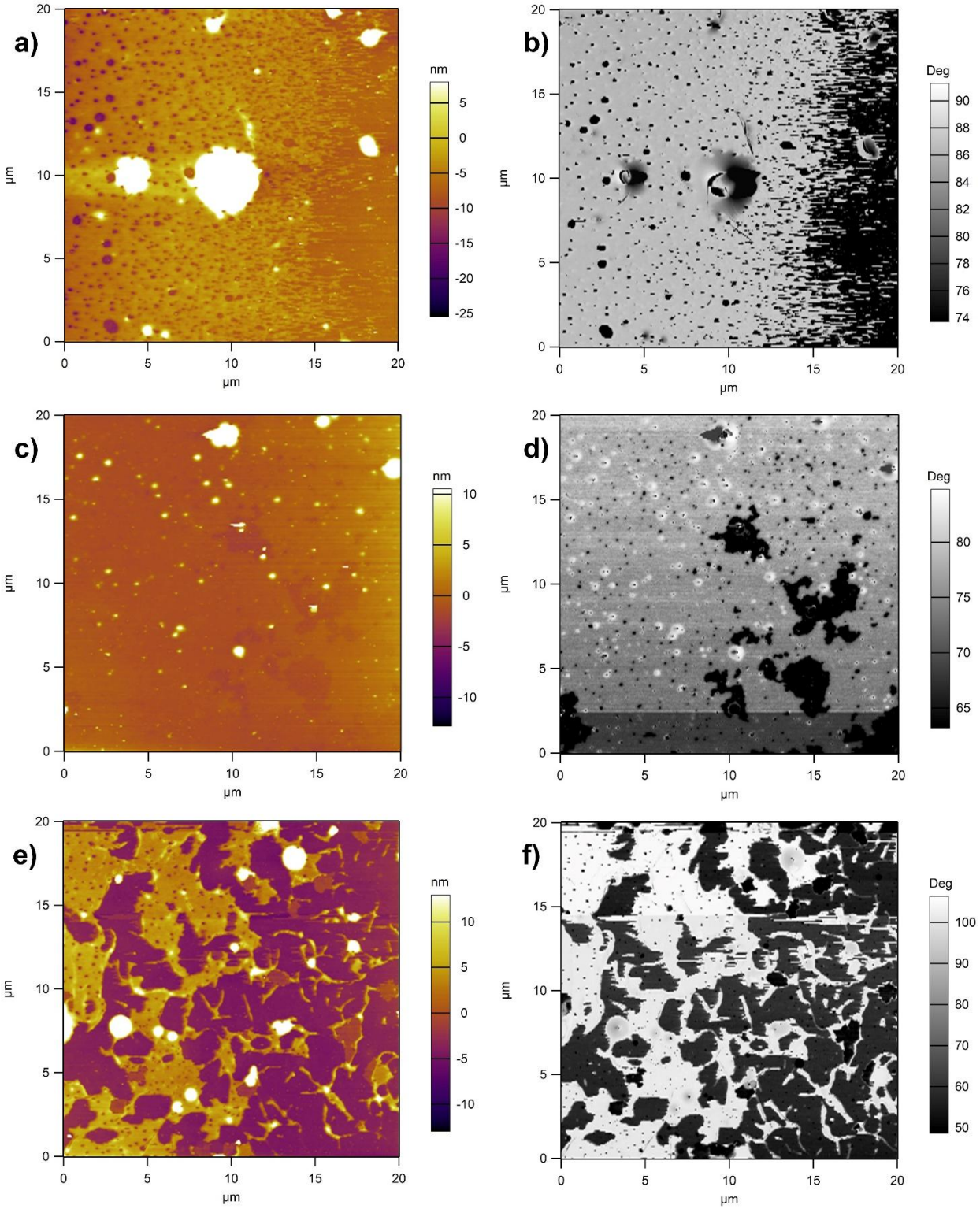

Figure 27. AFM topography images of C_3N_4-THF prepared sample II. (a, c, e) height images at three different positions, corresponding to (b, d, f) phase images, respectively.

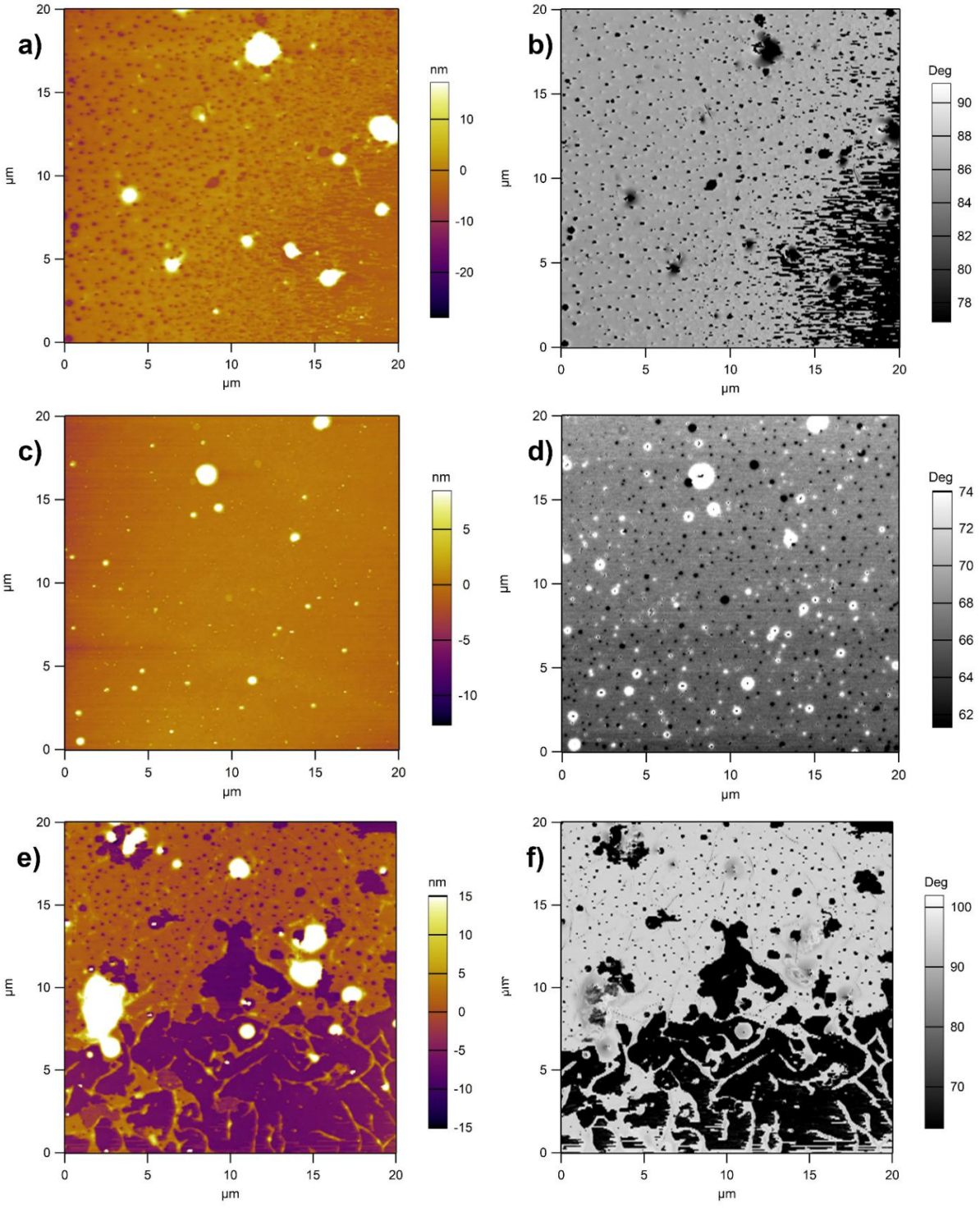

Figure 28. AFM topography images of C_3N_4-THF prepared sample III. (a, c, e) height images at three different positions, corresponding to (b, d, f) phase images, respectively.

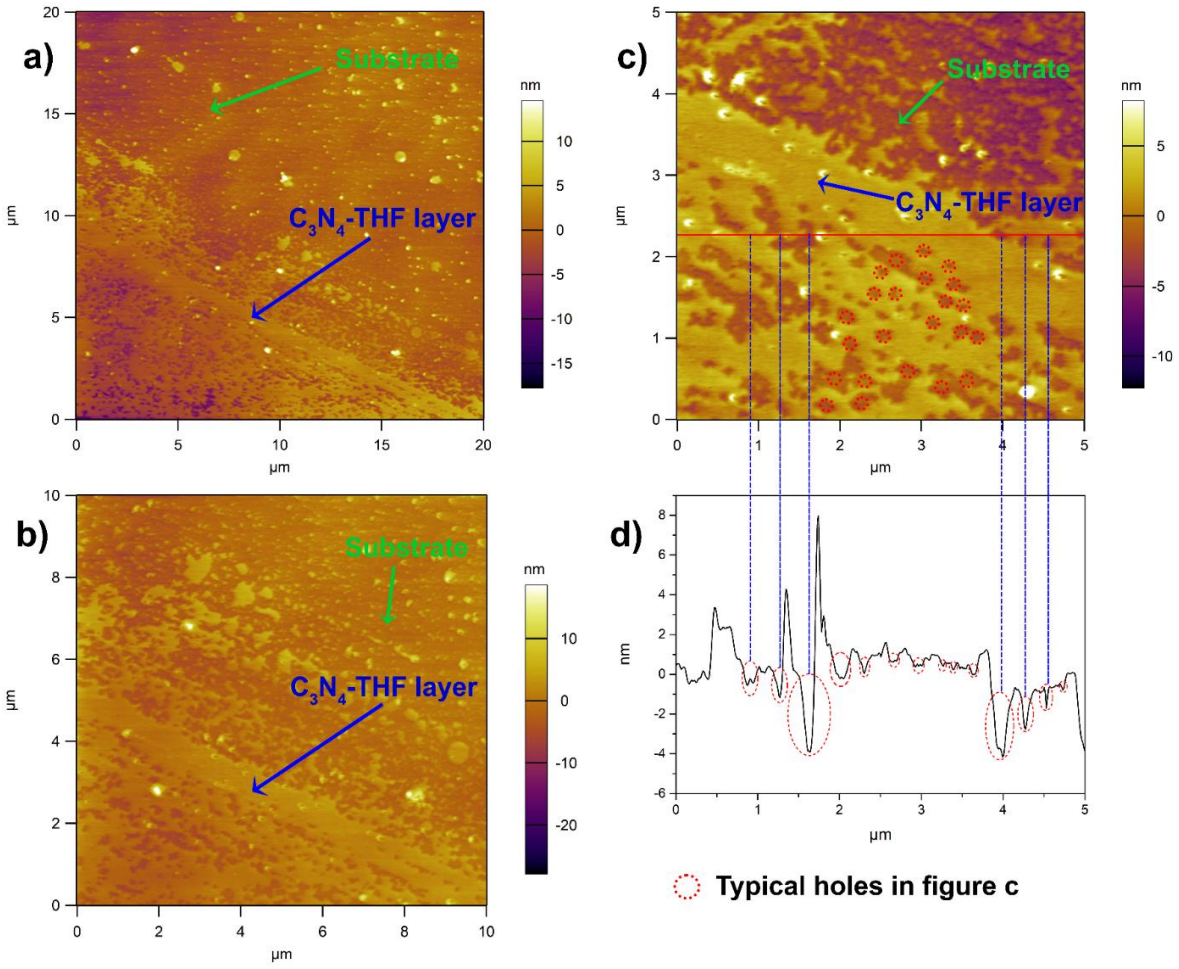

Figure 29. AFM topography images of C_3N_4-THF at different scales, corresponding with its height profile (c & d). The dark brown and dark yellow colors represent for the SiO_2 substrate, and C_3N_4-THF layer, respectively. Typical holes in figure 29c are marked as red circles. Figure 29d shows the height profile of the C_3N_4-THF layer and holes, corresponding with position of the holes in figure 29c.

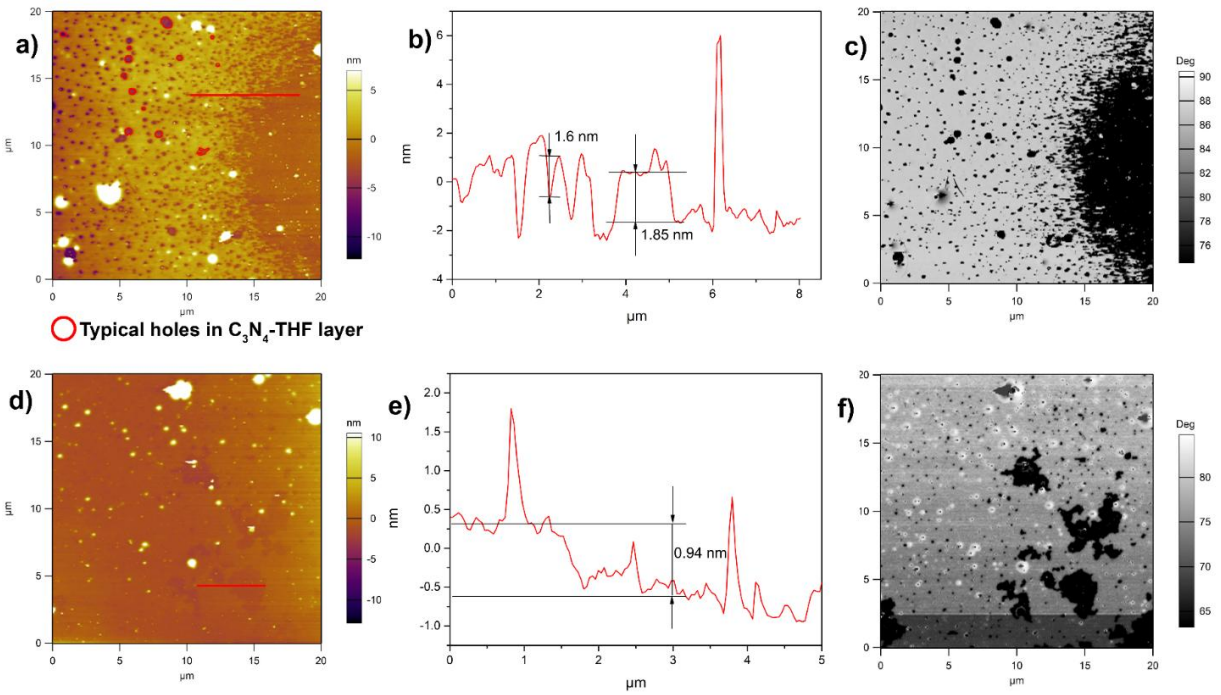

Figure 30. AFM topography images of C_3N_4-THF of different as-prepared samples. Sample I: (a) height image of C_3N_4-THF, corresponding with (b) height profile, and (c) phase image, respectively. Sample II: (a) height image of C_3N_4-THF, corresponding with (b) height profile, and (c) phase image, respectively.

FE-SEM was used to investigate the surface morphologies of dried samples (Figure 22k-o, Figure 31, Figure 32). As shown in Figure 22k, C_3N_4-bulk exhibited a lamellar structure with a smooth surface, which suggested multilayer stacking during the thermal polymerization process. This graphite-like structure has a low accessible surface-active site, due to its small specific surface area and hydrophobic property, preventing light adsorption and unfavorable for absorption of water during reaction. Moreover, C_3N_4-MA maintained a similar planar surface, but smaller sized fragments were formed (Figure 22l), while C_3N_4-DMF showed few layers of structure with clear paper-like at the edge of sheet particles due to self-assembly of the C_3N_4-DMF layer stacking by van der Waals forces during the drying process (Figure 22n). Interestingly, C_3N_4-IPA had a sphere-like morphology with diameters ranging from hundreds of nanometers to a few micrometers (Figure 22m). This formation could be explained by the monolayer observed by AFM with a centered sheet conjunction and a grid shape at the edge of layers (Figure 22c), forming a spherical structure to minimize surface energy. As a result, C_3N_4-IPA possessed a larger specific surface area, which is 4.65 times greater than C_3N_4-bulk in the S_{BET} results (Table 8). The C_3N_4-THF

sample showed large sheets of morphology interspersed with holey structure in the layers (Figure 22o), and the hybrid structures of layer sheets could lead to extra highly accessible surface active sites, leading to the highest photocatalytic performance in the forthcoming H_2 evolution study.

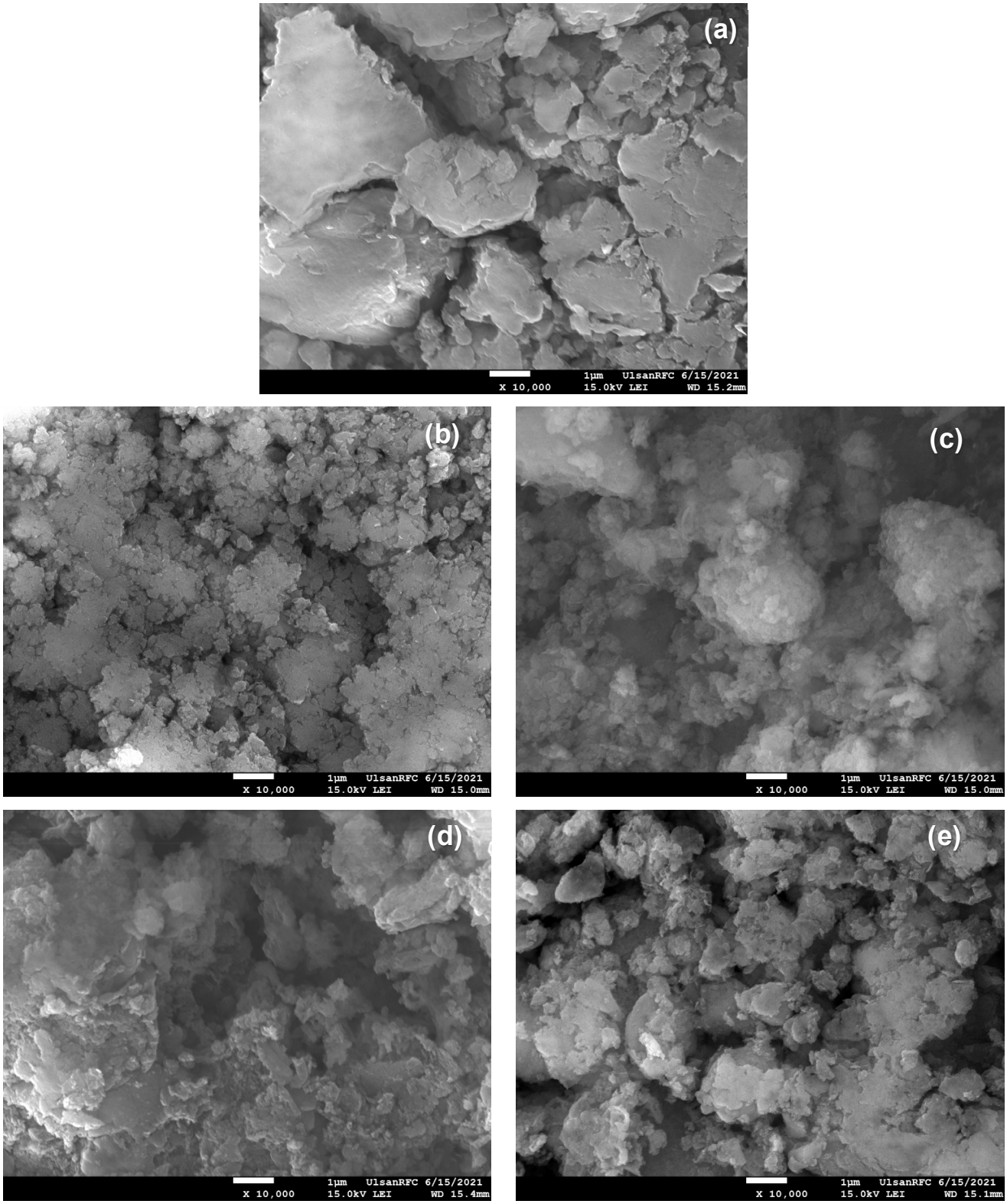

Figure 31. FE-SEM images of (a) C_3N_4-bulk, (b) C_3N_4-MA, (c) C_3N_4-IPA, (d) C_3N_4-DMF, and (e) C_3N_4-THF at different magnification.

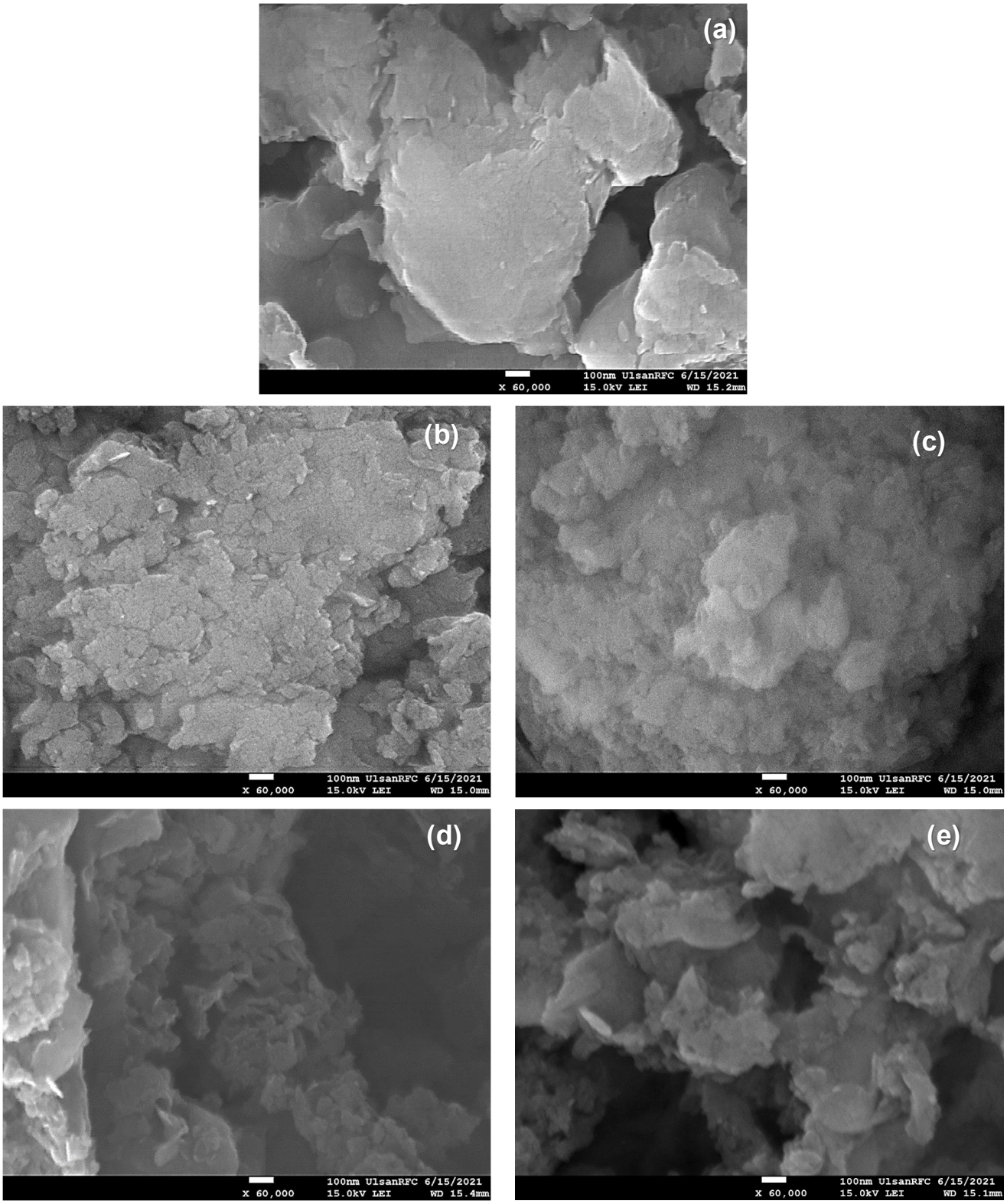

Figure 32. FE-SEM images of (a) C_3N_4-bulk, (b) C_3N_4-MA, (c) C_3N_4-IPA, (d) C_3N_4-DMF, and (e) C_3N_4-THF at different magnification.

The N_2 adsorption-desorption isotherms of all prepared samples are presented in Figure 33, and the acquired specific surface areas (S_{BET}) of the resultant samples are listed in Table 8. All isotherms had an H3 hysteresis loop and were classified as type IV by the IUPAC, indicating the mesoporous characteristic of all samples.[99] Overall, the vacuum-dried solvothermal treated samples had 3.16 times, 4.05 times, 4.65 times, and 4.77 times higher S_{BET} values than the C_3N_4-bulk, corresponding to C_3N_4-MA, C_3N_4-IPA, C_3N_4-DMF, and C_3N_4-THF, respectively, which is consistent with the morphology microstructures of the samples. In addition, the pore size distribution of the samples revealed that the majority of the pores are between 3 and 100 nm in size. The S_{BET} values of the vacuum-dried samples were obviously lower than the actual specific surface areas in the reaction media due to the π–π stacking effect and interactions between the various functional groups densifying layers of g-C_3N_4 during the drying process.

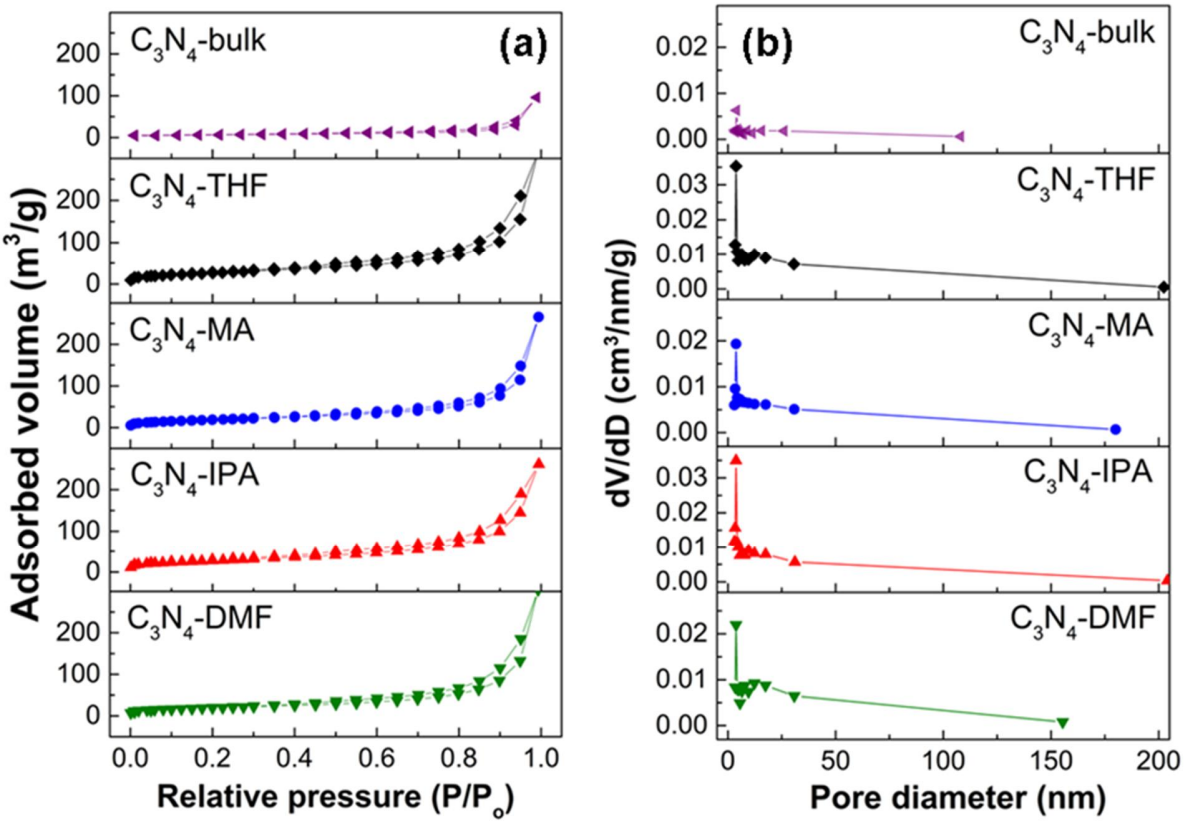

Figure 33. (a) N_2 adsorption/desorption isotherms onto bulk and freeze-dried g-C_3N_4 and (b) obtained pore diameter distribution.

Table 8. Textural data and bandgaps of the as-prepared g-C_3N_4 photocatalysts.

Sample	S_{BET} (m^2/g) [a]	V (cm^3/g) [a]	L (nm) [a]	Band gap (eV) [b]
C_3N_4-bulk	21.81	0.146	4.053	2.76
C_3N_4-MA	75.91	0.410	3.821	2.88[c]
C_3N_4-IPA	101.49	0.395	3.821	2.90[c]
C_3N_4-DMF	88.32	0.473	3.828	2.91[c]
C_3N_4-THF	103.98	0.488	3.852	2.91[c]

[a] Specific surface area, pore volume, and average pore size were determined via N_2 adsorption–desorption isotherm measurements.

[b] Estimated bandgaps were obtained from the UV-Vis DRS spectra.

[c] The band gap values were measured using vacuum-drying g-C_3N_4 samples by UV-DRS.

2.3.4. Mechanism of Solvolysis of g-C_3N_4 to Form Holey-defects Structure

Results of the DFT study on the charge density differences for all adsorbates are shown in Figure 35(a-d). This analysis showed an interaction between the O atom of the adsorbate (O_a) and the C atom of the sheet (C_s). It is to be noted that, in the sheet without any adsorbates, the charge was distributed only at the N atom (N_s) due to higher electronegativity of nitrogen than carbon (Figure 36), while after adsorption of DMF, charge density was found on both C_s and N_s. This result demonstrates interactions between the O_a in DMF with both C_s and N_s in aromatic ring (Figure 35d). For MA and IPA adsorbates, this charge distribution was observed solely on the C_s (Figure 35a & b), suggesting the interaction between O_a and C_s. Particularly, after adsorption of THF, charge densities were found on C_1 and C_2 of the s-heptazine sheet (Figure 35c), which suggests that the O atom of THF could attack both C_1 and C_2 atoms to break the C_1-N_s or C_2-N_s bonds, resulting in heptazine unit vacancy and nitrogen deficiency in heptazine units in the structure of C_3N_4-THF.

The crystal structure of the s-heptazine structure is depicted in Figure 34.

Top view

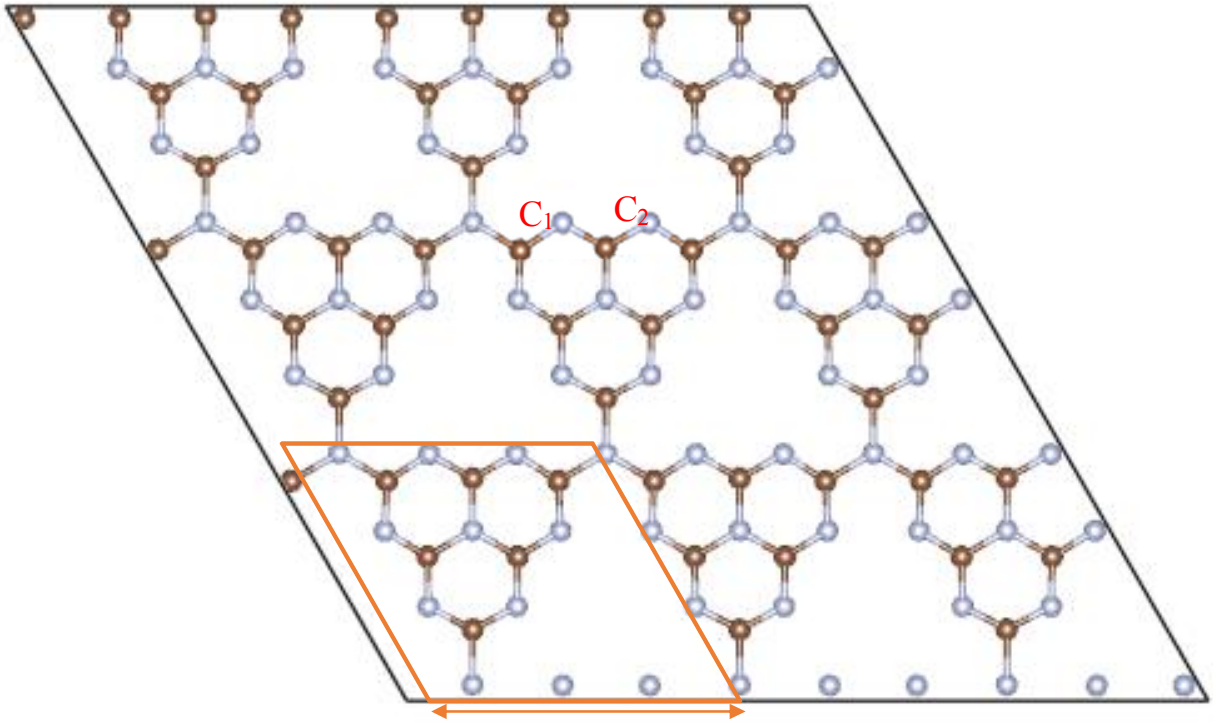

a= 7.13 Å

Side view

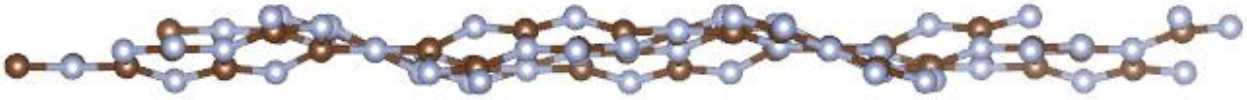

Figure 34. A 3x3 Unit cell of s-heptazine.

Top view

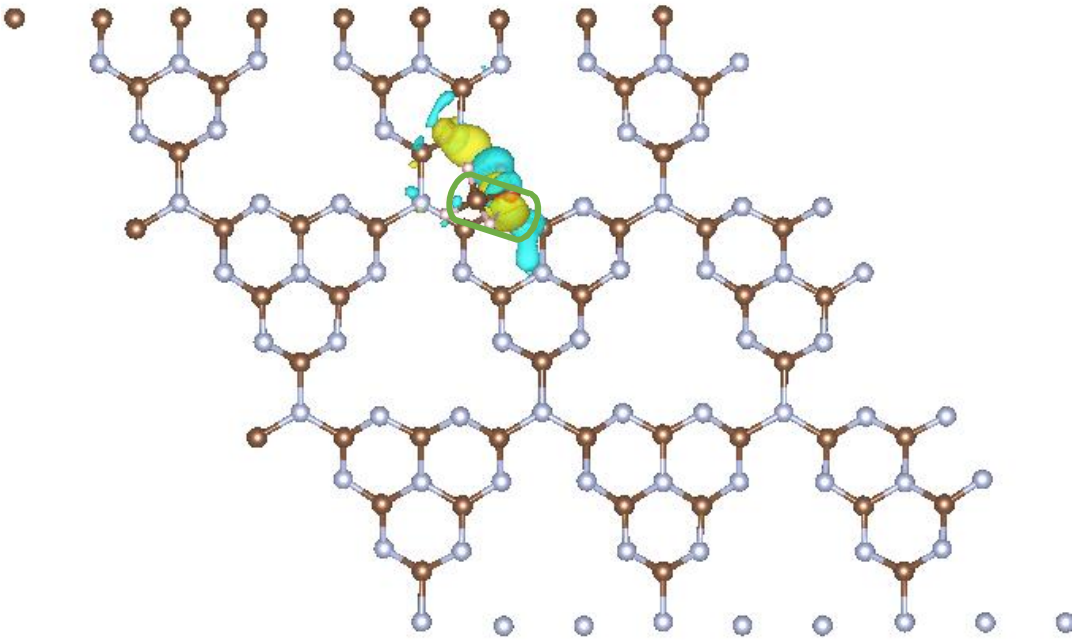

Angle view

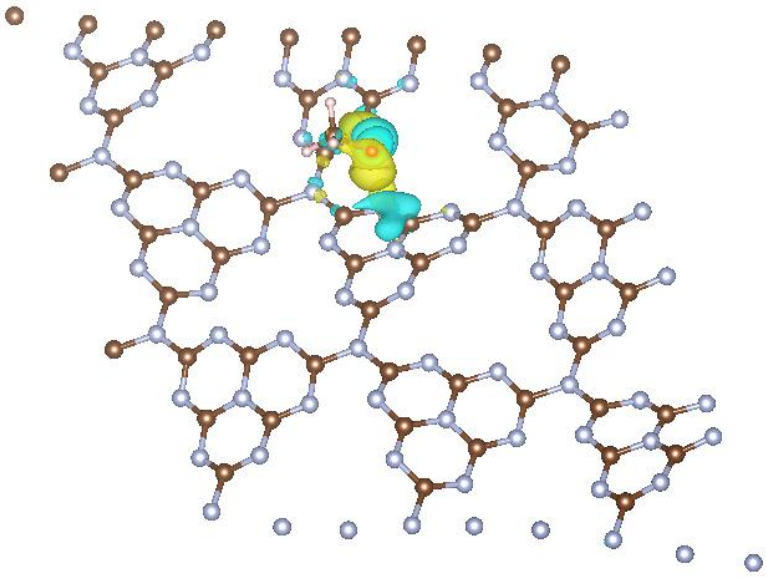

Figure 35a. The charge density for MA on s-heptazine sheet: interaction between O_a-C_s and H_a-N_s.

Top view

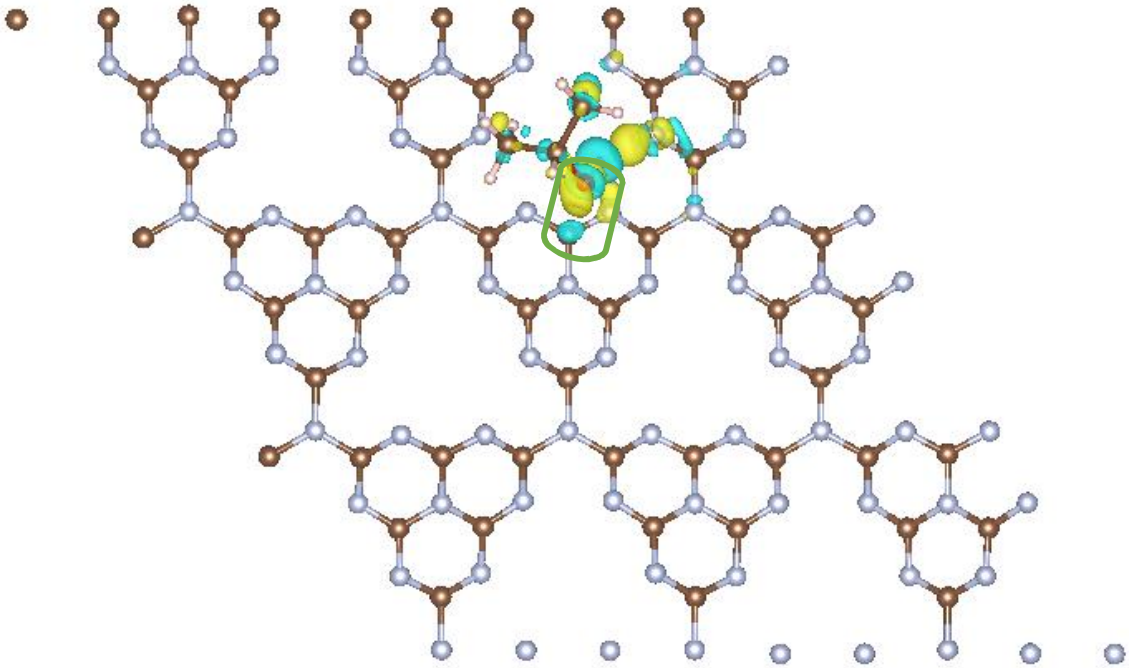

Angle view

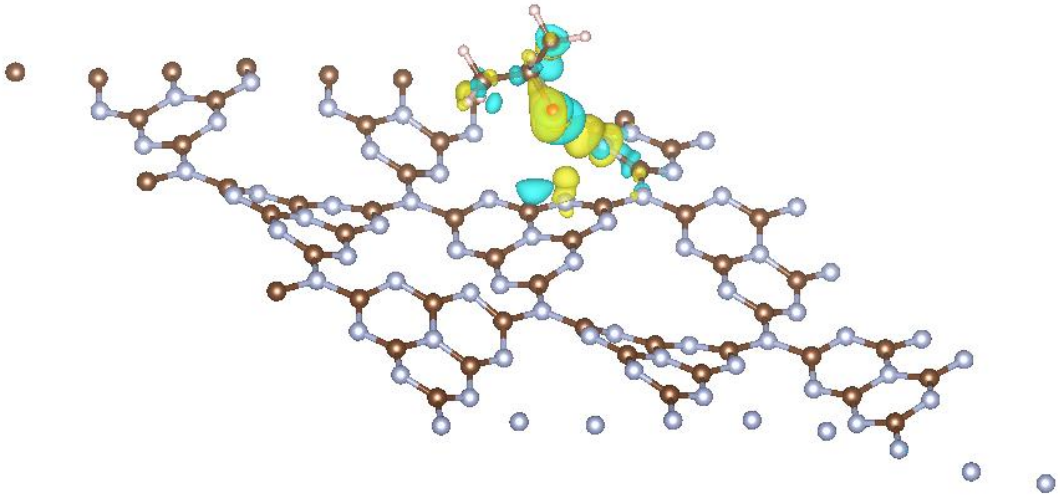

Figure 35b. The charge density for IPA on s-heptazine sheet: interaction between O_a-C_s and H_a-N_s.

Top view

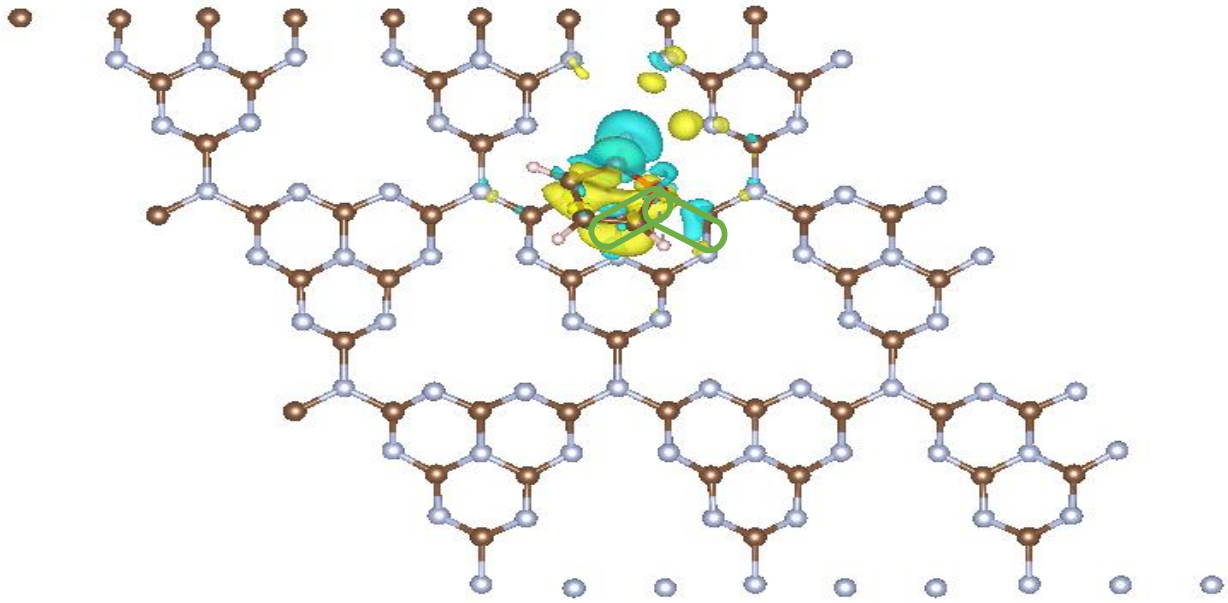

Angle view

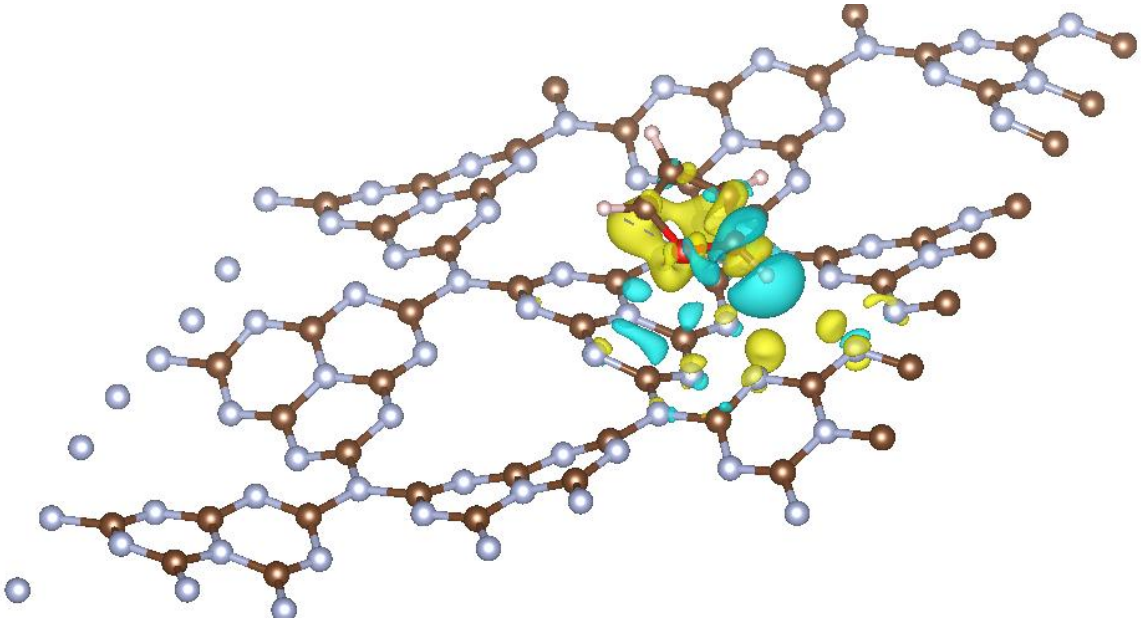

Figure 35c. The charge density for THF on s-heptazine sheet: interaction between O_a-C_1 and O_a-C_2 (C_1 and C_2 carbon positions were shown in Figure 34).

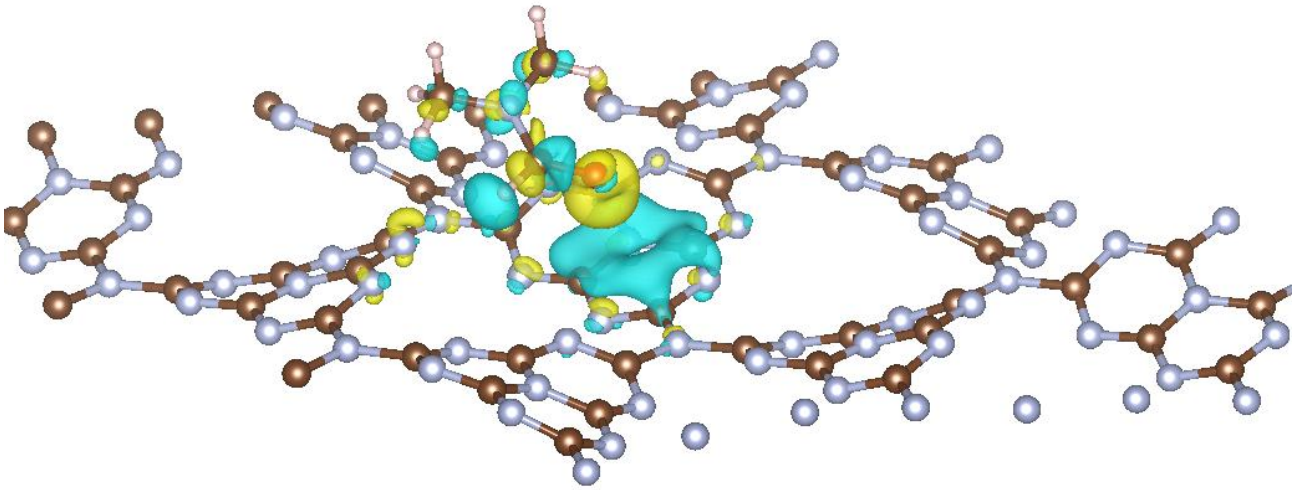

Figure 35d. The charge density for DMF on s-heptazine sheet: interaction between O_a-C_s and O_a-N_s.

In Figure 35, the aquamarine blue color and the yellow color represent the charge depletion (+) and the charge accumulation (-), respectively. And in the pristine sheet, charge accumulation was observed on nitrogen (Figure 36).

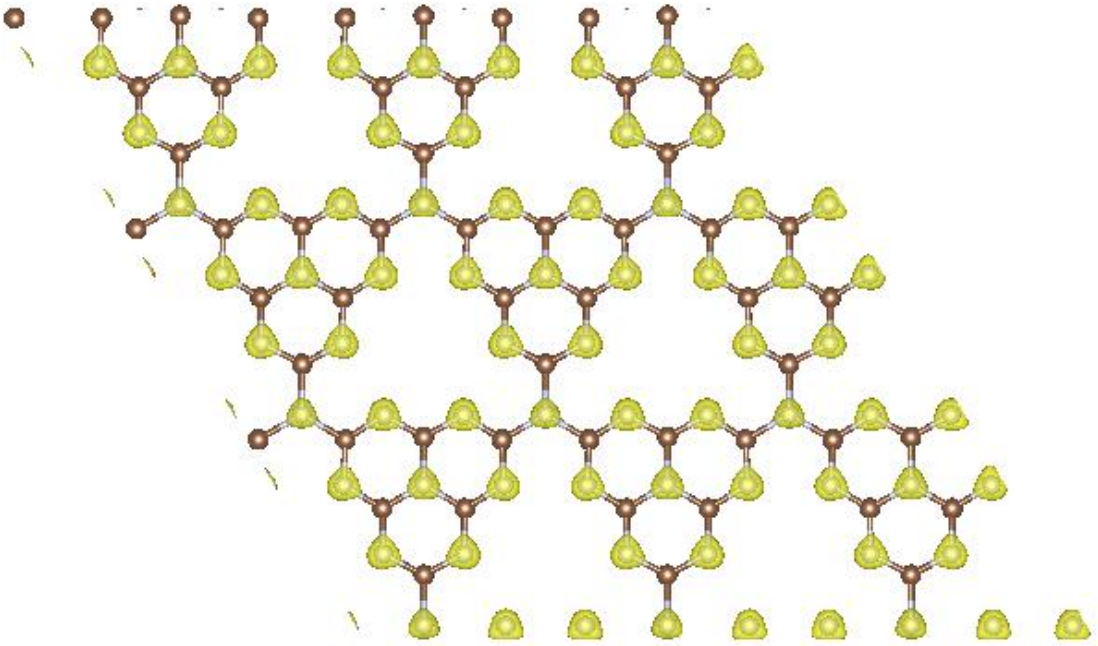

Figure 36. Charge distribution on N atoms as N accepts the charge (e^-) from C in pristine s-heptazine sheet.

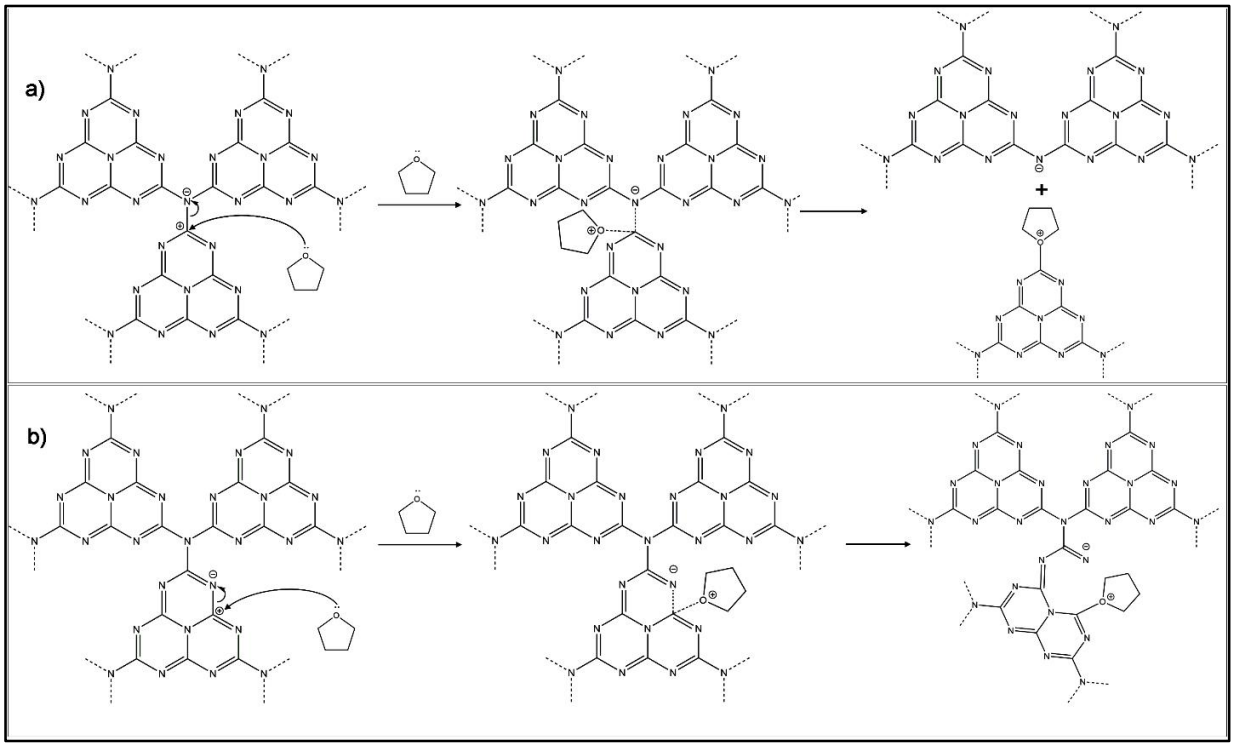

Scheme 2. Proposed S_N1 reaction pathway of THF interacting with g-C_3N_4 at (a) C_1 and (b) C_2 in the heptazine rings.

Based on the experimental results of the AFM nanostructures and XPS electronic structures of the samples and DFT calculations, a possible mechanism of THF solvolysis of g-C_3N_4 to achieve the holey structure of C_3N_4-THF is illustrated in Scheme 2.

According to charge density DFT calculations, charge accumulates on N atoms as N accepts charge (e^-) from C in the pristine s-heptazine sheet. As a result, charge depletion appears on C atoms (+) (Figure 36). In this S_N1 solvolysis reaction, the THF molecule acts as a nucleophile for nucleophilic substitution of C_1 or C_2 in the s-heptazine sheet. Consequently, the C_1-Ns bond and C_2-Ns bond are broken, causing a heptazine unit vacancy in the C_3N_4-THF structure and a nitrogen deficiency in the heptazine unit, respectively (Scheme 2). For MA and IPA, only the C_1-Ns bond is broken, resulting in skeleton fragmentation in C_3N_4-MA and heptazine unit vacancies in the C_3N_4-IPA edges, respectively. These processes follow the proposed S_N1 reaction pathway illustrated in Scheme 3.

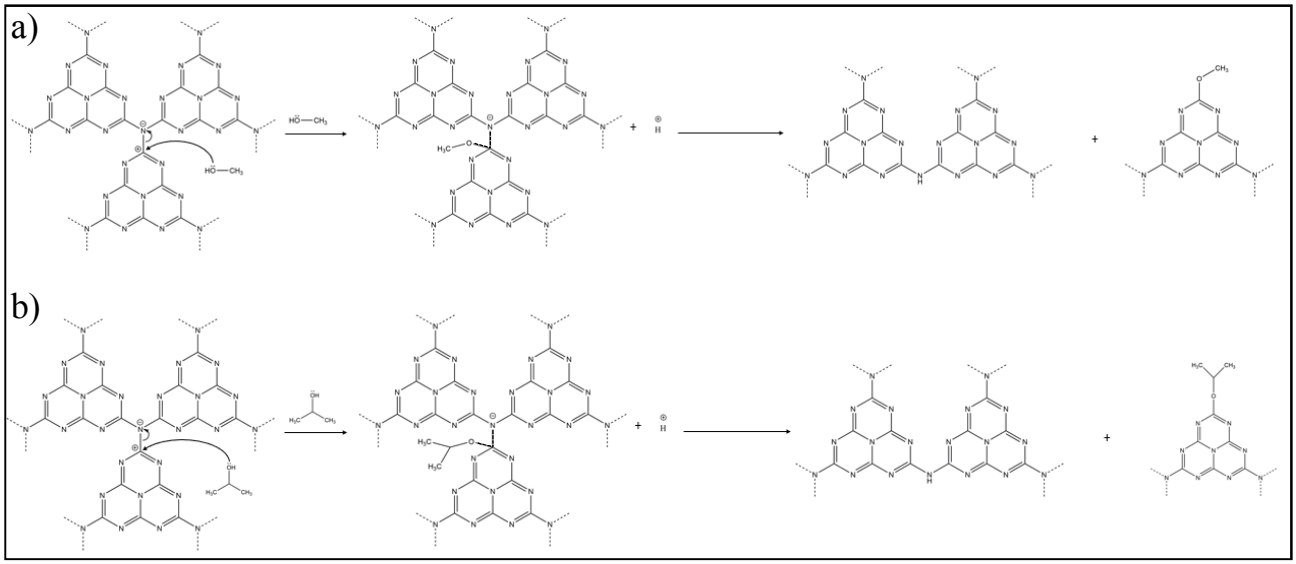

Scheme 3. Proposed S_N1 reaction pathway of (a) MA and (b) IPA interact with g-C_3N_4 at C_1 in the heptazine rings.

2.3.5. Optical Bandgap and Charge Carrier Separation and Transfer

As shown in Figure 37a, the UV-Vis spectra present the absorption regions of all prepared samples. The observed strong absorption around 320 nm lies in the range characteristic for the π-π* electronic transition in aromatic 1,3,5-triazine compounds. An additional absorption, very broad and weak, was observed in the visible region around 380-390 nm, which presumably belongs

to n-π* transitions involving lone pairs of nitrogen atoms in the polymer. Compared with C_3N_4-bulk, C_3N_4-DMF and C_3N_4-MA displayed a blue shift of the absorption edge, suggesting an increase in bandgap, while the two other samples, C_3N_4-IPA and C_3N_4-THF, showed a red shift of the absorption edge. The optical bandgap is attributed to transitions between the weakly localized π-π* states that come from sp^2 hybridization of C and N in the g-C_3N_4 framework. The second band transition in the framework occurs due to n–π* at higher wavelengths than the original bandgap. The values for these two band transitions were determined from the Tauc plot spectra, which were derived from UV-Vis spectra (Figure 37b-f).[100] [101]

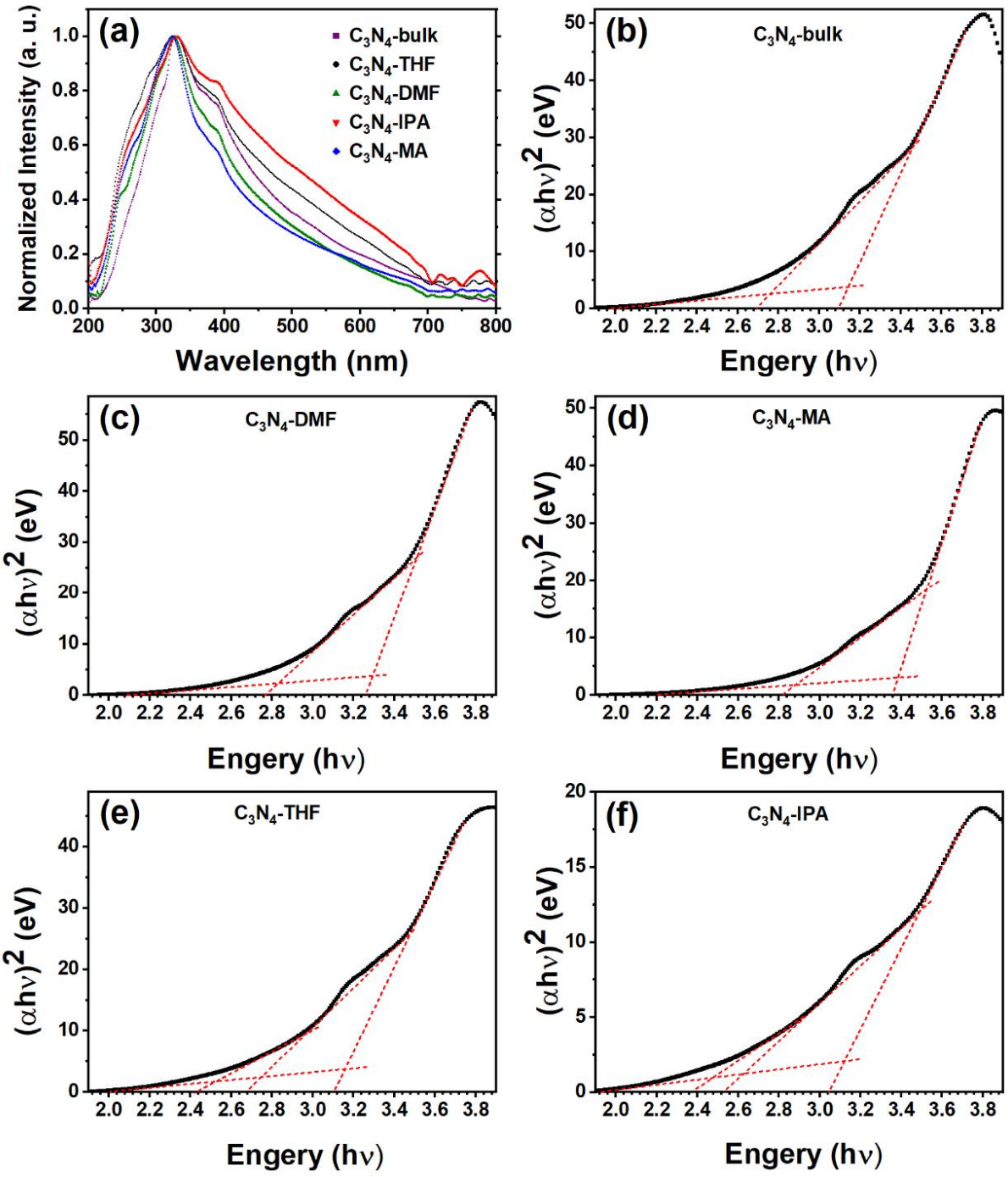

Figure 37. (a) UV-Vis absorption spectra and (b) (c) (d) (e) (f) corresponding Tauc plots of Energy (eV) and $(\alpha h\nu)^2$ for all prepared samples.

After solvothermal treatment, the original bandgap value (π–π* transition) of the C_3N_4-bulk changed from 3.15 to 3.30, 3.40, 3.10, and 3.15 eV for C_3N_4-DMF, C_3N_4-MA, C_3N_4-IPA, and C_3N_4-THF, respectively. The second transition between the bandgap (n–π*) changed from 2.7 in C_3N_4-bulk to 2.85, 2.85, 2.65, and 2.75 for C_3N_4-DMF, C_3N_4-MA, C_3N_4-IPA, and C_3N_4-THF, respectively. The increase of optical gaps from the bulk sample to C_3N_4-DMF, C_3N_4-MA is related to layer exfoliation and the quantum confinement effect (QCE). As we previously discussed, these two solvents do not affect holey-defects by removing heptazine units. Therefore, the optical bandgaps widen due to layer exfoliation compared to the bulk. However, for C_3N_4-IPA and C_3N_4-THF, the story is different. Here, there are two opposing parameters that can alter the optical absorption property. Thus, there is a seesaw relationship between these two parameters; the quantum confinement effect increases the bandgap, but the presence of holey-defects decreases the bandgap.[67] However, the band transitions results demonstrate that the light-harvesting capability originating from bandgap absorptions of the prepared samples is not sufficient for the visible range of light and has a marginal effect.

Interestingly, it is clear that a strong absorption tail (Urbach tail) is present in the absorption spectra of C_3N_4-IPA and C_3N_4-THF, which gives a significantly lower energy gap of ~2.48 and 2.52 eV, respectively. In these two cases, the tail absorption (evidenced by UV-Vis) can contribute significantly to the absorption of photons with energies lower than the optical gaps, a phenomenon known as enhanced sub-bandgap absorption. The presence of this tail in the UV-Vis spectrum may reflect the existence of disorders/defects, which leads to formation of localized states extended in the bandgap (known as mid-gap states). This slightly decreased bandgap after introduction of holey-defects was further confirmed by DFT calculations on the densities of states (DOS) for the pristine and holey structures of g-C_3N_4 (Figure 38). For pristine g-C_3N_4, the conduction band (CB) minimum and valence band (VB) maximum are all composed of C2p and N2p. In the holey structure of g-C_3N_4, the CB minimum and VB maximum are also composed of C2p and N2p. From the total DOS, the ΔE_g value ($E_{g\ pristine}$ -$E_{g\ holey}$) is approximately 0.04 eV, which are in good agreement with the experimental bandgap calculations. Moreover, the original optical gaps were calculated via UV-DRS graphs, and the data are reported in Table 8. The data from UV-DRS are lower than UV-Vis because when the powder form of the samples is analyzed, due to more stacked layers a lower bandgap value will be obtained compared to the dispersion of a single layer of sample in solvent due to the quantum confinement effect, as discussed above.

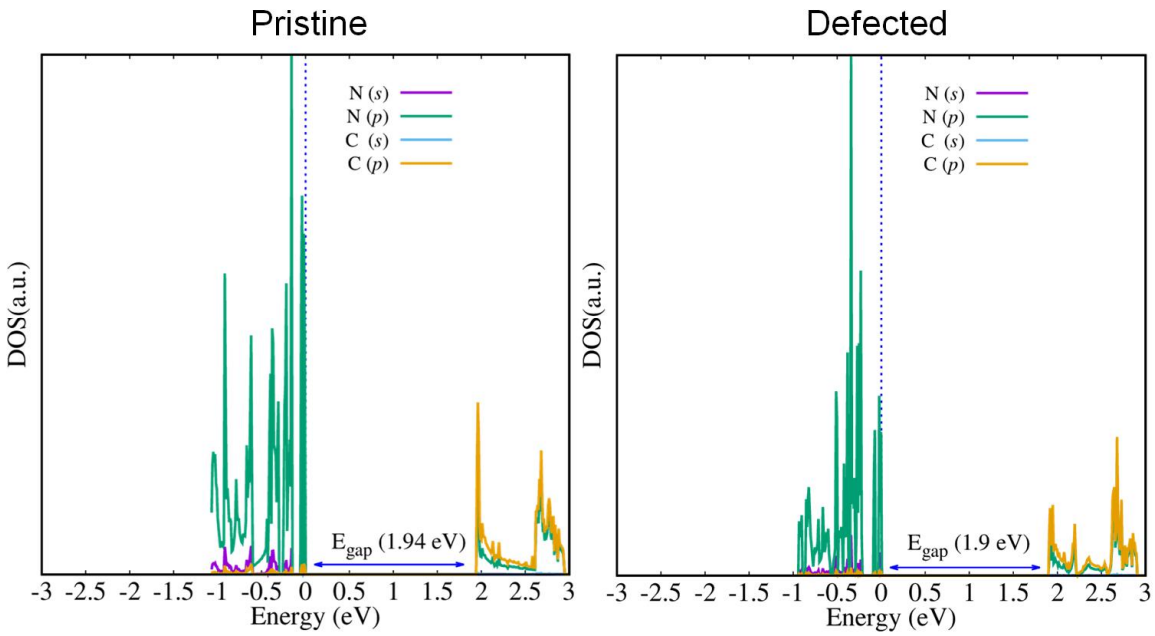

Figure 38. The densities of states (DOS) for the pristine and holey structures of g-C_3N_4.

It is widely accepted that effective photogenerated electron-hole pair separation is responsible for enhancing the photocatalytic activity of a semiconductor material.[102] PL, EIS, and TRPL were carried out to explore the intrinsic properties of photogenerated charge carrier separation on the surface of as-prepared g-C_3N_4 samples, as shown in Figure 39. The photoluminescence (PL) spectra of synthesized C_3N_4-bulk and solvothermal g-C_3N_4 were analyzed by PL with an excitation wavelength of 340 nm.[67] Figure 39a shows steady-state PL spectra of bulk and solvothermal treated samples at 340 nm excitation. Compared with C_3N_4-bulk, solvothermal treated samples showed much lower PL peak intensities, suggesting suppressed photogenerated charge recombination due to an increased charge diffusion rate in the as-prepared aromatic system. C_3N_4-DMF and C_3N_4-MA showed lower PL peak intensities than C_3N_4-bulk, implying that their ultrathin thickness of exfoliated nanosheets facilitates the efficient separation and transfer of charge carriers compared to the stacked structure. Additionally, the enlarged bandgap due to QCE also promotes the separation of charge carriers. Meanwhile, the recombination rate decreases more in C_3N_4-MA compared to C_3N_4-DMF because of formation of smaller lateral sizes, which reduce the charge diffusion length compared to bigger layers. C_3N_4-IPA also exhibited a quenched PL intensity compared to C_3N_4-bulk and C_3N_4-DMF as a result of

formation of thin nanosheets and also holey-defects formation, which together reduced the charge carrier recombination in the structure.

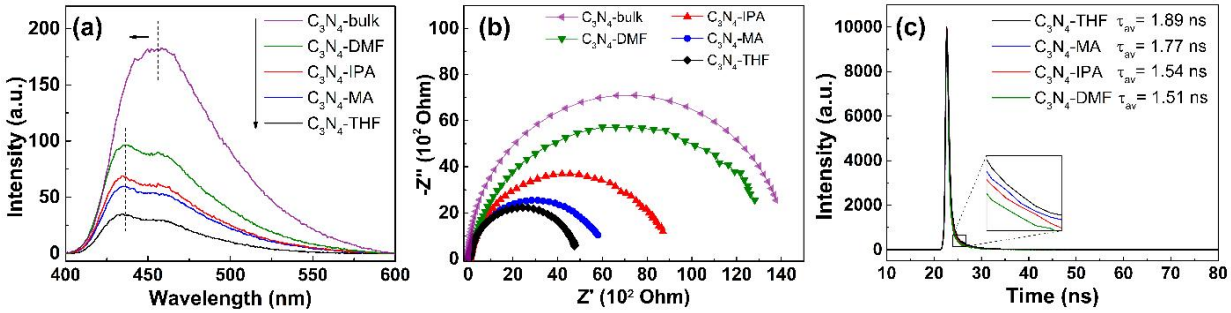

Figure 39. (a) PL emission spectra, (b) EIS Nyquist plots, and (c) TRPL spectra.

Among all of the samples, the smallest PL peak intensity was found for C_3N_4-THF, suggesting it had the lowest charge recombination rate, due to the formation of monolayer nanosheets with uniform holey-defects. The monolayer structure of the nanosheets will facilitate the charge diffusion length in the π-conjugated system. The formation of uniform holey-defects and nitrogen deficiencies in the as-prepared nanosheets provides extra dangling bonds that carry remaining lone electron pairs or vacant orbitals from the broken bonds. These extra dangling bonds are delocalized to the aromatic system, thus increasing the charge density and charge diffusion. Furthermore, the presence of uniform holes in the g-C_3N_4 sheets facilitate mass transfer in the system and as a result decrease the charge diffusion length, which both of them increased to charge separation and reduced charge recombination. On the other hand, the low charge recombination observed in C_3N_4-THF also confirms that mid-gap states induced by the uniform holey structure do not act as a recombination center trapping electron–hole pairs. Instead, these mid-gap states serve as separation centers to capture photogenerated electrons and inhibit charge recombination. This finding is very important because it confirms that subsequent holey-defects formation does not impair the electronic structure of the aromatic system or create abundant trap-site defects in C_3N_4-THF, which can seriously impede charge separation and transfer. In fact, the combinative synthesis method successfully merges the above merits created by exfoliation and uniform holey defect engineering in C_3N_4-THF, thus exerting a synergistic effect to impeding the charge recombination.

The charge transport process occurring in the samples directly reflects their capacity to shuttle and convey charge carriers to the targeted reactive sites. Thus, EIS measurements were carried out to obtain deeper insight into the charge transport behavior of the as-prepared catalysts.

EIS measurements investigate the charge transfer resistance at the catalyst electrode catalyst/electrolyte interface. A smaller radius of EIS Nyquist plot reflects a smaller resistance for charge carrier transfer at the catalyst/electrolyte interface. Among all the solvothermal treated samples, C_3N_4-THF showed the smallest radius of EIS Nyquist plot, demonstrating lower charge transfer resistance from the catalyst surface to reactant molecules (Figure 39b). The charge transfer facilitation at the interface indicates that uniform holey-defects sites at the surface of C_3N_4-THF do not act as recombination centers even as they act as transition energy states for charge carriers to easily catch reactant molecules. The trend for facilitated charge transfer at the interface for the samples confirms that solvothermal treatment of the C_3N_4-bulk modified the surface properties, which is beneficial for photocatalytic activity enhancement.[103]

The recombination lifetime of charge carriers is determined by four different types of recombination mechanisms, including band-to-band, trap-assisted in bulk, Auger, and surface recombination. To evaluate radiative/non-radiative recombination of photogenerated charge carriers, time-resolved fluorescence decay spectra were obtained under 430 nm laser excitation. The value of specific fluorescence lifetime was fitted following a sum of exponential decay model as shown in the equation below:[104]

$$F(\tau) = A_1 \exp\left(-\frac{\tau}{\tau_1}\right) + A_2 \exp\left(-\frac{\tau}{\tau_2}\right) + A_3 \exp\left(-\frac{\tau}{\tau_3}\right)$$

where $F(\tau)$ is the obtained dynamic attenuation curve, A_i (i = 1, 2, 3) represents the amplitude of the attenuation channel, and τ_i is the corresponding lifetime. Three exponentials were applied to fit the decay model. The average fluorescence lifetime (τ_{av}) was calculated as follows:

$$\tau_{av} = \frac{A_1\tau_1 + A_2\tau_2 + A_3\tau_3}{A_1 + A_2 + A_3}$$

A well-fitted triexponential decay function with three excited-state lifetimes and their respective percentages were used to determine the decay (Figure 39c, Table 9). The prolonged lifetime of fastest recombination (τ_1 and τ_2 the radiative recombination) in C_3N_4-THF assisted with the majority of the charge carriers parallel to the steady-state PL results confirmed that the relaxation of excited electrons through radiative recombination was strongly suppressed in the C_3N_4-THF sample. This phenomenon was observed for other solvothermal treated samples with the same trend of steady-state PL results. Indeed, for the surface recombination (τ_3, non-radiative recombination), the results show that the C_3N_4-MA sample has the longest lifetime followed by C_3N_4-THF but the weight ratio of τ_3 for C_3N_4-THF is higher than C_3N_4-MA. The two other

samples exhibit a lower lifetime for surface recombination. These results demonstrated that surface defects on C_3N_4-THF and C_3N_4-MA can trap the charge carriers and decrease the probability of radiative recombination compared to C_3N_4-IPA and C_3N_4-DMF. The average lifetime of charge carriers is shown in the inset of Figure 39c. Therefore, combined with the above steady-state PL spectroscopy and EIS data, we surmise that C_3N_4-THF possesses the strongest capability to not only separate photogenerated electron–hole pairs, but also transfer them to reactant molecules adsorbed on surface active sites, implying its outstanding competence as a high-performance photocatalytic toward H_2 evolution.

Table 9. Radiative fluorescence lifetimes and their corresponding percentages of photoexcited charge carriers in all prepared photocatalysts.

	τ_1 (ns)	A_1	τ_2 (ns)	A_2	τ_2 (ns)	A_3	τ_3 (ns)
C_3N_4-THF	0.51	0.66	2.7	0.28	13.36	0.06	1.89
C_3N_4-MA	0.48	0.67	2.65	0.28	14.16	0.05	1.77
C_3N_4- IPA	0.45	0.68	2.36	0.27	12.01	0.05	1.54
C_3N_4-DMF	0.42	0.69	2.43	0.26	12.15	0.05	1.51

2.3.6. Graphene Formation via The Solvothermal Treatment of g-C_3N_4

The new phenomenon of graphene formation via solvothermal treatment of g-C_3N_4 was detected in this study. The graphene content in resultant samples was investigated by an Olympus laser scanning confocal microscope (LSCM), Raman spectroscopy, thermogravimetric analysis (TGA), and high resolution powder X-ray diffraction (HRPXRD). The white color of C_3N_4-bulk was transformed into a light tan color (C_3N_4-MA, C_3N_4-IPA, C_3N_4-DMF) or brown color (C_3N_4-THF) after solvothermal treatment. Furthermore, LSCM was used to determine the origin of the solvothermal modified g-C_3N_4 samples color change from white color of C_3N_4-bulk (Figure 40f) to brown color of C_3N_4-THF. Figure 40(d & e) reveals the black spot and black blur spot of graphene nanoparticles that appeared in C_3N_4-THF samples, which caused the brown color of this sample after the reaction. Raman spectra of C_3N_4-THF at the black and black blur spots are shown in Figure 40(a & b), which confirmed the typical graphitic structure of graphene with two prominent peaks at 1345 cm^{-1} and 1599 cm^{-1}, ascribed to the D and G bands of graphene, respectively.[57] In contrast, the C_3N_4-bulk sample did not show any graphene peaks (Figure 40c). We further investigated the existence and crystalline structure of graphene by XRD analysis. The XRD spectra of C_3N_4-THF and C_3N_4-THF's residue after annealing the C_3N_4-THF sample at 700 ℃ in the Ar atmosphere are shown in Figure 40h, and Figure 40g, respectively. Self-assembly-graphene/Pt as a C_3N_4-THF's residue was obtained after annealing for 2 h at 700 ℃, while the g-C_3N_4 content in C_3N_4-THF sample was fully decomposed (Figure 40h & g, Figure 42). The XRD spectrum of self-assembly-graphene/Pt exhibited a broad peaks at 24.6 (*d*-spacing of 3.62 Å) and 43.1, which are attributed to the d_{002} and d_{100} of chemically converted graphene.[57] While the peaks at ca. 39.8, 46.4, and 67.6 belong to the (111), (200), and (220) crystalline planes of the Pt (Figure 40g), respectively.

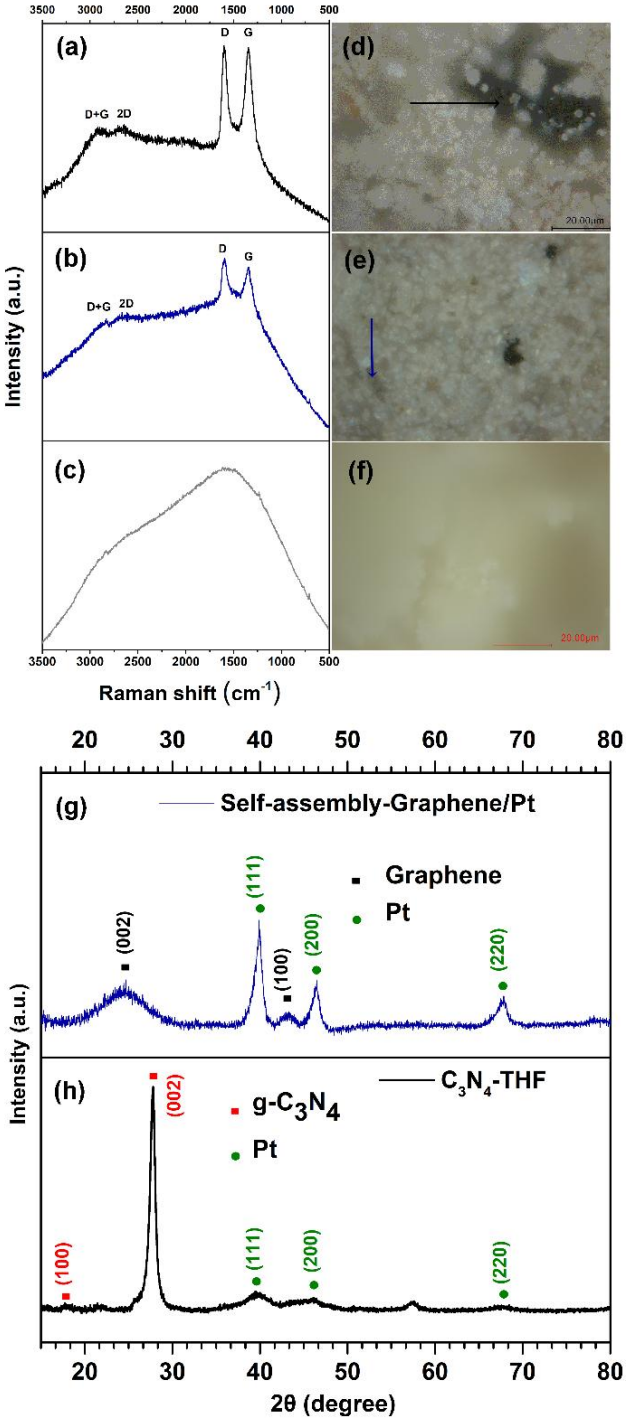

Figure 40. Raman spectra and LSCM images of C_3N_4-THF at different sites on the surfaces of the sample: (a & d) at the black spot, (b & e) at the black blur spot. (c & f) Raman spectra and LSCM images of C_3N_4-bulk. XRD spectra of (h) C_3N_4-THF and (g) C_3N_4-THF's residue (self-assembly-Graphene/Pt) after annealing C_3N_4-THF sample at 700 ℃ for 2 h in Ar atmosphere.

TGA was used to demonstrate thermal stability and graphene content in the as-prepared catalysts. The TGA thermograms in Figure 42 show weight lost by temperature function for C_3N_4-bulk, C_3N_4-MA, C_3N_4-IPA, C_3N_4-DMF, and C_3N_4-THF under argon atmosphere at a ramp rate of 10 ℃ min^{-1}. The first mass loss below 175 ℃ is ascribed to the loss of surface hydroxyl groups or water molecules adsorbed at the surface of the catalysts. The second mass loss, which occurs above 400 ℃, is related to decomposition of the C-N framework in g-C_3N_4. As clearly exhibited in Figure 42, a variety of rates for the second mass loss were observed for different g-C_3N_4 samples. Two factors can be discussed, the onset temperature (T_{ons}) and the mass loss rate. The first parameter of T_{ons} shows the temperature that decomposition of the C-N framework begins, and the second parameter (Mass loss rate, Figure 41) depicts the decomposition rate of the structure. Both parameters are related to the thermal stability of the g-C_3N_4 framework. The C_3N_4-bulk has the highest T_{ons} and the lowest mass loss rate, which is associated with the stacked graphitic structure. The changes of these two parameters for solvothermal treated samples are related to the structural changes compared to the bulk material. Exfoliation of the layers decreased the onset temperature and increased the mass loss rate of C_3N_4-DMF. Changes of these parameters were more pronounced after fragmentation of the exfoliated layers that occurred in C_3N_4-MA. Moreover, by introducing holey-defects in C_3N_4-IPA and C_3N_4-THF, led to the greatest changes, where the lowest T_{ons} and highest mass loss rate were obtained for C_3N_4-THF.

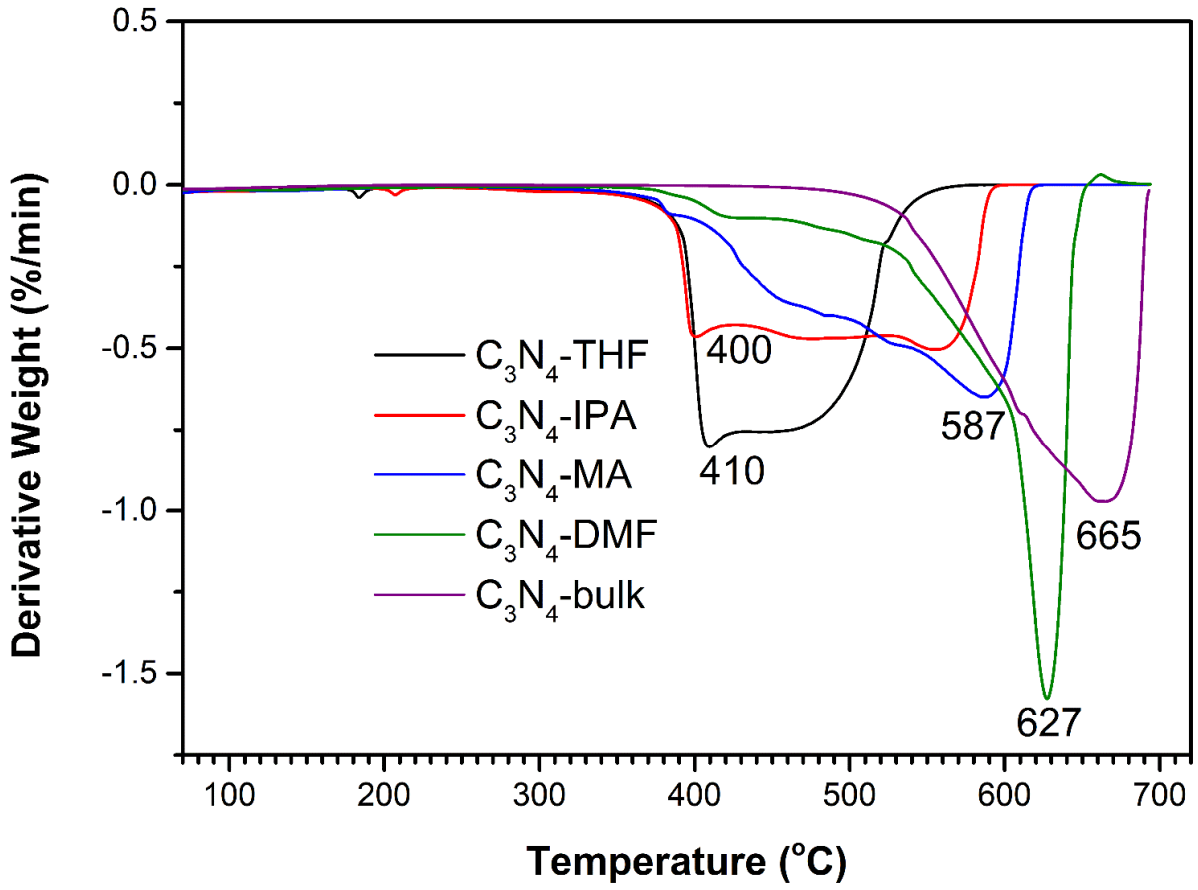

Figure 41. DTG curves of C_3N_4-bulk, C_3N_4-MA, C_3N_4-IPA, C_3N_4-DMF, and C_3N_4-THF.

The remaining weights of C_3N_4-DMF, C_3N_4-MA, C_3N_4-IPA, and C_3N_4-THF at 550 ℃ were 74.87, 38.71, 18.79, and 3.93 wt. %, respectively. The high-resolution TGA thermograms showed the remaining residue of resultant samples at 700 ℃ (inset of Figure 42). The approximate graphene content in the catalysts was calculated after subtracting the Pt percent by ICP-OES, displayed in Table 10. The total amount of Pt and graphene in C_3N_4-THF was 3.81 wt. %, higher than that of

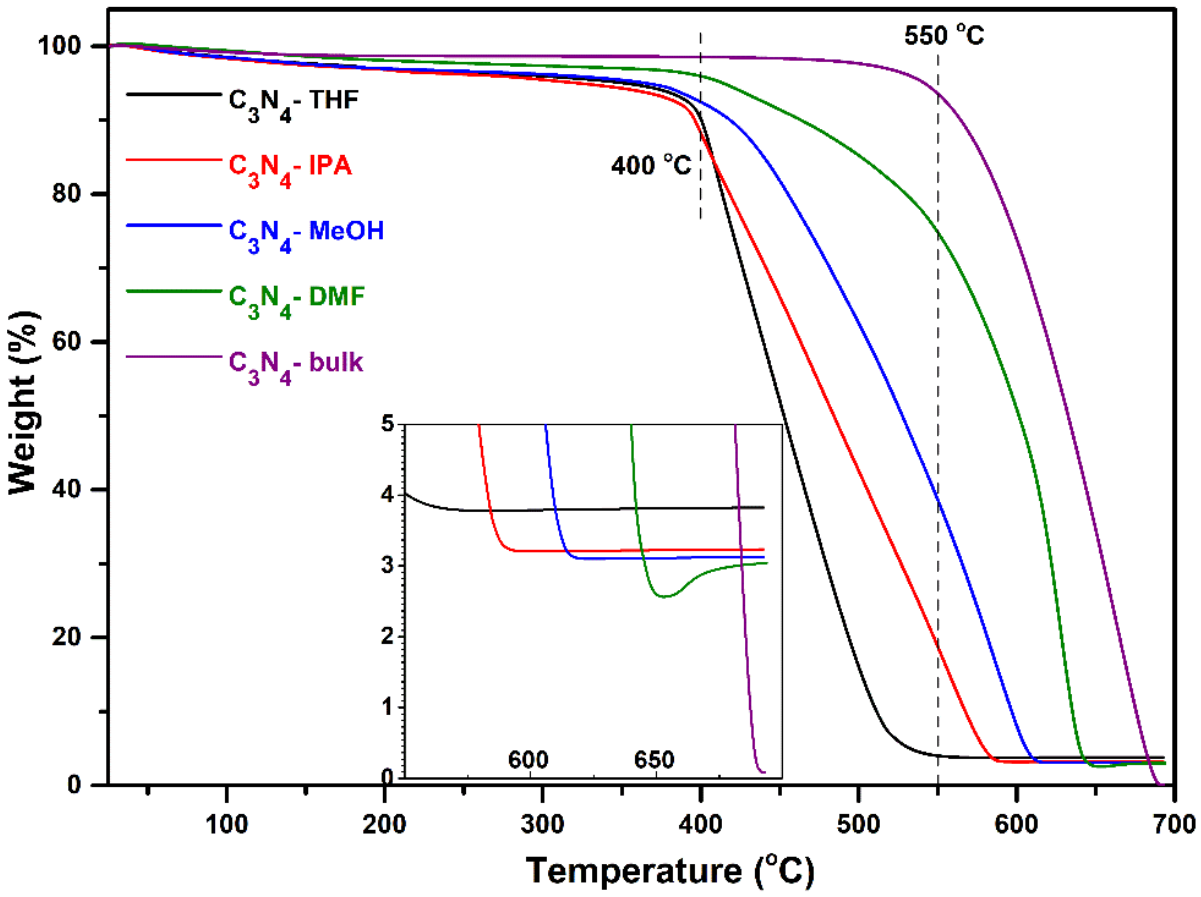

Figure 42. TGA thermograms and high-resolution inset of C_3N_4-bulk, C_3N_4-MA, C_3N_4-IPA, C_3N_4-DMF, and C_3N_4-THF.

the other samples, which contributed to better photocatalytic performance. Graphene, an exceptional electrical conductivity 2D material, could promote charge collection and separation at the interface surface of the photocatalyst due to its role as photoelectron mediator and acceptor.[105] The graphene content in C_3N_4-DMF, C_3N_4-IPA, C_3N_4-MA, and C_3N_4-THF were determined at 0.68, 0.94, 1.26, and 1.53 wt. %, respectively (Table 10). C_3N_4-IPA contains more graphene than C_3N_4-DMF, but its photocatalytic H_2 evolution is lower (Figure 50b). Accordingly, although graphene improved photocatalyst performance incrementally, it was not the main factor enhancing C_3N_4-THF's photoactivity significantly. The role of self-assembled graphene by solvothermal g-C_3N_4 in photocatalytic performance is still being investigated, where all of the other factors affecting catalyst performance are fixed.

Table 10. Approximate graphene content in the catalysts.

Sample	TGA Residue wt. %	Pt wt. %	Graphene wt. %	Total Pt and Graphene wt. %
C_3N_4-bulk	0	0	0	0
C_3N_4-MA	3.12	1.86	1.26	3.12
C_3N_4-IPA	3.23	2.29	0.94	3.23
C_3N_4-DMF	3.03	2.35	0.68	3.03
C_3N_4-THF	3.81	2.29	1.53	3.81

2.3.7. Photocatalytic Performance and Mechanism

2.3.7.1. Photocatalytic H_2 Evolution Performance Optimization

2.3.7.1.1. Equipment Calibration

To consider a more accurate photocatalyst performance evaluation, we purchased a new MFC (Model FC-3911V-H_2(%)+Ar(%) 0-100sccm-1/4SW) to control the gas carrier flow rate, and a new Carboxen 1000 column (Sigma-Aldrich) for the online GC gas measurement. The standard gas of H_2/Ar were supplied from MS Gas Coorporation including certification of analysis. The calibrations were performed before assessing photocatalytic hydrogen evolution of the photocatalysts. The MFC flow rate of the standard gases were set at 25 sccm, as same as thereafter experiments. The H_2 gas was measured via an automatic injection, online gas chromatography with a thermal conductive detector (TCD), and a Carboxen 1000 column (Sigma-Aldrich), Ar as a carrier gas, and the sample injection was set every 30 min. The column temperature was adjusted to be 40 °C, the detector temperature was 250 °C. The quantitative analysis of evolved hydrogen during the dehydrogenation reaction has been calculated according to the equation obtained from the linear calibration curve of hydrogen (Figure 43).

Table 11. Calibration data of H_2 concentration vs. GC peak area.

NEW COLUMN						
Total flowrate 25sccm, 25oC, 1atm						
No.	P (kPag)	T1 (oC)	Conc. H2, ppm	GC area 1 H2	GC area 2 H2	GC area aver. H2
1	0		0	0		0
2	0	23.3	160	8.44	8.64	8.54
3	0	21.9	400	12.49	12.19	12.34
4	0	19.9	600	14.34	14.27	14.305
6	0	20.6	800	17.49	17.93	17.71
7	0	19.8	1000	20.72	21.36	21.04
8	0	19.2	2000	40.01	39.51	39.76
9	0	18.8	3000	60.86	60.18	60.52
10	0	18.6	4000	85.14	84.72	84.93
11	0	18.2	5000	111.75	110.67	111.21
12	0	18.1	6000	143.28	143.89	143.585

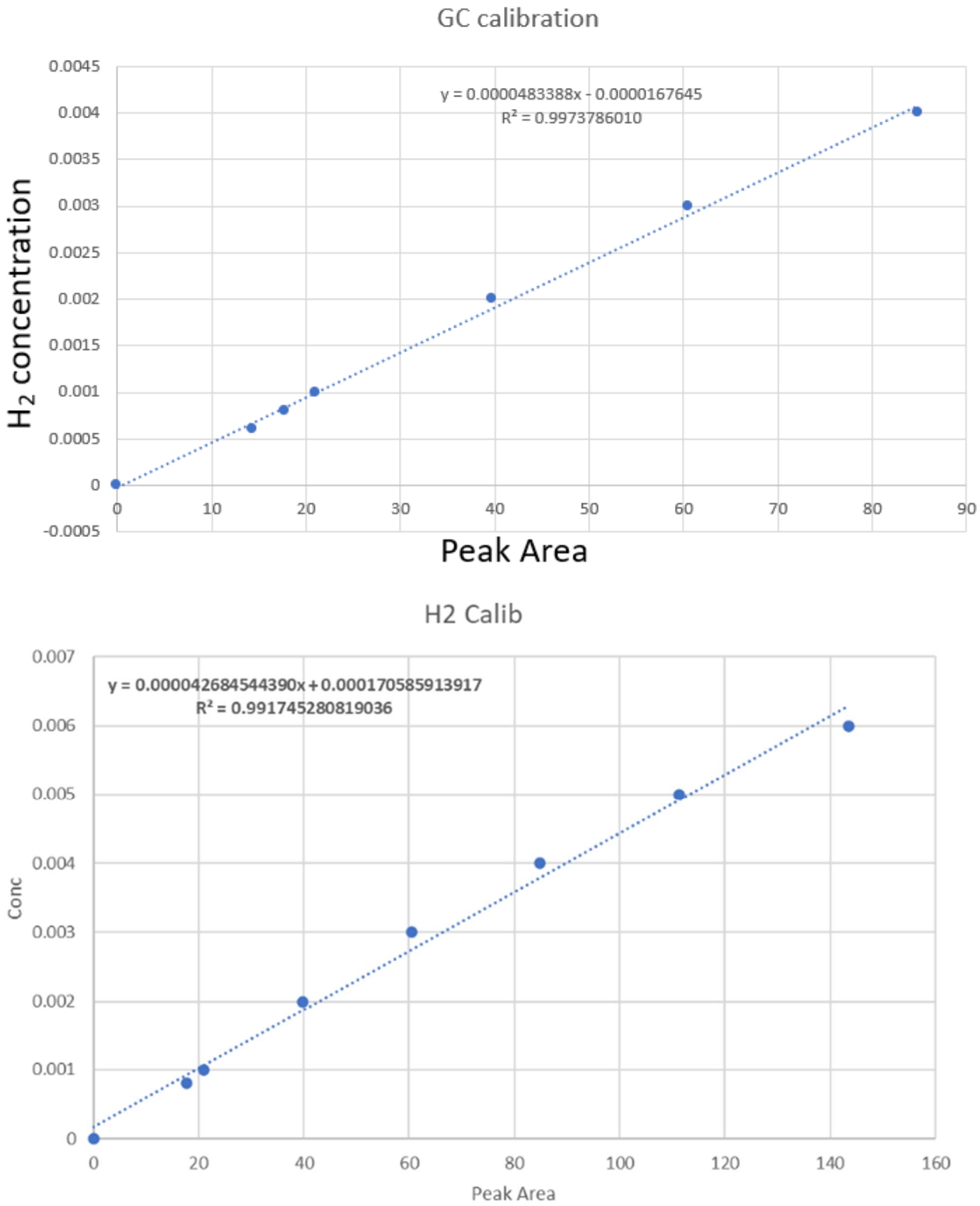

Figure 43. Calibration curves for the molecular hydrogen obtained from the GC-TCD.

2.3.7.1.2. Specific Reaction Conditions

2.3.7.1.2.1. Light Source Information

- Simulated sunlight source (Oriel® MiniSol model LHS-7320 Class ABA LED-based solar simulation, Newport, USA).
- The focused intensity of the light on the solution was 100 mW cm^{-2} (1 Sun simulated sunlight).
- Irradiation area: 50x50 mm

Ideal Spectral Match Defined by IEC 60904-9

Spectral Range (nm)	Total Irradiance Range	Ideal Percentage
400-500	13.8-23.0	18.4%
500-600	14.9-24.9	19.9%
600-700	13.8-23.0	18.4%
700-800	11.2-18.6	14.9%
800-900	9.4-15.6	12.5%
900-1100	11.9-19.9	15.9%

Figure 44. Ideal spectral match defined by IEC 60904-9 of LHS-7320 simulated sunlight.

MODEL LSH-7320 SOLAR SIMULATOR SPECIFICATIONS[1]

Illumination Area	2 inches x 2 inches (50 mm x 50 mm)
Maximum Power Output	110 mW/cm² (1.1 SUN)
Variable Output Control Wavelength	0.1 to 1.1 SUN
Range	400nm - 1100nm
Temporal Stability	A - IEC 60904-9 2007, JIS 8904-9 2017
Uniformity	B - IEC 60904-9 2007, JIS 8904-9 2017
Spectral Match	A - IEC 60904-9 2007, JIS 8904-9 2017
Nominal Working Distance	12.0 inches +/- 0.5 inch; 304 +/- 12mm
Alignment	Laser diode based optical alignment
Z Axis Head Adjustment from Base	7.5 inches - 17.75 inches (190 mm - 450 mm)
Head Rotation2	0 - 360º
Remote Interface	USB 2.0 (B-Type) or BNC TTL for ON/OFF
TTL Turn On/Off Transition Time	10ms
Weight	
Head (on vertical assembly stand)	9.3 lbs (4.2 kg)
Stand	9.0 lbs (4.1 kg)
Power Supply	1.8 lbs (0.8 kg)
Dimensions	
Height (on vertical assembly stand)	15.25 - 25.5 inches (387 - 648 mm)
Width	7.15 inches (184 mm)
Depth	14.0 inches (362 mm)
Operating Temperature Range	5ºC to 40ºC
Storage Temperature Range	-40ºC to 70ºC
Humidity	<85%, relative, non-condensing
Compliance	CE, RoHS
Power Requirements	100-240 VAC, 47-63 Hz, 2.8A max

NOTES: 1) Class A per IEC 60904-9 (2007) Section 5.4.2
2) Indents on mounting plate at 0º, 90º, 180º, and 270º orientations

Figure 45. LHS-7320 solar simulator specifications.

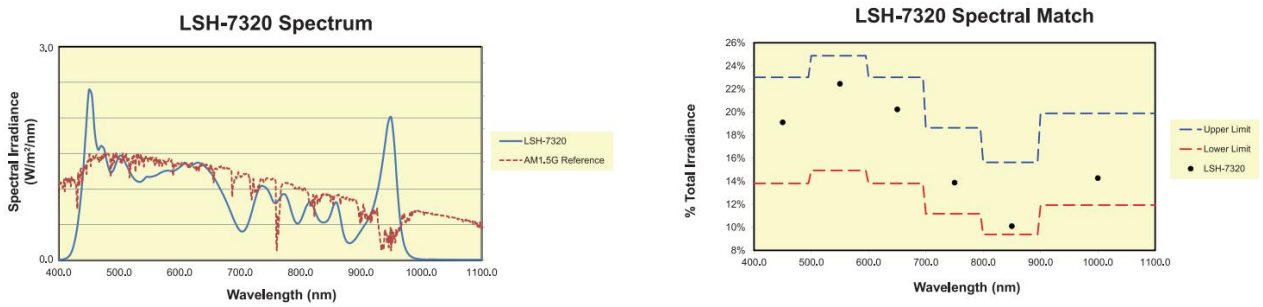

Figure 46. LHS-7320 spectrum and LHS-7320 spectral match.

2.3.7.1.2.2. Reactor

The quartz flask reactor (300 mL, diameter: 70 mm, and height: 80 mm) with a round water jacket for temperature control was used in all assessment photocatalytic H_2 evolution performance. Initially, we used the glass flask reactor at the same dimension. For more accurate photocatalytic H_2 evolution, we purchased a new quartz flask reactor for optimization of the photocatalytic performance.

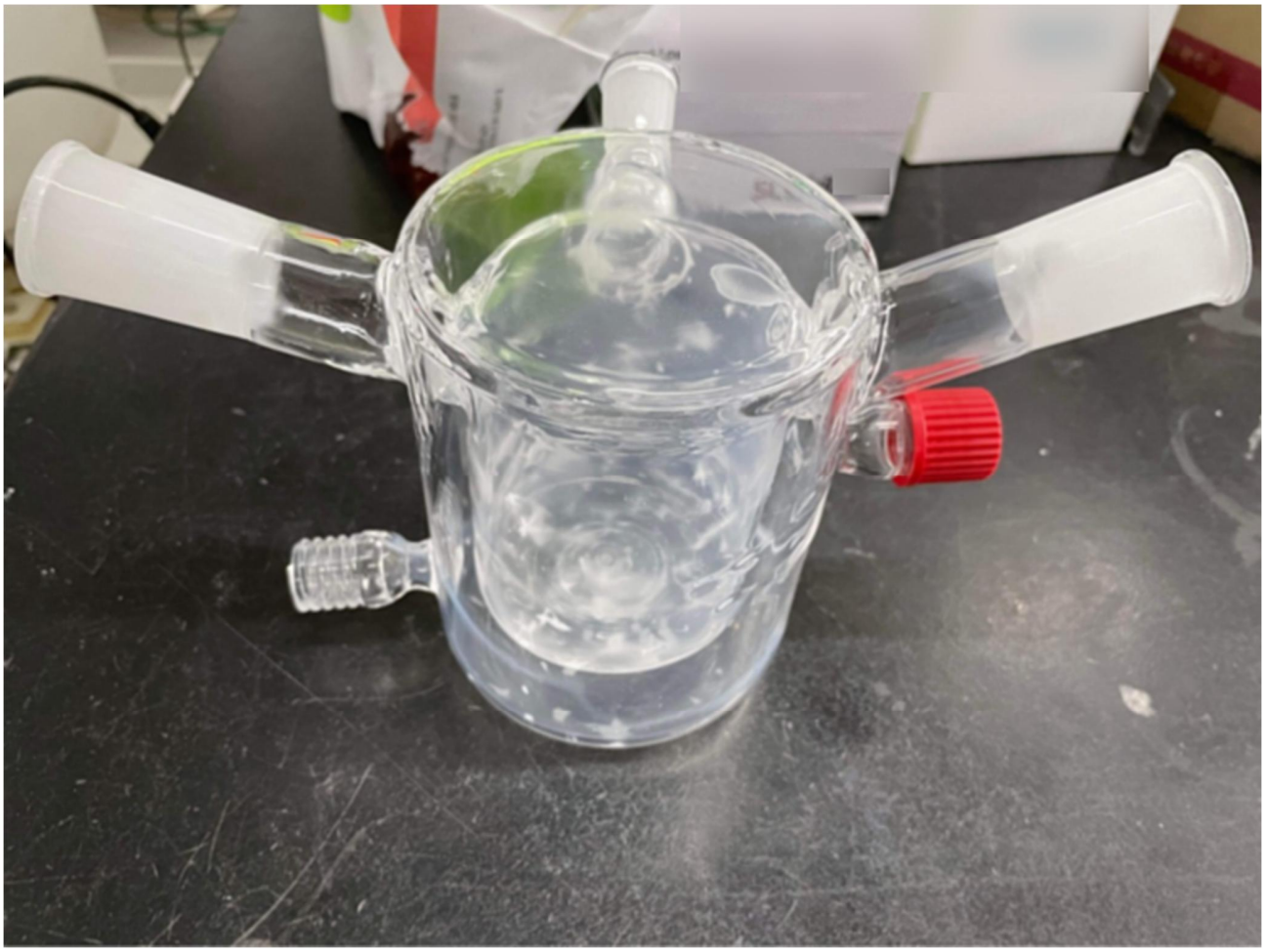

Figure 47. Quartz flask reactor (300 mL, diameter: 70 mm, and height: 80 mm), side view.

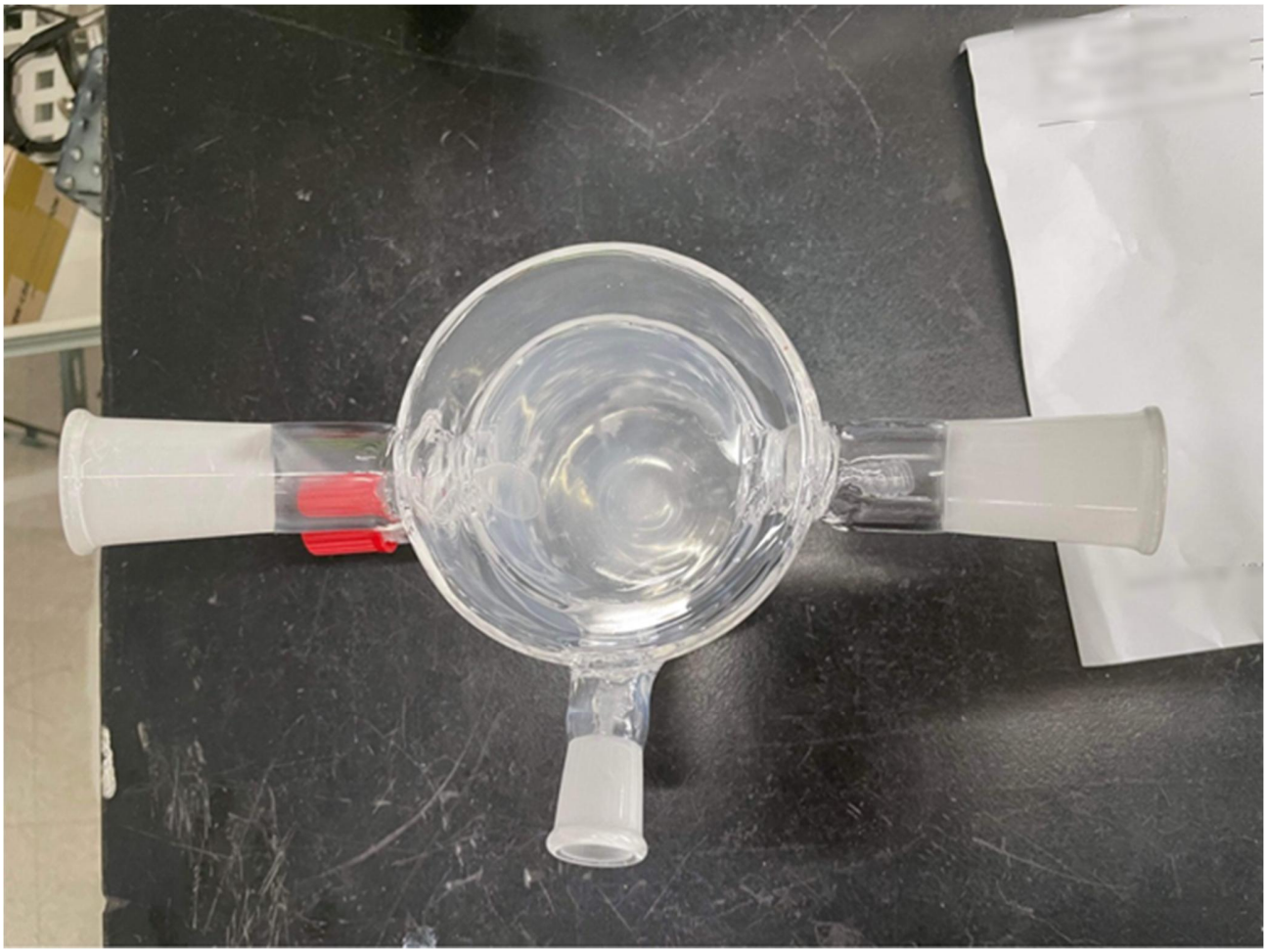

Figure 48. Quartz flask reactor (300 mL, diameter: 70 mm, and height: 80 mm), top view.

2.3.7.1.2.3. Online GC Gas Measurement Method

The evolved H_2 gas was measured via an automatic injection, online gas chromatography with a thermal conductive detector (TCD), and a brand new Carboxen 1000 column (Sigma-Aldrich).

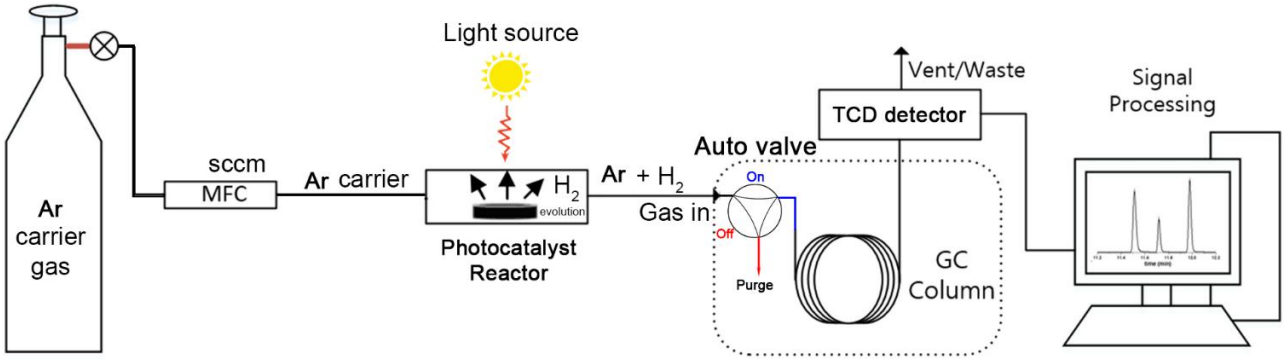

Figure 49. Online GC system for photocatalytic H_2 evolution measurement.

2.3.7.1.3. Reaction Media

2.3.7.1.3.1. Water Quality

The ultra-pure deionized water used for the experiments was supplied from Puris-Evo UP WATER SYSTEM, model Evo-UP Dio VF. The used water had a resistivity of 18.2 mΩ·cm at 25.2 °C, pH = 8.64.

Table 12. Water quality from Puris-Evo UP WATER SYSTEM.

Model	Evo-UP Dio VF
Flow Rate(Up to)	2.0
Product Quality	
· Resistivity(at 25°C) MΩ-cm	18.2
· TOC, ppb (μg/L)	<5
· Particles (0.2μm), EA/Mℓ	<1
· Bacteria, cfu/Mℓ	<1
· Endotoxin, EU/Mℓ	<0.001(*)
· Rnase, ng/Mℓ	<0.01(*)
· Dnase, pg/μℓ	<4(*)
· PH Sensor	

2.3.1.2.5. Sacrificial agent

Triethanolamine (TEOA, Sigma-Aldrich) was used as a sacrificial agent for photocatalytic H_2 evolution measurement. The concetration of TEOA was 10 % vol/vol, the pH value of TEOA and final reaction media were 10.99 and 10.01 ± 0.8, respectively.

2.3.7.1.3.2. Photosentisizer

Eosin Y was added as a photosensitizer with a mass ratio of 1:1 to the catalyst. The amount of photosentisizer was optimized to supply excess amount for the reaction. The pH value of reaction media was 10.01 ± 0.8 after adding Eosin Y.

2.3.7.1.3.3. Temperature

The reaction temperature was maintained at $22.0 \pm 0.5\,^{o}C$ via water jacket system of the reactor.

2.3.7.1.4. Optimization H_2 Production Rate

The benchmark of photocatalytic activity toward hydrogen evolution of as-prepared samples was optimized based on observing the dependence of H_2 production amounts vs. photocatalyst concentrations. All indicators were fixed except to change the photocatalyst mass for making the photocatalyst concentrations in a range of 0.0125 to 0.5 $mg.mL^{-1}$.

Photocatalytic H_2 evolution under visible-light irradiation in a quartz flask reactor (300 mL, diameter: 70 mm, and height: 80 mm) was implemented by a simulated sunlight source (Oriel® MiniSol model LHS-7320 Class ABA LED-based solar simulation, Newport, USA). The focused intensity of the light on the solution was 100 mW cm^{-2} (1 Sun). The amount of synthesized photocatalysts (calculated x mg in 100 mL ultra-pure DI water) was added to the quartz reactor, followed by adding Eosin Y as a photosensitizer. Then sonication was applied for 30 min at RT to form a homogeneous solution. Afterward, a high-purity flow of argon gas was blown through the system for 30 min to remove other impurity gases. Finally, 20 mL of TEOA solution was added to the reactor as a sacrificial reagent, and the system was purged with high-purity argon for 30 min to wipe out the air in the reactor. The evolved H_2 gas was measured via an automatic injection, online gas chromatography with a thermal conductive detector (TCD), and a Carboxen 1000 column (Sigma-Aldrich).

2.3.7.2. Photocatalytic Performance

Photocatalytic activity toward hydrogen evolution measurement was optimized to assess the photocatalytic performance of the solvothermal modified g-C_3N_4 materials. The evaluation system

and assessment method were considered for more accurate and transparent photocatalyst performance, which enables the comparison of different photocatalytic hydrogen evolution systems.[106-108] The detailed method is shown in the above section, which includes the specified reaction conditions, photocatalyst concentration at the stationary point, optimized H_2 production rate, apparent quantum yield (AQY) calculation, turnover frequency H_2 evolution (TOF) calculation, and equipment calibration. Under 1 Sun illumination of a Solar Simulator, the average H_2 evolution rates at the stationary point of C_3N_4-bulk, C_3N_4-IPA, C_3N_4-DMF, C_3N_4-MA, and C_3N_4-THF was as high as at 2242.8, 10999.1, 12531.1, 16595.6, and 31256.9 μmol h^{-1} g^{-1}, respectively (Figure 50, Figure 51, Figure 52). The stationary points of C_3N_4-THF, C_3N_4-DMF samples were obtained at 0.1 mg.mL^{-1}. These samples had a similar lateral size, where C_3N_4-THF, C_3N_4-DMF maintained the layer's size after the solvothermal reaction (Figure 22, Figure 24). While the highly etched C_3N_4-IPA, and smallest lateral size C_3N_4-MA sample achieved the stationary point at a lower concentration of 0.05, and 0.025 mg.mL^{-1}, respectively. The C_3N_4-bulk sample, which had the largest lateral size and highest agglomeration, obtained the stationary point at 0.2 mg.mL^{-1}. Notably, the photocatalyst performance at the stationary points had an inverse relation with the lateral size of nanosheets.

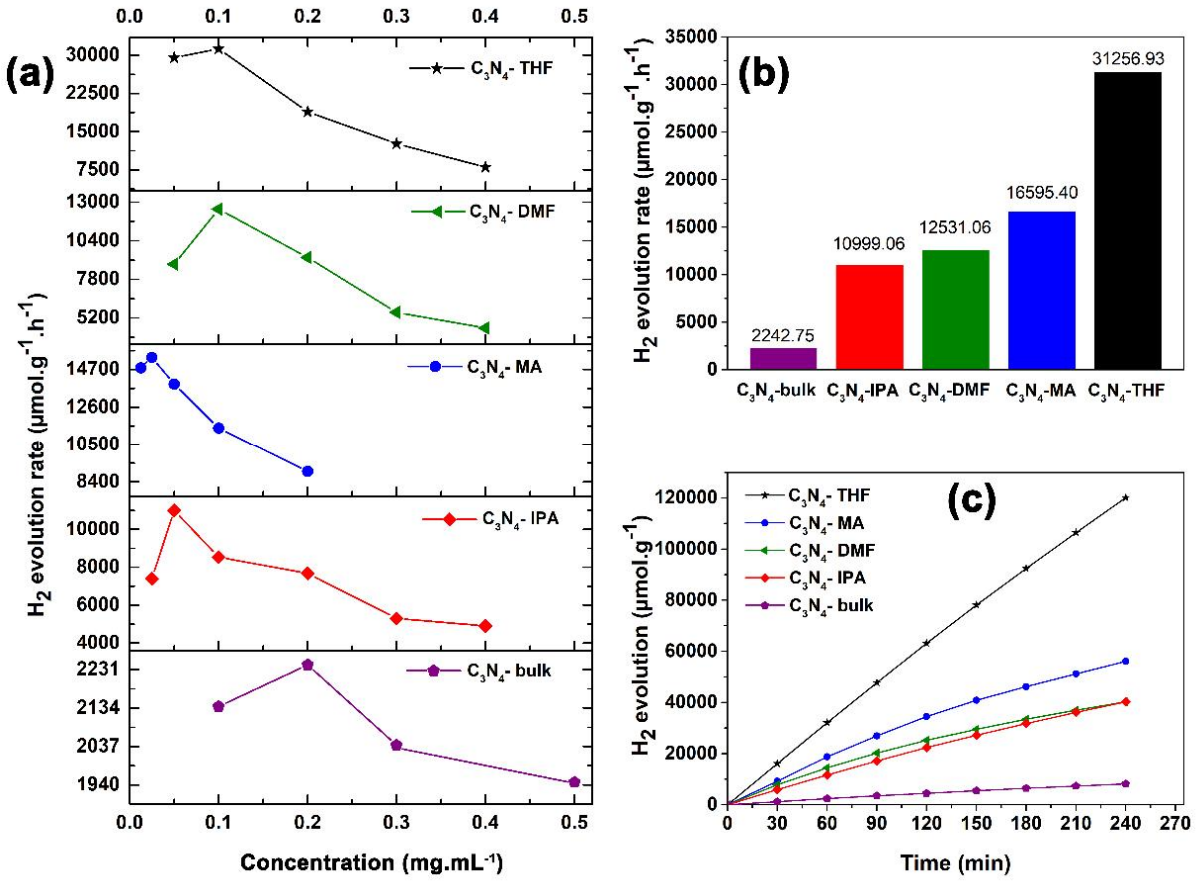

Figure 50. a) Dependence of amount of H_2 evolution rate on photocatalyst concentration for C_3N_4-bulk, C_3N_4-IPA, C_3N_4-DMF, C_3N_4-MA, and C_3N_4-THF. b) Averaged H_2 evolution rate at the stationary points of the corresponding photocatalyst. c) Amount of H_2 produced vs. reaction time of C_3N_4-bulk, C_3N_4-IPA, C_3N_4-DMF, C_3N_4-MA, and C_3N_4-THF at the stationary points.

Remarkably, the holey-defect C_3N_4-THF sample performed a superior H_2 evolution rate, which is 13.9, 2.8, 2.5, and 1.9 times higher than those of C_3N_4-bulk, C_3N_4-IPA, C_3N_4-DMF, C_3N_4-MA samples, respectively. For comparison, the superior H_2 evolution performance of solvothermal modified g-C_3N_4 catalysts and recent various g-C_3N_4-based materials in the literature are listed in Table 13. The 2D holey structured C_3N_4-THF achieved high performance of H_2 evolution among all recently reported g-C_3N_4-based photocatalysts.

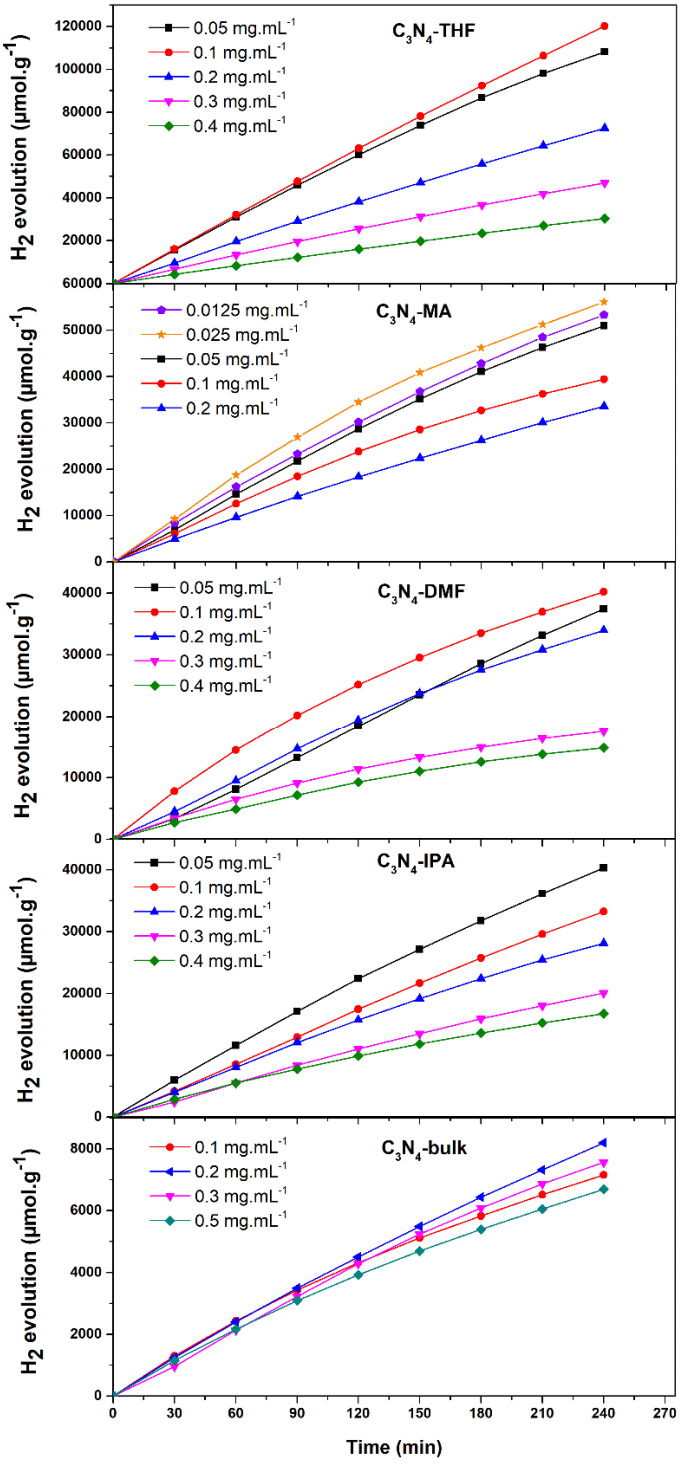

Figure 51. Optimization photocatalytic activity toward H_2 evolution of C_3N_4-bulk, C_3N_4-IPA, C_3N_4-DMF, C_3N_4-MA, and C_3N_4-THF.

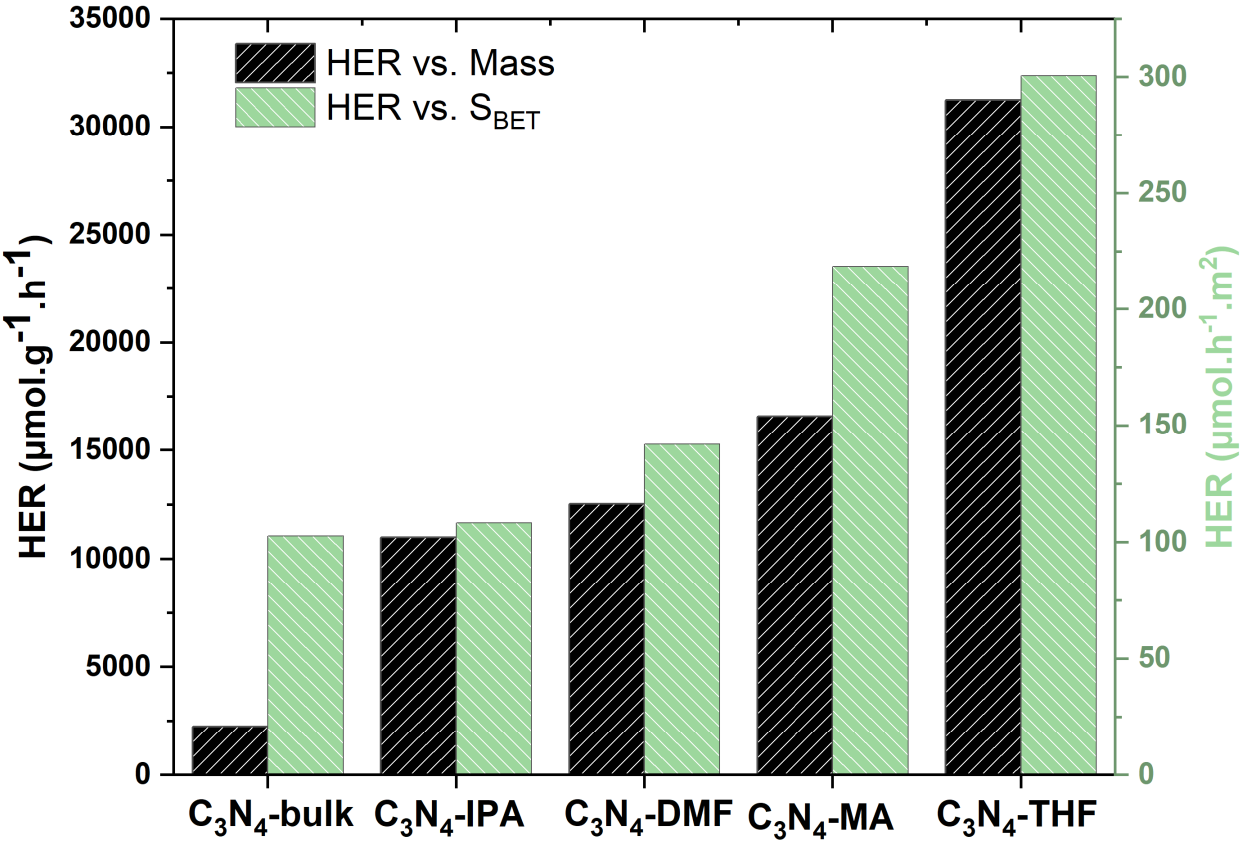

Figure 52. Photocatalytic hydrogen evolution rate (HER) of as-prepared samples: HER versus mass and surface area.

Table 13. Comparison of photocatalytic activity toward H_2 evolution of the reported g-C_3N_4 and its composites.

Materials	Co-catalyst	Sacrificial donor	Light source	Light Intensity (mW cm^{-2})	Hydrogen evolution rate (μmol h^{-1} g^{-1})
C_3N_4-THF This work	Pt, 2.3 wt. %	TEOA	Simulated sunlight (Newport, LHS-7320)	100	31256.9
PCN/OMs**[109]**	Pt, 3%	TEOA	300 W Xe lamp (λ ≥ 420 nm)	NR	4630
Hollow C_3N_4 nanospheres**[110]**	Pt, 3 wt. %	TEOA	300 W Xe lamp (λ ≥ 400.5 nm)	49.4	4480
EY-mpg-C_3N_4**[111]**	Pt, 1 wt. %	TEOA	300 W Xe lamp (λ ≥ 420 nm)	NR	3850
$NiFe_2O_4$/mpg-CN**[112]**	None	TEOA	300 W Xe lamp (λ ≥ 420 nm)	NR	1820
EY-g-C_3N_4-T**[113]**	Pt, 7 wt. %	TEOA	450 W Xe short arc lamp (λ ≥ 420 nm)	NR	1500
Flower MoS_2/g-C_3N_4**[114]**	Pt, 2 wt. %	Methanol	300 W Xe lamp (Newport) (λ ≥ 420 nm)	100	867.6
Quasi-sphere g-C_3N_4**[91]**	Pt, 3 wt. %	TEOA	300 W Xe lamp (λ ≥ 420 nm)	NR	613.4
Holey CNS**[73]**	Pt, 3 wt. %	TEOA	300 W Xe lamp (λ ≥ 400 nm)	NR	2320
g-C_3N_4 nanosheets**[115]**	Pt, 3 wt. %	TEOA	300 W Xe lamp (λ ≥ 420 nm)	NR	1860
OH-CN3**[92]**	Pt, 1 wt. %	Lactic acids	300 W Xe lamp (λ ≥ 420 nm)	NR	320
P-doped g-C_3N_4**[116]**	Pt, 1 wt. %	TEOA	300 W Xenon arc lamp (λ > 400 nm)	NR	1596
g-C_3N_4					108
g-C_3N_4-$SrTiO_3$:Rh**[117]**		Methanol		NR	2233

g-C_3N_4	Pt, wt 0.5%		300 W Xenon arc lamp (λ > 415 nm)		107
Se/Modified g-C_3N_4**[118]**	Pt, wt 1%	TEOA	150 W Xenon arc lamp (λ > 455 nm)	NR	1500
g-C_3N_4					932
CdS/g-C_3N_4/CuS**[119]**	None	Na_2S/Na_2SO_3	350 W Xenon arc lamp (λ > 420 nm)	70	1151.2
CdS					211.6
Carbon fiber/gC_3N_4**[120]**	Pt, wt 1%	TEOA	350 W Xenon arc lamp (λ > 420 nm)	180	1080
g-C_3N_4					234.8
rGO/g-C_3N_4**[121]**	Pt, wt 1%	Lactic acid	LEDs (3 W, 420 nm)	80	874
g-C_3N_4					667
O-containing groups/Modified g-C_3N_4**[122]**	Pt, wt 1%	Lactic acid	LEDs (420 nm)	90	752
g-C_3N_4					108
g-C_3N_4 with remove surface defects**[123]**	Pt, wt 3%	TEOA	450 W Xe lamp (λ > 420 nm)	NR	455
g-C_3N_4					102
Graphene/gC_3N_4**[124]**	Pt, wt 1.5%	Methanol	300 W Xenon arc lamp (λ > 400 nm)	180	451
g-C_3N_4					147
Ag/Ag_2S/g-C_3N_4**[125]**	Ag/Ag_2S	Methanol	LEDs (3 W, 365 nm)	80	500
g-C_3N_4					2
MWCNT/g-C_3N_4**[126]**	None	Methanol	300 W Xenon arc lamp (λ > 395 nm)	209	44
C-dots/g-C_3N_4/Ti**O_2**[127]	None	TEOA	350 W Xenon arc lamp	70	210
g-C_3N_4/Ti**O_2**					40
$Ni(OH)_2$-g-C_3N_4**[128]**	None	TEOA	350 W Xenon arc lamp (λ > 400 nm)	180	152
g-C_3N_4/0D-ZnO**[129]**	Pt, wt 1%	TEOA	300 W Xenon arc lamp (λ > 420 nm)	NR	322
g-C_3N_4					65
g-C_3N_4/SiC**[130]**	Pt, wt 1%	TEOA	300 W Xenon arc lamp (λ > 420 nm)	NR	182
g-C_3N_4					108

2.3.7.3. The AQY at The Stationary Point of C_3N_4-THF Calculation

The AQY is calculated by equation:

$$\mathrm{AQY}(\%) = \frac{\text{number of reacted electrons}}{\text{number of incident photons}} \times 100$$
$$= \frac{\text{number of evolved hydrogen molecules} \times 2}{\text{number of incident photons}} \times 100$$

The energy of one photon (E_{photon}) with wavelength of $\lambda_{inc}(\mathrm{nm})$ is calculated using the following equation:

$$E_{\text{photon}} = \frac{hc}{\lambda_{\text{inc}}}$$

The total energy of the incident monochromatic light (E_{total}) is calculated using the equation:

$$E_{total} = PSt$$

$$\text{Number of incident photons} = \frac{E_{\text{total}}}{E_{\text{photon}}} = \frac{PS\lambda_{\text{inc}}t}{hc}$$

Finally, the apprarent quantum yield is calculated as:

$$\mathrm{AQY}\ (\%) = \frac{2n_{H_2}N_{\mathrm{A}}hc}{PS\lambda_{inc}t} \times 100$$

Where $n_{\mathrm{H}_2,t}(\mathrm{mol})$ is the amount of H_2 evolved over the duration t of the incident light irradiation,

N_{A} (mol^{-1})is Avogadro's constant,

h (J.s) is Planck's constant,

c ($\mathrm{m.s}^{-1}$) is the speed of light,

P ($\mathrm{W.m}^{-2}$) is the power density of the incident monochromatic light,

$\lambda_{\mathrm{inc}}(\mathrm{m})$ is the wavelength of the monochromatic light,

t (s) is the duration of the incident light irradiation.

The average power density of the incident monochromatic light, using Bandpass 420 nm filter is measured as:

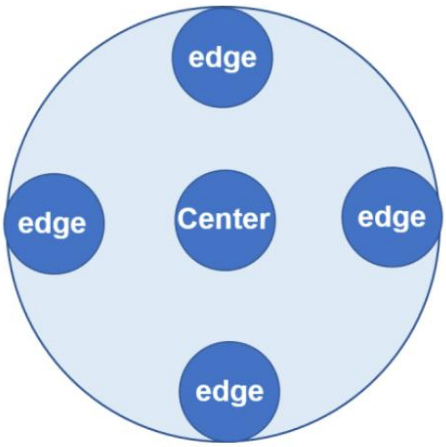

The schematic diagram of the test points for circle spots.

Calculation method:

$$\bar{E} = \frac{\overline{E_{center}}}{3} + 2\frac{\overline{E_{edge}}}{3}$$

$\overline{E_{center}}$: *the light intensity of the center of the spot*, W/m^2

$\overline{E_{edge}}$: *the light intensity of the edge of the spot*, W/m^2

The 843-R Power Meter and Thermopile Sensor (3 W, 10 mm, 0.19-11 μm Newport, MODEL: 919P-003-10, sensor size: Ø9.5 mm, detector active area of 0.71 cm^2) is used to evaluate the power density. The average power density is 1.09 $mW.cm^{-2}$. The circle irradiation area is 19.63 cm^2.

$$\text{A.Q.Y.}(\%) = \frac{2n_{H_2,t}N_A hc}{PS\lambda_{inc}t} \text{ x } 100$$

$$\text{A.Q.Y.}(\%) = \frac{2\text{x}90.58\text{x}10^{-6}(\text{mol})\text{x}6.02214076\text{x}10^{23}(\text{mol}^{-1})\text{x}6.62607015\text{x}10^{-34}(\text{J.s})\text{x}299{,}792{,}458(\text{m.s}^{-1})}{10.90(\text{W.m}^{-2})\text{x}0.001963\text{m}^2\text{x}420\text{x}10^{-9}(\text{m})\text{x}3600(\text{s})}$$

$$\text{A.Q.Y.}(\%) = 66.97\%$$

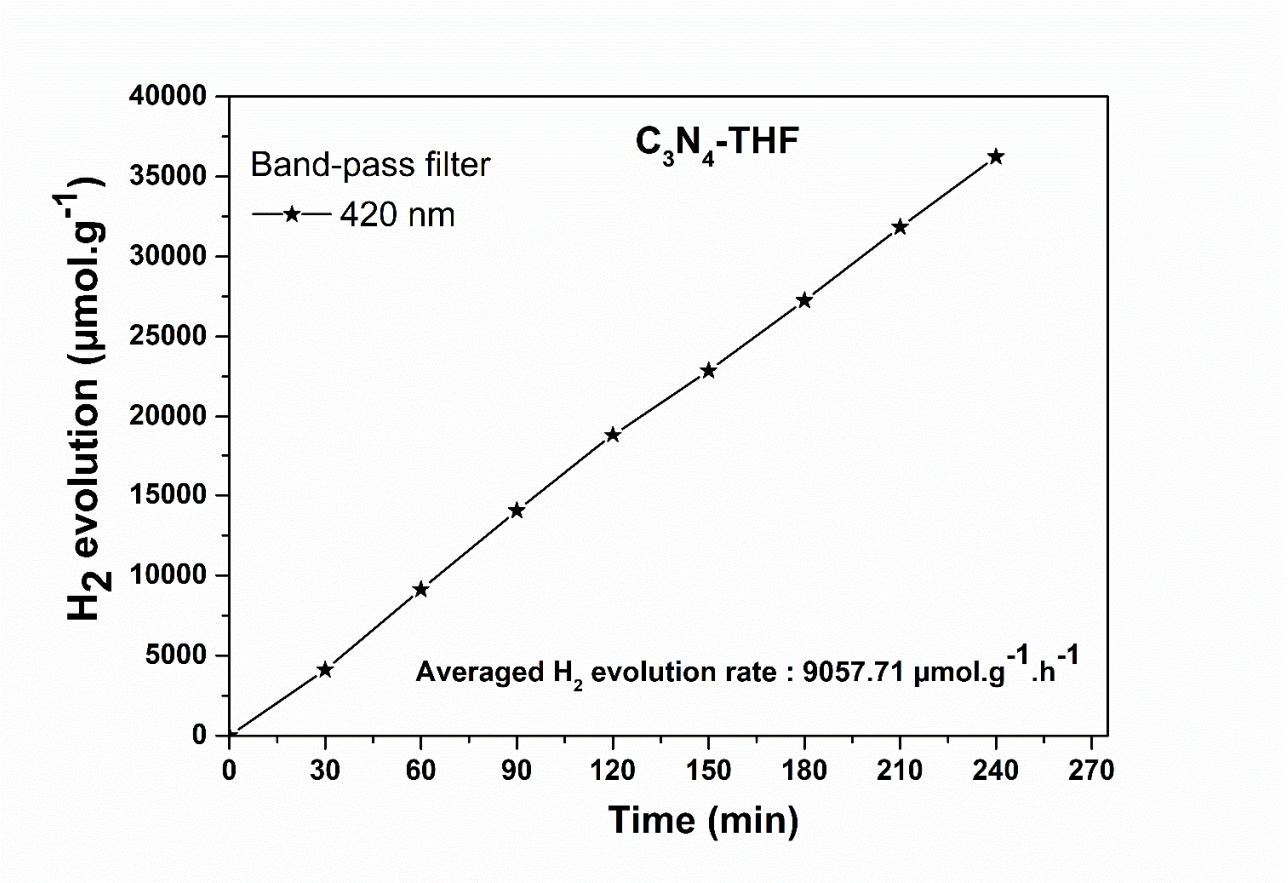

Figure 53. H_2 evolution of C_3N_4-THF at the stationary point (0.1 mg.mL^{-1}), using 420 nm bandpass filter (Newport 20BPF10-420 Bandpass Filter, 50.8x50.8 mm, 420±2 nm Center, 10±2 nm FWHM).

Turnover Number (TON), Turnover Frequency (TOF) Calculations

A summary of the data of all prepared samples is shown in Table 14. The actual Pt nanoparticles was shown in Table 5. The photocatalytic hydrogen evolution efficiency was acquired in the case of using 10 mg photocatalyst, and the actual Pt amount was determined by ICP-EOS.

The turnover number (TON) is calculated by using the following equation:

$$\text{TON} = \frac{\text{Number of moles of evolved } H_2}{\text{Number of moles of platinum on photocatalyst}}$$

The turnover frequency (TOF) is calculated by the equation:

$$TOF = \frac{TON}{t}$$

Whereas t is reaction time (h)

Table 14. Turnover Number (TON), Turnover Frequency (TOF) calculations for C_3N_4-IPA, C_3N_4-DMF, C_3N_4-MA, and C_3N_4-THF.

Sample	**H_2 Evolved (µmol)**	**Pt (%)**	**Pt (mol)**	**TON (4 h)**	**TOF**
C_3N_4-IPA	332.8591872	2.2925	0.000001175134814	283.2519157	70.81297892
C_3N_4-DMF	402.2190902	2.3527	0.000001205993316	333.5168487	83.37921217
C_3N_4-MA	394.0274799	1.8641	0.000000955537102	412.3623029	103.0905757
C_3N_4-THF	1201.349829	2.2858	0.000001171700396	1025.30462	256.3261549

Platinum Hydrogenation and Oxygenation Preparation

The hydrogenated C_3N_4-THF sample was prepared by hydrogen reduction of C_3N_4-THF in H_2 atmosphere for 12 h at 200 °C to obtain purely metallic Pt. In contrast, the oxygenated C_3N_4-THF sample was synthesized by oxidation of C_3N_4-THF in air for 12 h at 200 °C to achieve PtO sites in the product. Finally, as-prepared samples were applied to the photocatalytic H_2 evolution test at the stationary point (0.1 $mg.mL^{-1}$).

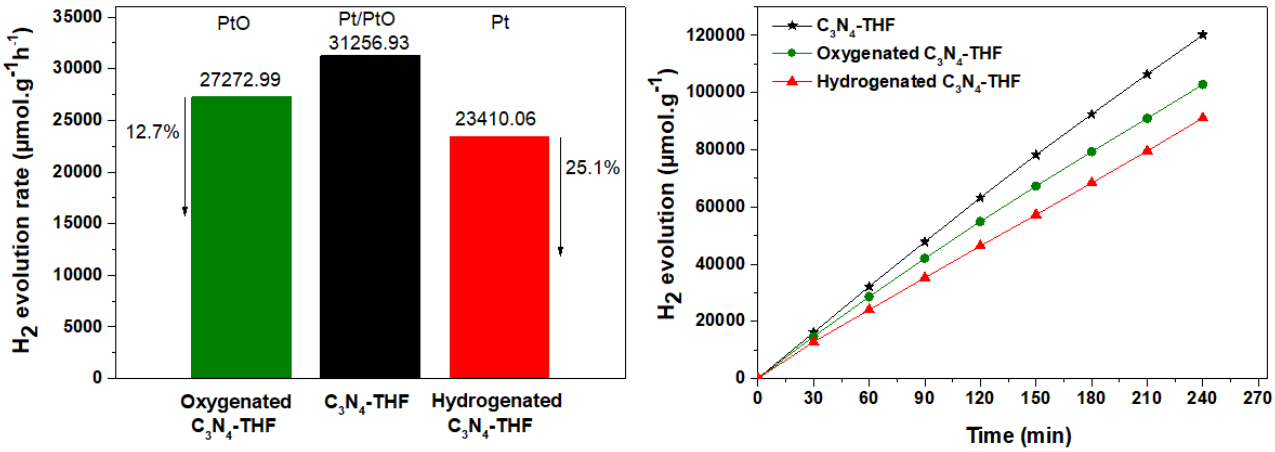

Figure 54. Photocatalytic H_2 evolution at the stationary point of C_3N_4-THF, oxygenated C_3N_4-THF, and hydrogenated C_3N_4-THF.

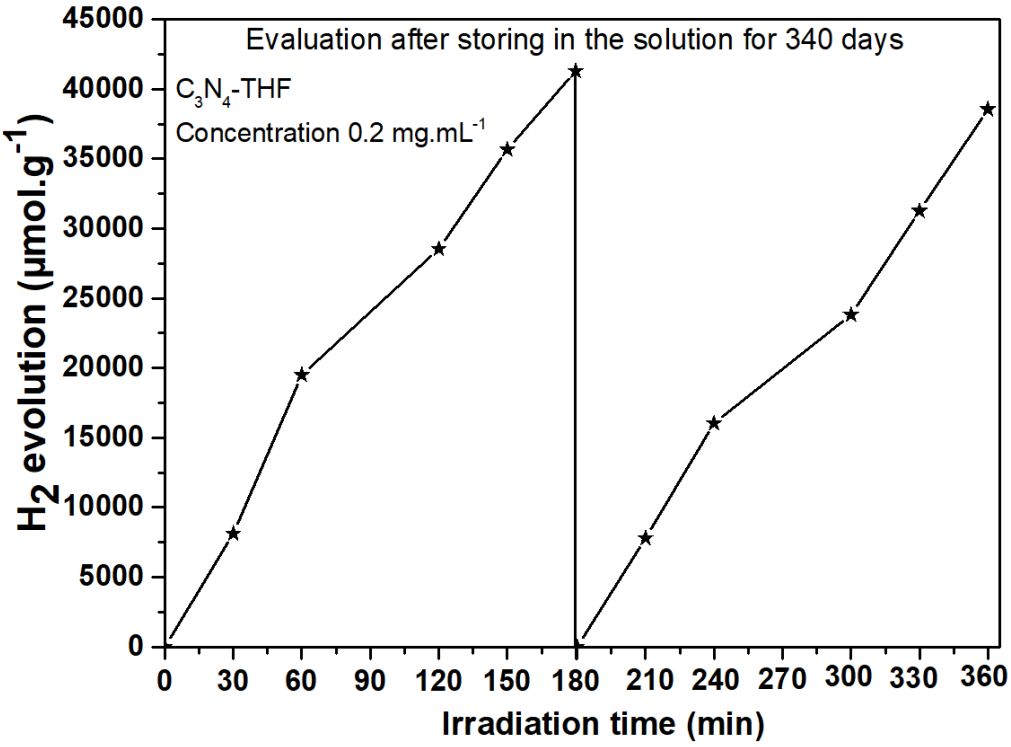

Figure 55. Photocatalytic H_2 evolution stability estimation of C_3N_4-THF. The first test of 3 h reaction was obtained on 08/2021. The product was stored in the solution for 340 days before the second test.

2.3.8. Photocatalytic Parameters and Mechanism

We proceeded to study the main factors that contributed to photocatalytic performance based on the above results, including oxygen doping; self-assembled graphene formation; platinum co-catalyst oxidation states; nanostructure of the resultant catalysts; electronic band structure; and holey-defects creation. Oxygen doping promotes the photocatalytic performance of g-C_3N_4.[17, 37, 92] The results in Table 4 (O_2/O_{total}) show that after solvothermal treatment of the C_3N_4-bulk, the oxygen content of the samples in the form of doping increased, which demonstrated that oxygen doping improved the photoactivity in solvothermal treated samples compared to bulk sample. Comparing the values of (O_2/O_{total}) for solvothermal treated samples does not give us a particular trend that can explain the different photocatalytic activity among them. A second parameter that can improve the photocatalytic activity of C_3N_4-bulk after solvothermal treatment is graphene formation, which occurred in all four different organic solvents at different weight percent values. Graphene formation contributed to local active sites as photoelectron mediator and acceptor, which boost electron charge carrier separation and transport, preventing electron

recombination in all solvothermal treated samples.[105] A co-catalyst (Pt) would be a leading factor whenever the catalyst had identical properties, but different structures of g-C_3N_4 were deposited with Pt species. Another parameter that should be considered is accessible active surface area. The exfoliation process of bulk g-C_3N_4 via solvothermal treatment to achieve the 2D monolayer g-C_3N_4 in reaction media was the key to maximize accessible surface active sites of the resultant catalysts. Based on the theoretical surface area of fully exposed 2D material sheets, the g-C_3N_4 monolayer dispersed in water could fabricate a liquid crystalline g-C_3N_4 dispersion that reaches the maximum surface area in reaction media value. All of the reasons mentioned above together contribute to boosting the activity of solvothermal treated g-C_3N_4 compared to the bulk material.

The questions then are, what is the main reason for the photoactivity differences among the solvothermal treated samples and how does solvothermal treatment in different organic solvents alter photoactivity so significantly?

Based on the basic rules for photocatalysis, the efficiency of a photocatalyst is determined by the synergistic effects of three basic steps of photocatalysis, (i) light absorption, (ii) charge separation, and (iii) surface transfer of photogenerated charge carriers. Here, we attempt to clarify the different photoactivities of the samples based on these three basic rules.

The photocatalytic activity of C_3N_4-THF toward H_2 evolution achieved the highest value among the samples (Figure 50). In the case of C_3N_4-THF, the introduction of a uniform holey structure and nitrogen-deficient framework not only extends the visible light absorption range but also suppresses radiative electron-hole recombination as demonstrated by PL results, whose origin is the increased low-energy photon excitations and band-to-tail charge transfer processes induced by the increased mid-gap states close to the band edges. These factors favor the proceeding of photocatalysis reactions. In addition to these electronic structure-induced favorable features, the presence of uniform holey defects combined with nitrogen deficiency assisted with the existence of dangling bonds in the layer structure play an important role in geometrically shortening the diffusion lengths of both the photoexcited electrons from the interior to edges of the layers and reactants from the surface to the interior of a particle along with the interlayer galleries. This structure also favors the photocatalysis reaction by lowering the bulk recombination probability of electrons and holes, and also promoting mass transport. While, in the case of C_3N_4-MA, just a decrease in charge carrier recombination participates in increasing photoactivity. Compared to

C_3N_4-THF, here light absorption did not show any enhancement and no mid-gap states produced. Although the formation of small nanosheets will increase edge sites for the reduction process and decrease charge diffusion length for electrons to catch the reactants. The formation of small nanosheets compared to larger ones in C_3N_4-DMF increases the charge transport rate along with the layer, as clearly shown in PL spectra, with the lower recombination obtained in C_3N_4-MA. A strange phenomenon occurred for C_3N_4-IPA which has a lower bandgap, lower recombination rate than C_3N_4-DMF, and also has hole-defects in the structure. However, C_3N_4-IPA had the worst photocatalytic activity among all solvothermal treated samples. Although holey-defects appear on the nanosheets, in some parts a grid like structure also exists in C_3N_4-IPA. This kind of grid formation can damage the π-conjugated structure, resulting in decreased photoactivity. The original UV-Vis spectra (Figure 56a) of the samples in solution form show the intensity of absorption in the π-π* and n-π* transition area for the (band-band transition) for C_3N_4-IPA is the lowest. Following this data, the π-π*/C_{total} ratio calculated from the XPS C1s core level spectra (Table 4) gave the lowest value for C_3N_4-IPA. Both results confirm that IPA disrupts the π-conjugated structure in some parts of the nanosheet, which sharply reduces photocatalytic activity.

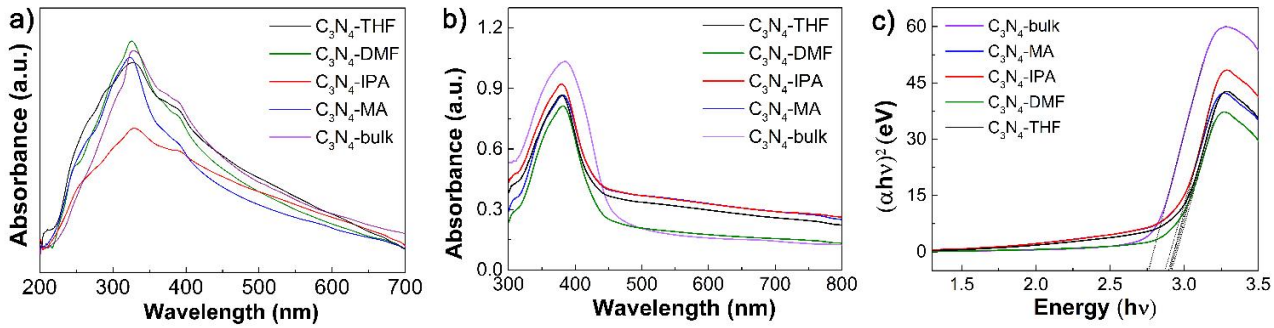

Figure 56. (a) UV-Vis of all samples, (b) UV-DRS of powder samples, and (c) corresponding Tauc plots of E(eV) and $(\alpha h\nu)^2$ for all prepared samples.

PtO and metallic Pt nanoparticles play critical roles as active sites for H_2 evolution on the host photocatalyst surface. In a previous study, we demonstrated that Pt^{2+} sites (in PtO) on g-C_3N_4 improved the hydrogen evolution rate by their favorable water adsorption along with hydrogen intermediates desorption and prevented the irreversible hydrogen evolution.[41] The C_3N_4-IPA showed higher than C_3N_4-DMF in optical properties, specific surface area, and charge transfer. However, its photocatalytic H_2 evolution rate is lower than C_3N_4-DMF (Figure 50b) because the C_3N_4-DMF sample formed a higher proportion of Pt^{2+} sites, and C_3N_4-IPA achieved only metallic

Pt sites (Pt^0) (Figure 19a). The C_3N_4-THF sample, which had the highest H_2 evolution rate, obtained both Pt^0 and Pt^{2+} oxidation states, suggesting a composite of Pt and PtO could play a key in photocatalytic H_2 evolution enhancement. The average number of H_2 evolution occurred on Pt-based sites per hour (TOF) of C_3N_4-THF is 3.62, 3.07, and 2.49 times higher than C_3N_4-IPA, C_3N_4-DMF, and C_3N_4-MA, respectively (Table 14). This result confirmed the effectiveness of H_2 evolution on Pt^0/Pt^{2+} sites of C_3N_4-THF in compared to C_3N_4-IPA (only Pt^0), C_3N_4-DMF (only Pt^{2+}), and C_3N_4-MA (only Pt^{2+}). The C_3N_4-THF was further treated with hydrogen and air to obtain purely metallic Pt site (Pt^0) and Pt^{2+} sites, respectively, described in Section 3.6, Supporting Information. As a result, the average H_2 evolution rates at the stationary point of C_3N_4-THF, oxygenated C_3N_4-THF, and hydrogenated C_3N_4-THF were 31256.93, 27272.99, and 23410.06 $\mu mol\ h^{-1}\ g^{-1}$, respectively (Figure 54). The photocatalytic H_2 evolution of oxygenated C_3N_4-THF, and hydrogenated C_3N_4-THF were reduced by 12.7% and 25.1% compared to C_3N_4-THF, respectively. The results of this experiment were consistent with the previous report.[131] They provided information for further research, such as optimizing the ratio of Pt/PtO co-catalyst on photocatalysts for enhanced H_2 evolution.

The highly H_2 evolution performance of as-prepared g-C_3N_4 photocatalysts also exhibits good stability. The storage of the photocatalysts in the air for over eleven months has shown no detectable change in their structure and optical properties. Furthermore, the C_3N_4-THF's photocatalytic activity can be well retained even after keeping the sample in the solution for 340 days, as shown in Figure 55.

The mechanism of the photocatalytic activity process for H_2 evolution is illustrated in Figure 57. Under simulated sunlight irradiation, the solvothermal modified g-C_3N_4 samples (Figure 57c, d, e) and EY (Figure 57a, b) absorb photons that supply energy higher or equal to the intrinsic bandgap of them. Next, the electrons are excited and transfer from the valence band to the conduction band and release positive holes in the valence band. At the same time, after adsorbing photons, EY reacts with TEOA to form EY^-, which transfers electrons to the conduction band of g-C_3N_4.[111] Subsequently, electrons move to the Pt co-catalyst particles (Figure 57b, d), or graphene layers on the surface of solvothermal g-C_3N_4 (Figure 57a, e), or g-C_3N_4 surface active sites (Figure 57c), where the H^+/H_2O is reduced to form H_2 molecules. Meanwhile, generated holes in the valence band can be oxidized and consumed by TEOA.

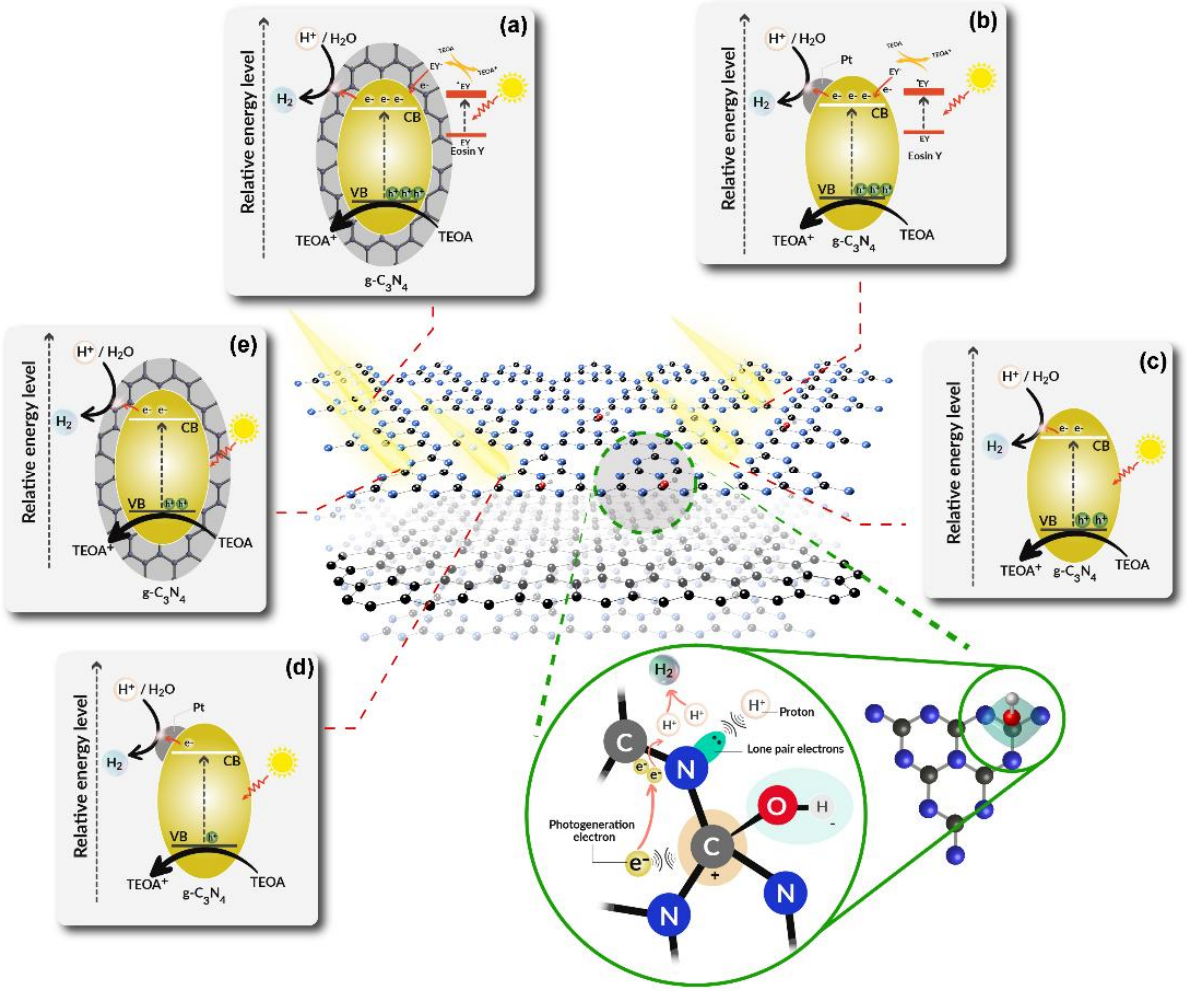

Figure 57. Schematic illustration of the photocatalytic mechanism for C_3N_4-THF under simulated sunlight irradiation.

2.4. Conclusions

Engineering holey-defects on 2D g-C_3N_4 nanosheets was successful accomplished by a facile solvothermal method in organic solvents. THF facilitates formation of a uniform holey structure of g-C_3N_4 but maintains the lateral size along with N vacancies in the heptazine units. The introduction of a uniform holey structure for C_3N_4-THF creates mid-gap states that reduces recombination centers for trapping charge carriers, shortens the charge diffusion length, enhances mass transfer, and increases charge separation. Pt oxidation states hold a important role of water adsorption and hydrogen intermediates desorption. It is found that the mixture of Pt/Pt^{2+} sites performs higher photocatalytic hydrogen evolution. As a result, holey-defect C_3N_4-THF achieved

superior photocatalytic H_2 evolution at the stationary point, which was 13.9, 2.8, 2.5, and 1.9 times higher than that of C_3N_4-bulk, C_3N_4-IPA, C_3N_4-DMF, and C_3N_4-MA, respectively. MA performs a strong etching effect that fragments the skeleton of the g-C_3N_4 layer into smaller size, while IPA produces an etching effect at the edges of g-C_3N_4 sheets but preserves the centered planar structure, resulting in an interesting sphere-like structure. DMF was found to be an excellent solvent for g-C_3N_4 exfoliation without creating a holey structured material. The newly observed phenomenon of self-assembled graphene creation via solvothermal treatment of g-C_3N_4 bulk was introduced, which contributed to photocatalytic performance due to the photoelectron mediator and acceptor role for graphene in the resultant samples. Through DFT calculations and experimental results, the mechanism of creating holey structures and N vacancies was proposed. Beside Hansen parameters, DFT adsorption energy calculation of used organic solvents on g-C_3N_4 sheets provided different behaviors of solvents for the solvolysis reaction of g-C_3N_4. The high production yield of g-C_3N_4 from DCDA and good stability of solvothermal modification of g-C_3N_4 made this method highly promising for mass production of sustainable photocatalyst for green hydrogen production.

CHAPTER 3

Overview of Chapter 3

This chapter presents the manuscript titled "Oxidized Platinum Cocatalyst and Self-Assembled Graphene over Graphitic Carbon Nitride for Photocatalytic Hydrogen Evolution", which was published in ACS Applied Nano Material Journal (ACS Appl. Nano Mater. 2023, 6, 11, 9825–9838).

Getting into green production process is the key for mass production of green hydrogen. Furthermore, the nanostructural design of graphitic carbon nitride (g-C_3N_4) plays a primary role in addressing the drawbacks posed by low surface area, which results in poor dispersion of accessible active sites in the reaction media of bare g-C_3N_4. Hence, we study the solid-state structure transformation through the solvothermal treatment of bulk g-C_3N_4 in an environmentally sustainable organic solvent. The grid-like structure of the monolayered g-C_3N_4 nanosheets was achieved using a facile solvothermal process. The formation of self-assembled graphene on g-C_3N_4 during the process facilitated charge transfer and separation on the photocatalyst, as confirmed by density functional theory calculations. The grid-like structure of the g-C_3N_4 contributed to the formation of a platinum oxide co-catalyst, while the formation of metallic platinum was observed in the bulk g-C_3N_4 sample. The platinum oxide co-catalyst enhanced the hydrogen evolution rate (HER) by inhibiting the reversible reaction pathway of hydrogen gas to protons. As a result, the platinum support on the grid-like structure of g-C_3N_4 and self-assembled graphene hybrid (hCN-G) achieve a photocatalytic H_2 evolution rate 7.5 times that of bulk g-C_3N_4 (CN-b). The hCN-G contained 2.04 wt.% graphene, which contributed significantly to the improvement in photocatalytic activity. The HER of hCN-G at the stationary point reached 16,832.9 µmol g^{-1} h^{-1} under 1 sun of simulated sunlight irradiation.

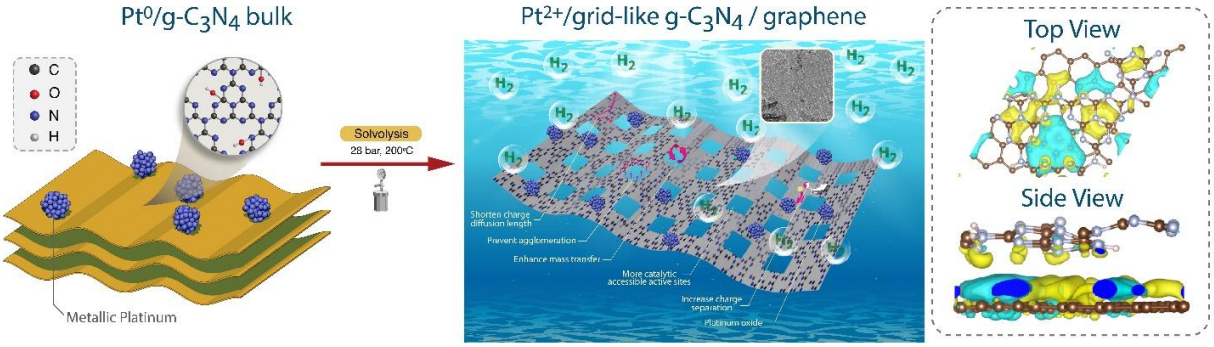

3. Oxidized Platinum Cocatalyst and Self-Assembled Graphene over Graphitic Carbon Nitride for Photocatalytic Hydrogen Evolution

3.1. Introduction

Among renewable energy sources, solar energy is considered the most favorable alternative energy source for fossil fuels, because it has the potential to exist for as long as civilization. The use of semiconductor materials in conjunction with hydrogen produced with solar power ("green" hydrogen) is a promising way to supply future generations with low-carbon energy. Polymeric graphitic carbon nitride (g-C_3N_4) is a merged organocatalyst and photocatalyst that has attracted considerable attention over the last decade as an effective medium-bandgap semiconductor for metal-free, visible-light-driven photocatalytic H_2 evolution due to its highly appropriate electronic band structure, high thermal and chemical stability, and potential for large-scale applications. Pristine g-C_3N_4 can be manufactured through pyrolysis of abundant precursors, such as cyanamide, dicyandiamide, melamine, thiourea, and urea.[20, 23, 28, 61, 63] However, pristine g-C_3N_4 has several drawbacks, including a low specific surface area,[66] a high electron-hole recombination rate, and poor electrical conductivity.[68]

The accessible surface active sites of g-C_3N_4 in the reaction media greatly influence photoactivity. Theoretically, two-dimensional (2D) graphene-like g-C_3N_4 is a promising material for numerous photocatalytic applications because of its large theoretical specific surface area in monolayer form. However, pristine g-C_3N_4 has a tendency to restack layers due to strong hydrogen bonds and van der Waals forces. In addition, the planar structure of pristine g-C_3N_4 sheets presents some drawbacks for photocatalytic H_2 evolution. For example, charge diffusion to the active site is long, mass transfer is low, and weak oxidizing and reducing active sites are often emerged on the basal plane. Creation of multiple holes in g-C_3N_4 nanosheets can significantly increase mass transport across the holes.[39, 132] Charge separation efficiency can also be improved by reducing charge diffusion length from the excited point to the nearest hole edge, instead of the sheet edge. Additionally, these hole defects effectively prevent 2D sheet aggregation by decreasing the number of interaction sites and hydrogen bonding between the g-C_3N_4 layers. Although the multiple-hole structure of g-C_3N_4 can be advantageous, creation of this form of g-C_3N_4 nanosheets requires the use of harmful organic solvent,[39] toxic ammonia-based reagents,[72, 73] strong acids,[75] or

hydrazine.[74] None of these methods is an environmentally sustainable or facile method for mass production of multiple-hole g-C_3N_4 nanosheets.

Graphene, a sheet of sp^2-bonded carbon atoms packed in a honeycomb lattice one atom thick, is used as a supporting material for photocatalysts due to its superior electron mobility (200,000 $cm^2 V^{-1} s^{-1}$) at room temperature (RT) and its electrical conductivity (2000 S m^{-1}), which allows it to efficiently accept and mediate photoinduced electrons from excited electron donors. More effective separation and migration of electron-hole pairs prevent recombination of charge carriers. Furthermore, 2D graphene has excellent environmental compatibility, an extremely high theoretical specific surface area (2630 $m^2 g^{-1}$), and a high absorption capacity.[105] As a result, graphene/g-C_3N_4 hybrids can mitigate high recombination rates, poor movement of charge carriers, and the low surface area of bare g-C_3N_4 and zero band gap of graphene, which limit their photocatalytic applications. Although the potential of graphene/g-C_3N_4 hybrids to serve as photocatalysts for H_2 evolution over the last decade has been studied, a facile method to achieve high performance and stability using a self-assembled graphene/g-C_3N_4 hybrid photocatalyst may offer new insights into sustainable photocatalysis in green H_2 production.

Platinum metal (Pt^0) and platinum oxide (Pt^{2+} in PtO) as co-catalysts in photocatalytic hydrogen evolution have been widely studied and are regarded as being among the most effective for photocatalytic processes.[133] In a previous report, Shi et al. demonstrated that the Pt^{2+} oxidation state is more favorable for H_2O adsorption and H_2 desorption compared to metallic state of Pt.[134] Moreover, PtO has a remarkable ability to suppress hydrogen oxidation reactions, which prefer the direction of H_2 generation.[93] The higher PtO nanoparticles amount on oxidized g-C_3N_4 can enhance photocatalytic H_2 evolution, as we reported previously.[39, 131] Thus, PtO support on the grid-like g-C_3N_4 and a graphene ternary hybrid photocatalyst is a promising approach to enhancing photoactivity toward H_2 evolution under visible light.

In this work, we describe the synthesis of a grid-like structure of g-C_3N_4 and a self-assembled graphene (hCN-G) composite using an observable high-pressure solvothermal treatment of bulk g-C_3N_4 in ethyl alcohol at 200 ℃. Platinum nanoparticles supported on hCN-G are synthesized through hydrogen reduction of the platinum precursor in an aqueous solution (Scheme 4). Monolayer g-C_3N_4 nanosheets with a grid-like morphology, self-assembled graphene, high proportion of Pt^{2+} oxidation state formation, and the high photoactivity of a PtO/graphene/g-C_3N_4

ternary hybrid were obtained. The hCN-G achieved a superior hydrogen evolution rate at an optimized point ca. 16,832.9 μmol g^{-1} h^{-1}, which is more than 7.5 times higher than that of CN-b. The earth-abundant dicyandiamide (DCDA) molecules and a simple synthesis with a green method enable simultaneous optimization of the structure of the g-C_3N_4 material and the creation of self-assembled graphene in mass production of the photocatalyst.

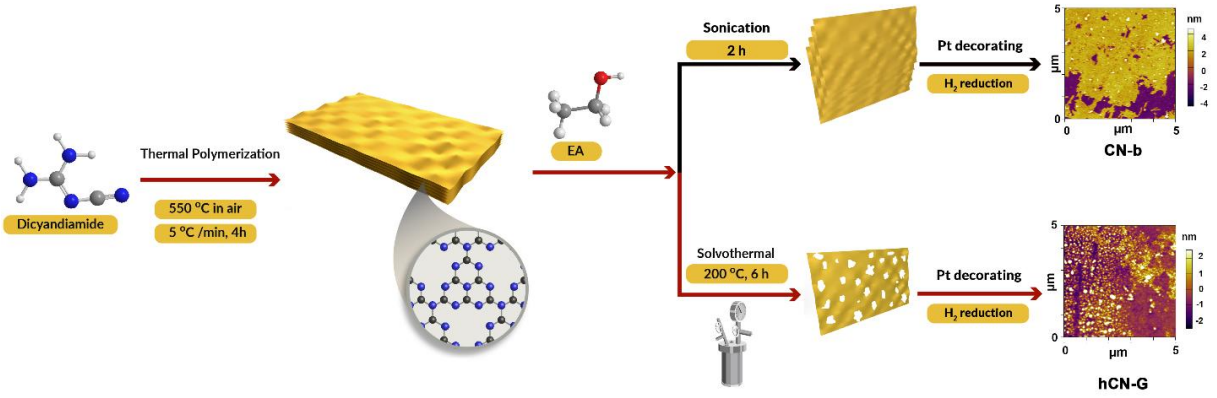

Scheme 4. Schematic for mass production of hCN-G and CN-b.

3.2. Experimental and Methods

3.2.1. Materials

Dicyandiamide (DCDA), triethanolamine (TEOA), chloroplatinic acid solution (H_2PtCl_6, 8 wt.% in H_2O), and Eosin Y were purchased from Sigma Aldrich. High-performance liquid chromatography–grade ethyl alcohol was purchased from Daejung Chemicals (Korea). High-purity argon gas was purchased from MS Gas Corporation (Korea). All chemicals were used as received without further purification.

3.2.2. Synthesis of CN-b and hCN-G

A 6 g sample of a DCDA precursor was placed in a rectangular crucible and covered, followed by annealing at 550 ℃ for 4 h in a muffle furnace at a ramping rate of 10 ℃/min. The resulting bulk g-C_3N_4 was vacuum dried at 80 ℃ for 12 h.

Next, 1 g of the prepared bulk g-C_3N_4 was placed in a 200 mL beaker containing 100 mL of ethyl alcohol and subjected to sonication for 1 h (Jeiotech UCP-10, 490 W) at approximately 22 ℃. Afterward, the suspension was transferred to a high-pressure microreactor (stirred reactor,

HR-8200, Korea), and a solvothermal reaction was allowed to proceed at 200 ℃ for 6 h. Deionized water was used to wash the resulting sample by centrifugation, followed by dilution to a 0.2 mg mL^{-1} suspension. Platinum was used as a co-catalyst. A calculated amount of 2 wt.% platinum was decorated on the resulting samples by hydrogen reduction in an aqueous phase at 60 ℃, using chloroplatinic acid as the platinum precursor, as previously described.[39, 57] The resulting samples were denoted CN-b and hCN-G.

3.2.3. Optimization of Photocatalytic H_2 Evolution

Photocatalytic green H_2 evolution under visible-light irradiation in a quartz flask reactor (300 mL, diameter: 70 mm, and height: 80 mm) was implemented using a simulated sunlight source (Oriel MiniSol, model LHS-7320, Class A.B.A., LED-based solar simulation, Newport Corporation, USA). The focused intensity of the light on the solution was 100 mW cm^{-2}. The evolved H_2 gas was measured via automatic injection, online gas chromatography with a thermal conductive detector, and a Carboxen 1000 column (Sigma-Aldrich).

3.2.3.1. Equipment Calibration

To consider a more accurate photocatalyst performance evaluation, we purchased a new MFC (Model FC-3911V-H_2(%)+Ar(%) 0-100sccm-1/4SW) to control the gas carrier flow rate, and a new Carboxen 1000 column (Sigma-Aldrich) for the online GC gas measurement. The standard gas of H_2/Ar were supplied from MS Gas Coorporation, including certification of analysis. The calibrations were performed before assessing photocatalytic hydrogen evolution of the photocatalysts. The MFC flow rate of the standard gases was set at 25 sccm, as same as thereafter experiments. The H_2 gas was measured via an automatic injection, online gas chromatography with a thermal conductive detector (TCD), and a Carboxen 1000 column (Sigma-Aldrich), Ar as a carrier gas, and the sample injection was set every 30 min. The column temperature was adjusted to be 40 °C, the detector temperature was 250 °C. The quantitative analysis of evolved hydrogen during the dehydrogenation reaction has been calculated according to the equation obtained from the linear calibration curve of hydrogen (Figure 58).

Table 15. Calibration data of H_2 concentration vs. GC peak area.

Total flowrate 25sccm, 25oC, 1atm						
No.	P (kPag)	T1 (oC)	Conc. H2, ppm	GC area 1 H2	GC area 2 H2	GC area aver. H2
1	0		0	0		0
2	0	23.3	160	8.44	8.64	8.54
3	0	21.9	400	12.49	12.19	12.34
4	0	19.9	600	14.34	14.27	14.305
6	0	20.6	800	17.49	17.93	17.71
7	0	19.8	1000	20.72	21.36	21.04
8	0	19.2	2000	40.01	39.51	39.76
9	0	18.8	3000	60.86	60.18	60.52
10	0	18.6	4000	85.14	84.72	84.93

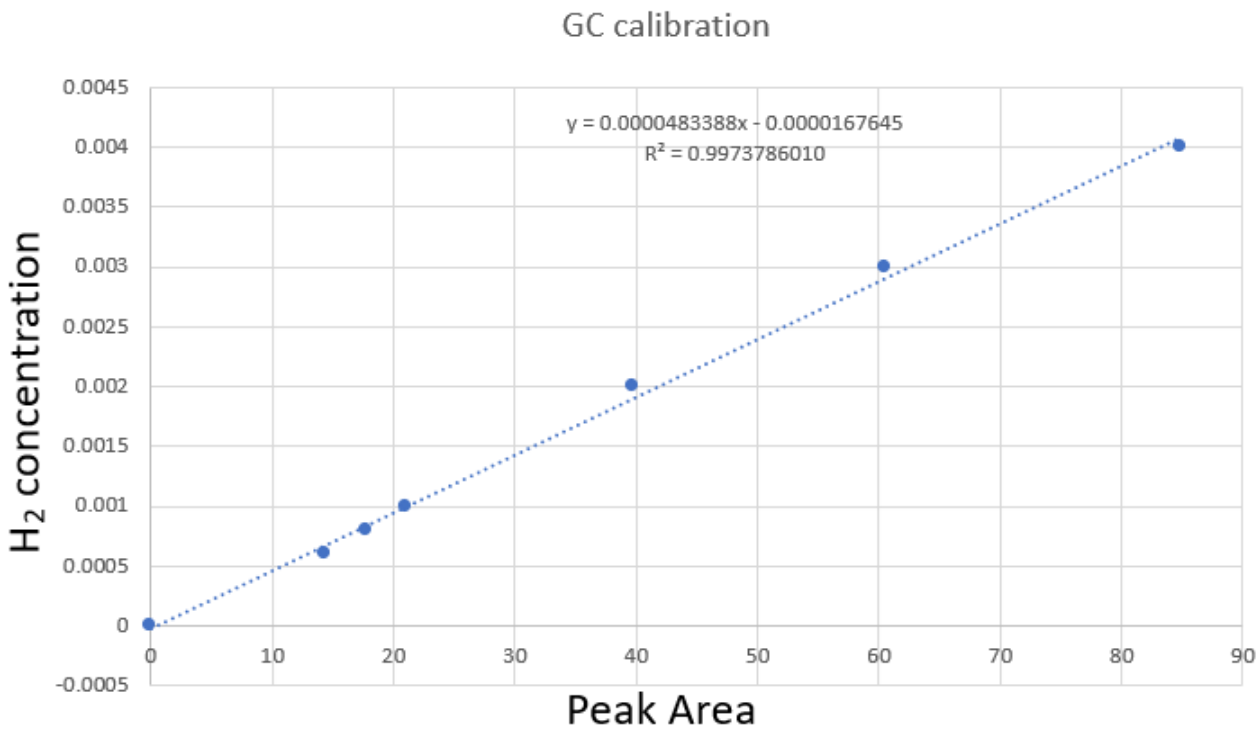

Figure 58. Calibration curves for the molecular hydrogen obtained from the GC-TCD.

3.2.3.2. Specific Reaction Conditions

3.2.3.2.1. Light Source Information

- Simulated sunlight source (Oriel® MiniSol model LHS-7320 Class ABA LED-based solar simulation, Newport, USA).
- The focused intensity of the light on the solution was 100 mW cm^{-2} (1 Sun simulated sunlight).
- Irradiation area: 50x50 mm.

Ideal Spectral Match Defined by IEC 60904-9

Spectral Range (nm)	Total Irradiance Range	Ideal Percentage
400-500	13.8-23.0	18.4%
500-600	14.9-24.9	19.9%
600-700	13.8-23.0	18.4%
700-800	11.2-18.6	14.9%
800-900	9.4-15.6	12.5%
900-1100	11.9-19.9	15.9%

Figure 59. Ideal spectral match defined by IEC 60904-9 of LHS-7320 simulated sunlight.

MODEL LSH-7320 SOLAR SIMULATOR SPECIFICATIONS[1]

Illumination Area	2 inches x 2 inches (50 mm x 50 mm)
Maximum Power Output	110 mW/cm² (1.1 SUN)
Variable Output Control Wavelength	0.1 to 1.1 SUN
Range	400nm - 1100nm
Temporal Stability	A - IEC 60904-9 2007, JIS 8904-9 2017
Uniformity	B - IEC 60904-9 2007, JIS 8904-9 2017
Spectral Match	A - IEC 60904-9 2007, JIS 8904-9 2017
Nominal Working Distance	12.0 inches +/- 0.5 inch; 304 +/- 12mm
Alignment	Laser diode based optical alignment
Z Axis Head Adjustment from Base	7.5 inches - 17.75 inches (190 mm - 450 mm)
Head Rotation2	0 - 360º
Remote Interface	USB 2.0 (B-Type) or BNC TTL for ON/OFF
TTL Turn On/Off Transition Time	10ms
Weight	
Head (on vertical assembly stand)	9.3 lbs (4.2 kg)
Stand	9.0 lbs (4.1 kg)
Power Supply	1.8 lbs (0.8 kg)
Dimensions	
Height (on vertical assembly stand)	15.25 - 25.5 inches (387 - 648 mm)
Width	7.15 inches (184 mm)
Depth	14.0 inches (362 mm)
Operating Temperature Range	5ºC to 40ºC
Storage Temperature Range	-40ºC to 70ºC
Humidity	<85%, relative, non-condensing
Compliance	CE, RoHS
Power Requirements	100-240 VAC, 47-63 Hz, 2.8A max

NOTES: 1) Class A per IEC 60904-9 (2007) Section 5.4.2
2) Indents on mounting plate at 0º, 90º, 180º, and 270º orientations

Figure 60. LHS-7320 solar simulator specifications.

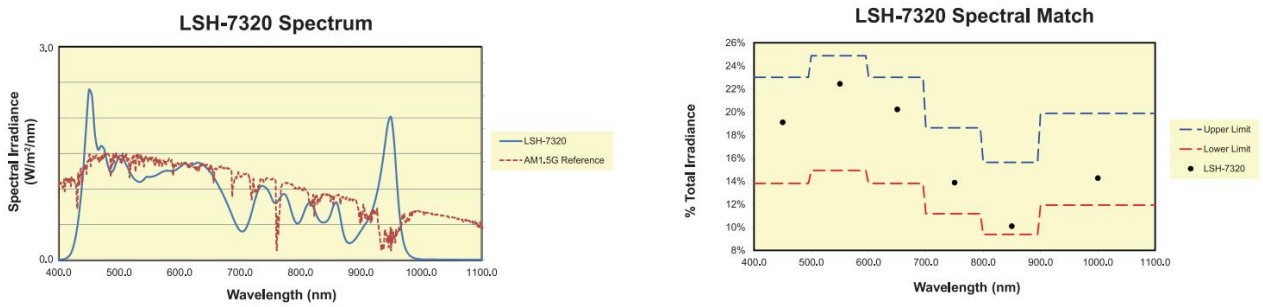

Figure 61. LHS-7320 spectrum and LHS-7320 spectral match.

3.2.3.2.2. Reactor

The quartz flask reactor (300 mL, diameter: 70 mm, and height: 80 mm) with a round water jacket for temperature control was used in all assessments of photocatalytic H_2 evolution performance.

3.2.3.2.3. Online GC Gas Measurement Method

The evolved H_2 gas was measured via an automatic injection, online gas chromatography with a thermal conductive detector (TCD), and a Carboxen 1000 column (Sigma-Aldrich).

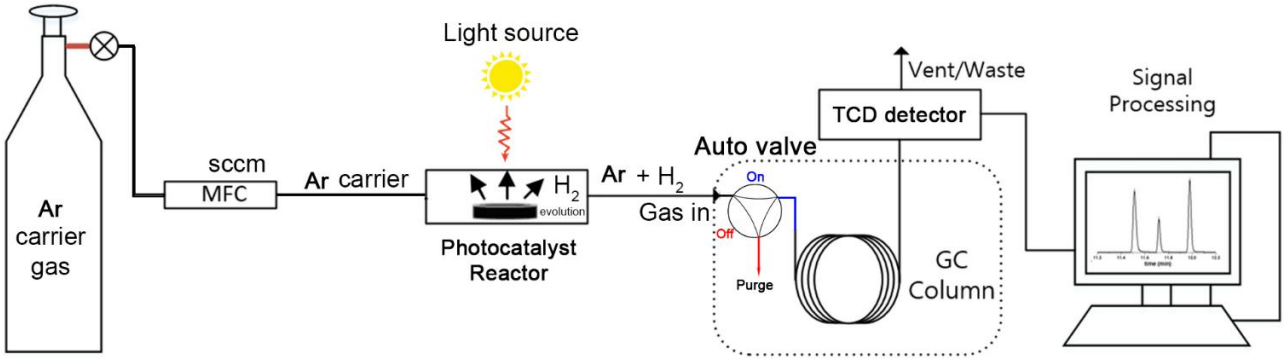

Figure 62. Online GC system for photocatalytic H_2 evolution measurement.

3.2.3.2.4. Reaction Media

3.2.3.2.4.1. Water quality

The ultra-pure deionized water used for the experiments was supplied from Puris-Evo UP WATER SYSTEM, model Evo-UP Dio VF. The used water had a resistivity of 18.2 mΩ·cm at 25.2 °C, pH = 8.64.

Table 16. Water quality from Puris-Evo UP WATER SYSTEM.

Model	Evo-UP Dio VF
Flow Rate(Up to)	2.0
Product Quality · Resistivity(at 25°C) MΩ-cm · TOC, ppb (μg/L) · Particles (0.2μm), EA/Mℓ · Bacteria, cfu/Mℓ · Endotoxin, EU/Mℓ · Rnase, ng/Mℓ · Dnase, pg/μℓ · PH Sensor	 18.2 <5 <1 <1 <0.001(*) <0.01(*) <4(*)

3.2.3.2.4.2. Sacrificial Agent

Triethanolamine (TEOA, Sigma-Aldrich) was used as a sacrificial agent for photocatalytic H_2 evolution measurement. The concentration of TEOA was 10 % vol/vol, the pH value of TEOA and final reaction media were 10.89 and 10.05 ± 0.8, respectively.

3.2.3.2.4.3. Photosentisizer

Eosin Y was added as a photosensitizer with a mass ratio of 1:1 to the catalyst. The amount of photosensitizer was optimized to supply an excess amount for the reaction. The pH value of reaction media was 10.05 ± 0.8 after adding Eosin Y.

3.2.3.2.4.4. Temperature

The reaction temperature was maintained at 20.0 ± 0.5°C via water jacket system of the reactor.

3.2.3.3. Optimization H_2 Production Rate

The benchmark of photocatalytic activity toward hydrogen evolution of as-prepared samples was optimized based on observing the dependence of H_2 production amounts vs. photocatalyst concentrations. All indicators were fixed except to change the photocatalyst mass for making the photocatalyst concentrations in a range of 0.05 to 0.4 $mg.mL^{-1}$.

Photocatalytic H_2 evolution under visible-light irradiation in a quartz flask reactor (300 mL, diameter: 70 mm, and height: 80 mm) was implemented by a simulated sunlight source (Oriel® MiniSol model LHS-7320 Class ABA LED-based solar simulation, Newport, USA). The focused

intensity of the light on the solution was 100 mW cm^{-2} (1 Sun). The amount of synthesized photocatalysts (calculated x mg in 90 mL ultra-pure DI water) was added to the quartz reactor, followed by adding Eosin Y as a photosensitizer. Then sonication was applied for 30 min at RT to form a homogeneous solution. Afterward, a high-purity flow of argon gas was blown through the system for 1 h to remove other impurity gases. Finally, 10 mL of TEOA solution was added to the reactor as a sacrificial reagent, and the system was purged with high-purity argon for 30 min to wipe out the air in the reactor. The evolved H_2 gas was conducted via an automatic injection, online gas chromatography with a thermal conductive detector (TCD), and a Carboxen 1000 column (Sigma-Aldrich).

3.2.3.5. The AQY at the Optimized Point of hCN-G

The AQY is calculated by equation[135]:

$$\text{AQY (\%)}=\frac{\text{number of reacted electrons}}{\text{number of incident photons}}\times 100=\frac{\text{number of evolved } H_2\times 2}{\text{number of incident photons}}\times 100$$

The energy of one photon (E_{photon}) with wavelength of λ_{inc}(nm) is calculated using the following equation:

$$E_{photon}=\frac{hc}{\lambda_{inc}}$$

The total energy of the incident monochromatic light (E_{total}) is calculated using the equation:

$$E_{total}=PSt$$

$$\text{Number of incident photons}=\frac{E_{total}}{E_{photon}}=\frac{PS\lambda_{inc}t}{hc}$$

Finally, the apprarent quantum yield is calculated as:

$$\text{AQY }(\%)=\frac{2n_{H_2}N_A hc}{PS\lambda_{inc}t}\times 100$$

Where $n_{H_2,t}$(mol) is the amount of H_2 evolved over the duration t of the incident light irradiation,

N_A (mol^{-1})is Avogadro's constant,

h (J.s) is Planck's constant,

c ($m.s^{-1}$) is the speed of light,

P ($W.m^{-2}$) is the power density of the incident monochromatic light,

λ_{inc}(m) is the wavelength of the monochromatic light,

t (s) is the duration of the incident light irradiation.

The average power density of the incident monochromatic light, using Bandpass 420 nm filter is measured as:

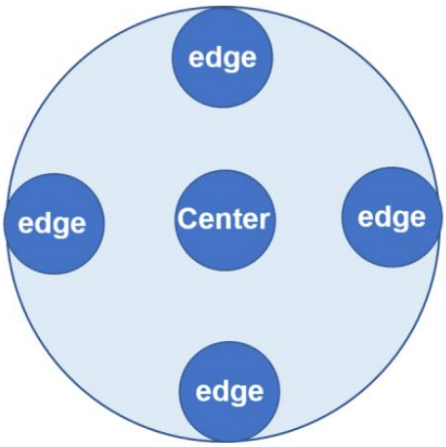

The schematic diagram of the test points for circle spots.

Calculation method:

$$\bar{E} = \frac{\overline{E_{center}}}{3} + 2\frac{\overline{E_{edge}}}{3}$$

$\overline{E_{center}}$: *the light intensity of the center of the spot*, W/m^2

$\overline{E_{edge}}$: *the light intensity of the edge of the spot*, W/m^2

The 843-R Power Meter and Thermopile Sensor (3 W, 10 mm, 0.19-11 μm Newport, MODEL: 919P-003-10, sensor size: Ø9.5 mm, detector active area of 0.71 cm^2) is used to evaluate the power density. The average power density is 1.06 mW. cm^{-2} (or 10.6 W. m^{-2}). The circle irradiation area is 19.63 cm^2.

$$\text{A.Q.Y.}(\%) = \frac{2n_{H_2,t}N_A hc}{PS\lambda_{inc}t} \text{ x } 100$$

$$\text{A.Q.Y.}(\%) = \frac{2\text{x}37.08\text{x}10^{-6}(\text{mol})\text{x}6.02214076\text{x}10^{23}(\text{mol}^{-1})\text{x}6.62607015\text{x}10^{-34}(\text{J.s})\text{x}299{,}792{,}458(\text{m.s}^{-1})}{10.60(\text{W.m}^{-2})\text{x}0.001963\text{m}^2\text{x}420\text{x}10^{-9}(\text{m})\text{x}3600(\text{s})} \times 100$$

$$\text{A.Q.Y.}(\%) = 28.20\ \%$$

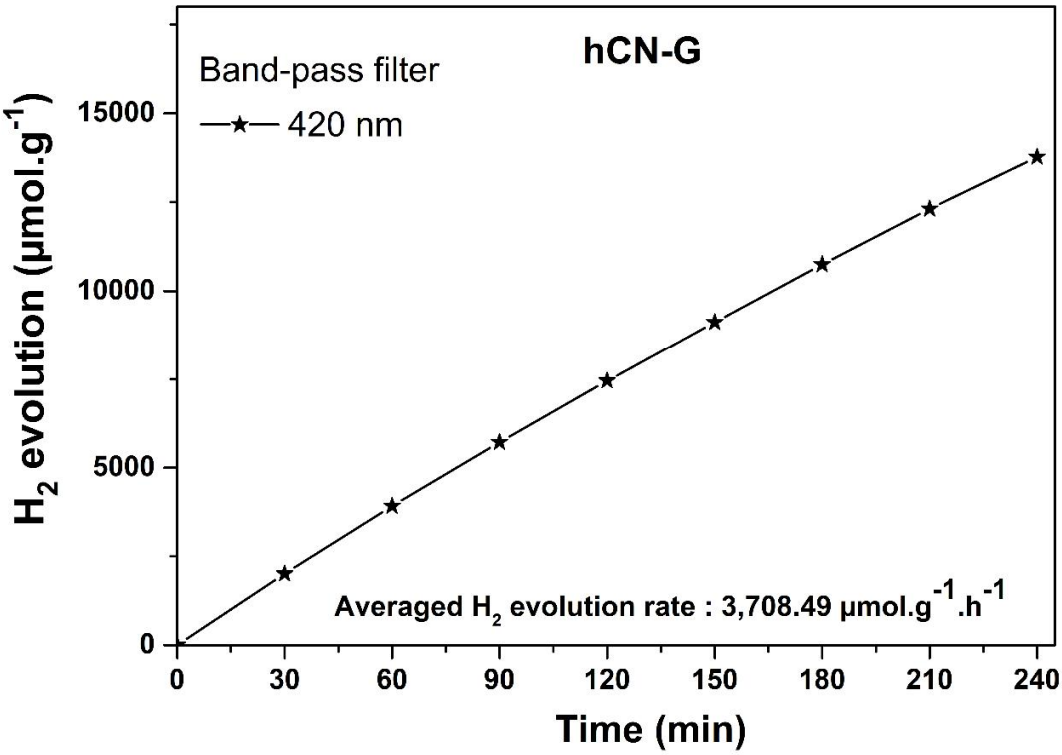

Figure 63. H_2 evolution of hCN-G using 420 nm bandpass filter (Newport 20BPF10-420 Bandpass Filter, 50.8x50.8 mm, 420±2 nm Center, 10±2 nm FWHM).

3.2.4. Characterizations

The crystalline structures of the prepared samples were measured using high-resolution powder X-ray diffraction (HRP-XRD) with a Cu Kα X-ray source at a wavelength 1.5415 Å and a scan rate of 2° (2θ)/min (Rigaku D/MAZX 2500 V/PC high-power diffractometer, Tokyo, Japan). Fourier-transform infrared spectroscopy (FT-IR; Nicolet 380 spectrometer, Thermo Scientific Nicolet iS5 with an iD1 transmission accessory, Waltham, MA, USA) was used to characterize the functional groups of the produced photocatalysts. X-ray photoelectron spectroscopy (Thermo Scientific K-Alpha system, Waltham, MA, USA) was used to analyze the composition, chemical state, and electronic state of the elements. The elemental composition (carbon, hydrogen, nitrogen, oxygen, and sulfur) of the samples was analyzed with an elemental analyzer (Flash 2000, Thermo Scientific). The platinum element composition of the prepared samples was determined by an

inductively coupled plasma–optical emission spectrometer (ICP-OES; 700-ES Varian, Mulgrave, Australia). Scanning electron microscopy (SEM; JSM-600F JEOL, Tokyo, Japan) was used to investigate the microstructure and the catalyst morphology. The microstructure and distribution of the platinum nanoparticles were examined using high-resolution transmission electron microscopy (HR-TEM; JEL-2100F JEOL, Tokyo, Japan). A spherical aberration–corrected scanning transmission electron microscope (CS-STEM, JEM-ARM300F, JEOL) with a 300 kV electron beam was used to study the grid-like structure of hCN-G samples at high spatial resolution. The lateral dimensions and height profiles of the resulting g-C_3N_4 sheets were measured by commercial atomic force microscopy (AFM, MFP-3D, Asylum Research). Raman spectra were obtained by confocal Raman microscopy with a 532 nm incident laser (Thermo Scientific). Thermogravimetric analysis (TGA) was measured by a TGA 550 (TA Instruments). UV-vis absorption spectra (Specord 210 Plus, AnalytikJena, Germany) and UV–vis diffuse reflectance spectra (SCINCO S-4100 Diffuse Reflectance-Ultraviolet/Visible Spectrophotometer) were used to examine the photocatalyst's optical characteristics. Photoluminescence spectroscopy was measured with a 473 nm diode laser at ambient temperatures (Agilent Technologies, Cary Eclipse fluorescence spectrophotometer, Santa Clara, CA, USA). Time-resolved photoluminescence (TR-PL) spectra were recorded under 400 nm laser excitation by a FS5 spectrofluorometer (Edinburgh Instruments Ltd, Livingston, UK).

3.2.5. Electrochemical Measurement

An electrochemical workstation (VSP BioLogic Science Instruments, Seyssinet–Pariset, France) was used to perform electrochemical impedance spectroscopy (EIS) measurements in a standard three-electrode system under UV irradiation at RT. EIS was carried out in an open circuit, following a 10-minute delay, in a frequency range of 100 kHz to 0.01 Hz and an amplitude of 10 mV at a direct current potential of +0.8 VSCE.

Drip-coating was used to prepare the membrane electrode. Following conventional procedures, 20 mg of catalyst powder was ground with 2 mg of activated carbon by mortar for 20 min to obtain a fine powder, which was then added to 100 µL of isopropanol (99.7%) and 30 µL of Nafion (5 wt.%) (Sigma Aldrich, Korea). A 10 mL solution of 1 M sodium hydroxide was used as the electrolyte. The working electrode was a 6 mm standard glassy carbon electrode, in which 10 µL of the sample was placed (1 µL of suspension at a time by micro-pipet). The reference

electrode was the RE-1BP (Ag/AgCl) electrode, while the counter electrode was a platinum wire. The SVC-3 voltammetry cell and the electrodes were purchased from ALS Co., Ltd. (Tokyo, Japan).

Transient photocurrent response measurement was performed under a 0.8 eV potential in 1 M NaOH solution. The working electrode was prepared on a 1 cm^2 fluorine-doped tin oxide (FTO) substrate by spraying coating a mixture containing 2 mg photocatalyst, 10 ml mixture of ethyl alcohol and DI water (v/v ratio: 1/1), and simulated sunlight was used as a light source. A RE-61AP (Hg/HgO) electrode was used as the reference, and a Pt wire was used as the counter electrode.

3.2.4. Computational Methods

All density functional theory (DFT) calculations were performed using a Perdew–Burke–Ernzerhof (PBE) generalized gradient approximation[77] in the Vienna ab initio simulation package,[136, 137] including D3-type dispersion corrections.[138] Projector-augmented wave pseudopotentials with a cutoff energy of 420 eV were used for the plane-wave basis set.[139] The Brillouin zone was sampled using a gamma-centered Monkhorst–Pack scheme with a k-spacing of $0.01 \times 2\pi$ $Å^{-1}$ for the PBE-based electronic structure calculations, while a hybrid function (HSE06) was used to accurately predict the electronic band structure and density of states.[140] The self-consistent convergence thresholds for force and energy were 0.02 eV $Å^{-1}$ and 1×10^{-6} eV, respectively. A 15 Å vacuum spacing was used to avoid the periodic artifacts between the periodic images. Charge-density difference plots and geometric visualizations were carried out using VESTA software.[80] Electronic band structures were plotted using the sumo python toolkit.[141]

3.3. Results and Discussion

3.3.1. Crystal Structure, Chemical Composition, Morphology and Microstructure

HRP-XRD was used to determine the crystallographic nature of the obtained samples (Figure 64A). Two peaks clearly visible at 13.1° and 27.7° in the XRD patterns were assigned to the respective g-C_3N_4 crystal planes (100) and (002). According to JCPDS 87-1526, these planes correspond to structural packing of repeating heptazine units in the plane and interlayer stackings of the conjugated aromatic system in layers, respectively.[83, 84] An additional broad feature at approximately 57.4° exhibited a refined crystallized structure with AB stacking of g-C_3N_4 triazine

layers in a hexagonal space group.[85] The primary crystalline structure of the g-C_3N_4 was maintained after the solvothermal reaction. The peaks corresponding to hCN-G exhibited a reduction in intensity compared with those of CN-b, indicating thinner layer peeling of the stacked multilayers after the solvothermal reaction, which was confirmed in subsequent AFM height profiles of the resultant samples.

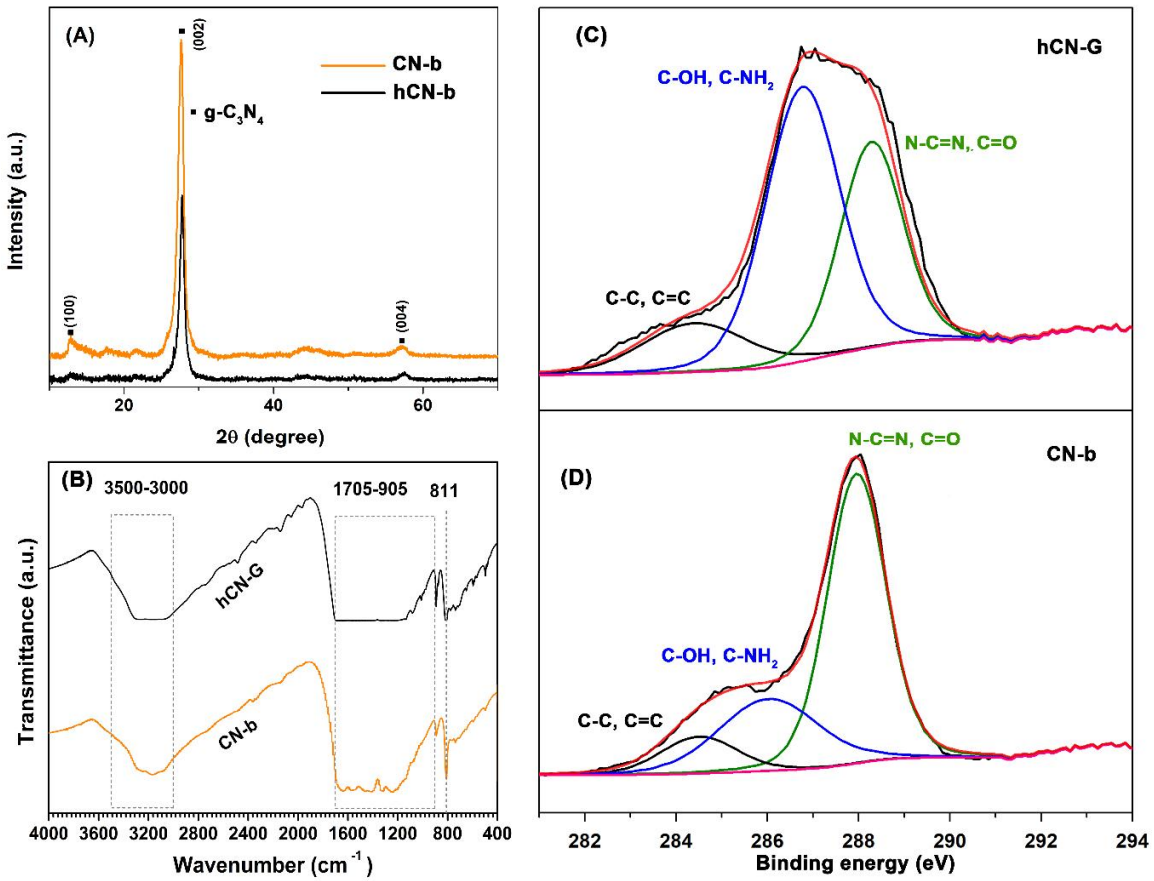

Figure 64. (A) HRP-XRD spectra, (B) FT-IR spectra, and (C, D) XPS C1s spectra of hCN-G and CN-b.

FT-IR spectra were used to examine the chemical structures of the resulting g-C_3N_4 samples (Figure 64B). The broadening of the bands between 3500 cm^{-1} and 3000 cm^{-1} can be ascribed to N-H and the stretching mode of the oxygen functional groups (O-H, -O-).[87] The hCN-G sample showed stronger and greater stretching compared with the CN-b sample, which can be attributed to the higher number of N-H groups after solvothermal reaction and an increase in the formation of oxygen groups.[88-90] Peaks between 1705 and 905 cm^{-1} and at 811 cm^{-1} correspond to the stretching mode of the C-N heterocycle and the C-C aromatic rings and the vibration mode of the tris-s-triazine motifs, respectively.[86] The crystallographic nature of the

hCN-G sample is similar to that of the initial bulk g-C_3N_4, which maintains the active sites of heptazine units in the structure after the reaction. The increase in oxygen functional groups was further confirmed by the elemental compositions of the samples, in which the C/O ratio decreased after the reaction (Table 17).

Table 17. Elemental compositions and atomic ratio calculations of the resultant samples.

Elemental analysis							
Sample	C (wt. %)	N (wt. %)	O (wt. %)	H (wt. %)	C/N (mol/mol)	C/O (mol/mol)	O/N (mol/mol)
CN-b	35.31	54.93	3.46	1.64	0.75	13.61	0.06
hCN-G	33.59	50.63	6.19	1.96	0.77	7.24	0.11

The masses of oxygen and hydrogen elements in hCN-G increased in comparison with the starting material (CN-b), which indicates that more oxygen functional groups were introduced into the g-C_3N_4 layers. While the C/N ratio was nearly maintained after the reaction (approximately 0.75), the weight percentages of nitrogen and carbon in the CN-b sample simultaneously decreased after the reactions, suggesting the removal of heptazine motifs by solvothermal reactions in ethyl alcohol. The loss of heptazine units to form a grid-like structure of g-C_3N_4 layers was further determined in the subsequent nanostructure morphology analysis.

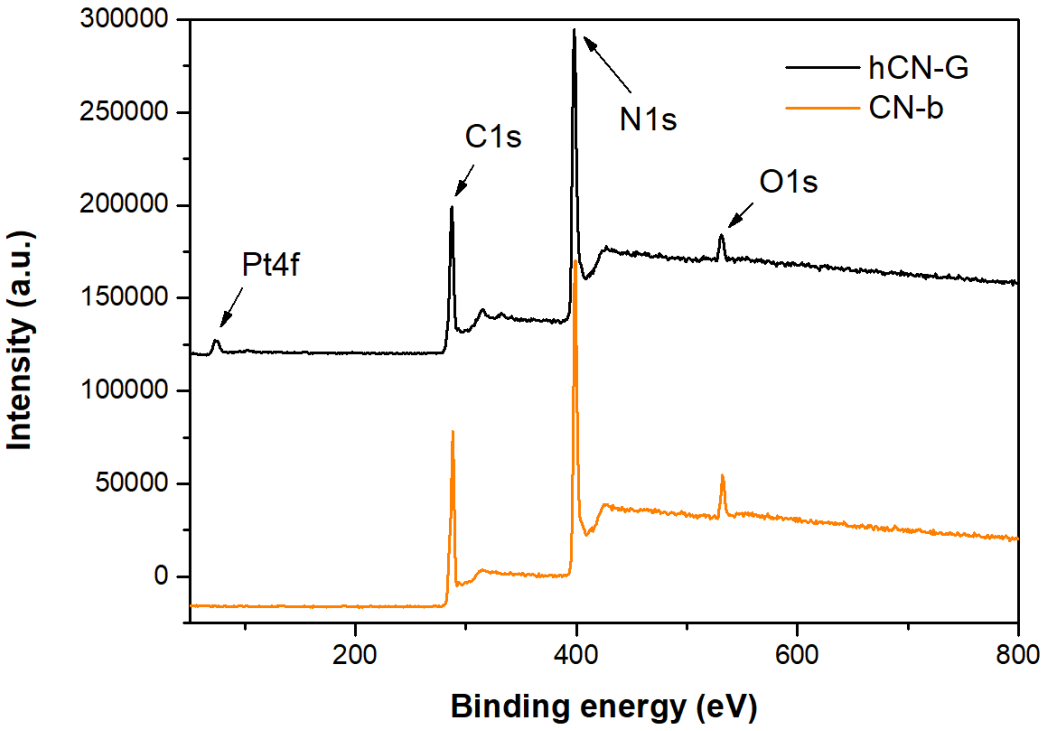

Figure 65. XPS survey spectra of CN-b and hCN-G.

The surface chemical states of as-prepared samples were investigated by XPS analysis. XPS survey spectra of CN-b and hCN-G (Figure 65) confirmed the existence of carbon, nitrogen, oxygen, and platinum. In deconvolution of the C1s XPS spectra (Figures 64C and D), the main carbon peaks at 284.6 eV and near 288.15 eV can be assigned to graphitic structure bonds (C-C) and sp^2-hybridized carbon atom bonds (N_2-C=N-), respectively.[17, 18, 92] The peak near 286.4 eV significantly increased after the reaction, which indicates the introduction of additional C-OH and C-NH_2 groups. The hydroxyl groups and amine groups correspond to the formation of oxygen functional group and increase in amine groups at the edges of the g-C_3N_4 layers, respectively. This result is consistent with earlier results, in which the number of hydroxyl groups increased and formation of multiholes in g-C_3N_4 layers introduced additional edge area inside the sheets.

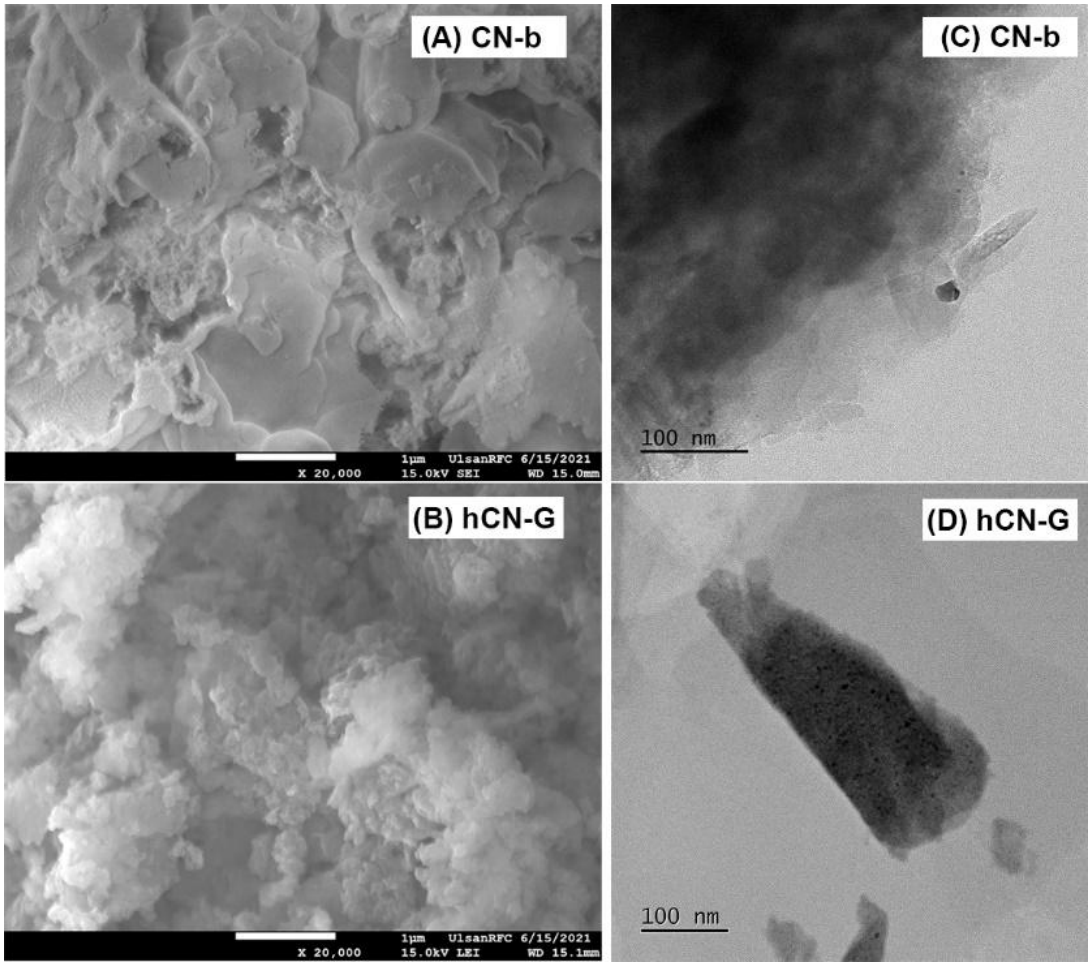

Figure 66. (A, B) FE-SEM images and (C, D) HR-TEM images of CN-b and hCN-G samples.

The surface morphology of each sample was captured by FE-SEM, HR-TEM, AFM, and CS-STEM. As shown in the FE-SEM images, CN-b exhibited a flake-like structure with smooth lamellar surfaces (Figure 66A), which indicated multilayer stacking resulting from thermal polymerization. The hCN-G sample displayed a cloud-like structure, resulting in a grid structure due to etching effects (Figure 66B). The HR-TEM images showed nanosheets of CN-b in multilayers (Figure 66C) and a folded layer of hCN-G (Figure 66D) due to the grid-like structure of hCN-G enabling self-folding behavior, resulting in a tubular shape.

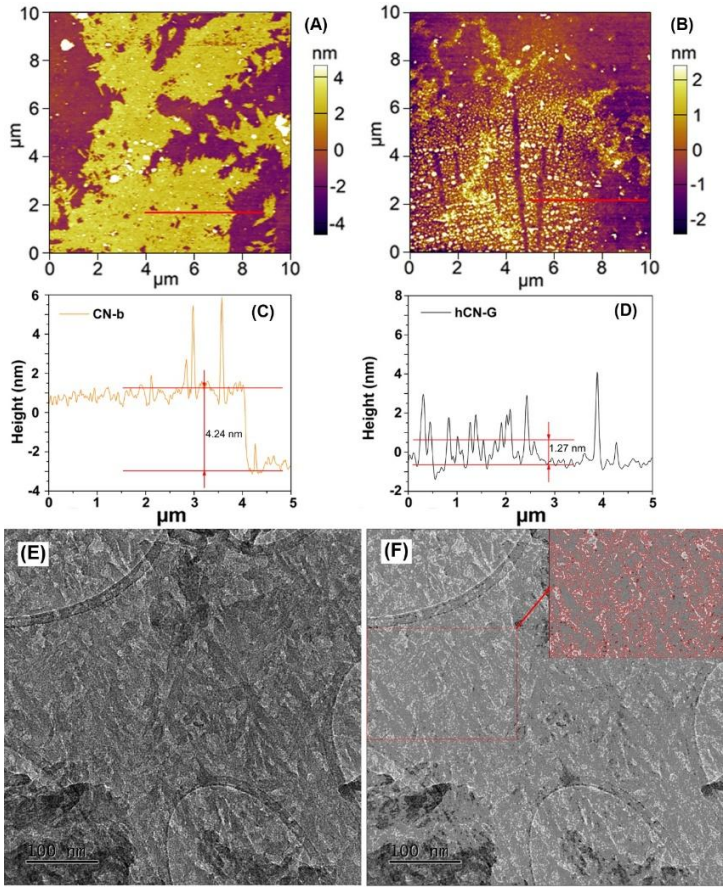

Figure 67. (A, B) AFM topography images of CN-b and hCN-G samples, corresponding to their height profiles (C, D). Spherical aberration–corrected scanning transmission electron microscope (CS-STEM) image of the hCN-G sample, (E) the original image, and (F) with color added to highlight the feature.

The grid-like structure of hCN-G was confirmed by AFM topography. In Figure 67, the hCN-G displays uniform holes on the planar surface of the layer (Figure 67B and Figure 68). The height profile of the hCN-G in Figure 3D verified the multihole structure of the layer, and the thickness of such a monolayer was approximately 1.3 nm. In contrast, the CN-b sample had a multilayer structure with a flake thickness of approximately 4.2 nm (Figure 67C). This result is consistent with the HRP-XRD analysis, in which the thickness of g-C_3N_4 was reduced after the solvothermal reaction. The grid-like hCN-G can be certified by high-resolution CS-STEM imagery (Figure 67E, Figure 67F). A grid-like structure is clearly visible in the highlighted image of the CS-STEM (Figure 67F).

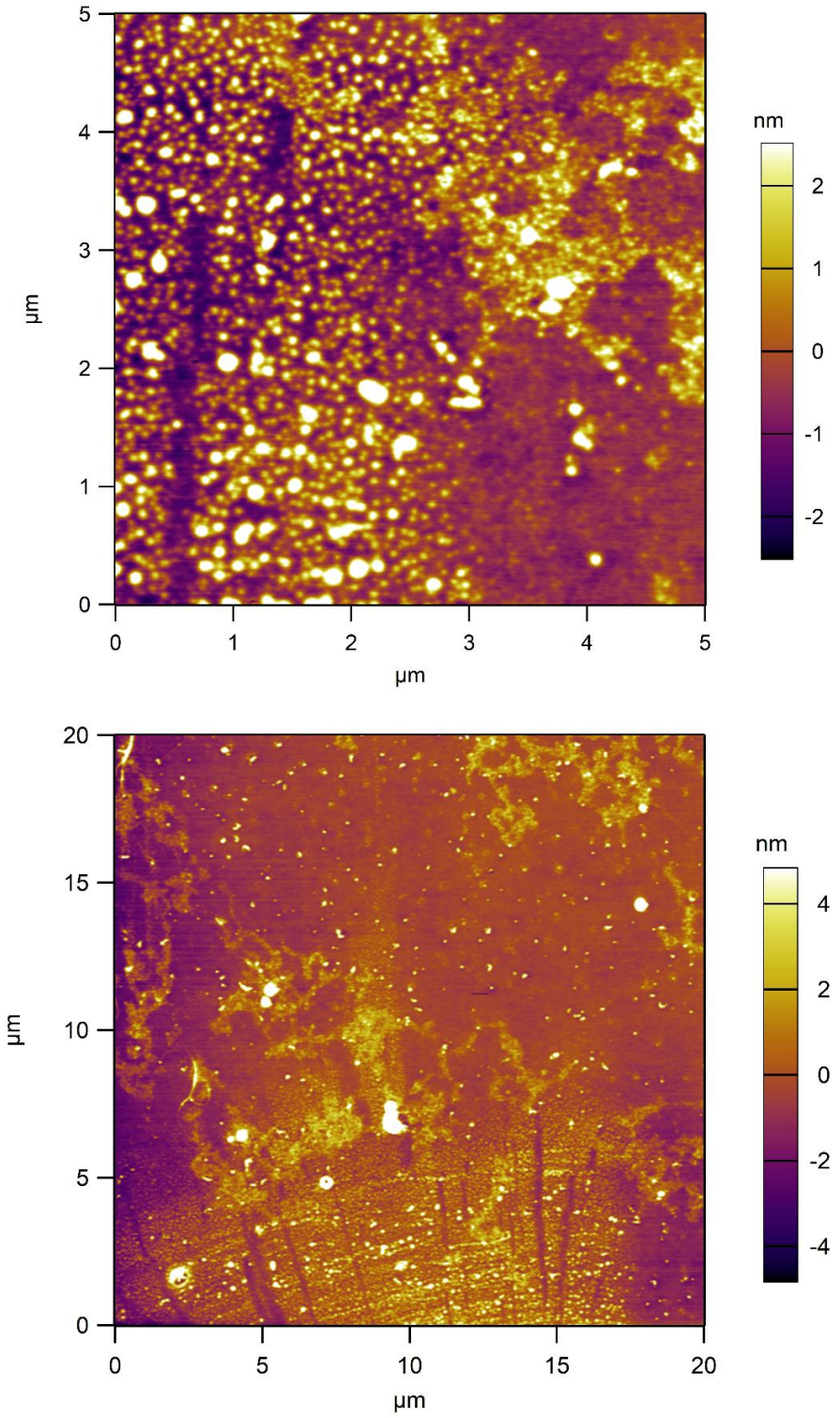

Figure 68. AFM topography at different scale of hCN-G sample.

Based on these practical observations, a DFT calculation on the charge density of ethyl alcohol and pristine g-C_3N_4 revealed an interaction between ethyl alcohol and the s-heptazine sheet. As shown in Figure 69, this charge distribution was an interaction between the oxygen atom of ethyl alcohol and the carbon atom on the heptazine sheet, which suggests that the oxygen atom of ethyl alcohol attacks the carbon atom on the sheet through an S_N1 reaction mechanism to break the C-N bonds and remove the heptazine units of g-C_3N_4, resulting in a multihole structure of hCN-G (Scheme 5). These uniform multiholes on the planar layer of hCN-G explain the folded tubular structures in the HR-TEM image and why the multiholes enable more accessible active sites of the photocatalyst.

Top view

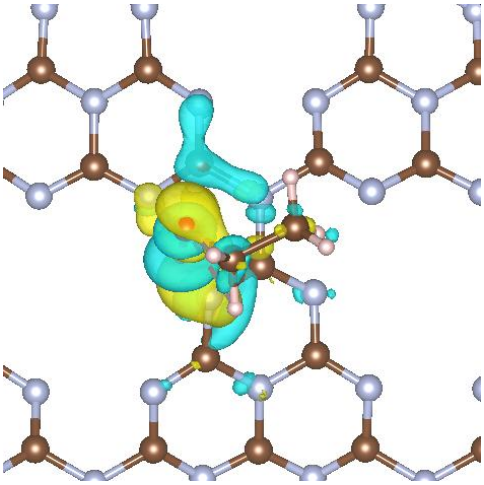

Side view

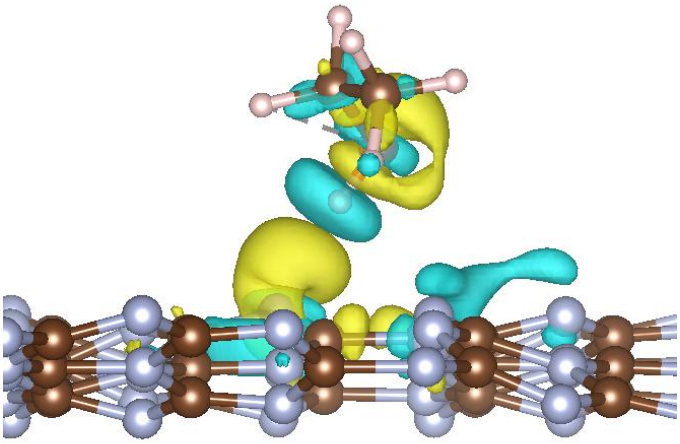

Figure 69. The charge density for ethyl alcohol on s-heptazine sheet: interaction between O atom of ethyl alcohol and C atom on the sheet. The adsorption energy = -0.94 eV /atom (-13.14 eV /g-C_3N_4).

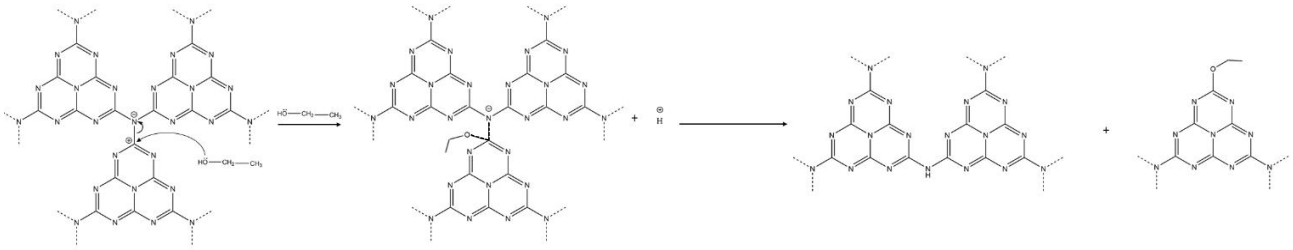

Scheme 5. Proposed S_N1 reaction pathway of ethyl alcohol interacts with g-C_3N_4 at C (N2-C-N) atom in the heptazine rings.

The new structure of hCN-G simultaneously created an advanced nanostructure for enhancing the photoactivity of the g-C_3N_4 photocatalyst and the formation of self-assembled graphene, which is discussed in Section 4.3.2. Furthermore, the grid-like structure of hCN-G with oxygen doping on the surface of the planar layer facilitated a better distribution of the co-catalyst platinum nanoparticles on the catalyst surface and generation of a higher platinum oxidation state (Pt^{2+} in PtO).

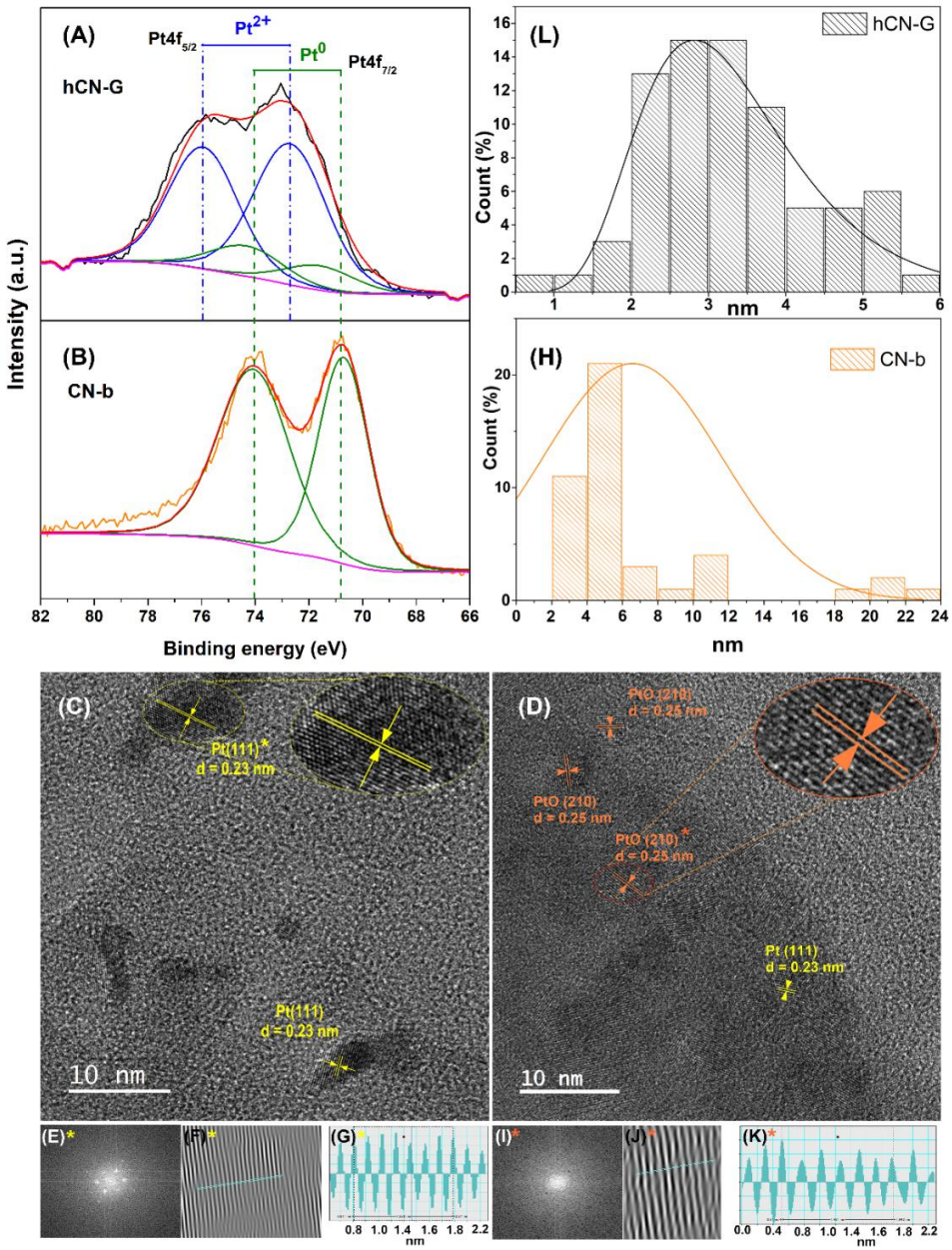

Figure 70. (A and B) High-resolution XPS Pt 4f spectra of CN-b and hCN-G. (C and D) HR-TEM images of CN-b and hCN-G, corresponding (E and I) Fast Fourier-transform (FFT) images, (F and J) high-resolution inverse FFT images, and (G and K) lattice fringe pattern images. (H and L) Co-catalyst nanoparticle size distributions.

Figure 71 shows high-resolution XPS spectra of O1s. The binding energies near 530.2 and 532.5 eV can be assigned to the C=O and O-H groups of CN-b, respectively, and resulted from the introduction of oxygen groups during pyrolysis in an atmosphere.[92] The new peak at 531.7 eV

in the hCN-G sample corresponds to the C-O group, which was caused by oxygen doping during the solvothermal process.[92] This result was consistent with the elemental analysis, which confirmed the introduction of additional oxygen functional groups on the surface of hCN-G after the reaction. As can be seen in Figure 66D and Figure 72, the co-catalyst nanoparticles over the hCN-G sample were uniformly distributed compared with an uneven distribution in location and size on the CN-b sample (Figure 66C).

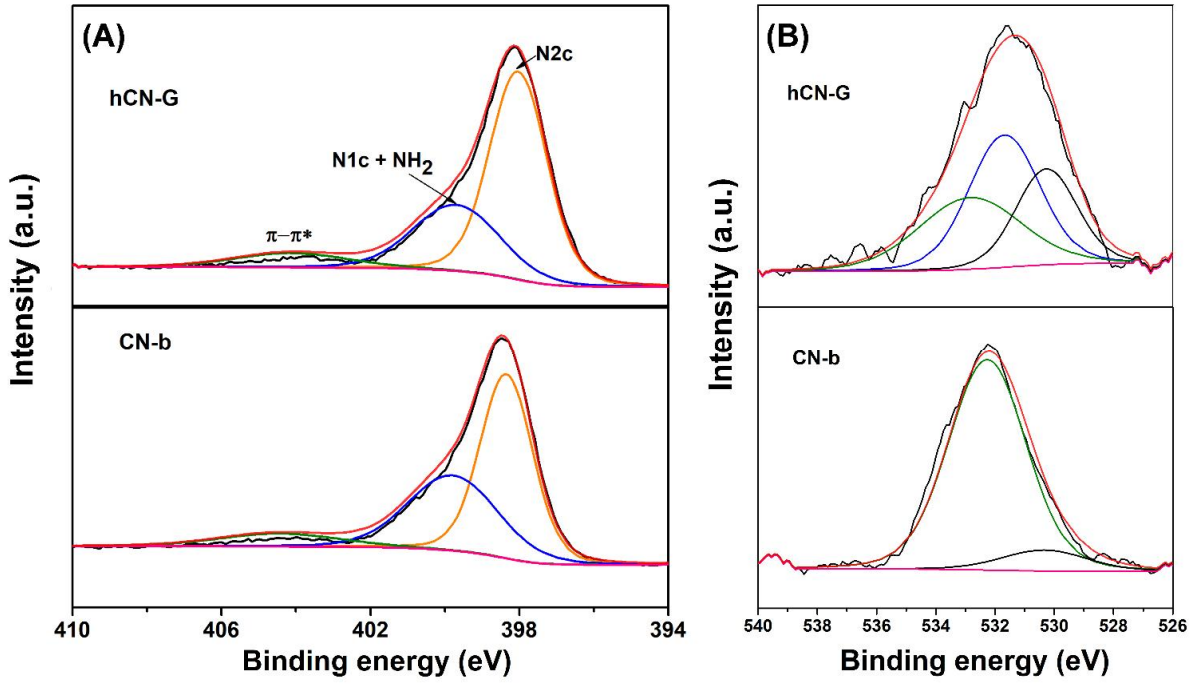

Figure 71. Deconvolution of (A) N1s and (B) O1s XPS spectra of CN-b and hCN-G, respectively.

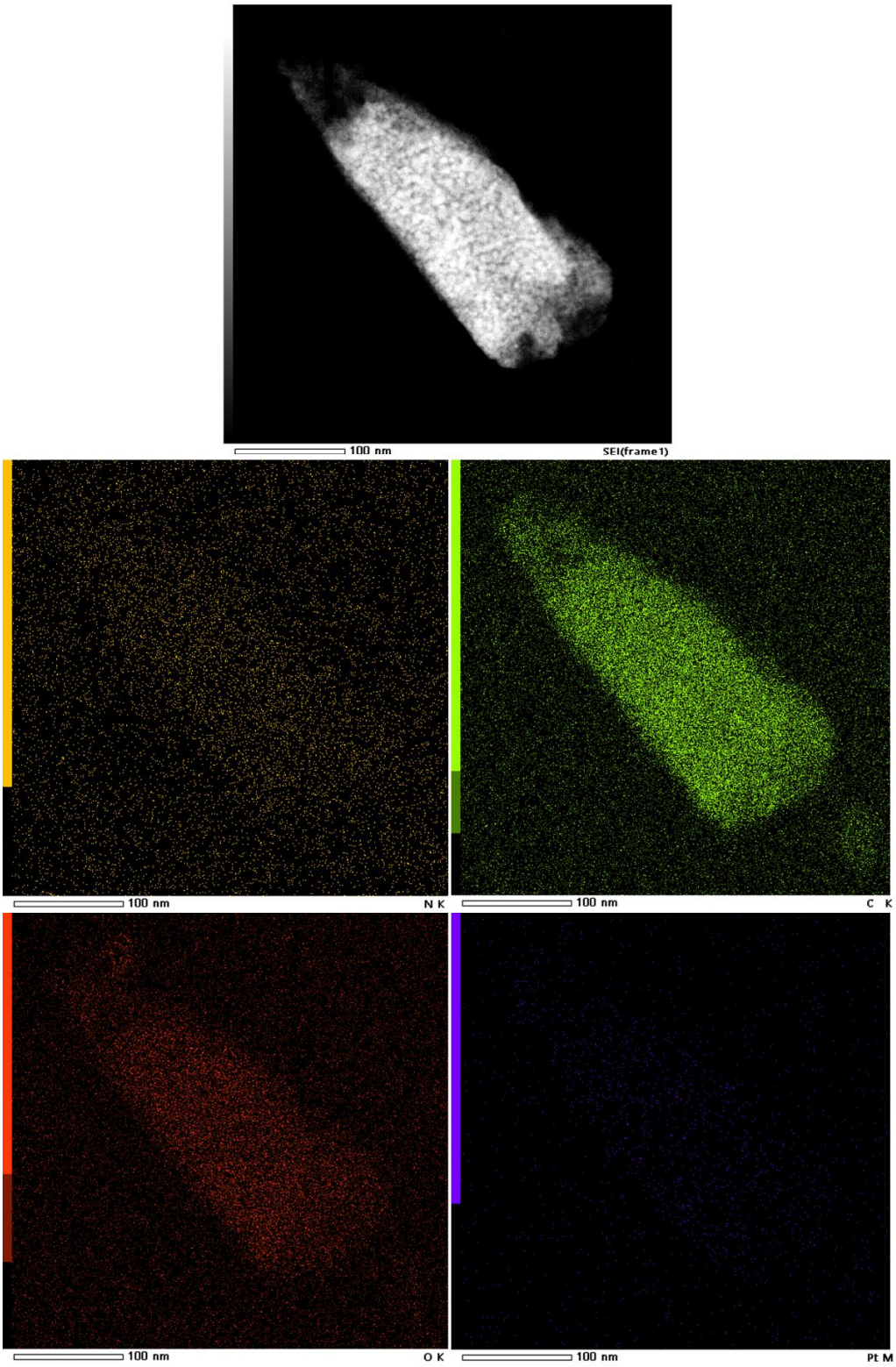

Figure 72. HR-TEM images of hCN-G corresponding to its STEMS images.

The size distribution of co-catalyst nanoparticles of the hCN-G sample ranged from 1 to 6 nm (typically 2.5 nm) (Figure 70D and L), while the size of the platinum nanoparticles on the CN-b sample showed an extensive range of up to 24 nm (mostly approximately 6 nm) (Figure 70C and H). The grid-like structure of hCN-G led to differentiation in platinum oxidation states (Figure 70A and D), including a high percentage of PtO and a low amount of metallic platinum nanoparticles compared with purely metallic platinum in the CN-b sample (Figure 70B and C). In the high-resolution XPS spectra, the metal platinum (111) peaks located at near 70.8 eV and 74.1 eV correspond to the binding energies of $Pt4f_{7/2}$ and $Pt4f_{5/2}$, respectively, and the Pt^{2+} state shows two bands at approximately 72.7 eV and 75.9 eV (Figure 70A and B).[57, 134] The mixture of platinum and PtO co-catalysts enhanced photocatalytic H_2 evolution in our previous study.[39] The formation of self-assembled graphene and the higher platinum oxidation states contributed to improved photocatalysis toward H_2 evolution.

The specific surface areas of CN-b and hCN-G were measured by N_2 adsorption-desorption isotherms at 77 K. Both CN-b and hCN-G isotherms exhibited an H3 hysteresis loop and are classified as type IV by the IUPAC standard (Figure 73, Table 18), indicating mesoporous structures in all samples. The specific surface area of hCN-G was 69.1 $m^2 g^{-1}$, which was 3.2 times that of CN-b (21.8 $m^2 g^{-1}$). The broad peak between 10 and 30 nm shown in Figure 73B indicates the inner pore size of hCN-G due to its multihole structure.

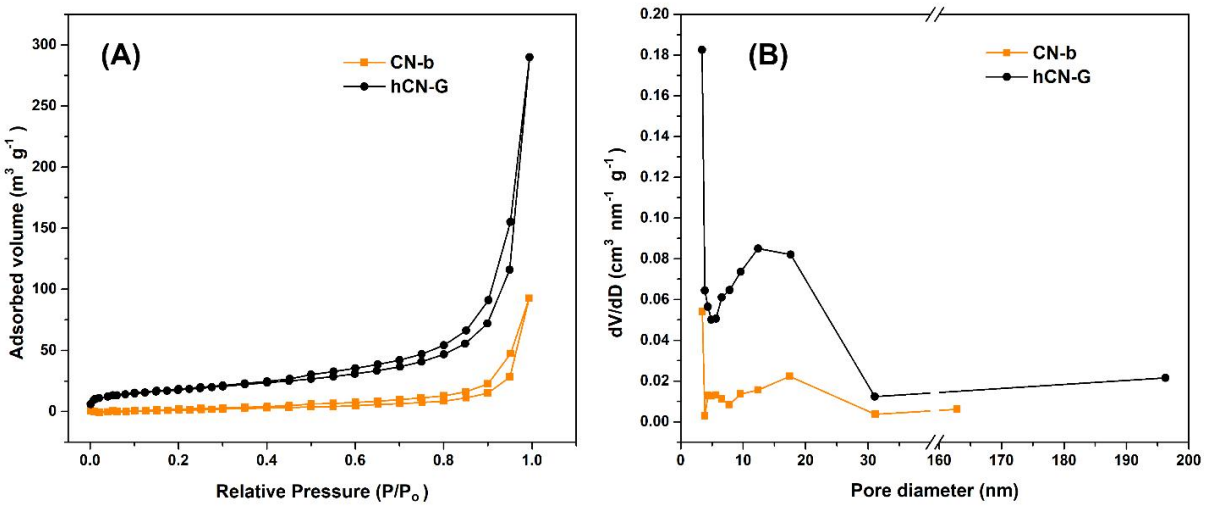

Figure 73. (A) N_2 adsorption-desorption isotherms of CN-b and hCN-G. (b) Pore-size distributions of CN-b and hCN-G.

Table 18. Textural data and bandgaps of the samples.

Sample	S_{BET} (m^2/g) [a]	V (cm^3/g) [a]	L (nm) [a]	Band gap (eV) [b]
CN-b	21.81	0.146	4.053	2.76
hCN-G	69.10	0.447	3.827	2.91[c]

[a] Specific surface area, pore volume, and average pore size were determined via N_2 adsorption–desorption isotherm measurements.

[b] Estimated bandgaps were obtained from the UV-Vis DRS spectra.

[c] The band gap values were measured using vacuum-drying g-C_3N_4 samples by UV-DRS.

3.3.2. Self-assembled Graphene as Electron Acceptor and Mediator for Accelerating Charge Transfer

Self-assembled graphene was formed through the solvothermal reaction process of bulk g-C_3N_4. The etching effect produced both holes on planar g-C_3N_4 and fragments, which could be a precursor to reforming graphene in the solvothermal condition. The light-yellow CN-b turned gray (hCN-G) after solvothermal treatment. The Raman spectrum of hCN-G at the black spot is shown in Figure 74B, which concurred with the graphene graphitic structure. The two distinct peaks at 1345 cm^{-1} and 1599 cm^{-1} correspond to the D and G bands of graphene, respectively.[57] The I_D/I_G ratio of approximately 1.1, indicating the introduction of sp^2 carbon in the form of graphitic domains, was similar to that of a typically reduced graphene oxide material.[54, 57] In contrast, the CN-b sample showed no sign of graphene's D and G peaks (Figure 74A).

TGA was used to determine the thermal stability of the g-C_3N_4 framework and graphene content from the residue after annealing the samples. Figure 74C depicts TGA thermograms of CN-b and hCN-G in an argon atmosphere at a ramping of 10 ℃ min^{-1}. The weight loss from 200 to 465 ℃ can be attributed to loss of oxygen functional groups of the photocatalysts. The mass loss occurred at temperatures higher than 465 °C due to C-N framework decomposition.

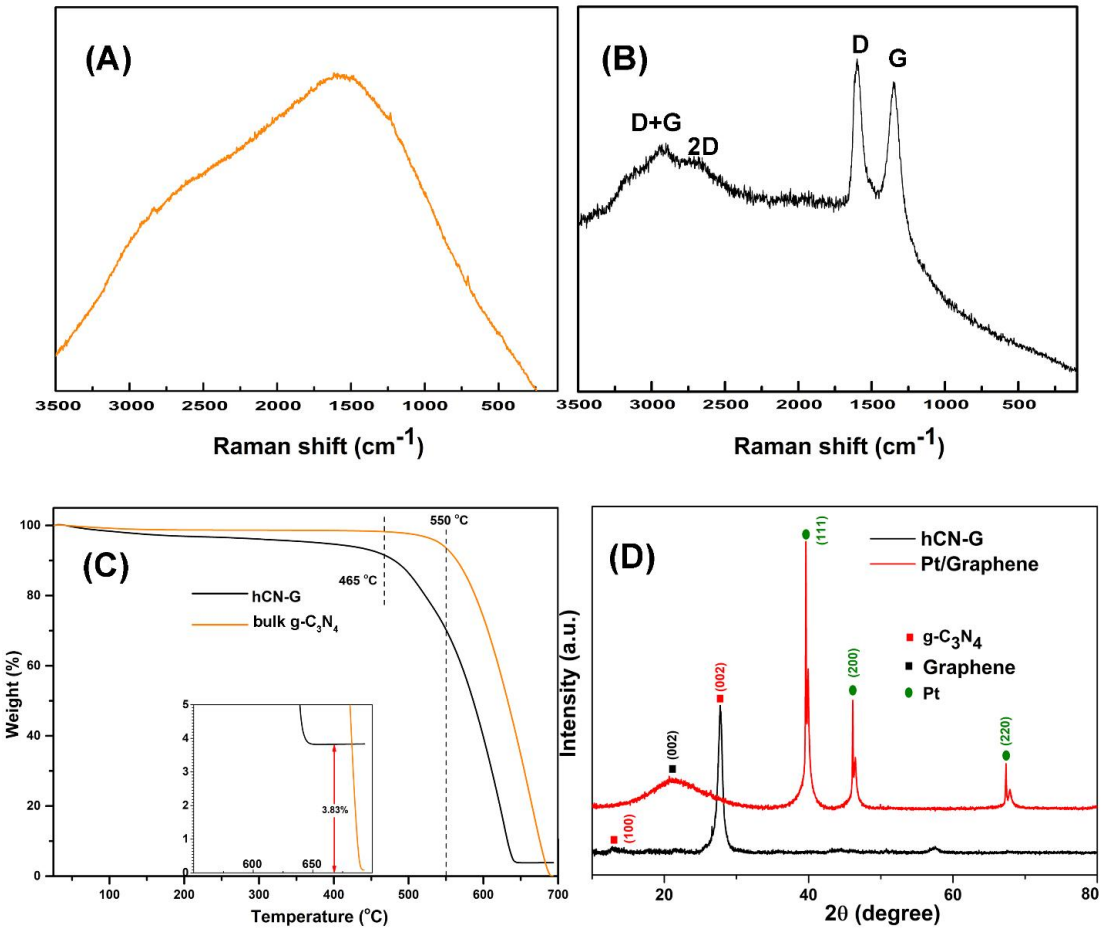

Figure 74. Raman spectra of (A) CN-b and (B) hCN-G, (C) TGA thermograms and high-resolution inset of the as-prepared samples, and (D) XRD patterns of hCN-G and Pt/graphene (TGA residue of hCN-G).

The remaining weights of CN-b and hCN-G at 700 ℃ were 0 wt.% and 3.83 wt.%, respectively (inset of Figure 74C). The amount of graphene in hCN-G was approximately 2.04 wt.%, after subtracting the platinum from the ICP measurement. Graphene is an exceptionally electrically conductive 2D material that can be used as a photoelectron acceptor and mediator at the surface of a photocatalyst to collect and separate excited charges.[105, 142] The residue of hCN-G after performing TGA to 700 °C was analyzed with HRP-XRD to define the crystalline structure of the graphene content of the sample (Figure 74D). The XRD spectrum of Pt/graphene revealed a peak at 21.4° (*d*-spacing of 4.15 Å), which can be attributed to the d_{002} interlayer distance of chemically converted graphene.[143] The prominent peak of the g-C_3N_4 at 27.7° (002) was lost, indicating that the g-C_3N_4 content in the hCN-G sample fully decomposed during annealing.

3.3.3. Optical Properties and Charge-carrier Separation and Transfer

The absorption properties and bandgaps of CN-b and hCN-G were analyzed by UV-vis absorption and UV-vis diffuse reflectance spectroscopy (UV-DRS) (Figure 75A, B, C). As shown in Figure 75A, CN-b and hCN-G exhibited characteristic absorptions near 385 nm and 380 nm, respectively. The absorption band of hCN-G extended beyond 650 nm, implying that it was capable of absorbing not only UV light, but visible light as well. This indicates the possibility of harvesting more photons under visible-light irradiation. The low energy absorption band of hCN-G was further confirmed by a DFT calculation, which showed an extended shoulder in the range of low absorbance and a much higher absorption coefficient compared with the hCN sample (Figure 75C, D). Based on UV-DRS spectra, Tauc plot spectra were used to calculate bandgap values. The Tauc plot equation is:[144]

$$(\alpha h\nu)^{1/n} = A(h\nu - E_g)$$

where α, h, ν, A, and E_g are the absorption coefficient, Planck constant, frequency of light, proportionality constant, and bandgap energy, respectively. Graphitic carbon nitride material is considered an indirect bandgap semiconductor, with an index value of n = 2 in Tauc's equation.[144] The estimated bandgap values (E_g) of the as-synthesized g-C_3N_4 were obtained from the intercepts of the tangents of the Tauc plot $(\alpha h\nu)^{0.5}$ curve vs. photon energy hν (Figure 75B). After solvothermal treatment, the bandgap value was approximately 2.91 eV, which was higher than the bandgap of CN-b (2.76 eV). This larger bandgap can be attributed to the well-known quantum confinement effect, in which the conduction and valence band edges shift in opposite directions, caused by exfoliation of hCN-G and multihole formation after solvothermal treatment.[145] The optical absorption property is altered by two opposing parameters: the quantum confinement effect increases the bandgap, but the holey defect density decreases it. Due to the formation of multiholes on the planar layer, hCN-G formed nanosheets in both the vertical and horizontal dimensions.

The optical absorption property of hCN-G is affected primarily by the quantum confinement effect rather than by its microscopic chemical structure. The bandgaps determined from UV-vis spectra of CN-b and hCN-G were 3.08 and 3.23 eV, respectively. The difference in

bandgap between CN-b and hCN-G in the solution phase (0.15 eV) is in agreement with the difference of this in the solid phase, which was measured by UV-DRS (Table S2).

The fundamental aspects of photocatalytic hydrogen evolution involve recombination of photogenerated electrons and holes, separation of photoexcited electrons, and migration and transfer of charge carriers.[40] Photoluminescence (PL), EIS, and TR-PL were used to study the properties of photoinduced electron-hole separation on the surface of the resulting samples (Figure 75D, Figure 75E, and Figure 75F). The PL spectra of synthesized CN-b and hCN-G were analyzed at an excitation wavelength of 340 nm. CN-b displayed a stronger fluorescence intensity, suggesting a higher charge-recombination capability. A significantly lower peak intensity was observed in hCN-G, indicating suppressed photoinduced charge recombination due to the increased charge-diffusion rate in the aromatic system of hCN-G. In addition, the blue shift of the PL peak from 456 nm of CN-b to 436 nm of hCN-G is consistent with the increase in bandgap energy.[146]

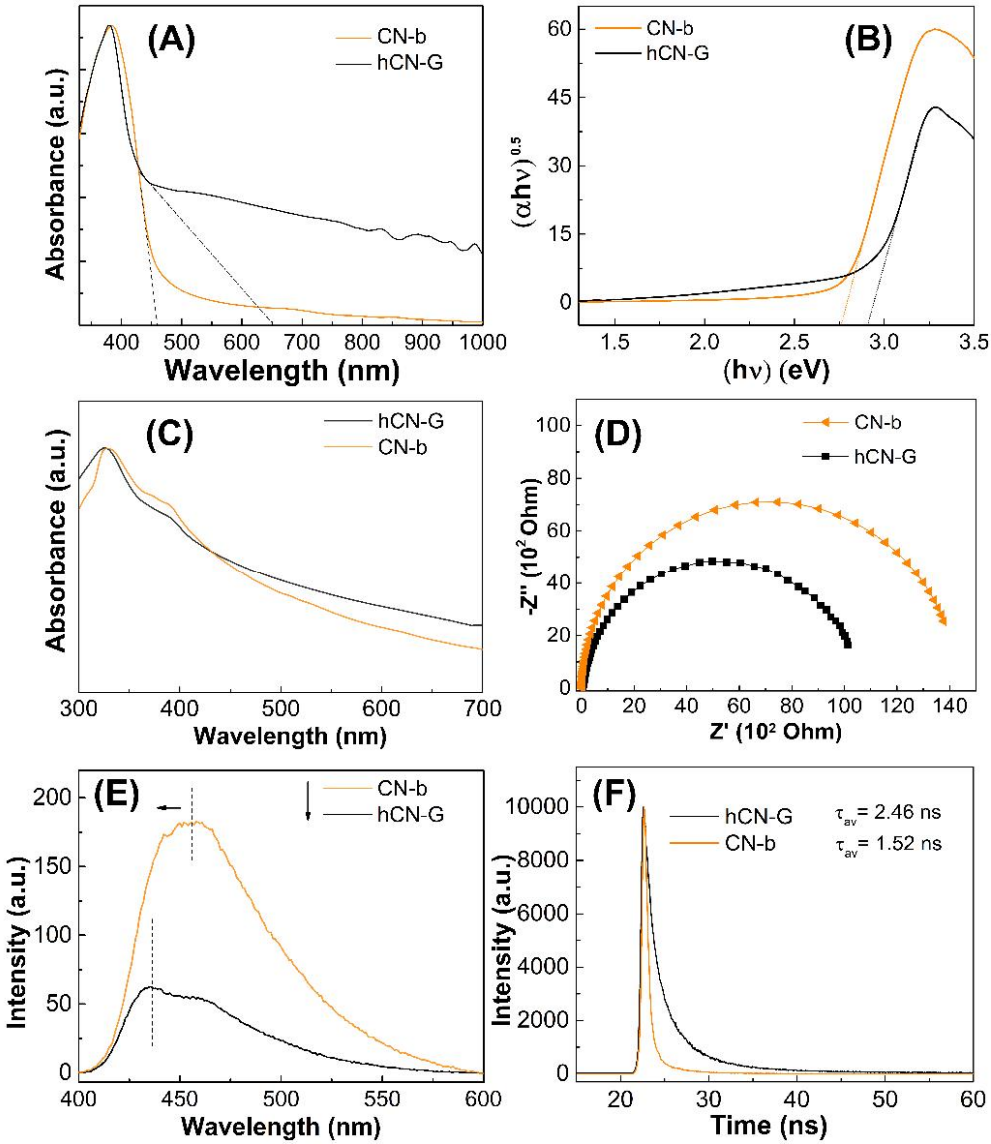

Figure 75. (A) UV-DRS spectra, (B) corresponding Tauc plots: hν (eV) and $(\alpha h\nu)^{0.5}$, (C) UV-vis absorption spectra, (D) EIS Nyquist plots, (E) PL emission spectra, and (F) TR-PL spectra for CN-b and hCN-G samples.

The recombination lifetimes of charge carriers can be determined through four mechanisms of band-to-band, trap-assisted in bulk, Auger, and surface recombination. Under 400 nm laser excitation, TR-PL decay spectra were measured to evaluate the radiative and non-radiative recombination of photoinduced electron-hole pairs. The decay rate was calculated using a well-fitted tri-exponential decay function with three excited-state lifetimes and their respective percentages (Figure 75F, Table S3). hCN-G exhibited a longer decay period (2.46 ns) than CN-b

(1.52 ns), indicating greater charge separation and transfer of photogenerated electron-holes in the hCN-G sample.

The charge-transfer processes in the resulting samples contributed to their capability to shuttle and transport charge carriers to evolution reactive sites. EIS was used to investigate the charge-transport behavior of the resulting photocatalysts. The hCN-G sample exhibited a smaller arc radius of the EIS Nyquist plot compared with CN-b (Figure 75D), indicating a reduced resistance of charge transfer from the catalyst surface to the molecules of the reactant. Additionally, we applied transient photocurrent measurements to exhibit charge separation and transfer through the bulk of the electrode to the surface, where the charge carriers can access to the reactants. The higher photocurrent response shows the higher charge separation efficiency in the catalyst structure. Compared to CN-b, the graphene formation in hCN-G accelerates charge carrier separation and diffusion through the carbon nitride structure and then effectively transfers them to the catalyst's surface, where the reaction will take place (Figure 76). Also, the grid-like structure in hCN-G efficiently decreases charge carrier diffusion length and thus reduces the recombination rate. According to charge-transfer facilitation at the interface, the multiholes on the surface of hCN-G prevent recombination and act as active sites for charge carriers to catch the reactant molecules easily. These results are consistent with the forthcoming DFT calculations, in which hCN-G displays strong electron coupling at the layer interface (Figure 78A, Figure 78B).

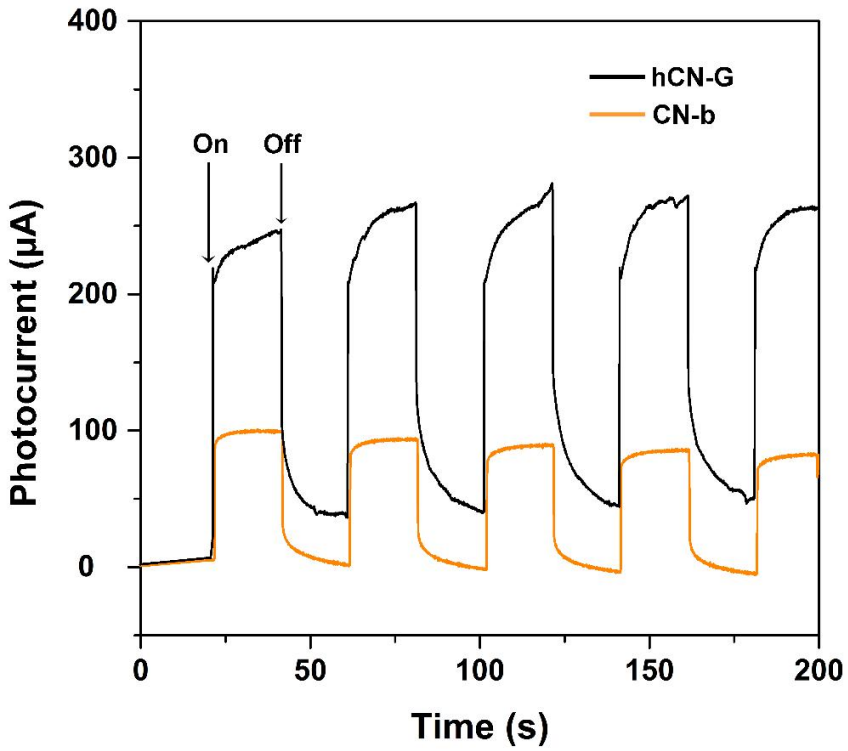

Figure 76. Transient photocurrent responses of CN-b and hCN-G electrodes in 0.1 M NaOH solution under visible-light irradiation.

3.3.4. DFT Calculations

The optimized geometries of graphene and multihole g-C_3N_4 (hCN) and the heterostructures of graphene and hCN are shown in Figure 77. The hCN structure was created by removing one unit of heptazine from a p(2×2) structure of pristine g-C_3N_4 and passivating the unsaturated nitrogen bond in hCN with hydrogen. The lattice parameters of the optimized graphene and hCN structures were 2.47 Å and 14.26 Å, respectively, which are in close agreement with lattice parameters reported previously for graphene (2.47 Å) and hCN (14.16 Å).[51] The hCN-G was prepared using the Atomistic ToolKit Virtual NanoLab (ATK-VNL) (version 2016).[147] The lattice parameter of the created hCN-G was 13.74 Å. The calculated lattice mismatch between graphene and hCN was reasonable at 2.4%.[148]

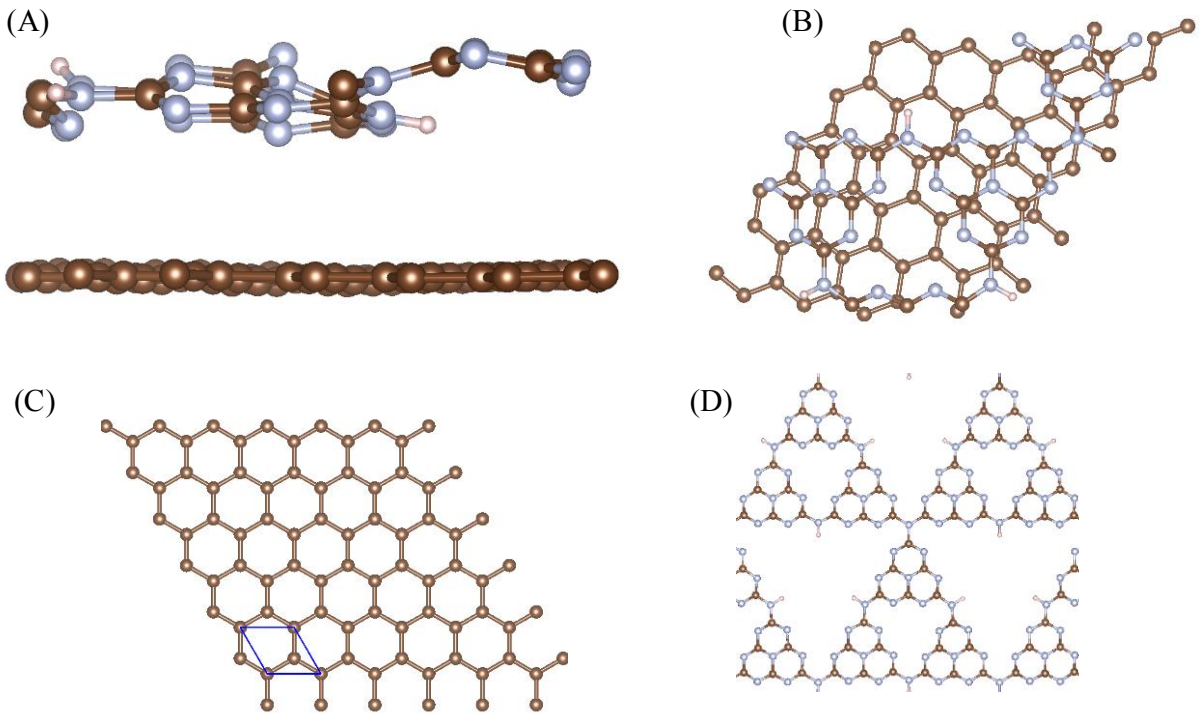

Figure 77. Optimized geometry for hCN-G for side view (A) and top view (B), for graphene (C) and for hCN (D).

To determine whether the designed hCN-G is chemically stable, the interface binding energy was computed as:[51]

$$\Delta E_b = E_{hCN-G} - E_{\text{graphene}} - E_{hCN} \qquad (1)$$

where $E_{hCN\text{-}G}$, $E_{graphene}$, and E_{hCN} are the ground-state energy of the hCN-G, graphene, and hCN, respectively. The computed binding energy (−2.27 eV) was relatively high and may be responsible for the reduced interlayer spacing (2.82 Å) between graphene and hCN compared with that between graphene and pristine g-C_3N_4 (3.03 Å).[51]

Calculations were conducted to gain insight into the observed improvement in hCN-G properties by computing the charge-density difference, band structure, density of states, and absorption coefficient.

The charge-density difference was calculated using the equation:[80]

$$\Delta\rho = \rho_{hCN-G} - \rho_{graphene} - \rho_{hCN}, \qquad (2)$$

where $\rho_{hCN\text{-}G}$, $\rho_{graphene}$, and ρ_{hCN} are the electron densities of hCN-G, graphene, and the hCN species, respectively.

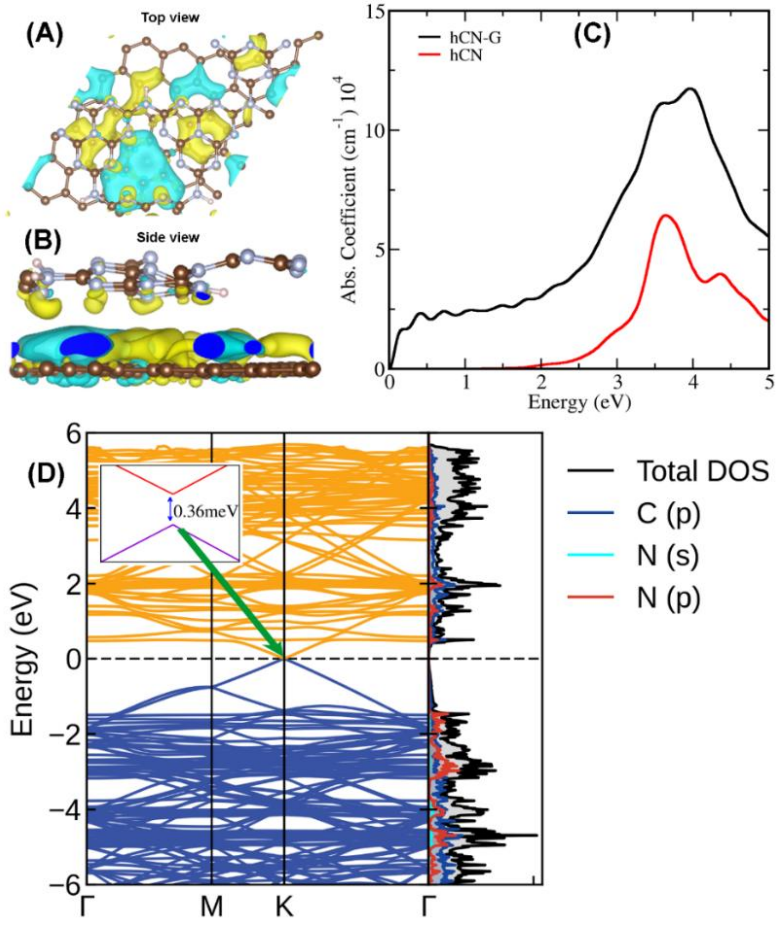

Figure 78. Charge-density difference plots: (A) side view and (B) top view, showing an electron-hole puddle on the graphene layer. Brown, silver, and pink balls represent carbon, nitrogen, and hydrogen atoms, respectively. (C) The absorption coefficient of hCN and the heterostructure (hCN-G). (D) Band structure and partial density of states for the heterostructure (hCN-G). The plot in the inset represents the enlarged view of the band edges at the band edges.

The charge-density plots (Figure 78A, Figure 78B) show the electron-hole puddle on the graphene substrate layer. The yellow and light-blue isosurfaces indicate charge accumulation and depletion in graphene and carbon nitride. The electron-hole puddle is evidence of strong electron coupling at the interface between hCN and graphene. As a result, graphene as an electron acceptor can open a pathway for photoexcited electrons from g-C_3N_4. This result supports the finding on

the charge-transfer process by EIS measurement and charge carriers' recombination lifetime in TR-PL analyses. From here, the increase in charge-transport behavior and the significant enhancement in prevention of charge recombination in hCN-G are understood to be due to the formation of electron-hole buddle.

To see whether this generated puddle contributes to the absorption spectra, we plotted the absorption coefficient of the hCN and the hCN-G (Figure 78C). Compared to hCN, the absorption coefficient of hCN-G showed a much higher optical absorption intensity for the whole range of energy. Notably, in the field of low energy, it appears that hCN-G has expanded in visible-light harvesting, as evidenced by a shoulder-like absorption band. Furthermore, enhanced optical absorption in the visible region of the solar spectrum is seen in the case of hCN-G compared with hCN, which indicates the improved performance of hCN-G for photoabsorption efficiency, as observed in our experiment. We further computed the electronic properties of hCN-G to obtain the chemical intuition for its increased visible-light response. In Figure 78D, the heterostructure illustrates the graphene-like character around the Fermi level (Figure 79), while features of the hCN (Figure 80) are visible just below the valence-band maxima and above the conduction-band minima. This indicates strong electron coupling at the interface, resulting in enhanced absorption, in agreement with a previously reported study.[148]

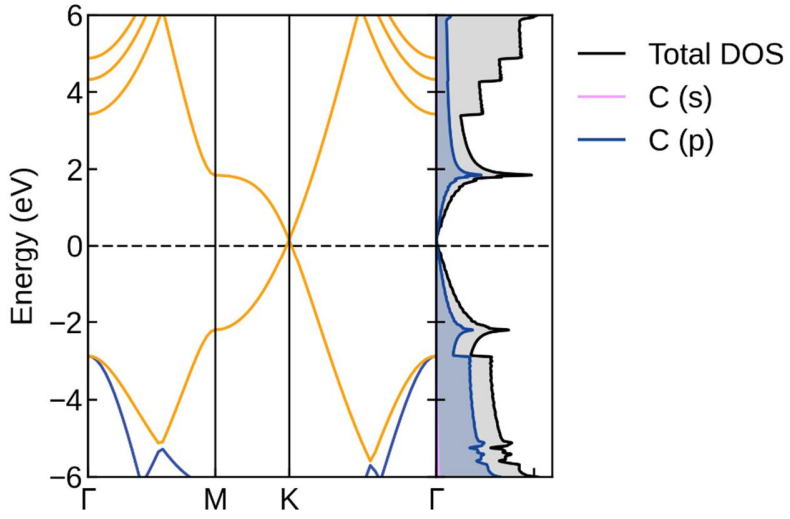

Figure 79. Band structure and partial density of states for graphene.

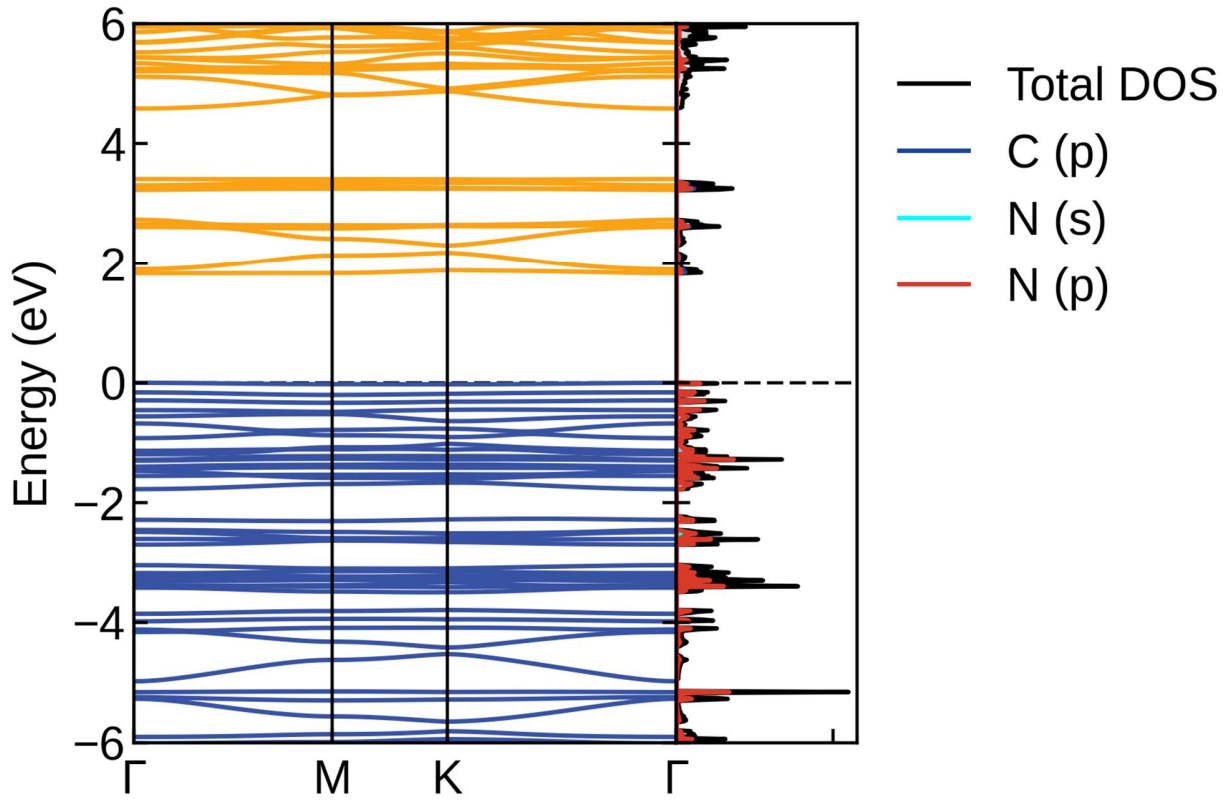

Figure 80. Band structure and partial density of states for holey g-C_3N_4 (hCN) structure.

3.3.5. Photocatalytic Activities

The photocatalytic activities of CN-b and hCN-G were measured under irradiation from a solar simulator, with platinum nanoparticles supported on the photocatalyst as a co-catalyst (2 wt. %), TEOA as a sacrificial agent, and Eosin Y as a photosensitizer. Photoactivity toward hydrogen evolution was optimized to measure the photocatalytic performance of the resulting photocatalysts. The transparent photocatalytic performance was assessed by a detailed evaluation system, which enabled comparisons among photocatalytic hydrogen evolution systems (Section 4.2.3).[46]

The optimized photoactivity point of hCN-G was at 0.1 mg.mL^{-1}, while the CN-b sample showed a stationary point at 0.2 mg.mL^{-1} (Figure 81A), because CN-b has a large lateral size and high agglomeration. The optimized photocatalyst performances at the stationary points are inversely proportional to the lateral size and porosity of the nanosheets. The average H_2 evolution rate at the optimized point of hCN-G was as high as 16,832.9 µmol g^{-1} h^{-1} (Figure 81D, Table 19),

which was more than 7.5 times that of CN-b (2241.2 μmol g^{-1} h^{-1}), corresponding to an amount of H_2 produced versus reaction time at different concentrations of photocatalysts (Figure 81B and C). Furthermore, the HER per unit of specific surface area (Figure 81D) of hCN-G was enhanced to 243.6 μmol h^{-1} m^2, an almost 2.4-fold improvement for CN-b.

This enhancement of the HER versus S_{BET} is lower than the improvement of HER versus the $Mass_{catalyst}$, which is understandable because 2D g-C_3N_4 material has a tendency to restack layers due to van der Waals forces during the drying process into a powder form for the Brunauer–Emmett–Teller specific surface area measurement. The colloidal dispersion form of hCN-G exists in the reaction media, which shows more advanced surface-accessible sites than it does in a powder form. These results indicate that the monolayer grid-like structure of hCN-G with a uniform multihole on the planar sheet and a large specific surface area promotes dispersion of platinum co-catalysts, maximizing the accessible active sites, and enhancing photocatalytic activity toward H_2 evolution.

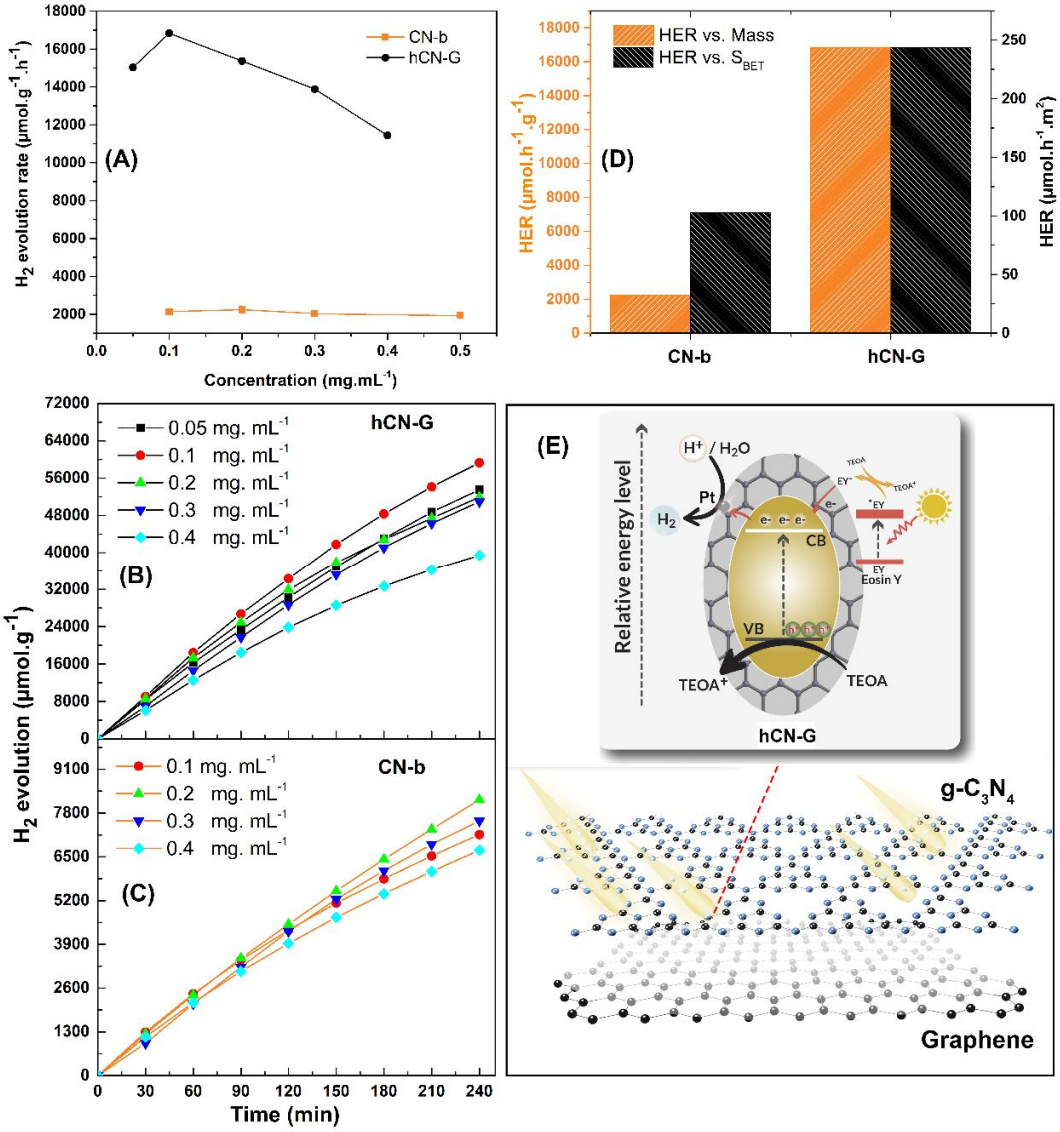

Figure 81. A) Optimization study on H_2 evolution rate vs. photocatalyst concentration for CN-b and hCN-G, corresponding to the amount of H_2 produced vs. reaction time at different concentrations of photocatalysts. B) hCN-G and C) CN-b. D) Averaged H_2 evolution rate at the optimized points vs. photocatalyst mass and specific surface area. E) Photocatalytic mechanism for hCN-G under simulated sunlight irradiation.

The hCN-G photocatalyst also exhibits good stability. The storage of the photocatalysts in the air for over 209 days has shown no detectable change in their structure and optical properties. The H_2 evolution performance of hCN-G was almost retained after seven months of storage at RT. Furthermore, the hCN-G possesses good stability during the photocatalytic H_2 evolution reaction,

as shown in Figure 82. Due to photocorrosion, the H_2 evolution rate of hCN-G briefly decreased at the beginning of each cycle. After the stability test, we further analyzed the crystalline structure (XRD, Figure 83) and nanostructure (AFM, Figure 84) of hCN-G after the stability test. It's shown that the crystal and morphology of hCN-G were maintained after the reaction.

Photocatalytic Cyclic Stability Test

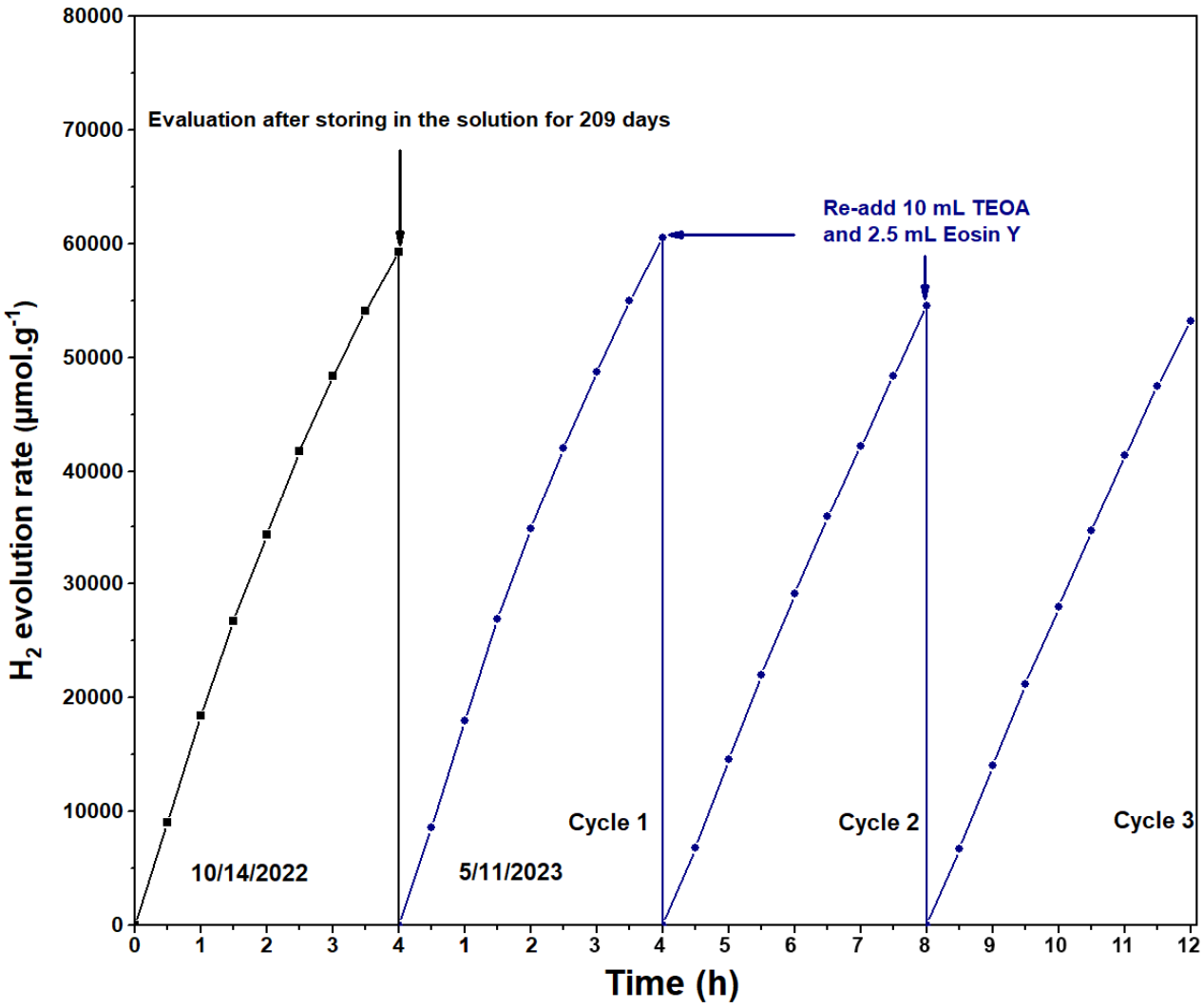

Figure 82. Cyclic stability test of hCN-G for photocatalytic H_2 production.

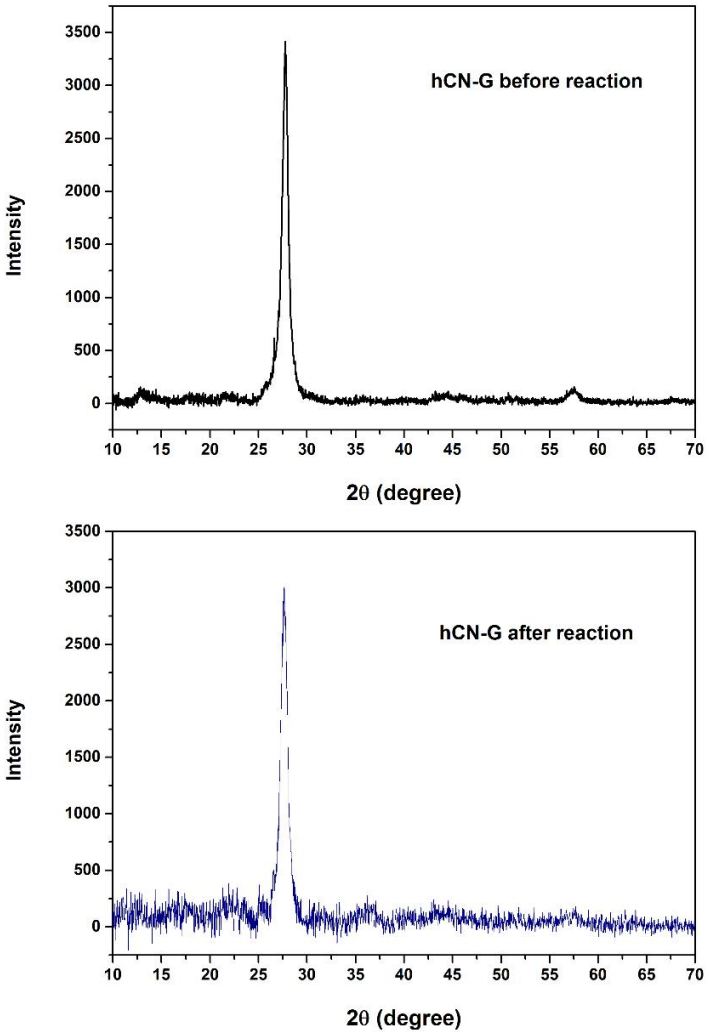

Figure 83. XRD spectra of hCN-G before and after the photocatalytic stability test.

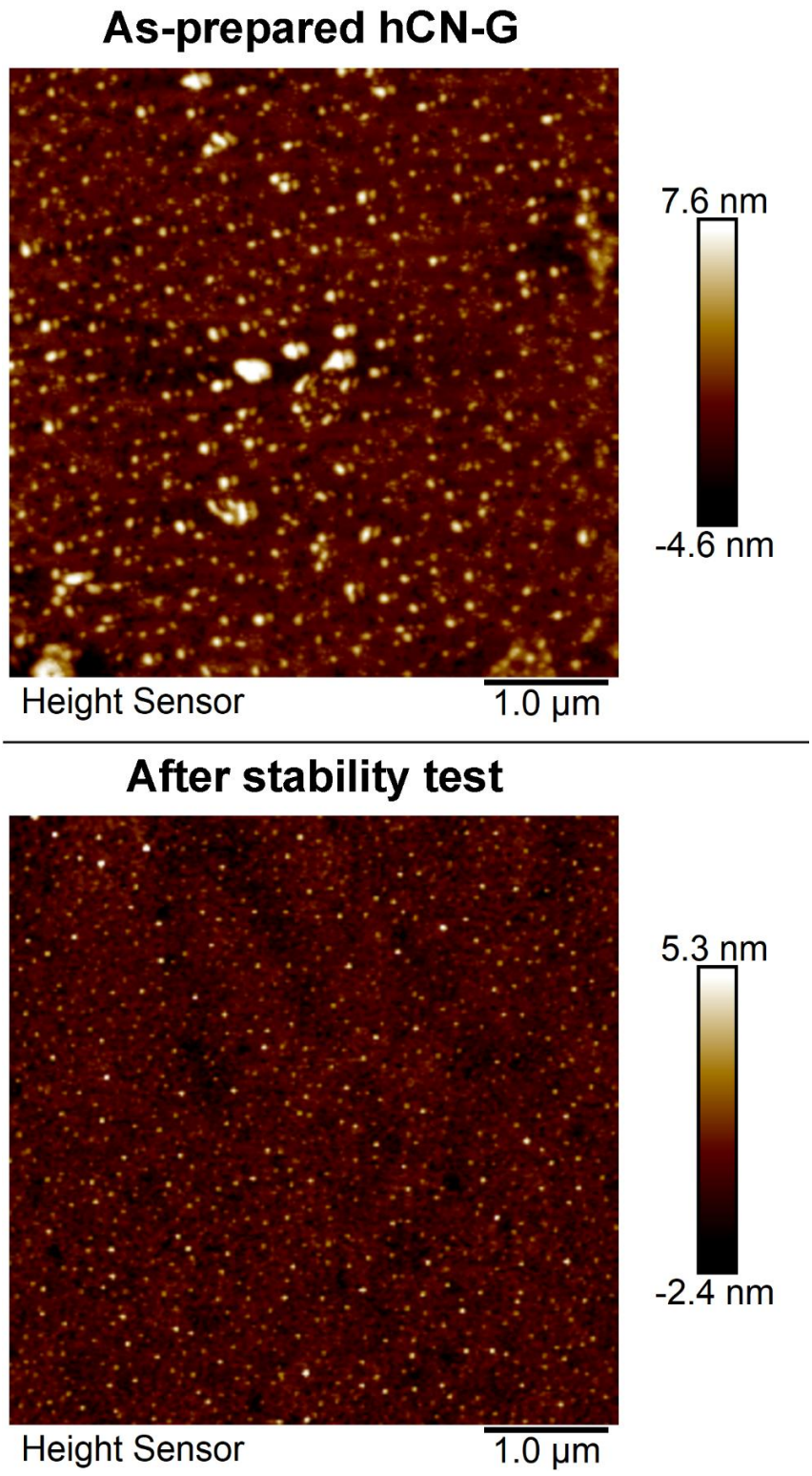

Figure 84. AFM images of hCN-G before and after the photocatalytic stability test.

A possible mechanism of the photocatalytic H_2 evolution is proposed in Figure 81E. Under 1 sun of a solar simulator irradiation, the hCN-G can absorb photons with energy equal to or greater than the intrinsic bandgap of hCN-G. Above that, the excited electrons transfer from the valence band to the conduction band and release the positive holes in the valence band. In parallel, EY reacts with TEOA to form EY^- after adsorbing photons, which then transport the electrons to g-C_3N_4's conduction band.[111] The electrons then move to the graphene layer on the surface of hCN-G and are transferred to the platinum co-catalyst particles, where the H^+/H_2O is reduced to create H_2 molecules. In contrast, the positive holes in the valence band are oxidized and consumed by TEOA.

Table 19. Comparison of photocatalytic activity toward H_2 evolution of the reported g-C_3N_4 and its composites.

Materials	Co-catalyst	Sacrificial donor	Photo-sensitizer	Light source	Light Intensity (mW cm^{-2})	Hydrogen evolution rate (μmol h^{-1} g^{-1})
hCN-G This work	Pt, 1.8 wt. %	TEOA	Eosin Y	Simulated sunlight (Newport, LHS-7320)	100	16,832.9
C_3N_4-THF**[39]**	Pt, 2.3 wt. %	TEOA	Eosin Y	Simulated sunlight (Newport, LHS-7320)	100	31,256.9
EY-mpg-C_3N_4**[111]**	Pt, 1 wt. %	TEOA	Eosin Y	300 W Xe lamp ($\lambda \geq 420$ nm)	NR	3,850
MMT/g-C_3N_4**[149]**	NiCoP, 15 wt. %	TEOA	Eosin Y	300 W Xe lamp ($\lambda \geq 420$ nm)	NR	10,930
MoS_2/g-C_3N_4	None	TEOA	Eosin Y	300 W Xenon arc lamp (New Port, 6279NS) ($\lambda \geq 420$ nm)	NR	1,787
g-C_3N_4/C@Ni_3S_4 /Ni_2P-30**[150]**	C@Ni_3S_4 /Ni_2P	TEOA	Eosin Y	300 W Xe lamp ($\lambda \geq 420$ nm)	NR	14,490

EY-g-C3N4-600**[113]**	Pt, 3 wt.%	TEOA	Eosin Y	400 W Hg lamp ($\lambda \geq 420$ nm)	6.79	1,500
CPCN-1***[151]**	Pt, 1 wt.%	TEOA	None	300 W Xe lamp ($\lambda \geq 420$ nm)	88.0	1,493.3
PCN/OMs**[109]**	Pt, 3%	TEOA	None	300 W Xe lamp ($\lambda \geq 420$ nm)	NR	4630
Hollow C_3N_4 nanospheres**[110]**	Pt, 3 wt. %	TEOA	None	300 W Xe lamp ($\lambda \geq 400.5$ nm)	49.4	4480
$NiFe_2O_4$/mpg-CN**[112]**	None	TEOA	None	300 W Xe lamp ($\lambda \geq 420$ nm)	NR	1820
EY-g-C_3N_4-T**[113]**	Pt, 7 wt. %	TEOA	None	450 W Xe short arc lamp ($\lambda \geq 420$ nm)	NR	1500
Flower MoS_2/g-C_3N_4**[114]**	Pt, 2 wt. %	Methanol	None	300 W Xe lamp (Newport) ($\lambda \geq 420$ nm)	100	867.6
Quasi-sphere g-C_3N_4**[91]**	Pt, 3 wt. %	TEOA	None	300 W Xe lamp ($\lambda \geq 420$ nm)	NR	613.4
Holey CNS**[73]**	Pt, 3 wt. %	TEOA	None	300 W Xe lamp ($\lambda \geq 400$ nm)	NR	2320
g-C_3N_4 nanosheets**[115]**	Pt, 3 wt. %	TEOA	None	300 W Xe lamp ($\lambda \geq 420$ nm)	NR	1860
OH-CN3**[92]**	Pt, 1 wt. %	Lactic acids	None	300 W Xe lamp ($\lambda \geq 420$ nm)	NR	320
P-doped g-C_3N_4**[116]**	Pt, 1 wt. %	TEOA	None	300 W Xenon arc lamp ($\lambda > 400$ nm)	NR	1596
g-C_3N_4			None			108
g-C_3N_4-$SrTiO_3$:Rh**[117]**	Pt, wt 0.5%	Methanol	None	300 W Xenon arc lamp ($\lambda > 415$ nm)	NR	2233
g-C_3N_4						107

Se/Modified g-C_3N_4**[118]**	Pt, wt 1%	TEOA	None	150 W Xenon arc lamp (λ > 455 nm)	NR	1500
g-C_3N_4						932
CdS/g-C_3N_4/CuS**[119]**	None	Na_2S/Na_2SO_3	None	350 W Xenon arc lamp (λ > 420 nm)	70	1151.2
CdS						211.6
Carbon fiber/gC_3N_4**[120]**	Pt, wt 1%	TEOA	None	350 W Xenon arc lamp (λ > 420 nm)	180	1080
g-C_3N_4						234.8
rGO/g-C_3N_4**[121]**	Pt, wt 1%	Lactic acid	None	LEDs (3 W, 420 nm)	80	874
g-C_3N_4						667
O-containing groups/Modified g-C_3N_4**[122]**	Pt, wt 1%	Lactic acid	None	LEDs (420 nm)	90	752
g-C_3N_4						108
g-C_3N_4 with remove surface defects**[123]**	Pt, wt 3%	TEOA	None	450 W Xe lamp (λ > 420 nm)	NR	455
g-C_3N_4						102
Graphene/gC_3N_4**[124]**	Pt, wt 1.5%	Methanol	None	300 W Xenon arc lamp (λ > 400 nm)	180	451
g-C_3N_4						147
Ag/Ag_2S/g-C_3N_4**[125]**	Ag/Ag_2S	Methanol	None	LEDs (3 W, 365 nm)	80	500
g-C_3N_4						2
MWCNT/g-C_3N_4**[126]**	None	Methanol	None	300 W Xenon arc lamp (λ > 395 nm)	209	44
C-dots/g-C_3N_4/Ti**O_2**[127]	None	TEOA	None	350 W Xenon arc lamp	70	210

g-C_3N_4/TiO_2						40
$Ni(OH)_2$-g-C_3N_4**[128]**	None	TEOA	None	350 W Xenon arc lamp (λ > 400 nm)	180	152
g-C_3N_4/0D-ZnO**[129]**	Pt, wt 1%	TEOA	None	300 W Xenon arc lamp (λ > 420 nm)	NR	322
g-C_3N_4						65

3.4. Conclusion

We fabricated self-assembled graphene on a grid-like structure of 2D g-C_3N_4 by an environmentally sustainable and simple solvothermal method in ethyl alcohol. The grid structure of a monolayer g-C_3N_4 nanosheet resulted in an enlarged surface area, more accessible active sites, and increased mass transfer and charge separation. The multihole structure of hCN-G in the reaction media advantageously prevented agglomeration and shortened the charge-diffusion length to the edges of the holes instead of the active sites at the layer boundaries. The introduction of graphene to hCN-G resolved the high charge-recombination rate of bare g-C_3N_4, in which graphene acts as an electron acceptor and mediator, followed by transfer of electrons to the high-percentage PtO co-catalyst nanoparticles, which direct the reversible reaction toward the generation of hydrogen gas. The resulting 2D hCN-G nanosheets achieved a performance of 16,832.9 μmol g^{-1} h^{-1}, a more than 7.5-fold improvement in photocatalytic hydrogen evolution compared with bulk g-C_3N_4. Our density functional theory calculations investigation validated the experimental observations of the electron-hole puddle on the graphene sheet and the enhanced photoabsorption in the visible region in hCN-G. The facile method with a low environmental impact demonstrated in this work is promising for the large-scale production of sustainable photocatalysts for practical applications in solar energy conversion.

CHAPTER 4

Overview of Chapter 4

Proceeding with the large-scale production of green hydrogen requires overcoming some technical problems for an efficient system. One of the critical issues of applying particulate photocatalysts for a huge area is the full dispersion of photocatalysts in reaction media. In order to resolve this important issue, we aim to create a highly dispersion of holey graphene/g-C_3N_4 in aqueous, which maximizes the catalyst surface accessible active sites in reaction media. Two-dimensional (2D) graphene has an extremely high specific surface area, excellent environmental compatibility, and high adsorption capacity. Therefore, graphene/g-C_3N_4 ternary hybrids can be ameliorated the high recombination rate and a low surface area besides the poor movement of the charges of g-C_3N_4. Herein, a high-surface-area-inspired water-soluble holey graphene/g-C_3N_4 colloidal nanoparticles for H_2 evolution was successfully synthesized using a facile mixing process of holey graphene oxide with oxidized g-C_3N_4 (HoCN-GO). The HoCN-GO has restored the initial valuable photocatalytic properties but kept highly soluble in water. The HoCN-GO photocatalyst performed a superior photocatalytic activity toward H_2 evolution at a rate of 11295.3 µmol g^{-1} h^{-1} under 1 Sun illumination of Solar Simulator, which is 16.2 times and 4.4 times higher than that of bulk g-C_3N_4 and oxidized g-C_3N_4, respectively.

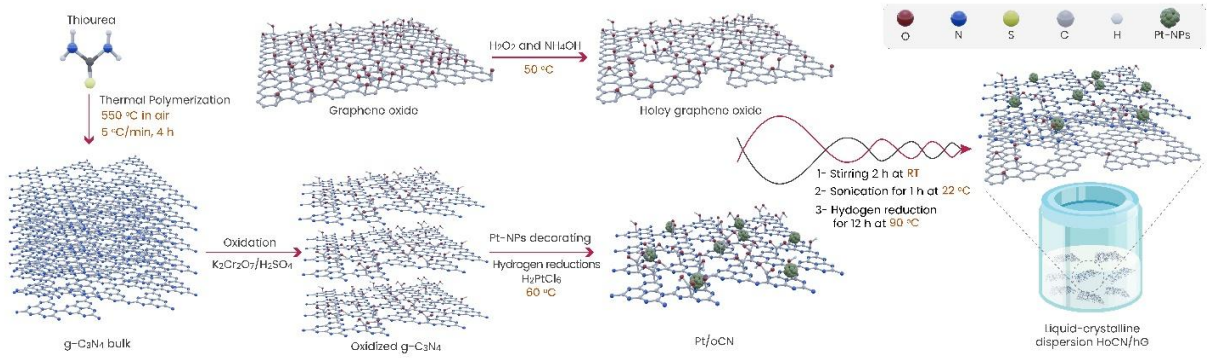

4. Highly Dispersion of Holey Graphene/g-C_3N_4 Composite for Photocatalytic Hydrogen Evolution Under Simulated Sunlight Irradiation

4.1. Introduction

Hydrogen is a clean alternative to fossil fuels due to its high gravimetric energy density, abundance on earth, and eco-friendliness. Production of hydrogen from water is a promising approach for solar energy conversion to clean chemical fuel. Photocatalytic hydrogen evolution reaction (HER) by half-reaction of water-splitting has been intensively studied for green, low-cost, and large-scale production of H_2 fuels. Hydrogen evolution brought by high-energy UV light has been extensively studied for over 40 years since Fujishima and Honda first discovered photoelectrochemical water splitting into H_2 over titanium dioxide electrodes.[3] However, the Earth's surface is only received by less than 5 percent of solar ultraviolet radiation.[6] Thus, recent research in semiconductor materials promoted by visible light has led to the development of photocatalysts for hydrogen evolution. As one of these materials, graphitic carbon nitride (g-C_3N_4) has proven to be an excellent visible-light-driven photocatalyst for hydrogen production.[16, 152] It is well known as a noble metal-free, Earth-abundant and low-cost photocatalyst for producing H_2 and H_2O_2 from water. Furthermore, g-C_3N_4 is commercially available, and it can be easily synthesized through the pyrolysis process of urea, thiourea, cyanamide, dicyandiamide, and melamine.[9] However, bulk g-C_3N_4 photoactivity is hampered by low surface area resulting in low colloidal dispersion in reaction media, which suffers low active site accessibility. The high recombination rate of charge carriers and poor electrical conductivity of multilayers of bare g-C_3N_4 also hindered its potential for practical use applications.[39] Therefore, the modification of pristine g-C_3N_4 to achieve high dispersion of photocatalysts in water and high electrical conductivity are crucial parameters to maximize their photoactivity. Following this work, many research groups attempted to maximize the solubility of g-C_3N_4 photocatalyst in water, including oxidation of bulk g-C_3N_4 methods,[26] hydroxides supported thermal polymerization of melamine.[18] Unfortunately, these methods obtained a very low yield of photocatalysts and poor recyclability.

Graphene is a 2D allotrope of carbon, whose structure is one-atom-thick planar sheets of sp^2-bonded carbon atoms that are densely packed in a honeycomb crystal lattice.[47] Graphene has both of fundamental study and also for a wide range of potential applications due to its excellent mechanical, thermal, optical, and electrical properties.[153] Moreover, graphene possesses a

superior electron transfer speed of 200,000 $cm^2 V^{-1} s^{-1}$, and it has a very high specific surface area of 2,630 $m^2 g^{-1}$, which makes graphene an ideal acceptor, mediator of photoinduced electrons from excited electron donors, and a good supporter to improve the photoactivity of the hybrid photocatalysts. Although 2D materials (graphene, g-C_3N_4) own a high specific surface area, which is promising to obtain maximized photocatalytic accessible active sites, however, due to the strong π–π interaction and van der Waals (vdW) forces between 2D sheets, these materials have a tendency of layer restacking to form multilayers during the photocatalytic reaction process. Consequently, the photoactivity of 2D materials reduces by reaction time due to the agglomeration, which causes a decrease in accessible active site concentration. To prevent the aggregation of graphene sheets, a solution method was recently employed to prepare holey graphene with numerous ultrasmall holes on the planar of graphene sheets.[154] The resulting holey graphene had a superior colloidal dispersion in water without agglomeration for years because the holes decreased interaction sites, enhanced hydrophilic properties due to the introduction of more functional groups at the hole edges, and reduced hydrogen bonding between layers.

Inspired from above benificial findings, several graphene/g-C_3N_4 heterostructures have been reported for various photocatalysis applications recently.[155] Song et al. reported a 2D g-C_3N_4@graphene@g-C_3N_4 sandwich structure through two-step thermal polymerization using melamine and graphene oxide (GO) precursor. The visible light adsorption of the photocatalyst was dramatically increased in the visible region due to the introduction of GO, and the hydrogen evolution rate increased 14.3 times compared to pristine g-C_3N_4. Using protonating g-C_3N_4 method by treatment of g-C_3N_4 and simply mixing with the innate negative charge on the surface of GO can fabricate a GO/g-C_3N_4 heterostructure, followed by chemical reduction to achieve RGO/g-C_3N_4 photocatalyst.[156, 157] Apart from conventional thermal annealing or merely mixing of GO and g-C_3N_4, a facile hydrothermal method can also afford the graphene/g-C_3N_4 composite with smaller sheet fragments.[155, 158, 159] In Chapter 2, we discovered the engineering holey defects on g-C_3N_4 via solvolysis in organic solvents by etching effects and simultaneously generating self-assembled graphene on holey g-C_3N_4 heterostructure,[39] which was significantly enhanced the photocatalytic toward H_2 evolution under simulated sunlight irradiation.

Herein, enlightened by the above beneficial of 2D/2D heterostructure of g-C_3N_4 with graphene and the complete solubility of holey graphene in water, we report a facile method for hydrogen reduced g-C_3N_4 and holey graphene oxide (HoCN-GO) hybridization preparation through a merely

mixing of chemically oxidized g-C_3N_4 (oCN) with holey graphene oxide (holey GO), followed by hydrogen reduction of oCN-GO at 90 °C (Scheme 1). The resulted 2D/2D of HoCN-GO heterostructure establishes a strong π–π interaction, vdW force, and hydrogen bonding between layers but still maintains a highly dispersion in the reaction media. The HoCN-GO interface showed strong electron-hole coupling to openning a pathway for photoexcited electron from g-C_3N_4 moves to holey GO layer for further evolution reaction, resulting in increasing charge transfer and separation, increased visible absoption for oCN, and resulting in photocatalytic toward H_2 evolution enhencement. Furthermore, holey GO works as a carrier to prevent agglomeration of HoCN-GO composite, which generates a highly dispersion of HoCN-GO in reaction media, which maximizing the accessible active sites of the photocatalyst. The effect of hydrogen reduction level on photoactiviy of HoCN has been studied. The HoCN-GO achieved a high hydrogen evolution rate at 11,295.3 μmol h^{-1} g^{-1} under the MAX-350's solar module irradiation, which folds over 16 times higher than that of bare g-C_3N_4. The large-scale synthesis of HoCN-GO from the earth-abundant precusors (thiourea and graphite) is promising for the mass production of green hydrogen through photocatalysis.

4.2. Experimental and Methods

4.2.1. Materials

Thiourea (CH_4N_2S, ≥99%), triethanolamine (TEOA, $C_6H_{15}NO_3$, 99%), chloroplatinic acid solution (H_2PtCl_6, 8 wt.% in H_2O), Eosin Y, sulfuric acid (H_2SO_4), potassium dichromate ($K_2Cr_2O_7$, 99 %), ammonium hydroxide solution (NH_4OH, 28.0-30.0% NH_3 basis), and hydrogen peroxide (H_2O_2, 30 % (w/w) in H_2O) were purchased from Sigma Aldrich. Graphene oxide (GO-V50) was purchased from Standard Graphene (Korea). High-purity argon gas was purchased from MS Gas Corporation (Korea). All chemicals were used as received without further purification.

4.2.2. Synthesis of chemically oxidized g-C_3N_4

Chemically oxidized g-C_3N_4 was synthesized through the chemical oxidation of bulk g-C_3N_4 as described in our previous reports.[39, 131] First, thiourea (CH_4N_2S) precusor was placed in a crucible covered with Al foil was annealed at 500 °C in air for 4 h with a ramping rate of 5 °C/min. The obtained yellow aggregates were well-ground to a powder (bulk g-C_3N_4) for further chemical oxidation. In a 250 mL flask, $K_2Cr_2O_7$ and H_2SO_4 were magnetically stirred for 40 min at RT. When the solution had turned brown, bulk g-C_3N_4 was added to the solution and stirred

continuously for 1 h. The solution was then diluted in DI water and cooled naturally before rinsing out multiple times to completely remove the acid until the pH of the dispersion reached 7. The undispersed g-C_3N_4 was eventually removed using a centrifuge and the water-dispersible chemically oxidized g-C_3N_4 was named oCN.

4.2.3. Synthesis of holey graphene oxide

Holey graphene oxide (holey GO) was synthesized by etching the GO with a mixture of ammonia solution and hydrogen peroxide. Briefly, NH_4OH (12.5 mL) and H_2O_2 (12.5 mL) were added to the GO dispersion (500 mL, 1 mg mL^{-1}). Subsequently, the mixture was placed in an oil bath at 50 °C and kept under magnetic stirring at 50 rpm 5 h. After the reaction, the excess reactants and byproducts in the etched GO solution were separated by centrifuging at 12,000 rpm for 90 min, and removed by discarding the supernatant.

4.2.4. Synthesis of hydrogen reduction of chemically oxidized g-C3N4/holey GO

First, a calculated amount of 3 wt. % platinum co-catalyst was decorated on resulting g-C_3N_4 samples by hydrogen reduction in aqueous phase at 90 ℃, using chloroplatinic acid as the platinum precursor, as previously described.[57, 160] Second, The study of hydrogen reduction of oCN (HoCN) by atomic hydrogen was carried out by applying the reaction in a oCN solution at 90 ℃ for a given time (0.25, 0.5, 1, 3, 5, 12, 18, or 24 h).[57] The stationary point of photocatalyst performance of HoCN was reached at 12 h of reaction. Finally, the hydrogen reduction of chemically oxidized g-C_3N_4/holey graphene oxide was obtained via a merely mixing of HoCN-12h and holey graphene oxide (holey GO) by stirring for 2 h at RT, following by subjected to sonication for 1 h (Jeiotech UCP-10, 490 W) at approximately 25 ℃. Then, the mixture was applied the atomic hydrogen reduction at 90 ℃ for 12 h. The resulting sample was named HoCN-GO.

4.2.5. Characterizations

The crystalline structures of the prepared samples were measured using high-resolution powder X-ray diffraction (HRP-XRD) with a Cu Kα X-ray source at a wavelength 1.5415 Å and a scan rate of 2° (2θ)/min (Rigaku D/MAZX 2500 V/PC high-power diffractometer, Tokyo, Japan). Fourier-transform infrared spectroscopy (FT-IR; Nicolet 380 spectrometer, Thermo Scientific Nicolet iS5 with an iD1 transmission accessory, Waltham, MA, USA) was used to characterize the functional groups of the produced photocatalysts. X-ray photoelectron spectroscopy (Thermo

Scientific K-Alpha system, Waltham, MA, USA) was used to analyze the composition, chemical state, and electronic state of the elements. The elemental composition (carbon, hydrogen, nitrogen, oxygen, and sulfur) of the samples was analyzed with an elemental analyzer (Flash 2000, Thermo Scientific). The platinum element composition of the prepared samples was determined by an inductively coupled plasma–optical emission spectrometer (ICP-OES; 700-ES Varian, Mulgrave, Australia). Scanning electron microscopy (SEM; JSM-600F JEOL, Tokyo, Japan) was used to investigate the microstructure and the catalyst morphology. The microstructure and distribution of the platinum nanoparticles were examined using high-resolution transmission electron microscopy (HR-TEM; JEL-2100F JEOL, Tokyo, Japan). A spherical aberration–corrected scanning transmission electron microscope (CS-STEM, JEM-ARM300F, JEOL) with a 300 kV electron beam was used to study the grid-like structure of hCN-G samples at high spatial resolution. The lateral dimensions and height profiles of the resulting g-C_3N_4 sheets were measured by commercial atomic force microscopy (AFM, Park NX20, Park Systems). The specific surface area of the samples were determined via a N_2 adsorption-desorption isotherms method at 77 K using a QUADRASORBTM SI Surface Area and Pore Size Analyzer (Quantachrome Instrument, Boynton Beach, FL, USA). Raman spectra were obtained by confocal Raman microscopy with a 532 nm incident laser (Thermo Scientific). Thermogravimetric analysis (TGA) was measured by a TGA 550 (TA Instruments). UV-vis absorption spectra (Specord 210 Plus, AnalytikJena, Germany) and UV–vis diffuse reflectance spectra (UV-Vis-NIR (%R), Agilent Technologies, Cary 5000, Santa Clara, CA, USA) were used to examine the photocatalyst's optical characteristics. Photoluminescence spectroscopy was measured with a 473 nm diode laser at ambient temperatures (Agilent Technologies, Cary Eclipse fluorescence spectrophotometer, Santa Clara, CA, USA). Time-resolved photoluminescence (TR-PL) spectra were recorded under 400 nm laser excitation by a FS5 spectrofluorometer (Edinburgh Instruments Ltd, Livingston, UK).

4.2.6. Electrochemical Measurement

An electrochemical workstation (VSP BioLogic Science Instruments, Seyssinet–Pariset, France) was used to perform electrochemical impedance spectroscopy (EIS) measurements in a standard three-electrode system under UV irradiation at RT. EIS was carried out in an open circuit, following a 10-minute delay, in a frequency range of 100 kHz to 0.01 Hz and an amplitude of 10 mV at a direct current potential of +0.8 VSCE.

Drip-coating was used to prepare the membrane electrode. Following conventional procedures, 20 mg of catalyst powder was ground with 2 mg of activated carbon by mortar for 20 min to obtain a fine powder, which was then added to 100 µL of isopropanol (99.7%) and 30 µL of Nafion (5 wt.%) (Sigma Aldrich, Korea). A 10 mL solution of 1 M sodium hydroxide was used as the electrolyte. The working electrode was a 6 mm standard glassy carbon electrode, in which 10 µL of the sample was placed (1 µL of suspension at a time by micro-pipet). The reference electrode was the RE-61AP (Hg/HgO) electrode, while the counter electrode was a platinum wire. The SVC-3 voltammetry cell and the electrodes were purchased from ALS Co., Ltd. (Tokyo, Japan).

4.3. Results and Discussion

4.3.1. Synthetic Strategy to Achieve Highly Dispersion of g-C_3N_4/Holey graphene oxide Composite

Scheme 6 shows a schematic representation of the synthesis procedure resulting in a highly dispersion of HoCN-GO in water. Based on a fully water-soluble property of holey graphene oxide, it was used as a carrier to maintain the dispersibility of g-C_3N_4 in the reaction media. First, fully dispersion in water of g-C_3N_4 was prepared through oxidation process of bulk g-C_3N_4, followed by loading Pt nanoparticles via hydrogen reduction method using chloroplatinic acid as Pt precursor. Second, a merely mixing method was used to create a water-soluble oCN-GO composite. The introduction of oxygen group in g-C_3N_4 via oxidation process generates a highly dispersion of oCN in water; however, it reduces the photoactivity due to a decrease in N-C photocatalytic active sites. Finally, to restore the accessible active sites on g-C_3N_4 layer, a hydrogen reduction of oCN-GO was applied for 12 h at 90 ℃ to obtain a highly dispersion of HoCN-GO.[57] The resulting 2D/2D HoCN-GO hybrid performed a superior photocatalytic toward H_2 evolution and highly dispersion in the reaction media.

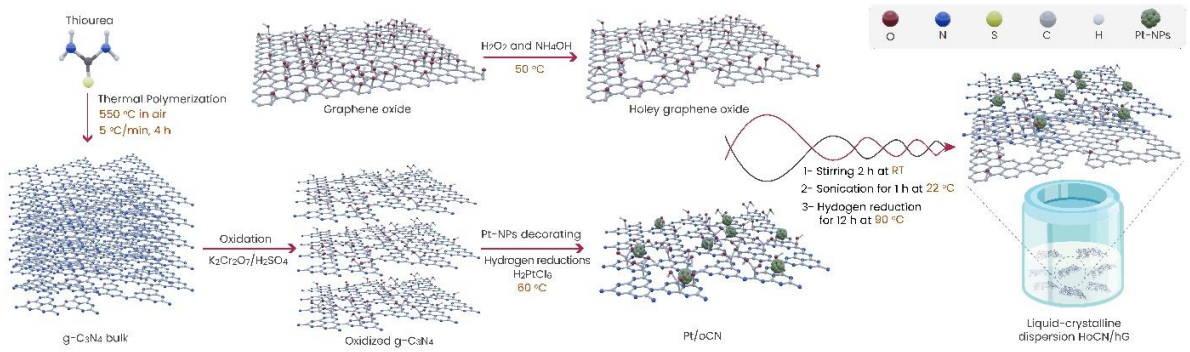

Scheme 6. Schematic of highly dispersion of HoCN-GO preparation.

4.3.2. Crystal Structure and Chemical Composition

The crystallographic nature and purity of the as-prepared samples were analyzed by XRD (Figure 85). The obtained samples show XRD patterns typical for conventional bulk thiourea-derived g-C_3N_4 with two clear peaks at 12.9° and 27.6°, which were ascribed to the (100) and (002) crystal planes of g-C_3N_4 (JCPDS 87-1526), respectively. These represented in-plane structural packing repeated heptazine motifs with interlayer spacing of 3.23 Å and a reflection at 6.86 Å.[27] An additional broad peak at 57.4° refined crystallized in the hexagonal space group with AB stacking of the triazine-based g-C_3N_4 layers.[85] As shown in Figure 85a, the general structure of g-C_3N_4 samples was maintained after the oxidation process with a thinner stacked layer due to the introduction of oxygen functional groups. Furthermore, a dramatically decreased intensity of the two main peaks of CN-bulk and HoCN/gG samples demonstrated a high exfoliation of the stacked layers in the graphitic structure due to the effective intercalating of porous graphene oxide.

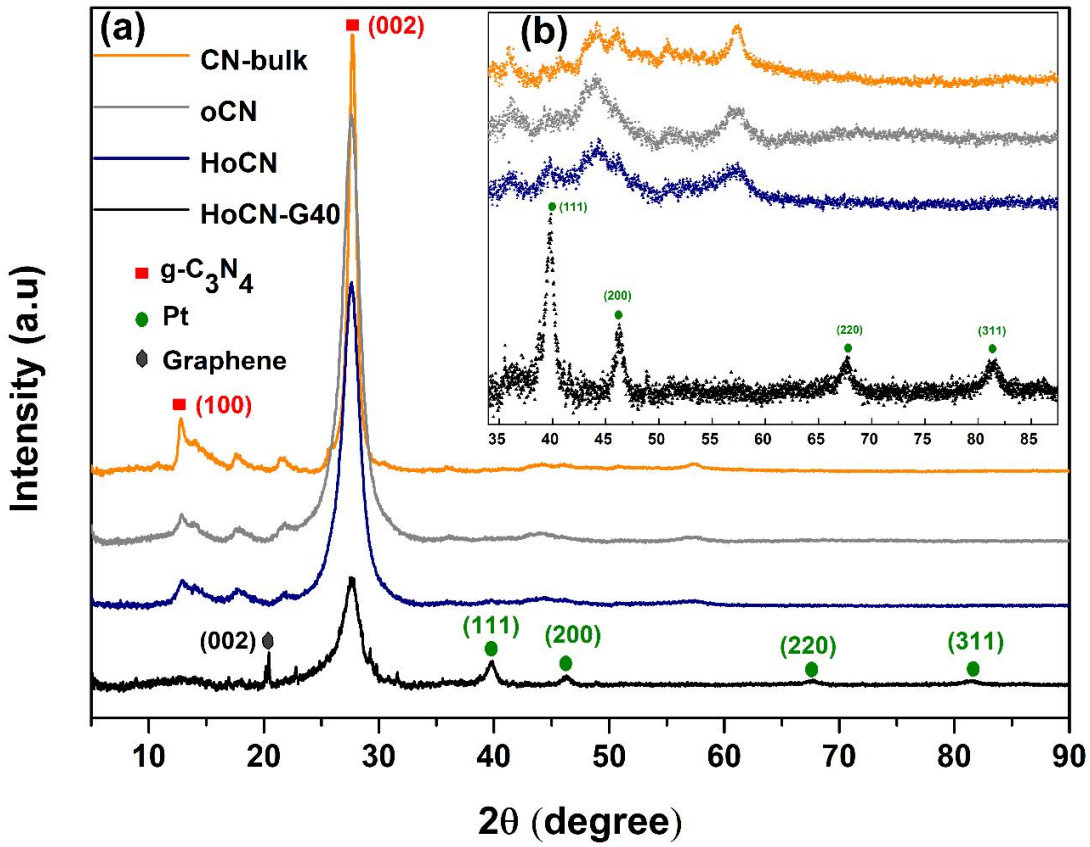

Figure 85. (a) XRD spectra of CN-bulk, oCN, HoCN, and HoCN-GO. (b) inset XRD spectra of CN-bulk, oCN, HoCN, and HoCN-GO.

The peaks at around 39.8, 46.3, 67.7, and 81.5^{o} belong to the face-centered cubic (fcc) structure of the platinum metal crystalline lattice, which was assigned to the (111), (200), (220), and (311) crystalline planes, respectively. Interestingly, as shown in the inset figure, HoCN-GO shows high-crystalline planes of Pt nanoparticles compared to CN-bulk, and HoCN (Figure 85b). This can be explained by a higher interaction between Pt nanoparticles and holey GO layers than Pt and g-C_3N_4, resulting in higher crystallinity of Pt nanoparticles in the composite.

An element analyzer (C, H, N, O, S) was used to determine the detailed elemental composition of the resultant samples (Table 20). Compared to CN-bulk, oxidized g-C_3N_4 possessed a much higher percentage of oxygen element, which resulted in a dramatic decrease in C/O ratio. These results explain a full dispersion property of oCN in water. After Pt decorating process in 12 h, C/O ratio of oCN slightly decreases from 4.14 to 3.91, which is a result of the catalytic reduction of oCN by atomic hydrogen spillover Pt.[57] The post-reduction of HoCN at 90 ^{o}C in 12 h effectively removed oxygen functional groups by atomic hydrogen spillover HoCN-GO surfaces (C/O of 2.22). Meanwhile, the photocatalytic active sites of C2p-N2p were indicatively restored. The N content is almost constant, suggesting that the initial structure of g-C_3N_4 is maintained after reactions.

Table 20. Element compositions and calculated C/N, O/N, C/O atomic ratios of the samples analyzed by elemental analysis.

Elemental analysis								
	Atomic percentage (atom %)					**Atomic ratio**		
Sample	C	N	O	H	S	C/N	O/N	C/O
CN-bulk	49.06	29.80	2.26	18.87	0.01	0.61	0.05	13.20
oCN	45.98	29.98	7.24	16.75	0.02	0.65	0.16	4.14
HoCN	44.24	28.69	7.33	19.74	0.00	0.65	0.17	3.91
HoCN-G40	25.19	28.79	12.95	32.52	0.00	1.14	0.51	2.22

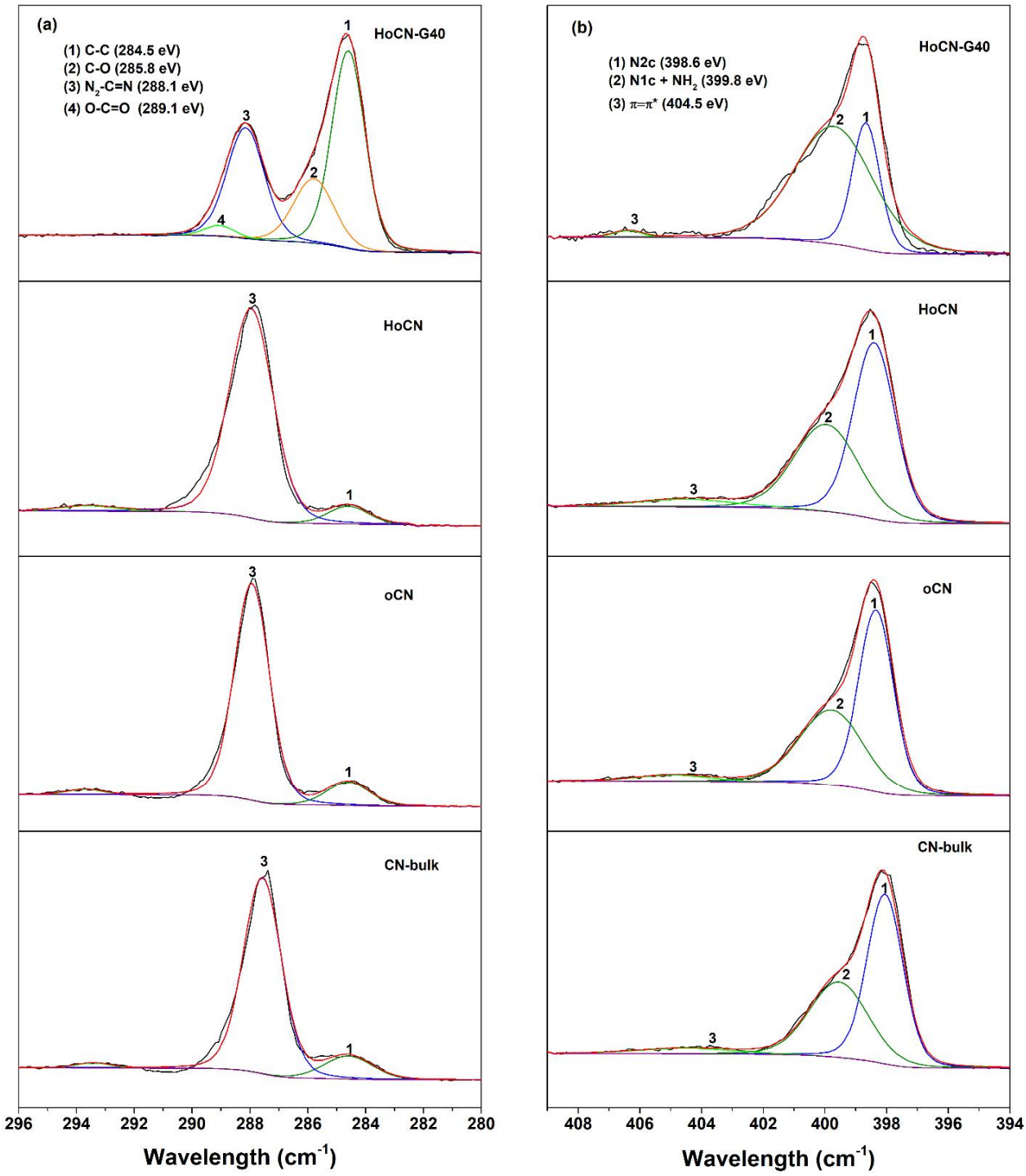

Figure 86. XPS spectra of CN-bulk, oCN, HoCN, and HoCN-G40. (a) C1s spectra, (b) N1s spectra.

The surface chemical states of as-prepared samples were investigated by XPS analysis. The C1s and N1s core level spectra deconvoluted into Gaussian shapes are shown in Figure 86. In the C1s XPS spectra (Figures 86a), the main carbon peaks at ca. 284.5 eV, 285.8 eV, 288.1 eV, and 289.1 eV were

attributed to graphitic structure (C=C or C-C) bonds, oxygen groups on the basal planar (C-O), carboxylic group at the edge (O-C=O), and sp^2-hybridized carbon atoms bonded with three N (N_2-C=N-), respectively. Core-level spectra of N1s were used to reveal the distribution of nitrogen-containing groups in the samples. The lowest energy contribution (ca. 398.6 eV) of the N1s spectrum is attributed to nitrogen bonded with two carbon atoms in a graphitic sp^2 network (Figures 86b), whereas the peak at ca. 399.8 eV corresponds to the overlap of signals from bridging nitrogen atoms such as tertiary N (-N<), and amino groups (-NH_x), revealing the presence of tris-triazine rings in the g-C_3N_4 framework. In addition, a weak signal positioned around 404.5 eV in N1s spectra can be assigned to the π electrons delocalization in g-C_3N_4 heterocycles.

4.3.3. Morphology and Microstructure

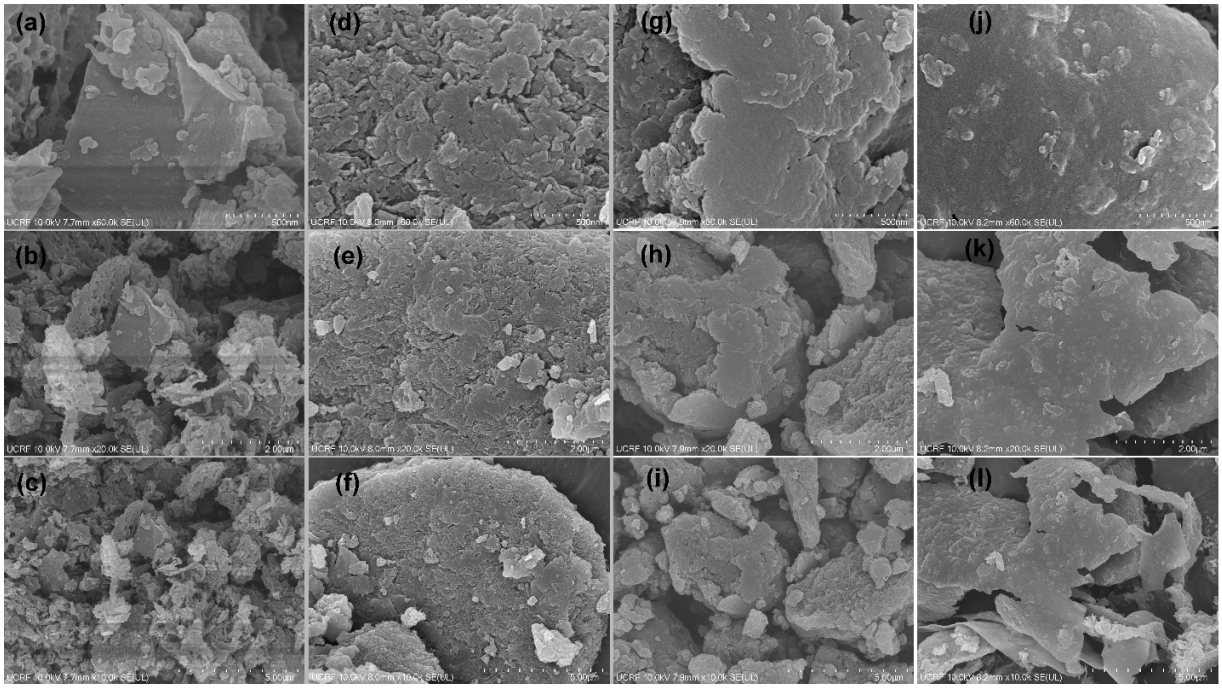

Figure 87. FE-SEM images of (a, b, c) CN-bulk, (d, e, f) oCN, (g, h, i) HoCN, and (j, k, l) HoCN-G40 at different magnifications.

The surface morphology and microstructure of each sample were captured by FE-SEM, HR-TEM, and AFM. As shown in Figure 87, CN-bulk derived from thiourea mainly displayed a flake-like structure with smooth lamellar surfaces (Figure 87a), which indicated multilayer stacking resulting from thermal polymerization. On the other hand, there are some layers with uneven holey structure, which indicates macroporous material from thiourea polymerization

(Figure 87b). After the oxidation process, the delocalized π system of g-C_3N_4 has been damaged, which results in a rough morphology of the oCN layers (Figure 87d). The hydrogen reduction of oCN not only removes the oxygen functional groups but also restores the graphitic structure of g-C_3N_4, thus restoring the photocatalytic active sites as well. Compared to oCN, a glossy surface of HoCN is displayed, suggesting that the delocalized π system in the structure has been restored. In Figure 87l, alternating layers result from the mixing of fully dispersive oCN with holey graphene oxide in a solution, followed by hydrogen reduction to restore the graphitic structure. Compared to HoCN layer, holey GO layer is smoother, thinner, and slightly transparent. This result demonstrates a good interaction between HoCN and holey GO due to a strong π – π interaction, hydrogen bonding, and van der Waals force.

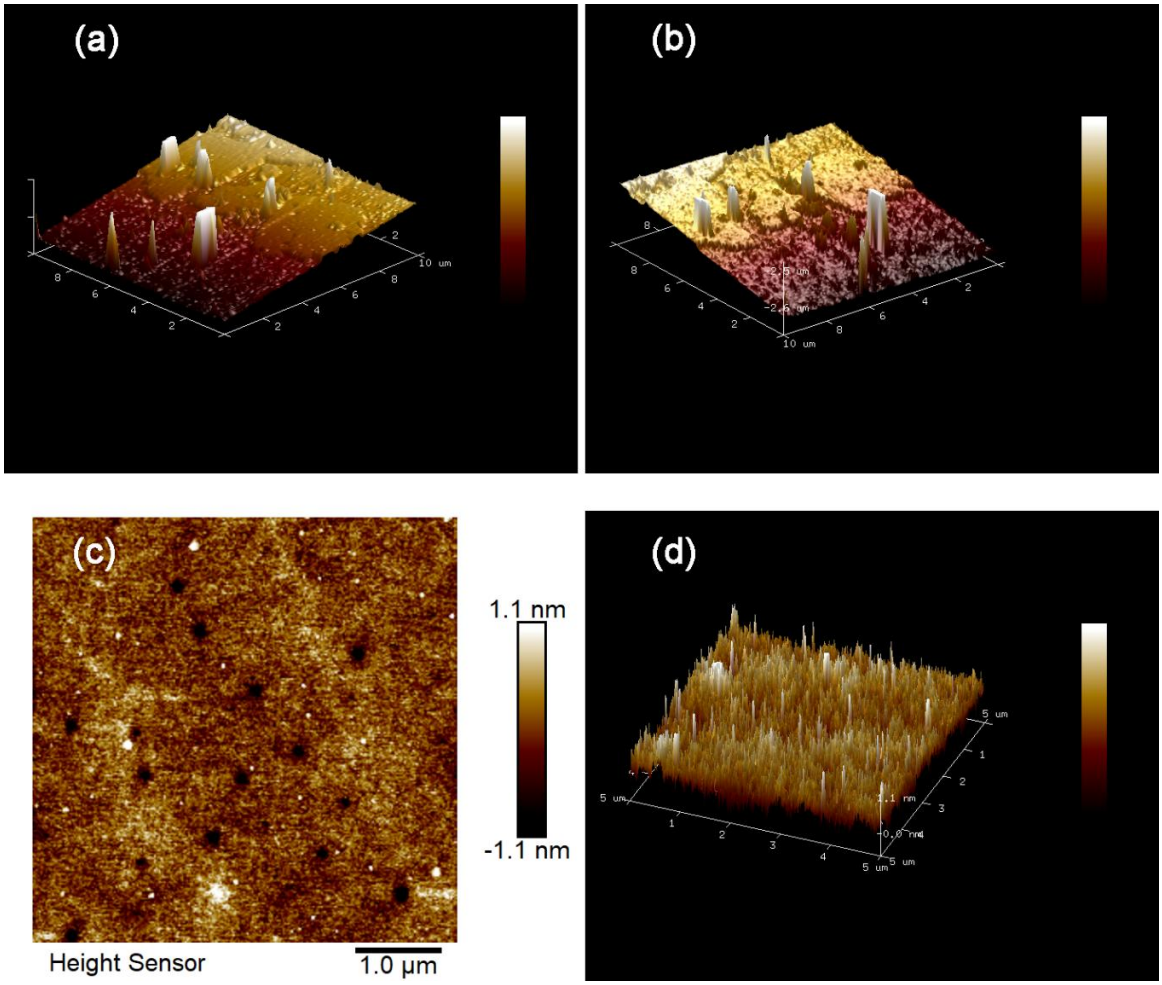

Figure 88. AFM topography of (a, b) HoCN-G40 in 3D, (c) holey GO image in 2D and (d) in 3D.

Moreover, AFM topography images of the bilayer of HoCN-G40 showed the morphology of layer by layer, which holey GO layer interspersed with HoCN layers (Figure 88 a & b). This result reveals the role of holey GO, which is fully dispersed in the reaction media, as a carrier to maintain high dispersion of hydrogen reduction of oxidized g-C_3N_4 (HoCN) layers. Interestingly, Pt nanoparticles, which are decorated on oCN surface layers, have been partially transferred into holey GO layer. Figure 88c displays the AFM image of the monolayer holey GO with Pt nanoparticles, which are shown as bright white spots. This result could be explained by a better interaction between holey GO and Pt nanoparticles than Pt nanoparticles on g-C_3N_4. As a result, holey GO contributes to capturing the unstable Pt nanoparticles existing in the reaction media. Figure 88d presents the 3D morphology of the monolayer holey GO, which clearly shows the holey structure of GO and the uniformly distributed Pt nanoparticles on the layer. These results support enhancing the effectiveness of photoinduced charge transfer and separation.

In addition, HR-TEM images have further confirmed the morphologies of the structural layers (Figure 89). While CN-bulk showed multilayer stacked form (Figure 89 a & b), HoCN sample displayed thinner structural layers due to its highly dispersed property in the solution (Figure 89 c & d). In particular, HoCN-40 exhibited the formation of holey GO layers supporting the HoCN layers (Figure 89 e & f). In the high-resolution image of inset Figure 89f, the g-C_3N_4 layer with a typical d-spacing structure of 0.35 nm was distributed above the layer of holey GO (Figure 89 h & j & k). This result confirmed the good interaction between HoCN and holey GO layers.

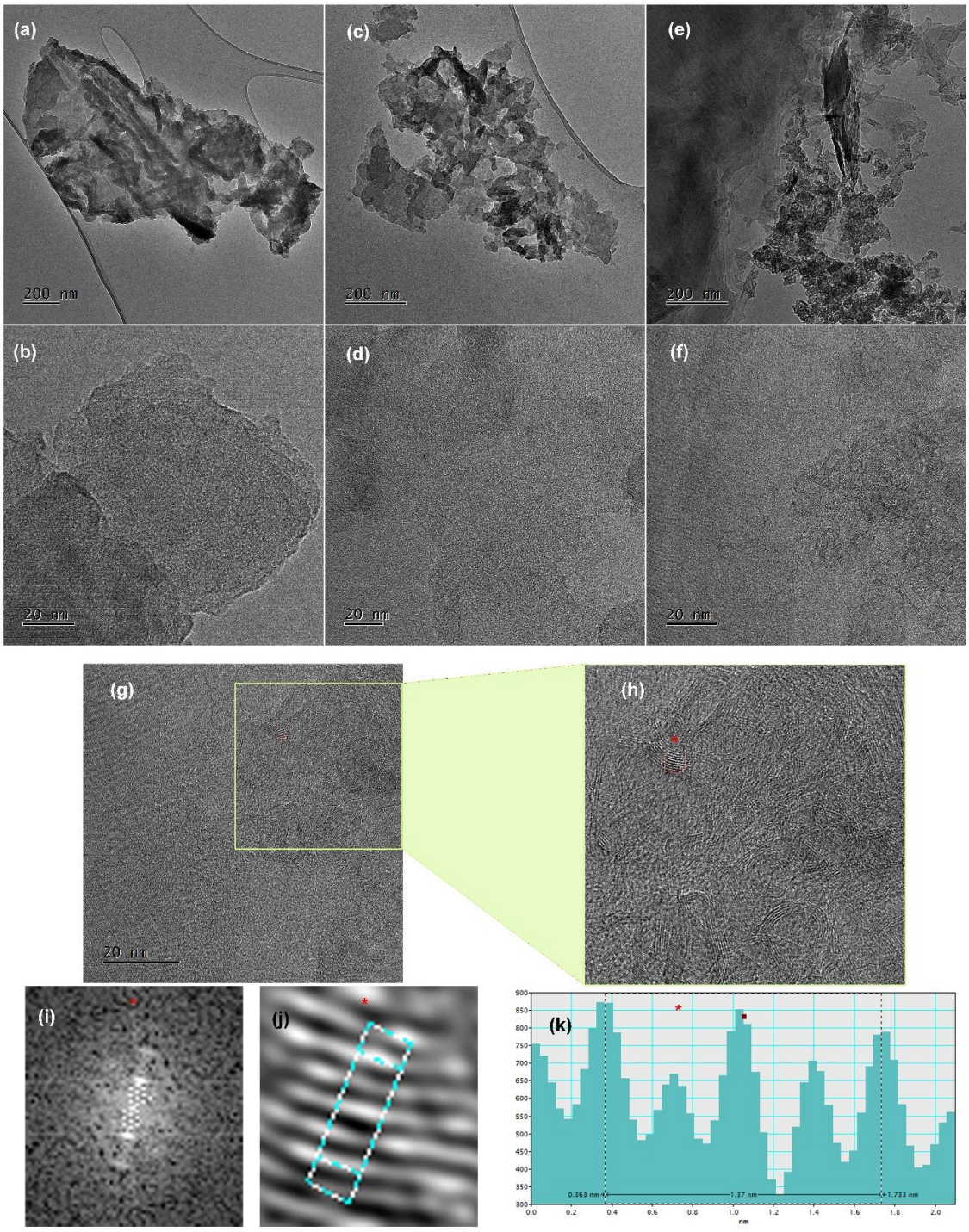

Figure 89. HR-TEM CS-STEM images of (a, b) CN-bulk, (c, d) HoCN, and (e, f) HoCN-G40. CS-STEM images of (g) HoCN-G40, (h) inset image of g, corresponding to (i) Fourier-transform (FFT) image, (j) High-resolution inverse FFT image (IFFT), and (k) lattice fringe pattern image, which shows a d-spacing of 0.35 nm of g-C_3N_4.

4.3.4. Optical Properties and Charge-carrier Separation and Transfer

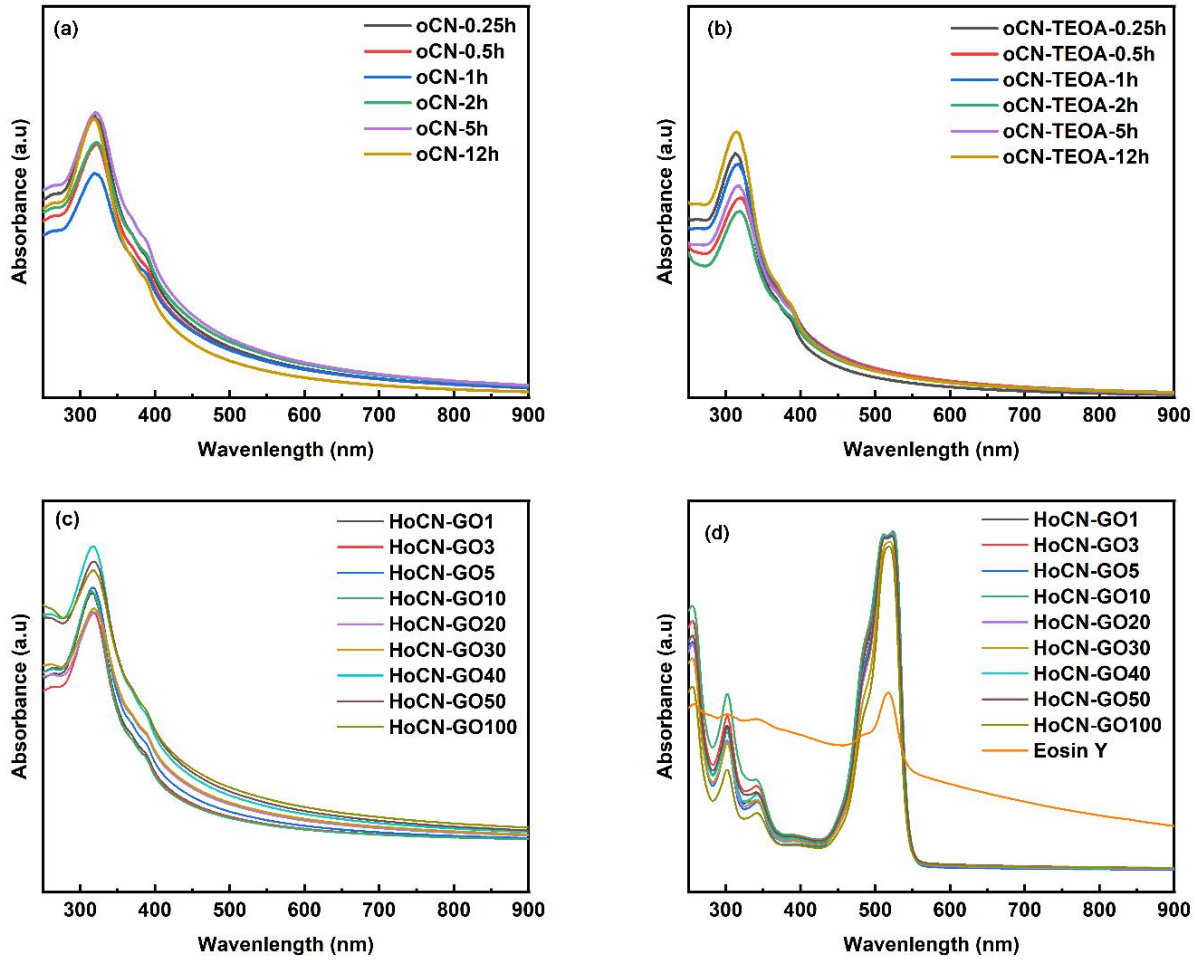

Figure 90. UV-Vis spectra of as-prepared samples. (a) UV-Vis spectra of oCN by reduction time, (b) UV-Vis spectra of oCN mixed with 10 % v/v TEOA, (c) UV-Vis spectra of oCN mixed with holey GO (GO number is a weight ratio of holey GO vs. oCN), and (d) UV-Vis spectra of HoCN-GO with eosin Y (EY).

The UV-Vis spectra present the absorption regions of all prepared samples (Figure 90). The observed strong absorption around 319 nm lies in the range characteristic for the π-π* electronic transition in aromatic 1,3,5-triazine compounds. An additional absorption, extensive and weak, was observed in the visible region around 380-390 nm, which presumably belongs to n-π* transitions involving lone pairs of nitrogen atoms in the polymeric g-C_3N_4 (Figure 90 a, b, & c). Compared to the oCN (Figure 90 a, b), the introduction of holey GO into HoCN-GO mixture exhibited a better light adsorption ability, indicating a better light harvesting capacity of HoCN-GO photocatalysts. Furthermore, adding EY to HoCN-GO mixture generated a significant light

adsorption area in a range of 430 – 562 nm, signifying a greater light adsorption ability in the visible range. The presence of a photosensitizer, EY, is very important in the reaction media of graphene-based photocatalysts, which resolved the light shielding effect of black color graphene solutions. The bandgap values of CN-bulk, oCN, HoCN, and HoCN-G40 from UV-DRS measurement were 2.82 eV, 2.87 eV, 2.90 eV, and 2.51 eV, respectively (Figure 91). It was found that the introduction of holey GO into HoCN not only enhanced the light adsorption ability of the photocatalyst significantly (Figure 91a) but also adjusted the bandgap to a lower energy point (Figure 91b). Thus, the light-harvesting capacity and visible light range adsorption are extremely extended, which contributes to enhancing the photoactivity of HoCN-G40.

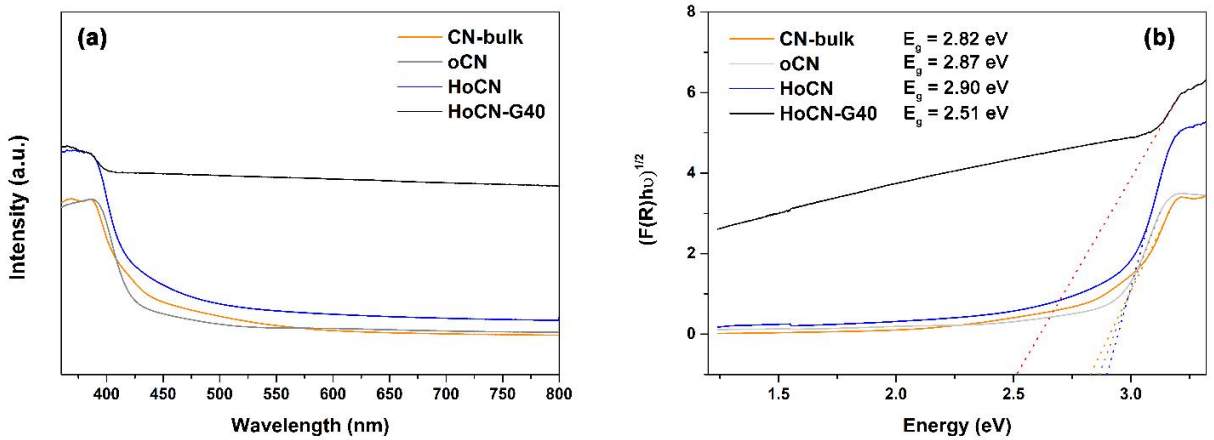

Figure 91. UV-DRS spectra. (a) UV-DRS spectra of powder samples, the intensity of absorbance. (b) corresponding Tauc plots of Energy (eV) and $(\alpha h\nu)^{1/2}$ for as-prepared samples.

The photoluminescence (PL) spectra of resultant samples were analyzed using PL with an excitation wavelength of 340 nm (Figure 92). Among all the hydrogen reduction of oCN samples by time, the HoCN-12h sample displayed a considerably lower intensity of PL peak. This reduction in peak intensity suggests a suppression of photogenerated charge recombination within the aromatic system, which was restored by removing oxygen functional groups (Figure 92 a & b). Moreover, when a larger amount of holey GO was added to the HoCN sample, lower intensities of the PL peak were observed (Figure 92 c & d), indicating a higher suppression of photoinduced charge recombination. The enhanced charge diffusion rate in the HoCN-GO samples played a vital role in achieving this suppression, enabling more efficient movement of charge carriers and reducing the recombination rate. Consequently, the HoCN-GO samples exhibited improved charge transport properties, leading to a significant reduction in the intensities of the PL peaks. These

results highlight the beneficial effect of incorporating holey GO and HoCN on the charge dynamics within the photocatalytic system.

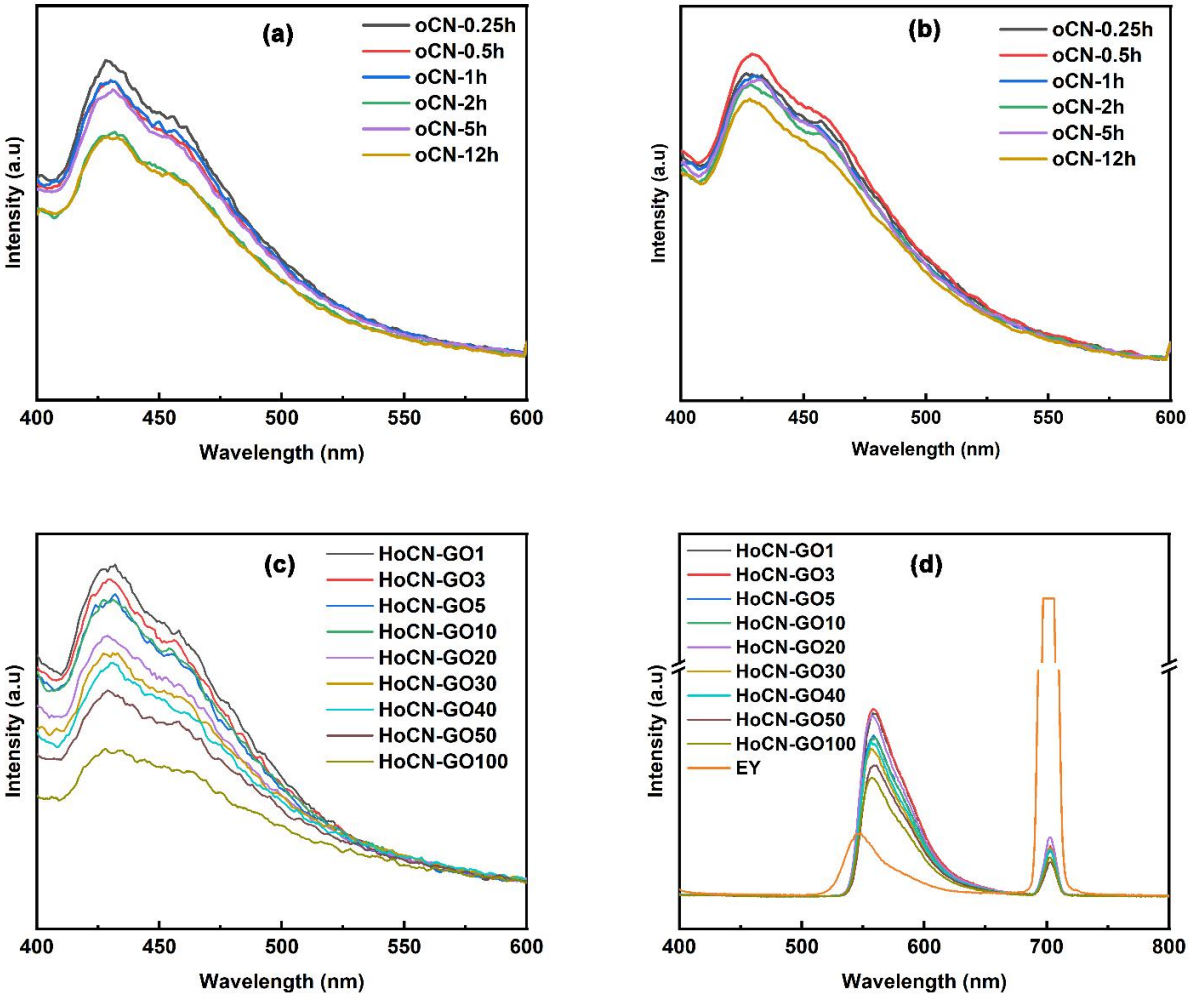

Figure 92. PL spectra of as-prepared samples. (a) PL spectra of oCN by reduction time, (b) PL spectra of oCN mixed with 10 % v/v TEOA, (c) PL spectra of oCN mixed with holey GO (GO number is a weight ratio of holey GO vs. oCN), and (d) PL spectra of HoCN-GO with eosin Y (EY).

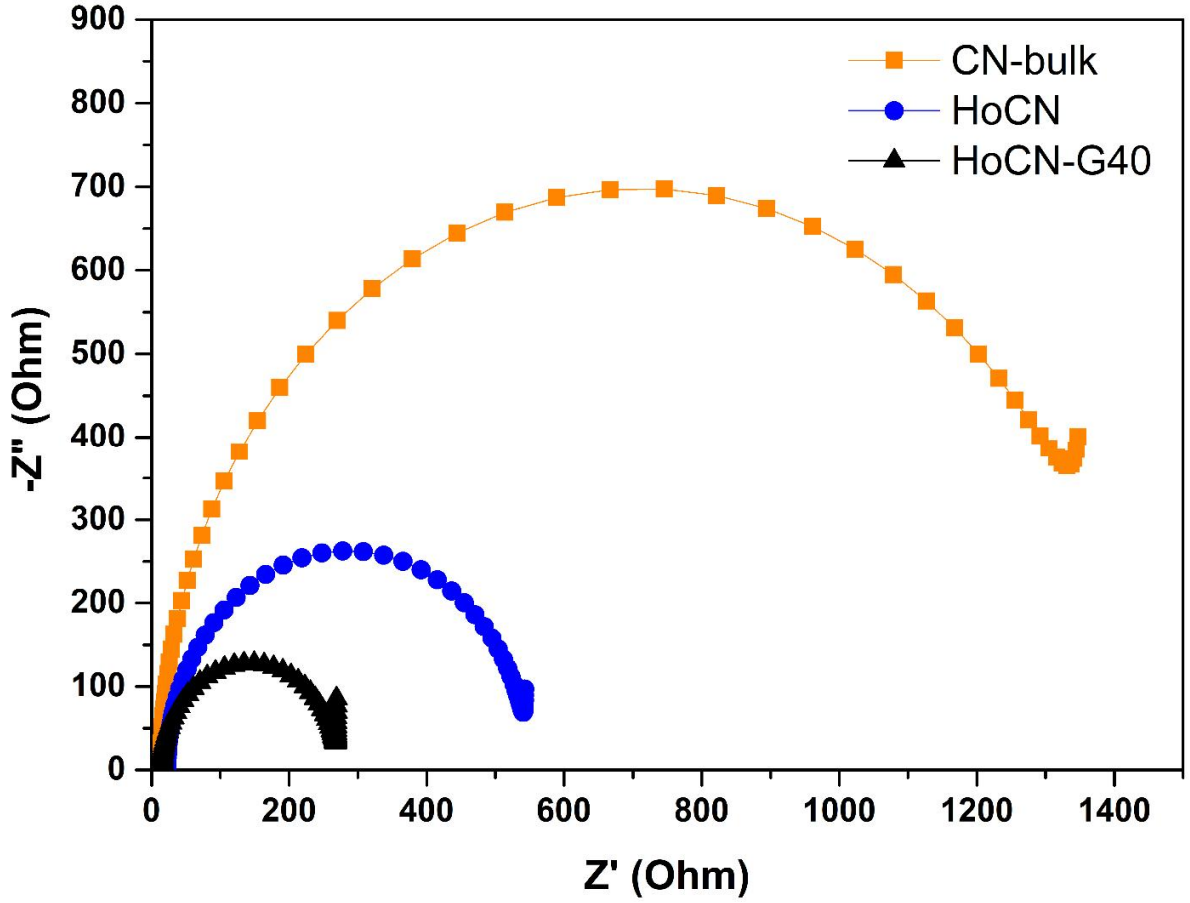

Figure 93. EIS Nyquist plots of as-prepared samples from EIS measurement.

The charge transport process is crucial for the efficient movement and conveyance of charge carriers to the desired reactive sites within the photocatalysts. Therefore, in-depth understanding of the charge transport behavior of the prepared catalysts was obtained through the utilization of electrochemical impedance spectroscopy (EIS) measurements. These measurements enable the examination of the charge transfer resistance at the interface between the catalyst electrode and the electrolyte. A smaller radius observed in the EIS Nyquist plot corresponds to a decreased resistance encountered during the transfer of charge carriers at the catalyst/electrolyte interface. Among as-prepared samples, it was found that HoCN-G40 displayed the smallest radius in the EIS Nyquist plot (Figure 93). This indicates that HoCN-G40 exhibited a lower charge transfer resistance from the catalyst surface to the reactant molecules involved in the reaction. The smaller resistance observed in HoCN-G40 suggests that it possesses enhanced charge transport characteristics, enabling more efficient movement and conveyance of charge carriers to the targeted reactive sites.

4.3.5. Photocatalytic Performance and Mechanism

Photocatalytic activity toward hydrogen evolution reaction was tested to assess the photocatalytic performance of as-prepared samples in the presence of 10% triethanolamine (TEOA) as a sacrificial agent under simulated sunlight irradiation by using the MAX-350's mirror solar module, which is able to shape the xenon spectrum similar to the sun spectrum in the wavelength range from 350nm to 1100nm. Platinum nanoparticles were used as a cocatalyst, which loaded on the catalyst by the hydrogen reduction of H_2PtCl_6 in aqueous. In addition, Eosin Y was added as a photosensitizer with a mass ratio of 2:1 to the photocatalyst.

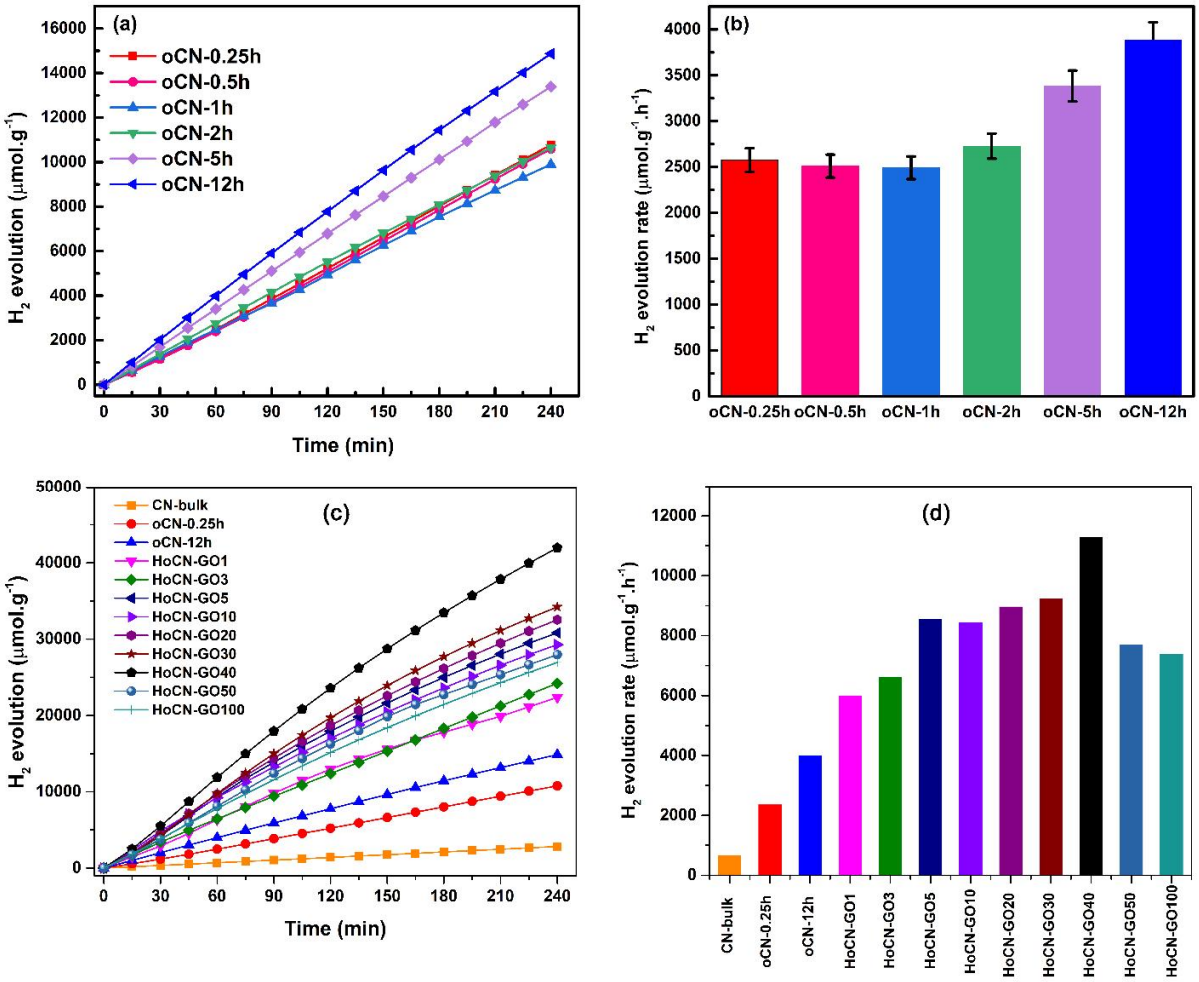

Figure 94. Photocatalytic hydrogen evolution under visible light irradiation.

The photocatalytic hydrogen evolution of oCN during the hydrogen reduction processing was screened by reduction time (Figure 94 a & b). It was found that after 12 h of hydrogen

reduction in oCN aqueous using H_2PtCl_6 as the initial precursor. The H_2 evolution rate of oCN after 15 min reduction was 2575.3 μmol h^{-1} g^{-1}. While after 12 h of reaction, the HER of oCN-12h reached a saturation value of 3884.2 μmol h^{-1} g^{-1}, which is 1.5 times higher than that of oCN-0.25h. Thus, the photocatalytic performance of holey GO/HoCN mixture was further examined using HoCN-12h.

The holey GO content added in oCN-12h to prepare resultant HoCN-GOx photocatalysts was optimized for photocatalytic hydrogen evolution (HoCN-GOx, where x is the weight percent of holey GO to HoCN) (Figure 94 c & d). The sample HoCN-GO40, which contained 40 wt % holey GO, displayed the highest H_2 evolution rate, as high as 11295.3 μmol h^{-1} g^{-1}, which are over 4.4 and 16.2 times higher than those of oCN and CN-bulk, respectively. Holey GO was designed as a suspension carrier to maintain the high dispersibility of HoCN-GO in reaction media due to its fully dispersed water properties. The stationary point of HoCN-GO for hydrogen evolution was achieved when 40 wt% of holey GO was used, which might maximize the accessible active sites of HoCN compared to the range HoCN-GO1 to HoCN-G30 samples. However, HoCN-GO50 and HoCN-GO100 samples dramatically decreased H_2 evolution performance, indicating that too large an amount of holey GO could block the accessible active sites of HoCN.

The mechanism of the photocatalytic activity process for H_2 evolution is illuminated in Figure 95. Under simulated sunlight irradiation, the HoCN-GO samples and EY can absorb the photons that supply energy higher or equal to the intrinsic bandgap of photocatalyst. After that, the electrons are excited and transferred from the valence band to the conduction band and release the positive holes in the valence band. At the same time, after adsorbing photons, EY reacts with TEOA to form EY^-, which transfers the electrons to conduction band of g-C_3N_4[111] Then, the electrons move to the Pt co-catalyst particles, or graphene layers, where the H^+/H_2O is reduced to form H_2 molecules. Meanwhile, the generated holes in the valence band can be oxidized and consumed by TEOA.

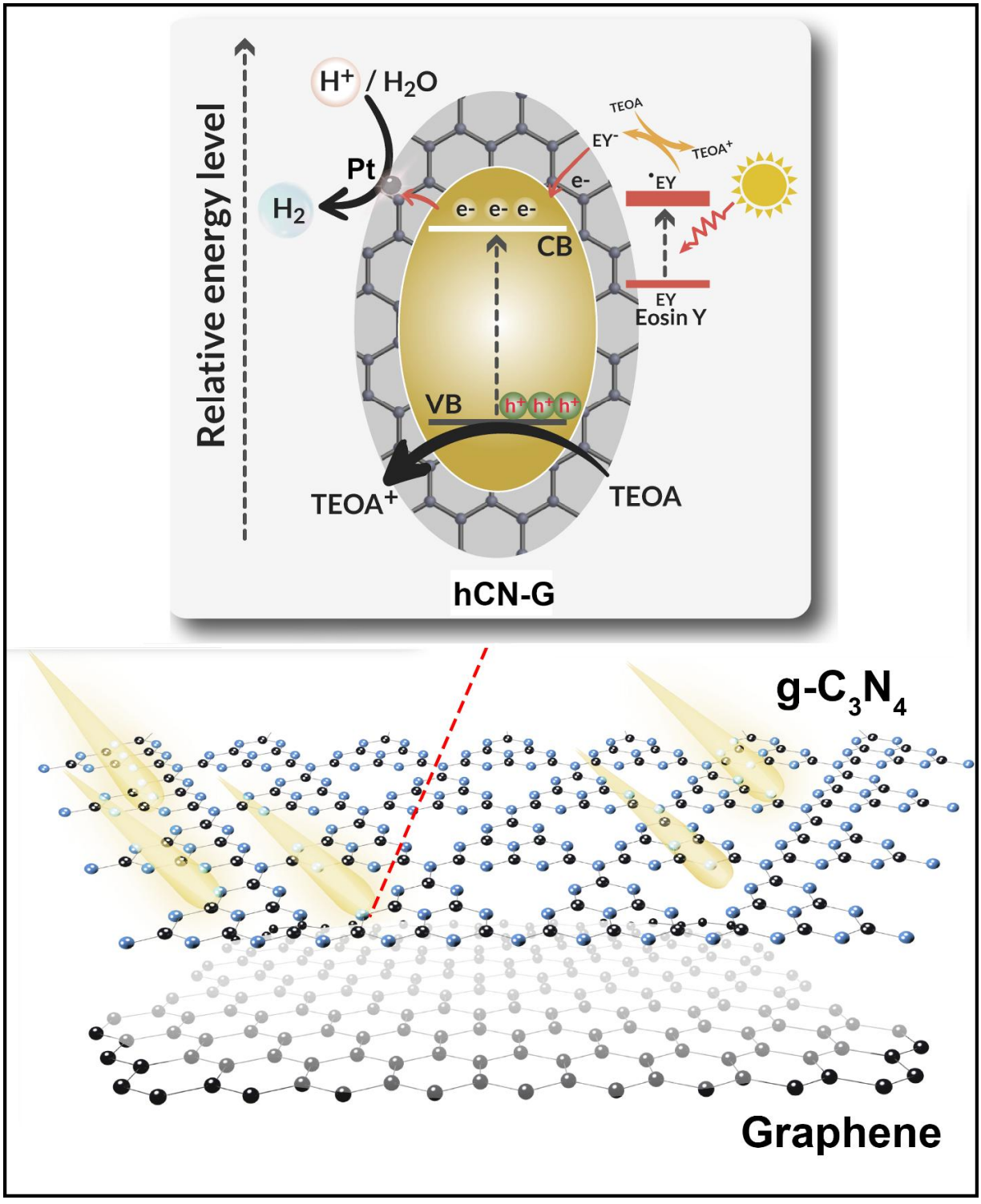

Figure 95. Photocatalytic hydrogen evolution under visible light irradiation.

4.4. Conclusion

In summary, this chapter provides a facile and large-scale production method for generating a highly dispersion of holey graphene/g-C_3N_4 in aqueous, which maximizes the catalyst surface accessible active sites in reaction media. The full exfoliation of g-C_3N_4 bulk into monolayer has been performed by using the oxidation method on bare g-C_3N_4. The resulting oCN is full dispersion in water. On the other hand, holey GO was prepared using the etching method, resulting in the highly dispersion in the aqueous solution even after applying the hydrogen reduction to remove the oxygen functional groups. Holey GO has functioned as the carrier to maintain high dispersion of HoCN-GO in reaction media after graphitic restoration by hydrogen reduction approach. The mass ratio of holey GO and HoCN was optimized to obtain the stationary point of photocatalytic toward hydrogen evolution. At the optimized point, the holey graphene content is enough for carrying the HoCN layers, but it is not blocking the accessible active sites of the photocatalyst also. As a result, HoCN-GO 40 wt% reached a stationary point of hydrogen evolution performance as high as 11295.3 $\mu mol\ h^{-1}\ g^{-1}$, which are over 4.4 and 16.2 times higher than those of oCN and CN-bulk, respectively. The approach introduced in this study provides a simple method for the mass production of advanced photocatalyst composite for a possible practical application of photocatalytic green hydrogen production by massive area sunlight harvesting.

CHAPTER 5

5. Conclusions and Outlook

5.1. Summary

In this doctoral thesis, we have established the facile method for generating an advanced monolayer of uniformly holey g-C_3N_4 using popular solvents instead of highly toxic chemicals (such as NH_3), strong organic acid, or hydrazine. Second, this work provided new insights to the optimization of the 2D holey g-C_3N_4 for photocatalytic H_2 evolution, where C_3N_4-THF shows the appropriate holey structure compared to C_3N_4-DMF (no holes), C_3N_4-MA (break the g-C_3N_4 structure and generate big holes), and C_3N_4-IPA (weak etching effectiveness). Third, this study supplied the optimal evaluation system and assessment method for a more accurate and transparent evaluation of g-C_3N_4 photocatalyst performance, which enables the comparison of different photocatalyst systems across the community of researchers in this area. During the optimization of photocatalyst performance, the stationary points are discovered for all the photocatalyst samples. We found an important relationship between photocatalyst performance and the lateral size of nanosheets of photocatalysts. This result is beneficial to further research, and it may interest researchers in the photocatalyst community to optimize the H_2 evolution rate. Fourth, the new phenomenon of self-assembled graphene formation during the solvolysis process, and the division of Pt oxidation states into Pt^0 and Pt^{2+} (in PtO form) in the C_3N_4-THF sample, which are demonstrated to enhance the photocatalyst performance. Fifth, the mechanism of solvolysis of g-C_3N_4 photocatalyst to form holey structure was revealed based on the practical experiments, Hansen parameters of the used chemicals, and density functional theory (DFT) calculations. Sixth, we aim to optimize the holey structure of such a monolayer of g-C_3N_4 photocatalyst for large-scale applications. Since the synthesis of g-C_3N_4 from DCDA has a high yield compared to other precursors (~55% vs. less than 5%), the highest active C_3N_4-THF catalyst achieves superior photocatalytic H_2 evolution performance and good stability. The proposed method has the potential to produce sustainable photocatalysts for the production of green hydrogen in large quantities.

Furthermore, we considered a step forward in developing a new two-dimensional grid-like g-C_3N_4 structure/self-assembled graphene/high proportion of Pt^{2+} oxidation state ternary hybrid for the production of large quantities of green hydrogen through photocatalysis. We provide an environmentally friendly approach for generating a highly porous monolayer of uniformly grid-

like g-C_3N_4 using a green solvent (ethyl alcohol) instead of toxic organic solvents. Continuation to previous research, we have supplied the role of self-assemble graphene as an electron mediator and acceptor in detail. Compared to CN-b, which has no graphene content, hCN-G photocatalytic performance provided a transparent result of self-assemble graphene contribution. The additional DFT calculations investigate the enhanced photoabsorption in the visible region in hCN-G and the electron-hole puddle on the graphene sheet, which reveals the effectively preventing the high recombination rate of photoinduced electron/hole. We aim to produce advanced highly porous g-C_3N_4 nanosheets for large-scale applications by using a non-toxic solvent and a simpler method of solvothermal treatment of bulk g-C_3N_4, instead of second annealing g-C_3N_4 as shown in the previous work. This extensive research on the important role of graphene and oxidized Pt cocatalyst could provide helpful information in fabricating advanced 2D/2D graphene/g-C_3N_4-based photocatalysts, whereas the photoexcited electron is directed to H_2 evolution reaction. Thus, the bottleneck of high recombination of charge of g-C_3N_4 will be resolved. The highly porous g-C_3N_4 photocatalyst may interest the photo-electrocatalysis communities due to the porosity being one of the most important parameters for making effective electrodes.

This thesis also expresses a solution for the practical large-scale production of green hydrogen via particulate photocatalysis. By successfully creating highly dispersion of holey graphene/g-C_3N_4 in aqueous (which maximizes the catalyst surface accessible active sites in reaction media), we suggest a possible protocol for applied homogeneous photocatalyst to harvesting the sunlight at the tremendous area through a sustainable and high stability photocatalysis system.

5.2. Outlook

5.2.1. Photoreforming of Graphene Oxide over Graphitic Carbon Nitride Photocatalyst

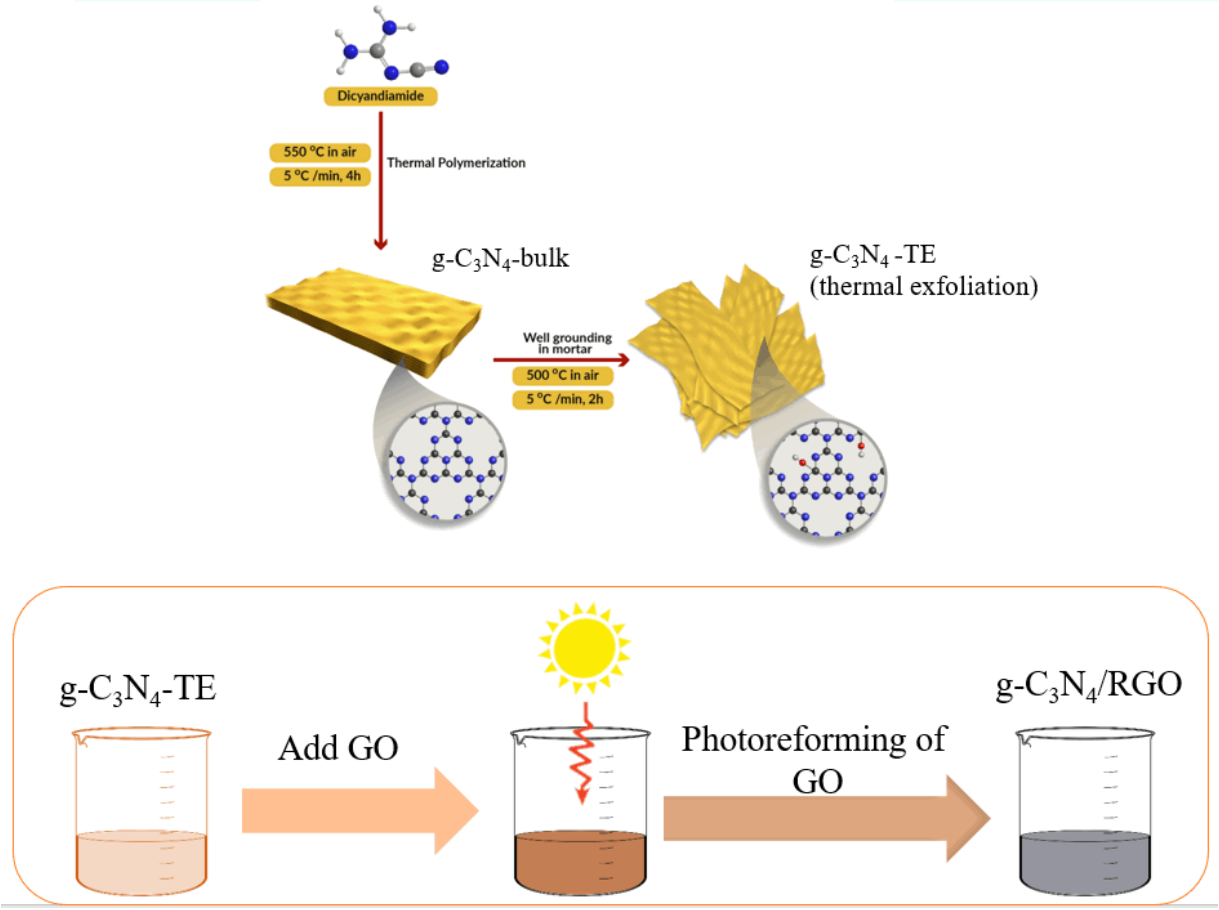

Figure 96. Schematic of mass production of g-C_3N_4/RGO by photoreforming of GO over thermally exfoliated g-C_3N_4.

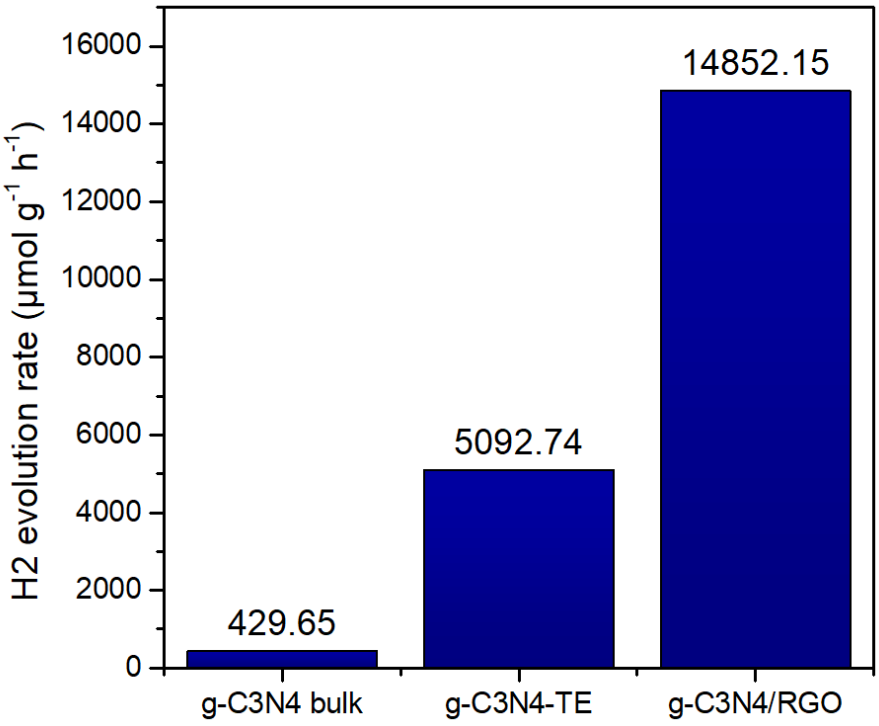

Figure 97. Photocatalytic hydrogen evolution performance of g-C_3N_4/RGO by photoreforming of GO over thermally exfoliated g-C_3N_4 samples.

5.2.2. Artificial Leaf-like Structure of Atomic Metal on Graphene/Graphitic Carbon Nitride as Gradient Photocatalyst for Overall Water Splitting

The research provides a facile method of synthesizing a nature-inspired leaf-like structure of graphene/graphitic carbon nitride (G/gC_3N_4) with atomic metal loading on the nanoscale photocatalyst as bifunctional design cocatalysts. The resulting photocatalyst of atomic scale metal (Pt-G/gC_3N_4-Ru) works as a gradient photocatalyst for overall water splitting application, in which the direction of electrons and holes are separated by synthesized design purposes, which resolves the barrier of the charges recombination in such nanoparticles photocatalysts. As a result, the bifunction of the as-designed (Pt-G/gC_3N_4-Ru) photocatalyst serves a protocol way for the charges orientation flows, which further take place in the water reduction and oxidation reaction. The achievements in this research indicate the large-scale applicability viability as well as technical challenges toward practical mass green hydrogen production via overall water splitting.

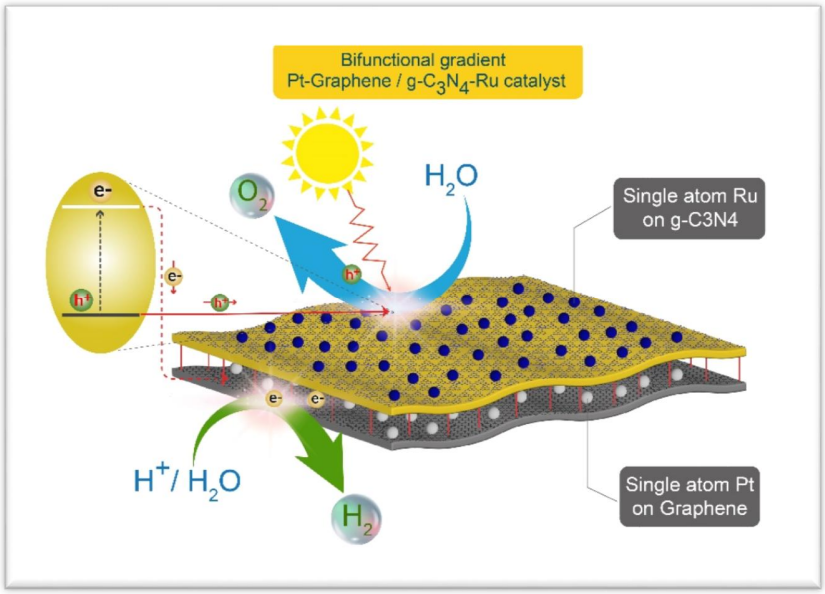

Figure 98. The overall water splitting process on atomic scale metal (Pt-G/gC_3N_4-Ru) gradient photocatalyst under sunlight irradiation.

Large-scale Synthesis of Chemically Oxidized g-C_3N_4

Regarding large-scale production, DCDA was chosen as a precursor for a high-yield synthesis of g-C_3N_4 bulk. Chemically oxidized g-C_3N_4 was obtained via chemical oxidation of the bulk g-C_3N_4 powders in $K_2Cr_2O_7$ and concentrated H_2SO_4 according to the method described in our previous study.

Large-scale Synthesis of Graphene Oxide (GO)

As-synthesized graphene oxide was prepared using the modified Hummers method from expanded graphite, prepared by microwave-assisted thermal expansion of expandable graphite according to the method described in our previous study.

Synthesis of Atomic Scale Metal (Pt-G/gC_3N_4-Ru) Gradient Photocatalyst

Herein, the single atom Pt supported on graphene oxide (Pt/G) and the single atom Ru decorated on chemically oxidized g-C_3N_4 (Ru/gC_3N_4) are synthesized via 1,10-phenanthroline ligand medicated method.[4] (Pt-G/gC_3N_4-Ru) is synthesized by making covalent bonds between Ru/gC_3N_4 and Pt/G via amide group formation (Figure 5-5). As designed, the Pt/G will be received the electron transfer from g-C_3N_4 active sites, following H_2 evolution on the surface of Pt/G, which is the most effective for hydrogen generation. At the same time, Ru/gC_3N_4 side will be appeared the water oxidation process to produce O_2. As a result, an overall water splitting reaction will be

performed without sacrificial agents requirement. The 2D structure of (Pt-G/gC_3N_4-Ru) gradient photocatalyst leads to maximizing the catalytic surface active sites, while the single atom of Pt and Ru maximizes the H_2 and O_2 evolution performance, respectively.

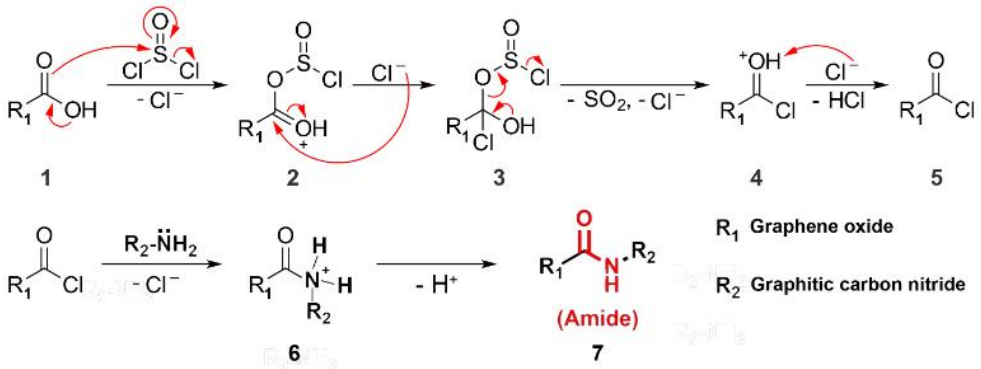

Figure 99. Proposed mechanism for GO and g-C_3N_4 amide group formation.

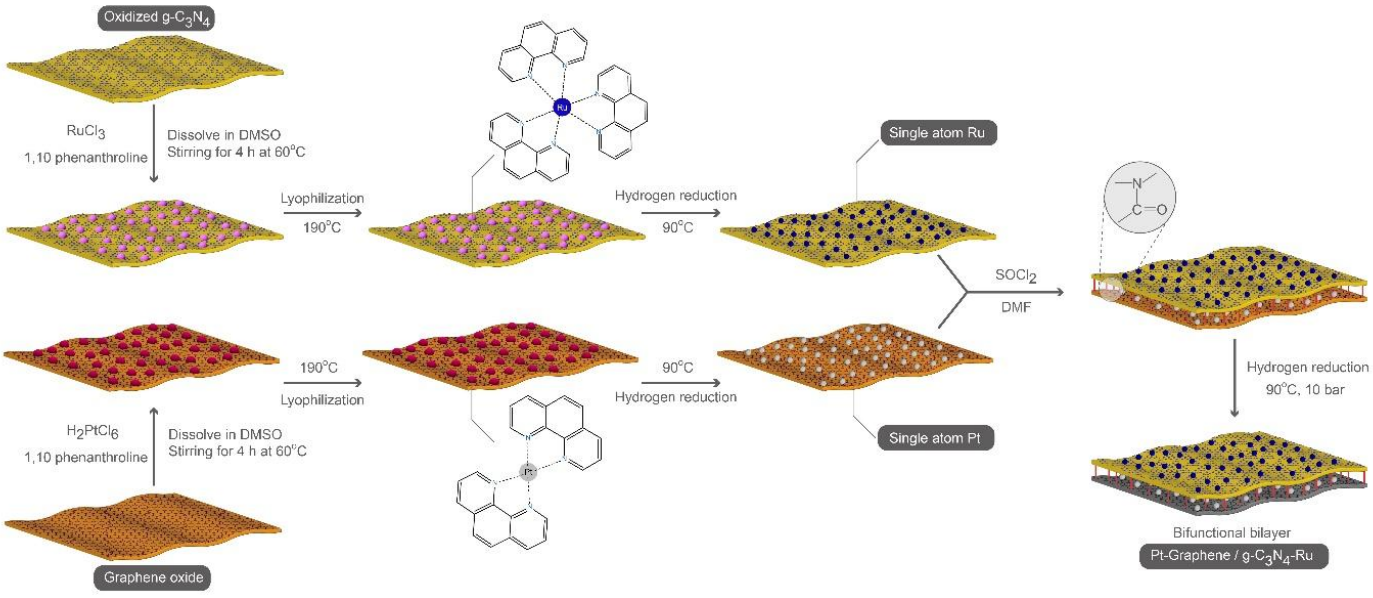

Figure 100. Illustration for the synthesis of atomic scale metal leaf-like structure Pt-G/gC_3N_4-Ru gradient photocatalyst.

References

[1] R.B. Jackson, P. Friedlingstein, C. Le Quéré, S. Abernethy, R.M. Andrew, J.G. Canadell, P. Ciais, S.J. Davis, Z. Deng, Z. Liu, J.I. Korsbakken, G.P. Peters, Global fossil carbon emissions rebound near pre-COVID-19 levels, Environmental Research Letters, 17 (2022) 031001.
[2] R.F. Service, Hydrogen Cars: Fad or the Future?, Science, 324 (2009) 1257-1259.
[3] A. Fujishima, K. Honda, Electrochemical Photolysis of Water at a Semiconductor Electrode, Nature, 238 (1972) 37-38.
[4] D.M. Kammen, T.E. Lipman, Assessing the Future Hydrogen Economy, Science, 302 (2003) 226-229.
[5] "Hydrogen Production Cost Estimate Using Biomass Gasification," U.S. National Renewable Energy Laboratory, October, 2011.
[6] NTP (National Toxicology Program), Report on Carcinogens, Fifteenth Edition, U.S. Department of Health and Human Services, Research Triangle Park, 2021.
[7] G. Zhang, Z.-A. Lan, X. Wang, Surface engineering of graphitic carbon nitride polymers with cocatalysts for photocatalytic overall water splitting, Chemical Science, 8 (2017) 5261-5274.
[8] C. Zhao, Z. Chen, R. Shi, X. Yang, T. Zhang, Recent Advances in Conjugated Polymers for Visible-Light-Driven Water Splitting, Advanced Materials, 32 (2020) 1907296.
[9] W.-J. Ong, L.-L. Tan, Y.H. Ng, S.-T. Yong, S.-P. Chai, Graphitic Carbon Nitride (g-C3N4)-Based Photocatalysts for Artificial Photosynthesis and Environmental Remediation: Are We a Step Closer To Achieving Sustainability?, Chemical Reviews, 116 (2016) 7159-7329.
[10] Q. Wang, K. Domen, Particulate Photocatalysts for Light-Driven Water Splitting: Mechanisms, Challenges, and Design Strategies, Chemical Reviews, 120 (2020) 919-985.
[11] Q. Lu, Y. Yu, Q. Ma, B. Chen, H. Zhang, 2D Transition-Metal-Dichalcogenide-Nanosheet-Based Composites for Photocatalytic and Electrocatalytic Hydrogen Evolution Reactions, Advanced Materials, 28 (2016) 1917-1933.
[12] J. LIEBIG, Uber einige Stickstoff - Verbindungen, Annalen der Pharmacie, 10 (1834) 1-47.
[13] E.C. Franklin, THE AMMONO CARBONIC ACIDS, Journal of the American Chemical Society, 44 (1922) 486-509.
[14] X. Wang, S. Blechert, M. Antonietti, Polymeric Graphitic Carbon Nitride for Heterogeneous Photocatalysis, ACS Catalysis, 2 (2012) 1596-1606.
[15] F. Goettmann, A. Fischer, M. Antonietti, A. Thomas, Metal-free catalysis of sustainable Friedel–Crafts reactions: direct activation of benzene by carbon nitrides to avoid the use of metal chlorides and halogenated compounds, Chemical Communications, (2006) 4530-4532.
[16] X. Wang, K. Maeda, A. Thomas, K. Takanabe, G. Xin, J.M. Carlsson, K. Domen, M. Antonietti, A metal-free polymeric photocatalyst for hydrogen production from water under visible light, Nature Materials, 8 (2009) 76-80.
[17] Z. Gu, Z. Cui, Z. Wang, K.S. Qin, Y. Asakura, T. Hasegawa, S. Tsukuda, K. Hongo, R. Maezono, S. Yin, Carbon vacancies and hydroxyls in graphitic carbon nitride: Promoted photocatalytic NO removal activity and mechanism, Applied Catalysis B: Environmental, 279 (2020) 119376.
[18] I. Krivtsov, D. Mitoraj, C. Adler, M. Ilkaeva, M. Sardo, L. Mafra, C. Neumann, A. Turchanin, C. Li, B. Dietzek, R. Leiter, J. Biskupek, U. Kaiser, C. Im, B. Kirchhoff, T. Jacob, R. Beranek, Water-Soluble Polymeric Carbon Nitride Colloidal Nanoparticles for Highly Selective Quasi-Homogeneous Photocatalysis, 59 (2020) 487-495.

[19] F. Goettmann, A. Fischer, M. Antonietti, A. Thomas, Chemical Synthesis of Mesoporous Carbon Nitrides Using Hard Templates and Their Use as a Metal-Free Catalyst for Friedel–Crafts Reaction of Benzene, Angewandte Chemie International Edition, 45 (2006) 4467-4471.
[20] Q. Liang, Z. Li, Z.-H. Huang, F. Kang, Q.-H. Yang, Holey Graphitic Carbon Nitride Nanosheets with Carbon Vacancies for Highly Improved Photocatalytic Hydrogen Production, 25 (2015) 6885-6892.
[21] G. Liu, T. Wang, H. Zhang, X. Meng, D. Hao, K. Chang, P. Li, T. Kako, J. Ye, Nature-Inspired Environmental "Phosphorylation" Boosts Photocatalytic H2 Production over Carbon Nitride Nanosheets under Visible-Light Irradiation, 54 (2015) 13561-13565.
[22] J. Liu, W. Li, L. Duan, X. Li, L. Ji, Z. Geng, K. Huang, L. Lu, L. Zhou, Z. Liu, W. Chen, L. Liu, S. Feng, Y. Zhang, A Graphene-like Oxygenated Carbon Nitride Material for Improved Cycle-Life Lithium/Sulfur Batteries, Nano Letters, 15 (2015) 5137-5142.
[23] X. Song, Y. Hu, M. Zheng, C. Wei, Solvent-free in situ synthesis of g-C3N4/{001}TiO2 composite with enhanced UV- and visible-light photocatalytic activity for NO oxidation, Applied Catalysis B: Environmental, 182 (2016) 587-597.
[24] Z. Zhang, D. Jiang, D. Li, M. He, M. Chen, Construction of SnNb2O6 nanosheet/g-C3N4 nanosheet two-dimensional heterostructures with improved photocatalytic activity: Synergistic effect and mechanism insight, Applied Catalysis B: Environmental, 183 (2016) 113-123.
[25] D.H. Wang, J.N. Pan, H.H. Li, J.J. Liu, Y.B. Wang, L.T. Kang, J.N. Yao, A pure organic heterostructure of μ-oxo dimeric iron(iii) porphyrin and graphitic-C3N4 for solar H2 roduction from water, Journal of Materials Chemistry A, 4 (2016) 290-296.
[26] T.K.A. Nguyen, T.-T. Pham, H. Nguyen-Phu, E.W. Shin, The effect of graphitic carbon nitride precursors on the photocatalytic dye degradation of water-dispersible graphitic carbon nitride photocatalysts, Applied Surface Science, 537 (2021) 148027.
[27] P.A. Nguyen, Q.D. Dao, T.T. Dang, T.V.A. Hoang, J.S. Chung, E.W. Shin, Highly dispersed PtO over g-C3N4 by specific metal-support interactions and optimally distributed Pt species to enhance hydrogen evolution rate of Pt/g-C3N4 photocatalysts, Chemical Engineering Journal, 464 (2023) 142765.
[28] K. Wang, Q. Li, B. Liu, B. Cheng, W. Ho, J. Yu, Sulfur-doped g-C3N4 with enhanced photocatalytic CO2-reduction performance, Applied Catalysis B: Environmental, 176-177 (2015) 44-52.
[29] G. Zhang, J. Zhang, M. Zhang, X. Wang, Polycondensation of thiourea into carbon nitride semiconductors as visible light photocatalysts, Journal of Materials Chemistry, 22 (2012) 8083-8091.
[30] G.P. Mane, S.N. Talapaneni, K.S. Lakhi, H. Ilbeygi, U. Ravon, K. Al-Bahily, T. Mori, D.-H. Park, A. Vinu, Highly Ordered Nitrogen-Rich Mesoporous Carbon Nitrides and Their Superior Performance for Sensing and Photocatalytic Hydrogen Generation, Angewandte Chemie International Edition, 56 (2017) 8481-8485.
[31] Y. Cui, G. Zhang, Z. Lin, X. Wang, Condensed and low-defected graphitic carbon nitride with enhanced photocatalytic hydrogen evolution under visible light irradiation, Applied Catalysis B: Environmental, 181 (2016) 413-419.
[32] K.S. Lakhi, D.-H. Park, K. Al-Bahily, W. Cha, B. Viswanathan, J.-H. Choy, A. Vinu, Mesoporous carbon nitrides: synthesis, functionalization, and applications, Chemical Society Reviews, 46 (2017) 72-101.

[33] D.J. Martin, P.J.T. Reardon, S.J.A. Moniz, J. Tang, Visible Light-Driven Pure Water Splitting by a Nature-Inspired Organic Semiconductor-Based System, Journal of the American Chemical Society, 136 (2014) 12568-12571.
[34] M.K. Bhunia, S. Melissen, M.R. Parida, P. Sarawade, J.-M. Basset, D.H. Anjum, O.F. Mohammed, P. Sautet, T. Le Bahers, K. Takanabe, Dendritic Tip-on Polytriazine-Based Carbon Nitride Photocatalyst with High Hydrogen Evolution Activity, Chemistry of Materials, 27 (2015) 8237-8247.
[35] Q. Han, B. Wang, Y. Zhao, C. Hu, L. Qu, A Graphitic-C3N4 “Seaweed” Architecture for Enhanced Hydrogen Evolution, Angewandte Chemie International Edition, 54 (2015) 11433-11437.
[36] M. Fronczak, K. Demby, P. Strachowski, M. Strawski, M. Bystrzejewski, Graphitic Carbon Nitride Doped with the s-Block Metals: Adsorbent for the Removal of Methyl Blue and Copper(II) Ions, Langmuir, 34 (2018) 7272-7283.
[37] S. Guo, Y. Zhu, Y. Yan, Y. Min, J. Fan, Q. Xu, Holey structured graphitic carbon nitride thin sheets with edge oxygen doping via photo-Fenton reaction with enhanced photocatalytic activity, Applied Catalysis B: Environmental, 185 (2016) 315-321.
[38] Y. Li, Z. He, L. Liu, Y. Jiang, W.-J. Ong, Y. Duan, W. Ho, F. Dong, Inside-and-out modification of graphitic carbon nitride (g-C3N4) photocatalysts via defect engineering for energy and environmental science, Nano Energy, 105 (2023) 108032.
[39] T.T. Dang, T.K.A. Nguyen, K.C. Bhamu, T. Mahvelati-Shamsabadi, V.K.H. Van, E.W. Shin, K.-H. Chung, S.H. Hur, W.M. Choi, S.G. Kang, J.S. Chung, Engineering Holey Defects on 2D Graphitic Carbon Nitride Nanosheets by Solvolysis in Organic Solvents, ACS Catalysis, 12 (2022) 13763-13780.
[40] P.K. Das, R. Poonchi Sivasankaran, M. Arunachalam, K.R. Subhash, J.-S. Ha, K.-S. Ahn, S.H. Kang, Highly efficient and stable g□C3N4 decorated Ta3N5 nanotube on n-Si substrate for solar water oxidation, Applied Surface Science, 565 (2021) 150456.
[41] M. Michalska, V. Matějka, J. Pavlovský, P. Praus, M. Ritz, J. Serenčíšová, L. Gembalová, M. Kormunda, K. Foniok, M. Reli, G. Simha Martynková, Effect of Ag modification on TiO2 and melem/g-C3N4 composite on photocatalytic performances, Scientific Reports, 13 (2023) 5270.
[42] J.-H. Zhang, M.-J. Wei, Z.-W. Wei, M. Pan, C.-Y. Su, Ultrathin Graphitic Carbon Nitride Nanosheets for Photocatalytic Hydrogen Evolution, ACS Applied Nano Materials, 3 (2020) 1010-1018.
[43] Y. Zhu, A. Marianov, H. Xu, C. Lang, Y. Jiang, Bimetallic Ag–Cu Supported on Graphitic Carbon Nitride Nanotubes for Improved Visible-Light Photocatalytic Hydrogen Production, ACS Applied Materials & Interfaces, 10 (2018) 9468-9477.
[44] Y. Zhu, X. Zheng, Y. Lu, X. Yang, A. Kheradmand, Y. Jiang, Efficient upconverting carbon nitride nanotubes for near-infrared-driven photocatalytic hydrogen production, Nanoscale, 11 (2019) 20274-20283.
[45] Z. Zhao, Y. Dai, J. Lin, G. Wang, Highly-Ordered Mesoporous Carbon Nitride with Ultrahigh Surface Area and Pore Volume as a Superior Dehydrogenation Catalyst, Chemistry of Materials, 26 (2014) 3151-3161.
[46] K.S. Novoselov, A.K. Geim, S.V. Morozov, D. Jiang, Y. Zhang, S.V. Dubonos, I.V. Grigorieva, A.A. Firsov, Electric Field Effect in Atomically Thin Carbon Films, Science, 306 (2004) 666-669.
[47] A.K. Geim, K.S. Novoselov, The rise of graphene, Nature Materials, 6 (2007) 183-191.

[48] P. Kumar, D. Laishram, R.K. Sharma, A. Vinu, J. Hu, M.G. Kibria, Boosting Photocatalytic Activity Using Carbon Nitride Based 2D/2D van der Waals Heterojunctions, Chemistry of Materials, 33 (2021) 9012-9092.
[49] G. Xie, K. Zhang, B. Guo, Q. Liu, L. Fang, J.R. Gong, Graphene-Based Materials for Hydrogen Generation from Light-Driven Water Splitting, Advanced Materials, 25 (2013) 3820-3839.
[50] J. Zhang, J. Yu, M. Jaroniec, J.R. Gong, Noble Metal-Free Reduced Graphene Oxide-ZnxCd1−xS Nanocomposite with Enhanced Solar Photocatalytic H2-Production Performance, Nano Letters, 12 (2012) 4584-4589.
[51] A. Du, S. Sanvito, Z. Li, D. Wang, Y. Jiao, T. Liao, Q. Sun, Y.H. Ng, Z. Zhu, R. Amal, S.C. Smith, Hybrid Graphene and Graphitic Carbon Nitride Nanocomposite: Gap Opening, Electron–Hole Puddle, Interfacial Charge Transfer, and Enhanced Visible Light Response, Journal of the American Chemical Society, 134 (2012) 4393-4397.
[52] P. Lindgren, G. Kastlunger, A.A. Peterson, A Challenge to the G ~ 0 Interpretation of Hydrogen Evolution, ACS Catalysis, 10 (2020) 121-128.
[53] M.Z. Rahman, T. Edvinsson, J. Gascon, Hole utilization in solar hydrogen production, Nature Reviews Chemistry, 6 (2022) 243-258.
[54] T.T. Dang, V.H. Pham, S.H. Hur, E.J. Kim, B.S. Kong, J.S. Chung, Superior dispersion of highly reduced graphene oxide in N,N-dimethylformamide, J Colloid Interface Sci, 376 (2012) 91-96.
[55] A. O'Neill, U. Khan, P.N. Nirmalraj, J. Boland, J.N. Coleman, Graphene Dispersion and Exfoliation in Low Boiling Point Solvents, The Journal of Physical Chemistry C, 115 (2011) 5422-5428.
[56] M. Ayán-Varela, S. Villar-Rodil, J.I. Paredes, J.M. Munuera, A. Pagán, A.A. Lozano-Pérez, J.L. Cenis, A. Martínez-Alonso, J.M.D. Tascón, Investigating the Dispersion Behavior in Solvents, Biocompatibility, and Use as Support for Highly Efficient Metal Catalysts of Exfoliated Graphitic Carbon Nitride, ACS Applied Materials & Interfaces, 7 (2015) 24032-24045.
[57] V.H. Pham, T.T. Dang, K. Singh, S.H. Hur, E.W. Shin, J.S. Kim, M.A. Lee, S.H. Baeck, J.S. Chung, A catalytic and efficient route for reduction of graphene oxide by hydrogen spillover, J. Mater. Chem. A, 1 (2013) 1070-1077.
[58] C.F. Goodeve, J.A. Kitchener, The mechanism of photosensitisation by solids, Transactions of the Faraday Society, 34 (1938) 902-908.
[59] G. Zhang, Z.-A. Lan, L. Lin, S. Lin, X. Wang, Overall water splitting by Pt/g-C3N4 photocatalysts without using sacrificial agents, Chemical Science, 7 (2016) 3062-3066.
[60] F.K. Kessler, Y. Zheng, D. Schwarz, C. Merschjann, W. Schnick, X. Wang, M.J. Bojdys, Functional carbon nitride materials — design strategies for electrochemical devices, Nature Reviews Materials, 2 (2017) 17030.
[61] J. Fang, H. Fan, M. Li, C. Long, Nitrogen self-doped graphitic carbon nitride as efficient visible light photocatalyst for hydrogen evolution, Journal of Materials Chemistry A, 3 (2015) 13819-13826.
[62] L. Shi, T. Wang, H. Zhang, K. Chang, J. Ye, Electrostatic Self-Assembly of Nanosized Carbon Nitride Nanosheet onto a Zirconium Metal–Organic Framework for Enhanced Photocatalytic CO2 Reduction, 25 (2015) 5360-5367.

[63] Y. Shiraishi, Y. Kofuji, H. Sakamoto, S. Tanaka, S. Ichikawa, T. Hirai, Effects of Surface Defects on Photocatalytic H2O2 Production by Mesoporous Graphitic Carbon Nitride under Visible Light Irradiation, ACS Catalysis, 5 (2015) 3058-3066.
[64] Y. Shiraishi, S. Kanazawa, Y. Sugano, D. Tsukamoto, H. Sakamoto, S. Ichikawa, T. Hirai, Highly Selective Production of Hydrogen Peroxide on Graphitic Carbon Nitride (g-C3N4) Photocatalyst Activated by Visible Light, ACS Catalysis, 4 (2014) 774-780.
[65] K. Schwinghammer, B. Tuffy, M.B. Mesch, E. Wirnhier, C. Martineau, F. Taulelle, W. Schnick, J. Senker, B.V. Lotsch, Triazine-based Carbon Nitrides for Visible-Light-Driven Hydrogen Evolution, 52 (2013) 2435-2439.
[66] J. Zhang, B.D. Frank, B. Kumru, B.V.K.J. Schmidt, Graphitic Carbon Nitride Stabilized Water-in-Water Emulsions, 42 (2021) 2000433.
[67] P. Niu, L. Zhang, G. Liu, H.-M. Cheng, Graphene-Like Carbon Nitride Nanosheets for Improved Photocatalytic Activities, 22 (2012) 4763-4770.
[68] C. Ye, J.-X. Li, Z.-J. Li, X.-B. Li, X.-B. Fan, L.-P. Zhang, B. Chen, C.-H. Tung, L.-Z. Wu, Enhanced Driving Force and Charge Separation Efficiency of Protonated g-C3N4 for Photocatalytic O2 Evolution, ACS Catalysis, 5 (2015) 6973-6979.
[69] Y. Zheng, L. Lin, X. Ye, F. Guo, X. Wang, Helical Graphitic Carbon Nitrides with Photocatalytic and Optical Activities, 53 (2014) 11926-11930.
[70] S. Zhang, J. Li, M. Zeng, J. Li, J. Xu, X. Wang, Bandgap Engineering and Mechanism Study of Nonmetal and Metal Ion Codoped Carbon Nitride: C+Fe as an Example, 20 (2014) 9805-9812.
[71] Z. Song, T. Lin, L. Lin, S. Lin, F. Fu, X. Wang, L. Guo, Invisible Security Ink Based on Water-Soluble Graphitic Carbon Nitride Quantum Dots, 55 (2016) 2773-2777.
[72] B. Antil, L. Kumar, K.P. Reddy, C.S. Gopinath, S. Deka, Direct Thermal Polymerization Approach to N-Rich Holey Carbon Nitride Nanosheets and Their Promising Photocatalytic H2 Evolution and Charge-Storage Activities, ACS Sustainable Chemistry & Engineering, 7 (2019) 9428-9438.
[73] G. Li, Z. Xie, S. Chai, X. Chen, X. Wang, A facile one-step fabrication of holey carbon nitride nanosheets for visible-light-driven hydrogen evolution, Applied Catalysis B: Environmental, 283 (2021) 119637.
[74] L. Shi, L. Yang, W. Zhou, Y. Liu, L. Yin, X. Hai, H. Song, J. Ye, Photoassisted Construction of Holey Defective g-C3N4 Photocatalysts for Efficient Visible-Light-Driven H2O2 Production, Small, 14 (2018) 1703142.
[75] M. Sun, H.-X. Guan, W.-D. Zhang, Y.-X. Yu, Strong organic acid-assistant synthesis of holey graphitic carbon nitride for efficient visible light photocatalytic H2 generation, International Journal of Hydrogen Energy, 44 (2019) 23091-23100.
[76] P. Giannozzi, S. Baroni, N. Bonini, M. Calandra, R. Car, C. Cavazzoni, D. Ceresoli, G.L. Chiarotti, M. Cococcioni, I. Dabo, A. Dal Corso, S. de Gironcoli, S. Fabris, G. Fratesi, R. Gebauer, U. Gerstmann, C. Gougoussis, A. Kokalj, M. Lazzeri, L. Martin-Samos, N. Marzari, F. Mauri, R. Mazzarello, S. Paolini, A. Pasquarello, L. Paulatto, C. Sbraccia, S. Scandolo, G. Sclauzero, A.P. Seitsonen, A. Smogunov, P. Umari, R.M. Wentzcovitch, QUANTUM ESPRESSO: a modular and open-source software project for quantum simulations of materials, Journal of Physics: Condensed Matter, 21 (2009) 395502.
[77] J.P. Perdew, K. Burke, M. Ernzerhof, Generalized Gradient Approximation Made Simple, Physical Review Letters, 77 (1996) 3865-3868.

[78] N. Marzari, D. Vanderbilt, A. De Vita, M.C. Payne, Thermal Contraction and Disordering of the Al(110) Surface, Physical Review Letters, 82 (1999) 3296-3299.
[79] S. Grimme, J. Antony, S. Ehrlich, H. Krieg, A consistent and accurate ab initio parametrization of density functional dispersion correction (DFT-D) for the 94 elements H-Pu, The Journal of Chemical Physics, 132 (2010) 154104.
[80] K. Momma, F. Izumi, VESTA 3 for three-dimensional visualization of crystal, volumetric and morphology data, Journal of Applied Crystallography, 44 (2011) 1272-1276.
[81] Index, Density Functional Theory2009, pp. 235-238.
[82] R. David, A. Tuladhar, L. Zhang, C. Arges, R. Kumar, Effect of Oxidation Level on the Interfacial Water at the Graphene Oxide–Water Interface: From Spectroscopic Signatures to Hydrogen-Bonding Environment, The Journal of Physical Chemistry B, 124 (2020) 8167-8178.
[83] Y. Xiao, G. Tian, W. Li, Y. Xie, B. Jiang, C. Tian, D. Zhao, H. Fu, Molecule Self-Assembly Synthesis of Porous Few-Layer Carbon Nitride for Highly Efficient Photoredox Catalysis, Journal of the American Chemical Society, 141 (2019) 2508-2515.
[84] J. Fang, H. Fan, Z. Zhu, L.B. Kong, L. Ma, "Dyed" graphitic carbon nitride with greatly extended visible-light-responsive range for hydrogen evolution, Journal of Catalysis, 339 (2016) 93-101.
[85] T. Suter, V. Brázdová, K. McColl, T.S. Miller, H. Nagashima, E. Salvadori, A. Sella, C.A. Howard, C.W.M. Kay, F. Corà, P.F. McMillan, Synthesis, Structure and Electronic Properties of Graphitic Carbon Nitride Films, The Journal of Physical Chemistry C, 122 (2018) 25183-25194.
[86] J. Wen, J. Xie, X. Chen, X. Li, A review on g-C3N4-based photocatalysts, Applied Surface Science, 391 (2017) 72-123.
[87] R.C. Pawar, S. Kang, J.H. Park, J.-h. Kim, S. Ahn, C.S. Lee, Room-temperature synthesis of nanoporous 1D microrods of graphitic carbon nitride (g-C3N4) with highly enhanced photocatalytic activity and stability, Scientific Reports, 6 (2016) 31147.
[88] H. Katsumata, F. Higashi, Y. Kobayashi, I. Tateishi, M. Furukawa, S. Kaneco, Dual-defect-modified graphitic carbon nitride with boosted photocatalytic activity under visible light, Scientific Reports, 9 (2019) 14873.
[89] J. Fu, B. Zhu, C. Jiang, B. Cheng, W. You, J. Yu, Hierarchical Porous O-Doped g-C3N4 with Enhanced Photocatalytic CO2 Reduction Activity, 13 (2017) 1603938.
[90] J. Huang, H. Wang, H. Yu, Q. Zhang, Y. Cao, F. Peng, Oxygen Doping in Graphitic Carbon Nitride for Enhanced Photocatalytic Hydrogen Evolution, 13 (2020) 5041-5049.
[91] J. Wang, Z. Yang, W. Yao, X. Gao, D. Tao, Defects modified in the exfoliation of g-C3N4 nanosheets via a self-assembly process for improved hydrogen evolution performance, Applied Catalysis B: Environmental, 238 (2018) 629-637.
[92] S. Yu, J. Li, Y. Zhang, M. Li, F. Dong, T. Zhang, H. Huang, Local spatial charge separation and proton activation induced by surface hydroxylation promoting photocatalytic hydrogen evolution of polymeric carbon nitride, Nano Energy, 50 (2018) 383-392.
[93] Y. Hang Li, J. Xing, Z. Jia Chen, Z. Li, F. Tian, L. Rong Zheng, H. Feng Wang, P. Hu, H. Jun Zhao, H. Gui Yang, Unidirectional suppression of hydrogen oxidation on oxidized platinum clusters, Nature Communications, 4 (2013) 2500.
[94] V.W.-h. Lau, I. Moudrakovski, T. Botari, S. Weinberger, M.B. Mesch, V. Duppel, J. Senker, V. Blum, B.V. Lotsch, Rational design of carbon nitride photocatalysts by identification of cyanamide defects as catalytically relevant sites, Nature Communications, 7 (2016) 12165.
[95] T.S. Ahmadi, Z.L. Wang, T.C. Green, A. Henglein, M.A. El-Sayed, Shape-Controlled Synthesis of Colloidal Platinum Nanoparticles, 272 (1996) 1924-1925.

[96] N. Miyashita, T. Yasuda, H. Kiuchi, Hydrogen Reduction of Aqueous Chloroplatinic Acid Solution, Shigen-to-Sozai, 110 (1994) 1089-1093.
[97] J.H. Jensen, J.C. Kromann, The Molecule Calculator: A Web Application for Fast Quantum Mechanics-Based Estimation of Molecular Properties, Journal of Chemical Education, 90 (2013) 1093-1095.
[98] B. Erdem, M. Cebe, Determination of Steric Effect on the Esterification of Different Alcohols with Propanoic Acid over Cation-exchange Resin Catalyst Dowex 50Wx4, Zeitschrift für Physikalische Chemie, 225 (2011) 125-136.
[99] Y. Jiang, Z. Sun, C. Tang, Y. Zhou, L. Zeng, L. Huang, Enhancement of photocatalytic hydrogen evolution activity of porous oxygen doped g-C3N4 with nitrogen defects induced by changing electron transition, Applied Catalysis B: Environmental, 240 (2019) 30-38.
[100] L. Cai, J. Hu, M. Li, P. Yin, Hybrid catalysts of molybdovanadophosphoric acid and g-C3N4 with tunable bandgaps, Dalton Transactions, 49 (2020) 10724-10728.
[101] P. Babu, S. Mohanty, B. Naik, K. Parida, Serendipitous Assembly of Mixed Phase BiVO4 on B-Doped g-C3N4: An Appropriate p–n Heterojunction for Photocatalytic O2 evolution and Cr(VI) reduction, Inorganic Chemistry, 58 (2019) 12480-12491.
[102] S. Tonda, S. Kumar, S. Kandula, V. Shanker, Fe-doped and -mediated graphitic carbon nitride nanosheets for enhanced photocatalytic performance under natural sunlight, Journal of Materials Chemistry A, 2 (2014) 6772-6780.
[103] Z. Fang, Y. Hong, D. Li, B. Luo, B. Mao, W. Shi, One-Step Nickel Foam Assisted Synthesis of Holey G-Carbon Nitride Nanosheets for Efficient Visible-Light Photocatalytic H2 Evolution, ACS Applied Materials & Interfaces, 10 (2018) 20521-20529.
[104] J. Han, H.Y. Zou, M.X. Gao, C.Z. Huang, A graphitic carbon nitride based fluorescence resonance energy transfer detection of riboflavin, Talanta, 148 (2016) 279-284.
[105] N. Zhang, M.-Q. Yang, S. Liu, Y. Sun, Y.-J. Xu, Waltzing with the Versatile Platform of Graphene to Synthesize Composite Photocatalysts, Chemical Reviews, 115 (2015) 10307-10377.
[106] S. Cao, L. Piao, Considerations for a More Accurate Evaluation Method for Photocatalytic Water Splitting, Angewandte Chemie International Edition, 59 (2020) 18312-18320.
[107] M. Qureshi, K. Takanabe, Insights on Measuring and Reporting Heterogeneous Photocatalysis: Efficiency Definitions and Setup Examples, Chemistry of Materials, 29 (2017) 158-167.
[108] M. Melchionna, P. Fornasiero, Updates on the Roadmap for Photocatalysis, ACS Catalysis, 10 (2020) 5493-5501.
[109] K. Li, L. Wang, Z. Chen, X. Yang, Y.-X. Yu, W.-D. Zhang, Y. Wang, Y. Shi, K.P. Loh, Q.-H. Xu, Photocatalytic Hydrogen Evolution under Ambient Conditions on Polymeric Carbon Nitride/Donor-π-Acceptor Organic Molecule Heterostructures, Advanced Functional Materials, 30 (2020) 2005106.
[110] J. Sun, J. Zhang, M. Zhang, M. Antonietti, X. Fu, X. Wang, Bioinspired hollow semiconductor nanospheres as photosynthetic nanoparticles, Nature Communications, 3 (2012) 1139.
[111] S. Min, G. Lu, Enhanced Electron Transfer from the Excited Eosin Y to mpg-C3N4 for Highly Efficient Hydrogen Evolution under 550 nm Irradiation, The Journal of Physical Chemistry C, 116 (2012) 19644-19652.
[112] M. Aksoy, G. Yanalak, E. Aslan, İ.H. Patır, Ö. Metin, Visible light-driven hydrogen evolution by using mesoporous carbon nitride-metal ferrite (MFe2O4/mpg-CN; M: Mn, Fe, Co

and Ni) nanocomposites as catalysts, International Journal of Hydrogen Energy, 45 (2020) 16509-16518.
[113] J. Xu, Y. Li, S. Peng, G. Lu, S. Li, Eosin Y-sensitized graphitic carbon nitride fabricated by heating urea for visible light photocatalytic hydrogen evolution: the effect of the pyrolysis temperature of urea, Physical Chemistry Chemical Physics, 15 (2013) 7657-7665.
[114] Y. Liu, X. Xu, J. Zhang, H. Zhang, W. Tian, X. Li, M.O. Tade, H. Sun, S. Wang, Flower-like MoS2 on graphitic carbon nitride for enhanced photocatalytic and electrochemical hydrogen evolutions, Applied Catalysis B: Environmental, 239 (2018) 334-344.
[115] S. Yang, Y. Gong, J. Zhang, L. Zhan, L. Ma, Z. Fang, R. Vajtai, X. Wang, P.M. Ajayan, Exfoliated Graphitic Carbon Nitride Nanosheets as Efficient Catalysts for Hydrogen Evolution Under Visible Light, Advanced Materials, 25 (2013) 2452-2456.
[116] J. Ran, T.Y. Ma, G. Gao, X.-W. Du, S.Z. Qiao, Porous P-doped graphitic carbon nitride nanosheets for synergistically enhanced visible-light photocatalytic H2 production, Energy & Environmental Science, 8 (2015) 3708-3717.
[117] H.W. Kang, S.N. Lim, D. Song, S.B. Park, Organic-inorganic composite of g-C3N4–SrTiO3:Rh photocatalyst for improved H2 evolution under visible light irradiation, International Journal of Hydrogen Energy, 37 (2012) 11602-11610.
[118] P. Martín-Ramos, J. Martín-Gil, R.C. Dante, F. Vaquero, R.M. Navarro, J.L.G. Fierro, A simple approach to synthesize g-C3N4 with high visible light photoactivity for hydrogen production, International Journal of Hydrogen Energy, 40 (2015) 7273-7281.
[119] F. Cheng, H. Yin, Q. Xiang, Low-temperature solid-state preparation of ternary CdS/g-C3N4/CuS nanocomposites for enhanced visible-light photocatalytic H2-production activity, Applied Surface Science, 391 (2017) 432-439.
[120] J. Zhang, F. Huang, Enhanced visible light photocatalytic H2 production activity of g-C3N4 via carbon fiber, Applied Surface Science, 358 (2015) 287-295.
[121] Q. Sun, P. Wang, H. Yu, X. Wang, In situ hydrothermal synthesis and enhanced photocatalytic H2-evolution performance of suspended rGO/g-C3N4 photocatalysts, Journal of Molecular Catalysis A: Chemical, 424 (2016) 369-376.
[122] X. Wu, F. Chen, X. Wang, H. Yu, In situ one-step hydrothermal synthesis of oxygen-containing groups-modified g-C3N4 for the improved photocatalytic H2-evolution performance, Applied Surface Science, 427 (2018) 645-653.
[123] J.S. Kim, J.W. Oh, S.I. Woo, Improvement of the photocatalytic hydrogen production rate of g-C3N4 following the elimination of defects on the surface, Catalysis Today, 293-294 (2017) 8-14.
[124] Q. Xiang, J. Yu, M. Jaroniec, Preparation and Enhanced Visible-Light Photocatalytic H2-Production Activity of Graphene/C3N4 Composites, The Journal of Physical Chemistry C, 115 (2011) 7355-7363.
[125] D. Jiang, L. Chen, J. Xie, M. Chen, Ag2S/g-C3N4 composite photocatalysts for efficient Pt-free hydrogen production. The co-catalyst function of Ag/Ag2S formed by simultaneous photodeposition, Dalton Transactions, 43 (2014) 4878-4885.
[126] A. Suryawanshi, P. Dhanasekaran, D. Mhamane, S. Kelkar, S. Patil, N. Gupta, S. Ogale, Doubling of photocatalytic H2 evolution from g-C3N4 via its nanocomposite formation with multiwall carbon nanotubes: Electronic and morphological effects, International Journal of Hydrogen Energy, 37 (2012) 9584-9589.

[127] Y. Li, X. Feng, Z. Lu, H. Yin, F. Liu, Q. Xiang, Enhanced photocatalytic H2-production activity of C-dots modified g-C3N4/TiO2 nanosheets composites, Journal of Colloid and Interface Science, 513 (2018) 866-876.
[128] J. Yu, S. Wang, B. Cheng, Z. Lin, F. Huang, Noble metal-free Ni(OH)2–g-C3N4 composite photocatalyst with enhanced visible-light photocatalytic H2-production activity, Catalysis Science & Technology, 3 (2013) 1782-1789.
[129] J. Wang, Y. Xia, H. Zhao, G. Wang, L. Xiang, J. Xu, S. Komarneni, Oxygen defects-mediated Z-scheme charge separation in g-C3N4/ZnO photocatalysts for enhanced visible-light degradation of 4-chlorophenol and hydrogen evolution, Applied Catalysis B: Environmental, 206 (2017) 406-416.
[130] B. Wang, J. Zhang, F. Huang, Enhanced visible light photocatalytic H2 evolution of metal-free g-C3N4/SiC heterostructured photocatalysts, Applied Surface Science, 391 (2017) 449-456.
[131] D.Q. Dao, T.K. Anh Nguyen, S.G. Kang, E.W. Shin, Engineering Oxidation States of a Platinum Cocatalyst over Chemically Oxidized Graphitic Carbon Nitride Photocatalysts for Photocatalytic Hydrogen Evolution, ACS Sustainable Chemistry & Engineering, 9 (2021) 14537-14549.
[132] Q. Han, B. Wang, J. Gao, Z. Cheng, Y. Zhao, Z. Zhang, L. Qu, Atomically Thin Mesoporous Nanomesh of Graphitic C3N4 for High-Efficiency Photocatalytic Hydrogen Evolution, ACS Nano, 10 (2016) 2745-2751.
[133] J. Xing, H.B. Jiang, J.F. Chen, Y.H. Li, L. Wu, S. Yang, L.R. Zheng, H.F. Wang, P. Hu, H.J. Zhao, H.G. Yang, Active sites on hydrogen evolution photocatalyst, Journal of Materials Chemistry A, 1 (2013) 15258-15264.
[134] Y. Shi, Z.-R. Ma, Y.-Y. Xiao, Y.-C. Yin, W.-M. Huang, Z.-C. Huang, Y.-Z. Zheng, F.-Y. Mu, R. Huang, G.-Y. Shi, Y.-Y. Sun, X.-H. Xia, W. Chen, Electronic metal–support interaction modulates single-atom platinum catalysis for hydrogen evolution reaction, Nature Communications, 12 (2021) 3021.
[135] H. Wang, C. Qian, J. Liu, Y. Zeng, D. Wang, W. Zhou, L. Gu, H. Wu, G. Liu, Y. Zhao, Integrating Suitable Linkage of Covalent Organic Frameworks into Covalently Bridged Inorganic/Organic Hybrids toward Efficient Photocatalysis, Journal of the American Chemical Society, 142 (2020) 4862-4871.
[136] G. Kresse, J. Furthmüller, Efficient iterative schemes for ab initio total-energy calculations using a plane-wave basis set, Physical Review B, 54 (1996) 11169-11186.
[137] G. Kresse, J. Furthmüller, Efficiency of ab-initio total energy calculations for metals and semiconductors using a plane-wave basis set, Computational Materials Science, 6 (1996) 15-50.
[138] S. Grimme, J. Antony, S. Ehrlich, H. Krieg, A consistent and accurate ab initio parametrization of density functional dispersion correction (DFT-D) for the 94 elements H-Pu, J Chem Phys, 132 (2010) 154104.
[139] P.E. Blöchl, Projector augmented-wave method, Physical Review B, 50 (1994) 17953-17979.
[140] H.J. Monkhorst, J.D. Pack, Special points for Brillouin-zone integrations, Physical Review B, 13 (1976) 5188-5192.
[141] M.I. Kairi, S. Dayou, N.I. Kairi, S.A. Bakar, B. Vigolo, A.R. Mohamed, Toward high production of graphene flakes – a review on recent developments in their synthesis methods and scalability, Journal of Materials Chemistry A, 6 (2018) 15010-15026.

[142] A. Iwase, Y.H. Ng, Y. Ishiguro, A. Kudo, R. Amal, Reduced Graphene Oxide as a Solid-State Electron Mediator in Z-Scheme Photocatalytic Water Splitting under Visible Light, Journal of the American Chemical Society, 133 (2011) 11054-11057.
[143] N. Li, K. Zhang, K. Xie, W. Wei, Y. Gao, M. Bai, Y. Gao, Q. Hou, C. Shen, Z. Xia, B. Wei, Reduced-Graphene-Oxide-Guided Directional Growth of Planar Lithium Layers, Advanced Materials, 32 (2020) 1907079.
[144] P. Makuła, M. Pacia, W. Macyk, How To Correctly Determine the Band Gap Energy of Modified Semiconductor Photocatalysts Based on UV–Vis Spectra, The Journal of Physical Chemistry Letters, 9 (2018) 6814-6817.
[145] X. She, J. Wu, J. Zhong, H. Xu, Y. Yang, R. Vajtai, J. Lou, Y. Liu, D. Du, H. Li, P.M. Ajayan, Oxygenated monolayer carbon nitride for excellent photocatalytic hydrogen evolution and external quantum efficiency, Nano Energy, 27 (2016) 138-146.
[146] Y. Wang, P. Du, H. Pan, L. Fu, Y. Zhang, J. Chen, Y. Du, N. Tang, G. Liu, Increasing Solar Absorption of Atomically Thin 2D Carbon Nitride Sheets for Enhanced Visible-Light Photocatalysis, Advanced Materials, 31 (2019) 1807540.
[147] Atomistic Simulation Software | QuantumATK - Synopsys n.d. .
[148] G. Di Liberto, Á. Morales-García, S.T. Bromley, An unconstrained approach to systematic structural and energetic screening of materials interfaces, Nature Communications, 13 (2022) 6236.
[149] J. Xu, Y. Qi, W. Wang, L. Wang, Montmorillonite-hybridized g-C3N4 composite modified by NiCoP cocatalyst for efficient visible-light-driven photocatalytic hydrogen evolution by dye-sensitization, International Journal of Hydrogen Energy, 44 (2019) 4114-4122.
[150] Y. Qi, J. Xu, M. Zhang, H. Lin, L. Wang, In situ metal–organic framework-derived c-doped Ni3S4/Ni2P hybrid co-catalysts for photocatalytic H2 production over g-C3N4 via dye sensitization, International Journal of Hydrogen Energy, 44 (2019) 16336-16347.
[151] H. Wang, B. Wang, Y. Bian, L. Dai, Enhancing Photocatalytic Activity of Graphitic Carbon Nitride by Codoping with P and C for Efficient Hydrogen Generation, ACS Applied Materials & Interfaces, 9 (2017) 21730-21737.
[152] J. Liu, Y. Liu, N. Liu, Y. Han, X. Zhang, H. Huang, Y. Lifshitz, S.-T. Lee, J. Zhong, Z. Kang, Metal-free efficient photocatalyst for stable visible water splitting via a two-electron pathway, Science, 347 (2015) 970-974.
[153] C. Lee, X. Wei, J.W. Kysar, J. Hone, Measurement of the Elastic Properties and Intrinsic Strength of Monolayer Graphene, Science, 321 (2008) 385-388.
[154] L. Mao, H. Park, R.A. Soler-Crespo, H.D. Espinosa, T.H. Han, S.T. Nguyen, J. Huang, Stiffening of graphene oxide films by soft porous sheets, Nature Communications, 10 (2019) 3677.
[155] Q. Han, N. Chen, J. Zhang, L. Qu, Graphene/graphitic carbon nitride hybrids for catalysis, Materials Horizons, 4 (2017) 832-850.
[156] W.-J. Ong, L.-L. Tan, S.-P. Chai, S.-T. Yong, A.R. Mohamed, Surface charge modification via protonation of graphitic carbon nitride (g-C3N4) for electrostatic self-assembly construction of 2D/2D reduced graphene oxide (rGO)/g-C3N4 nanostructures toward enhanced photocatalytic reduction of carbon dioxide to methane, Nano Energy, 13 (2015) 757-770.
[157] L. Xie, J. Ni, B. Tang, G. He, H. Chen, A self-assembled 2D/2D-type protonated carbon nitride-modified graphene oxide nanocomposite with improved photocatalytic activity, Applied Surface Science, 434 (2018) 456-463.

[158] Y. Li, D. Zhang, Q. Chen, C. Chao, J. Sun, S. Dong, Y. Sun, Synthesis of rGO/g-C3N4 for methyl orange degradation in activating peroxydisulfate under simulated solar light irradiation, Journal of Alloys and Compounds, 907 (2022) 164500.
[159] Z. Gu, B. Zhang, Y. Asakura, S. Tsukuda, H. Kato, M. Kakihana, S. Yin, Alkali-assisted hydrothermal preparation of g-C3N4/rGO nanocomposites with highly enhanced photocatalytic NOx removal activity, Applied Surface Science, 521 (2020) 146213.
[160] Q. Duc Dao, T. Kim Anh Nguyen, T. Truong Dang, S. Gu Kang, H. Nguyen-Phu, L. Thi Do, V. Kim Hieu Van, K.H. Chung, J. Suk Chung, E. Woo Shin, Anchoring highly distributed Pt species over oxidized graphitic carbon nitride for photocatalytic hydrogen evolution: The effect of reducing agents, Applied Surface Science, 609 (2023) 155305.